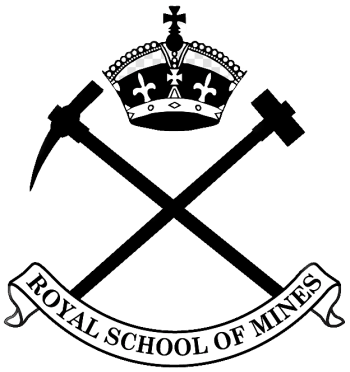


Department of Earth Science and Engineering
Royal School of Mines
Imperial College London

Impacts as a palaeomagnetic recording mechanism in meteorites

by

Thomas Leo North

Thesis submitted for the degree of Doctor of Philosophy
and Diploma of Imperial College London

February 2023

Abstract

This thesis investigates the relationship between impacts and meteorite palaeomagnetism. Using numerical modelling techniques, laboratory shock physics experiments and magnetic measurements, this work finds impact events capable of both recording and erasing meteorite magnetisations, storing the magnetisation of multiple ancient palaeofields at different times as well as controlling the magnetic domain state on the grain-scale.

Chondritic meteorites (chondrites) are among the most primitive meteorites in the Solar System, show no sign of high-temperature melting, but are often found to host a thermoremanence, recorded during their formation around 4.5 billion years ago. Their unmelted and 'unshocked' nature has previously disregarded impacts as significant factors in their evolution. However, recent studies have suggested that low-velocity impacts on the highly-porous chondrite parent bodies lead to the recording of thermoremanences. This mechanism has been developed theoretically and tested numerically, but never tested in the laboratory. It is one of the major goals of my PhD thesis to experimentally test this theory.

Beyond primitive chondrites, another major goal of this thesis is to demonstrate the importance of impacts as a palaeomagnetic recording mechanism, source of demagnetisation and how the magnetisation is able to inform about past impact events. I have modelled the shock-response of a Martian meteorite to understand how multiple palaeomagnetic signatures may be recorded in a single meteorite. Results show highly-localised shear heating heated a fraction of the magnetic carriers present in each impact, recording partial-thermoremanences at different times. Using micromagnetic modelling, the affect of stress on the remanence state of magnetite in the absence of any heating or an external magnetic field has also been explored. The results suggest many meteorites have likely had their remanences altered since recording, even in very weak, 'cold' impacts, < 0.1 GPa.

Acknowledgements

First and foremost I would like to thank my supervisors, Adrian Muxworthy and Gareth Collins, for their time, effort and patience over this project. In particular, I thank Adrian for showing me the true importance of good science, in the face of projects that are challenging and inconvenient, as well as an appreciation for great food and wine. Gareth, one of the finest teachers I have ever had the joy to learn under, I thank for his patience and immeasurable of knowledge about all things impactful. I thank both Adrian and Gareth for their immense contributions to magnetism and shock physics, respectively, for inspiring this project and so many others.

Secondly, I would to thank Tom Davison, without whom I would still be figuring out which colour best associates with temperature (it's red). His time to check in with me weekly and constant availability at the end of an email has been massively appreciated over the past 4 years, and of course, the groundbreaking work he and Gareth have done over the past decade that has carved the way for this project.

I also extend my thanks to the researchers that have donated their time and efforts to this project. To Daniel Eakins, my unofficial supervisor, for his time and acute expertise in impact experiments, and to his colleagues David Chapman and Liam Smith for their help in the manufacturing of meteorites. I thank Wyn Williams for his time and teaching which has enabled me to pursue an understanding of magnetism at the nanoscale. I thank Russell Stracey and Joseph Meggyesi at Imperial College for their generosity and time with their laboratories. Finally, a special thanks to the whole of the hackspace team at Imperial College, where over the years I have made a mess of their metalwork benches and 3D printers.

I am grateful to the developers and maintainers of the iSALE shock physics code, Kai Wünnemann, Jay Melosh, Dirk Elbeshausen, and Boris Ivanov, and to Phil Bland, whose fundamental ideas have inspired much of this thesis.

I thank my research group, the Natural Magnetism Group, past and present, but in particular Evie Baker, Joe Perkins, Alison Cowan and Jack Turney, who are some of the most wonderful people I have ever been lucky to have shared a desk, lunch and time with.

A number of people outside of the academic sphere have been encouraging throughout my PhD—the WEPS, my housemates who have had to put up with me along the way, Conor, Claire and Mark. My Uncle Dan, who encouraged me to follow my pursuit of a PhD in the first

place, and to my brother Alex, who like me becomes intensely dedicated to the things he finds most interesting. My parents, who have offered me endless support in countless ways to make my own decisions and follow my passions, safe in the knowledge they will always encourage me to continue on any path, have enabled me to chase this dream. And finally, to Claire, whose unfaltering love and support has allowed me to prioritise my education. Her emotional awareness, deft planning and love of food have made my social life a joy for the last decade, for which no amount of thank yous can do justice.

Dedication

For Mum, Dad, Alex and Claire.

I, Thomas Leo North, confirm that the work presented in this thesis is my own. Where information has been derived from other sources, I confirm that this has been indicated in the thesis.

Thomas Leo North, February 2023

The copyright of this thesis rests with the author. Unless otherwise indicated, its contents are licensed under a Creative Commons Attribution-Non Commercial 4.0 International Licence (CC BY-NC). Under this licence, you may copy and redistribute the material in any medium or format. You may also create and distribute modified versions of the work. This is on the condition that: you credit the author and do not use it, or any derivative works, for a commercial purpose. When reusing or sharing this work, ensure you make the licence terms clear to others by naming the licence and linking to the licence text. Where a work has been adapted, you should indicate that the work has been changed and describe those changes. Please seek permission from the copyright holder for uses of this work that are not included in this licence or permitted under UK Copyright Law.

Thomas Leo North, February 2023

"The best proof that there's intelligent life in outer space is the fact that it hasn't come here. Two possibilities exist: either we are alone in the Universe, or we are not. Both are equally terrifying."

Arthur C. Clarke

Contents

Abstract **2**

Acknowledgements **3**

1 Introduction **21**

1.1 Introduction to the thesis 21

1.2 Asteroidal processes in the early solar system 23

1.2.1 The formation of the first solar system solids 23

1.2.2 The formation of primitive asteroids and planetesimals 25

1.2.3 Turbulence in the Solar Nebula 26

1.2.4 The role of magnetic fields in the Solar Nebula 26

1.3 Chondritic meteorites 27

1.3.1 The chondrite classification and nomenclature 28

1.3.2 The planetesimal model 29

1.3.3 Chondrites from the planetesimal interior 31

1.3.4 The chondrite parent dynamo 31

1.3.5 Radioactivity in the chondrite planetesimal 32

1.3.6 Chondrule ages too young for differentiated accretion 33

1.3.7 Chondrite groups: a product of burial or different parents? 34

1.4 Impact-induced lithification of chondrites 34

1.4.1 An impact mechanism for recording remanent magnetisation 36

1.4.2 A synopsis of chondrite magnetism 37
1.4.3 Planetary migration from chondrite magnetism 39
1.5 Thesis objectives 40
1.5.1 Overview 40

2 Background to Meteorite Magnetism 43

2.1 Introduction 43
2.2 Fundamentals of rock magnetism 43
2.2.1 Magnetic moment 43
2.2.2 Diamagnetism and paramagnetism 44
2.2.3 Magnetic susceptibility 44
2.3 Ferromagnetism 46
2.3.1 Ferrimagnetism and antiferromagnetism 47
2.3.2 Exchange coupling 47
2.3.3 Curie temperature and Néel point 48
2.4 Magnetic domain theory 50
2.4.1 A balance of energies 51
2.4.2 Magnetic hysteresis 55
2.4.3 Recording fidelity of different domain states 57
2.4.4 Domain state observations from hysteresis parameters 58
2.5 Natural remanent magnetisation 59
2.5.1 Characteristic remanent magnetisation 59
2.5.2 Magnetic relaxation 60
2.5.3 Types of remanence in rocks and meteorites 61
2.6 Palaeomagnetic methods 62
2.6.1 Thermal demagnetisation 63

2.6.2 Alternating field demagnetisation 63

2.7 Interpreting palaeomagnetic data from meteorites 65

2.7.1 Magnetic meteorite mineralogy 66

3 The iSALE Shock Physics Code 68

3.1 An introduction to iSALE 68

3.2 Fundamental equations 69

3.3 Material models 71

3.3.1 Equations of state 71

3.3.2 Strength models 75

3.3.3 The OHNAKA thermal softening model 78

3.3.4 The Simon approximation 78

3.3.5 The $\epsilon - \alpha$ porosity compaction model 78

3.4 Mesoscale modelling 80

3.4.1 Lagrangian tracers 81

3.4.2 pySALESetup 82

4 Recording Magnetic Fields During Impact-induced Compaction 83

4.1 Introduction 83

4.1.1 Motivation and aims 85

4.1.2 Experiment overview 85

4.2 Numerical modelling an impact experiment 86

4.2.1 The recovery fixture criteria 87

4.2.2 The Sawaoka capsule 88

4.2.3 Material models 89

4.3 Capsule optimisation using iSALE-2D 91

4.3.1 Solid capsule simulations 92

4.3.2 An 'air-gap' to reduce shock wave interference 95
4.3.3 Capsule with low-impedance shock attenuation 'pillow' 99
4.3.4 Final capsule design 102
4.4 Capsule manufacture 102
4.5 Experiments: manufacturing chondrites 104
4.5.1 Sample material composition 105
4.5.2 Working in a controlled magnetic field 108
4.5.3 Magnetic mapping the target chamber 111
4.5.4 Sample preparation 112
4.5.5 Shot Procedure 113
4.5.6 Machining of samples from recovered capsules 120
4.6 Results: Magnetic Analysis of Recovered Samples 122
4.6.1 Thermal demagnetisation of the synthetic chondrites 122
4.6.2 Directional magnetic data recorded in synthetic chondrites 124
4.6.3 Unblocking spectra of synthetic chondrites 126
4.6.4 Hysteresis parameters 128
4.6.5 Magnetic properties of aluminium-6061 129
4.6.6 Porosity calculation: SEM and Micro-CT imaging 130
4.7 Discussion 134
4.7.1 Comparison of demagnetisation data to iSALE modelling 135
4.7.2 Relationship between the NRM and magnetising field 137
4.8 Shock classification of synthetic chondrites 137
4.9 Implications for the chondrite parent body 139
4.10 Conclusions 140

5 The Heterogeneous Response of a Martian Meteorite to Planar Shock 142

5.1 Introduction . . . 142

5.2 Methods . . . 144

5.2.1 The iSALE-2D Shock Physics Code . . . 145

5.2.2 ALH 84001 as a Four Material System . . . 146

5.2.3 Equations of State . . . 147

5.2.4 Strength Models . . . 148

5.2.5 Simulation Design . . . 150

5.2.6 Lagrangian Tracers . . . 151

5.2.7 Shock Wave Amplitude . . . 152

5.2.8 Temperature Nomenclature . . . 152

5.2.9 Thermal Equilibrium . . . 153

5.3 Results . . . 154

5.3.1 Reference Simulations . . . 154

5.3.2 Plastic Deformation and Shear Heating in ALH 84001 . . . 156

5.3.3 Influence of Mesoscale Structure . . . 157

5.3.4 Limiting Shear Strength . . . 160

5.3.5 Temperature Dependence on Shock Wave Amplitude . . . 163

5.4 Discussion . . . 163

5.4.1 A Mechanism for Heterogeneous Heating . . . 164

5.4.2 Thermal History Recorded in Magnetic Carriers . . . 166

5.4.3 Effect of shock pulse width on heterogeneous heating . . . 168

5.4.4 Constraints on Shock History from Paleomagnetism . . . 169

5.4.5 New Constraints on the Shock History of ALH 84001 . . . 171

5.4.6 Ejection from Mars . . . 173

5.5 Conclusions . . . 174

6 Micromagnetic Modelling: Effects of Stress on Magnetic Recording Fidelity 176

6.1 Introduction 176

6.2 Micromagnetic modelling code: MERRILL 178

6.3 Methods 180

6.3.1 Grain size and shape 180

6.3.2 Initial magnetic states 181

6.3.3 Applying stress in MERRILL 181

6.3.4 Crystalline (Miller) indices and equal area projection 185

6.4 Results 185

6.4.1 Effect of uniaxial stress on equidimensional SD magnetite 186

6.4.2 SV-SD threshold for equidimensional SV magnetite 188

6.4.3 Effect of uniaxial stress on equidimensional SV magnetite $\geq$ 100 nm . . . 191

6.4.4 Effect of uniaxial stress on elongated SD magnetites 192

6.4.5 Effect of uniaxial stress on elongated SV magnetites 193

6.5 Discussion 197

6.5.1 Stress-induced change to the remanence of SD magnetites 199

6.5.2 Stress-induced change to the remanence of SV magnetites 200

6.5.3 Comparison to analytical SD theory and experimental data 203

6.5.4 Palaeomagnetic implications for meteorites 204

6.6 Conclusions 206

7 Conclusions 209

7.1 Summary of Results 210

7.1.1 TRM recorded in shock experiments on synthetic chondrites 210

7.1.2 Heterogeneous heating in Martian meteorite ALH 84001 211

7.1.3 On the relationship between stress and remanence in SV magnetite . . . 212

7.2 Future Work 213

7.2.1 Manufacturing more synthetic chondrites 213

7.2.2 Meteorite shock response: investigating cross-sections with iSALE 214

7.2.3 Further research on the importance of the single-vortex domain state in meteorites 215

Bibliography **216**

List of Tables

4.1 Tillotson parameters for the aluminium and fused quartz 90

4.2 Mie-Grüneisen parameters for polycarbonate 90

4.3 $\epsilon - \alpha$ porosity properties for silica 91

4.4 Magnetic measurements at collision site 111

4.5 Magnetic measurements across target chamber 112

4.6 Sample chamber measurements 113

4.7 Impact experiment shot velocities 115

4.8 Synthetic chondrite hysteresis parameters 129

5.1 Tillotson parameters for gabbro and chromite 148

5.2 Strength model parameters for Horoman and Norwegian dunite 150

5.3 Peak and equilibrium temperature summary for impacts $3 - 67$ GPa 167

6.1 Explored magnetic states for magnetite 181

List of Figures

1.1 Young Solar Nebula Timeline 24

1.2 Planetesimal model: 'Onion shell' 30

1.3 Planetesimal model: chondritic crust 32

2.1 Diamagnetism and paramagnetism 45

2.2 Ferromagnetic coupling 46

2.3 Two-dimensional spin wave sketch 48

2.4 2D domain states 51

2.5 Basic domain structure 54

2.6 Hysteresis loop 55

2.7 Thermal demagnetisation and partial-TRM 64

4.1 Sawaoka capsule design 89

4.2 Capsule schematic: solid capsule 93

4.3 Shot experiment simulation images from solid capsule 94

4.4 Peak temperature and pressure summary: solid capsule 95

4.5 Capsule schematic: air-gap architecture 96

4.6 Shock wave propagation through capsule with air-gap 97

4.7 Example statistical analysis of capsule air-gap parameters 98

4.8 Peak temperature and pressure summary: air-gap only 99

4.9 Capsule schematic: low-impedance attenuation 'pillow' 100

4.10 Peak temperature and pressure summary: pillow only 101

4.11 Shot experiment simulations: final capsule results 103

4.12 Peak temperature and pressure summary: final capsule design 104

4.13 Capsule architecture comparison: peak pressure and post-shock temperature summary 105

4.14 Capsule technical sheet 106

4.15 Aluminium capsule 107

4.16 Helmholtz cage 109

4.17 Helmholtz coil geometry 109

4.18 Shot recovery experiment setup 112

4.19 Piston Design 113

4.20 External experimental setup 114

4.21 Light gate data for impact experiments 116

4.22 Velocity variation modelling 117

4.23 'Catch can' momentum trap 118

4.24 Aluminium momentum traps 119

4.25 Capsule mount on gun barrel 120

4.26 Post-shock capsule compression 121

4.27 Thermal demagnetisation data from synthetic chondrites 123

4.28 Directional magnetic data for shot experiments 125

4.29 Magnetic unblocking spectra for synthetic chondrites 126

4.30 Major hysteresis of synthetic chondrites 129

4.31 Magnetic analysis of aluminium offcut 130

4.32 Micro-CT image of post-shock machined capsule 131

4.33 Exposed sample image from impact experiments 132

4.34 SEM images of synthetic chondrite 133

4.35 Thresholding SEM images for porosity calculation 134

4.36 Demagnetisation data vs iSALE modelling of shock experiments 136

4.37 Synthetic chondrite NRM vs field intensity 138

5.1 ALH 84001 mesoscale sample selection 146

5.2 Dunite material strength model 149

5.3 iSALE mesoscale simulation schematic 151

5.4 Post-shock pressure, temperature and material maps for both cross-sections . . . 155

5.5 Peak temperature and pressure distributions for both samples 156

5.6 Shear zones mapped to tracer dislocations 157

5.7 Pressure and temperature distributions for rotated samples 158

5.8 Material-reduced post-shock temperature maps for cross-section S1 160

5.9 Rotated cover plate results compared to the 'reference' simulation 161

5.10 Pressure and temperature comparison between the two dunite material models . 162

5.11 Equilibrium temperature vs bulk pressure across the full shock pressure range . 164

5.12 Peak temperatures recorded by each material across the full pressure range . . . 165

5.13 Temperature evolution through time as sample approaches thermal equilibrium . 166

5.14 Temperature maxima in sub-volumes of the sample as it approaches thermal equilibrium 169

6.1 Single domain and single vortex structures 178

6.2 Stress direction application 183

6.3 Stress field acting on grain assemblage 184

6.4 Equal area plot schematic 186

6.5 Uniaxial stress on equidimensional SD grains 187

6.6 Stress-induced remanence transition from SD to SV 189

6.7 SV to SD transition for equidimensional magnetite 190

6.8 Stress threshold dependence on θ 191

6.9 Average response of 80 nm SV assemblage to stress 191

6.10 Equal area projections for equidimensional 100 nm and 150 nm SV magnetites . 193

6.11 Equal area plots for 50 nm, 50% elongated SD magnetite 194

6.12 Vortex rotation from long to short directions for 100 nm elongated magnetite . . 196

6.13 Vortex rotation to easy direction for 200 nm magnetite 197

6.14 Threshold of stress-induced rotation: histograms per grain size 198

6.15 Changes in magnetisation relative to stress axis for assemblages 206

Chapter 1

Introduction

1.1 Introduction to the thesis

Remanent magnetisation recorded in terrestrial rocks has been examined in palaeomagnetic studies for more than a century to better understand magnetic phenomena such as Earth's geodynamo (Brunhes, 1906) and plate tectonics (Glen, 1982). Similarly, the remanent magnetisation recorded in extraterrestrial rocks (meteorites) can provide a valuable insight into magnetic phenomena within the solar system. Martian meteorites are thought to retain information of an ancient dynamo on Mars (Weiss et al., 2000), iron meteorites are thought to be the solid remains of a once-molten planetesimal core (Brecher and Albright, 1977; Tarduno et al., 2012; Nichols et al., 2016, 2021) and primitive rocky meteorites may host an ancient magnetisation that originated from the young Sun (Banerjee and Hargraves, 1972; Brecher and Arrhenius, 1974; Fu et al., 2014; Wang et al., 2015; Bryson et al., 2020a; Borlina et al., 2021). Both the magnitude and direction of a remanent magnetisation can be measured, offering a unique opportunity to examine the complex chemical, thermal and shock history of a sample and its magnetising environment (Dunlop and Özdemir, 1997).

The mechanism by which the remanence was acquired is key to the interpretation of the data. Terrestrial rocks are known to record the geomagnetic field through a number of mechanisms, including cooling from a high temperature (thermoremanent magnetisation, TRM), sedimentation (chemical action or crystal growth; chemical remanent magnetisation, CRM),

as well as passively from being present on the Earth's surface, where mineral magnetisations slowly align with the background field (viscous remanent magnetisation, VRM; Tauxe et al., 2010). However, for meteorites, this is often poorly understood. It is unknown which of these mechanisms are responsible for the magnetisation observed in extra-terrestrial samples as there are competing theories as to the physical, thermal and chemical processes suffered by meteorites. Some meteorites have clearly undergone chemical alteration and host heterogeneously oriented magnetisations, recorded by different crystal populations (Cournede et al., 2015); some meteorites are pristine, 'unshocked' and largely unaltered, yet demagnetise only when they are heated to high 'unblocking' temperatures (Muxworthy et al., 2017) — this is often associated with meteorites that have been subjected to high temperatures in the past and can inform about magnetic carriers present in the rock. Likely sources of heating in meteorites vary depending on their type. For meteorites that display evidence of melting or partial-melting, such as the IAB iron meteorites, there was likely a source of high-temperature metamorphism such as a massive impact on their parent asteroid (Nichols et al., 2018). However for other primitive, unmelted meteorites (such as the ordinary and carbonaceous chondrite groups) that have remained largely unaltered since their formation on their parent asteroid or 'planetesimal', the origin of a high-temperature component of the natural remanent magnetisation (NRM) is more difficult to explain.

Contradictory evidence between thermal and metamorphic histories of extraterrestrial samples has led some palaeomagnetic researchers to conclude that primitive meteorites originate from a small number of differentiated planetesimals which, in catastrophic impacts, disaggregated into the different classes of meteorites that have been recovered (Wood, 1958; Carporzen et al., 2011; Weiss and Elkins-Tanton, 2013). However, these conclusions are contentious, refuted by astropetrological studies which cannot reconcile the relative abundance of ^{26}Al in chondrites with differentiation of the parent body (e.g. Van Schmus and Wood, 1967; Kunihiro et al., 2004), as well as other palaeomagnetism investigations which have recovered magnetic fabrics consistent with impacts (Muxworthy et al., 2017) and randomly orientated chondrule magnetisations that have persisted since before accretion (Fu et al., 2014).

In this chapter, I introduce key concepts and processes that occurred in the early solar

system. This will set the scene of why it is so important palaeomagnetic studies are able to determine the origin of the magnetisation in primitive meteorites. I present a brief history about the formation of some of the most primitive meteorite groups and the leading theories as to how they formed in the solar system before giving an overview of the thesis.

1.2 Asteroidal processes in the early solar system

The solar system is understood to have evolved from the gravitational collapse of a molecular cloud comprised of dust and gas over 4.5 billion years ago (Bouvier and Wadhwa, 2010). Following the collapse, the majority of the mass was concentrated into the centre, forming the Sun, while the remaining material flattened to form a protoplanetary disk. This evolutionary period of the solar system is known as the Solar nebula. Turbulence through the mid-plane of the disk then encouraged collisions, which in turn caused dust particles to clump together or 'accrete' to form centimetre-sized pebbles and subsequently metre-sized boulders (Cuzzi and Weidenschilling, 2006). Further collisions and gas interaction lead these to eventually form large asteroids (planetesimals) ∼10-100 km in size (Wurm et al., 2004). Accretion is understood to have been a relatively gentle process in order to enable adhesion between particles during collisions (Cuzzi et al., 2008). This would have lead to very high porosities (∼70%), where the first-generation bodies resembled 'rubble piles' (Weidenschilling and Cuzzi, 2006).

1.2.1 The formation of the first solar system solids

Calcium-aluminium-rich inclusions (CAIs) are the oldest known solids to have formed in the Solar system (Amelin et al., 2002; Bouvier and Wadhwa, 2010). CAIs are the most primitive solids on record, dated to have formed some 4567 million years ago (Ma) as fine-grained condensates (Connelly et al., 2012). The condensation of CAIs is often used to date the beginning of the solar system.

Chondrules are understood to have formed within 7 Myr of CAI condensation; reported ages range between 4567-4560 Ma (Connelly et al., 2017), implying the oldest chondrules formed

contemporaneously with CAIs. The chondrule formation timescale lies within agreement of the typical ∼6 Myr lifetime of protoplanetary disks (Haisch et al., 2005; Li and Xiao, 2016; Richert et al., 2018) and the associated nebula magnetic field (Fu et al., 2014; Wang et al., 2015).

There are two leading chondrule formation hypotheses: nebula shocks (lightning), and protoplanetary collisions (Wakita et al., 2017). Discussing the validity and which of these processes is responsible for chondrule formation is beyond the scope of this study. However, as protoplanetary collisions would have occurred after the formation of the chondrite parent bodies, it is highly likely chondrules found in chondritic meteorites were formed by nebula lightning (Fig. 1.1; Connelly et al., 2017).

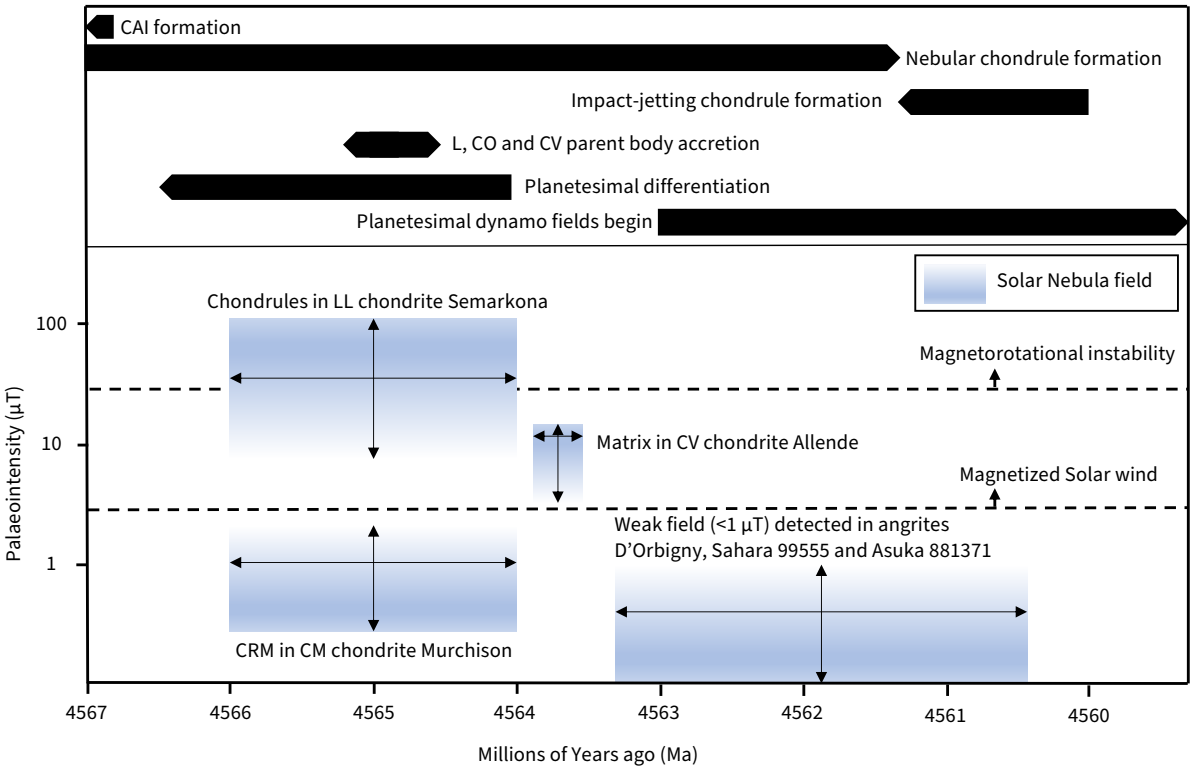


Figure 1.1: A timeline of events in the early solar system. The timeline is compiled using data from Connelly et al. (2017) (Pb-Pb ages for CAI and chondrule formation), Dodds et al. (2021) (dynamo onset time), Fu et al. (2014) (Semarkona data), Muxworthy et al. (2017) (Allende palaeofield), Kletetschka et al. (2003) (Murchison CRM measurement), Doyle et al. (2015) (L, CO and CV parent body ages) and Wang et al. (2017) (angrite measurements). There is a decline in the Solar Nebula field intensity between 4566 Ma until around 4560.5 Ma where studies of recovered meteorites suggest the intensity had decayed to a point where it was unable to impart measurable remanence.

1.2.2 The formation of primitive asteroids and planetesimals

Evolution from primordial, first-generation bodies or 'rubble piles' (Weidenschilling and Cuzzi, 2006), to the lithified and comparably low-porosity asteroids that exist today, required significant porosity depletion and densification. Several processes have been proposed for rock fabric development and the reduction of porosity in asteroids, including gravitational compaction (Fujimura et al., 1983), metamorphism (Stacey et al., 1961), compaction due to overburden (Cain et al., 1986) or impact-induced compaction (Davison et al., 2010; Beitz et al., 2013; Bland et al., 2014; Forman et al., 2016). As the lithostatic pressure generated by the gravitational field of even the largest planetesimals has been shown to be too low for the depletion of porosity observed in meteorites (Weidenschilling and Cuzzi, 2006), chondrites are known to have experienced little metamorphism since accretion and other asteroids dominated by lithostatic overburden are still highly porous (Britt et al., 2002), it is highly likely that impacts are the mechanism responsible for the lithification of planetesimals (Forman et al., 2016).

Evidence for impacts compacting first-generation bodies towards asteroids and planetesimals has been found in some of the most primitive meteorites on record (Bland et al., 2011). Stony chondritic meteorites have been shown to have had an initial matrix porosity between 70-80%, lithified in low-velocity (< 2 km/s) and low-intensity ($< 4 - 5$ GPa) impacts (Bland et al., 2014) to have present-day porosities between 0 - 41% (Macke et al., 2011). These observations also agree with anisotropy of magnetic susceptibility (AMS) measurements (Gattacceca et al., 2005), which have identified impact-induced compaction as the most promising mechanism for fabric development and subsequent densification in primitive meteorites. The repeated, multi-stage impact history required for lithification of these meteorites from an initially porous parent body (Lindgren et al., 2015) has also been observed in heterogeneous compaction effects (Forman et al., 2016). The depletion in porosity required to produce samples consistent with recovered meteorites has been demonstrated in numerical models (Davison et al., 2016) which also predict temperatures in agreement with palaeomagnetic temperature estimates (Fu et al., 2014; Muxworthy et al., 2017; Bryson et al., 2020a).

1.2.3 Turbulence in the Solar Nebula

Accretion models using non-turbulent nebulae have found accretion to be *too* efficient, where large planetesimals grow too quickly, within $\sim 10^4 - 10^5$ Myr (Weidenschilling, 2000). Instead, models which favour turbulence in the mid-plane of the protosolar disk find that accretion was driven by impacts and the bodies which form are more consistent with terrestrial planets (Cuzzi et al., 2008). Gas and dust, spiralling inward from ongoing disk accretion into the Sun, transferred angular momentum into gravitational potential energy which provided a sufficient energy source to maintain turbulence (Cuzzi et al., 2008). However, the mechanism responsible for the transport of angular momentum into turbulent kinetic motion is undetermined. There are a number of good candidates to explain the transport, including the baroclinic instability (Klahr and Bodenheimer, 2003), vertical shear instability (VSI) (Urpin and Brandenburg, 1998; Stoll and Kley, 2014), gravitational instability (Gammie, 2002), Rossby-wave instability (Lovelace and Romanova, 2014), convective over-stability (Latter, 2016), and non-ideal magnetohydrodynamic (MHD) turbulence, namely the magnetocentrifugal wind (MCW) (Blandford and Payne, 1982; Bai, 2014) and magnetorotational instability (MRI) (Balbus and Hawley, 1992). Studying the strength of the magnetic field that permeated the Solar Nebula and how it decayed over time is a direct way to infer which of these processes is responsible for the turbulence that drives accretion in planetary nebulae (Wadhwa et al., 2007).

1.2.4 The role of magnetic fields in the Solar Nebula

The reduction of angular momentum and the subsequent nebula turbulence that fused together dust particles to begin the planet forming process can be attributed to magnetic fields in the Solar Nebula, depending on their strength (Cuzzi et al., 2008). Identifying the strength of the magnetic field in the terrestrial planet forming region ($\sim$0.5-4 AU) is therefore key to developing a broad understanding of the role of magnetism in the early solar system. Astronomical observations of distant protoplanetary disks cannot reveal the strength or depth of nebula fields. However, using meteorites that have been collected on Earth, palaeomagnetic studies are able to glimpse into their magnetic histories which may shed light on planetesimal or Solar Nebula

fields (Fig. 1.1).

There have been many palaeomagnetic studies of primitive meteorites and extraterrestrial solids that have discussed the origin of the magnetisation stored inside; while some studies have focused on a steady magnetic field of parent body dynamo origin (e.g., Stacey et al., 1961; Carporzen et al., 2011; Weiss and Elkins-Tanton, 2013; Wang et al., 2015), others have identified transient nebula fields as the potential palaeofield hosted within (e.g., Levy, 1978; Nagata, 1979; Banerjee and Hargraves, 1972; Fu et al., 2014). The origin of the field stored within meteorites is a subject of active debate due to the uncertainties around the formation of the meteorite parent bodies.

In the case of a nebula origin for the magnetising field, the most likely candidate for the component recorded is the vertical, out-of-plane component of the Solar Nebula field (Cournede et al., 2015). Moderated by MHD turbulence, this component has an estimated relative intensity between 10 μT (Crutcher, 2012) and 100 μT (Wardle, 2007), inherited from the collapse of the protosolar molecular cloud (Brecher and Arrhenius, 1974). This estimate is consistent with palaeofield strengths measured in primitive meteorites; Fu et al. (2014) recovered nebula field strengths between 5 and 54 μT at 2.5 AU around 2-3 Myr after the beginning of the solar system, while Muxworthy et al. (2017) found a palaeofield recorded in the Allende chondritic meteorite with a strength between ∼7-15 μT, likely originating from a nebula field 3-4 Myr after CAI formation. These measurements align closely with magnetic field strength estimates predicted by planetary accretion governed by magnetic fields around the Sun (Bai and Stone, 2013; Bai, 2014).

1.3 Chondritic meteorites

Chondritic meteorites (chondrites) are a class of primitive stony meteorites that formed close to the beginning of the solar system (Connelly et al., 2012). Within the chondrite record are some of the oldest samples ever recovered, making their importance to understanding planet formation invaluable. Chondrites make up the most abundant meteorite class (∼ 86% of total meteorite falls (Bischoff and Geiger, 1995)), understood to originate from the asteroid belt where

collisions and gravitational perturbations alter their trajectories to Earth-crossing orbits.

Chondrites are identified by the presence of chondrules - non-porous, igneous spherules that are understood to be one of the first solids to have formed in the solar system - embedded in a fine-grained silicate matrix. Bulk porosities (the percentage of pore space within the rock) for chondrites have been found to range from 0 to 41% (Macke et al., 2011), with variation between petrologic subtypes and shock classifications (Van Schmus and Wood, 1967). Calculating meteorite porosities are non-trivial, and are calculated using a combination of digital imaging and gas pycnometry (Consolmagno et al., 2008). Recovered chondrites show a significant decrease in porosity between shock stage S1 and S2 (Stöffler et al., 1991), symptomatic of a history of shock compression. Aside from a fusion crust obtained during atmospheric entry to Earth, chondrites have remained relatively unaltered since their formation and present no evidence of melting or differentiation.

In addition to chondrules and CAIs, chondrites have also been found to contain the earliest rock fabrics in the solar system, preserved in the matrix material that surround chondrules (Bland et al., 2011). The magnetic carriers found in the matrix, such as magnetite and pyrrhotite, are often found to host a remanent magnetisation that is different in intensity and alignment from the remanence found in chondrules (Fu et al., 2014; Muxworthy et al., 2017). While chondrules were most likely magnetised prior to their accretion onto the chondrite parent bodies (Fu et al., 2014), the matrix-hosted remanence was likely to have been acquired during the chondrite formation process or subsequent parent body alteration, evidenced by a shared magnetic orientation (Weiss et al., 2010b; Muxworthy et al., 2017).

1.3.1 The chondrite classification and nomenclature

The pristine nature of chondrites has driven the assumption that they originated from small planetesimals, up to several hundreds of kilometres in diameter, but failed to form planets. Catastrophic collisions between planetesimals likely resulted in the destruction and fragmentation of these parent bodies. Scattered throughout the solar system, some fraction of the debris has since moved into an Earth-crossing orbit and fallen to the surface of our planet

(Weidenschilling, 2000).

Due to similarities between the mineralogy and petrology of separate chondritic meteorite falls (Van Schmus and Wood, 1967), the existence of multiple parent bodies is the most accepted origin scenario for chondrites in the meteorite community. Collected from different geographical locations and at different times in history, chondrites are able to be classified into parent groups according to their mineralogy, chemical composition, degree of weathering, oxygen isotope compositions and degree of shock metamorphism (Van Schmus and Wood, 1967; Clayton and Mayeda, 1999; Stöffler et al., 1991; Scott et al., 1992; Wlotzka, 1993; Bischoff and Geiger, 1995). Within their parent groups, chondrites can be classified further by their petrologic type, that is, the degree to which they have been thermally or aqueously altered (this is a number from 1-7, with 1 being the most aqueously altered and 7 being the most thermally metamorphosed). This has led to naming conventions such as 'CV3' for samples from the Vigarano chondrite. Carbonaceous or C-type chondrites are the most primitive members of the chondrite family, while the V acknowledges the geographical location that the first member of the meteorite family was collected - Vigarano, Italy, in the case of the CV chondrites. Subsequent chondrite falls that match the petrology and mineralogy of the first chondrite of that type, for example the Allende meteorite, collected in Mexico, 1969, would then also be categorised as a CV chondrite. In total, there are 30 different chondrite classification groups (Van Schmus and Wood, 1967).

1.3.2 The planetesimal model

In the following sections, I discuss the planetesimal model for chondrite origin. Since the nature of the parent bodies for many meteorite sub-types are unknown, a number of studies have suggested a scenario where multiple meteorite groups may originate from a single, moon-sized differentiated parent body (Elkins-Tanton et al., 2011; Weiss and Elkins-Tanton, 2013). Palaeomagnetic studies of CV chondrite Allende (Weiss et al., 2010b; Carporzen et al., 2011) and the Angrite meteorite group (Weiss et al., 2008a), as well as numerical modelling of radioisotope abundances for global planetesimal melting (Sahijpal et al., 2007; Elkins-Tanton et al., 2011), provide evidence where both chondritic and achondritic meteorites could have formed in an 'onion shell structure' (Fig. 1.2). Large interior regions suffered total melting,

resulting in a large iron-metallic core, surrounded by a partially melted mantle that would have produced a variety of differentiated, melted and partially-melted meteorites (Wood, 1958). Partial melting throughout the parent body could then have maintained an unmelted chondritic crust (Weiss et al., 2008a; Weiss and Elkins-Tanton, 2013). The differences in composition and shock classification of chondrite subgroups can then be explained by their formation depth within the chondritic crust - the most thermally metamorphosed chondrites originate near the crust-mantle boundary, while the most primitive and unaltered originate from the planetesimal surface (Fig. 1.3).

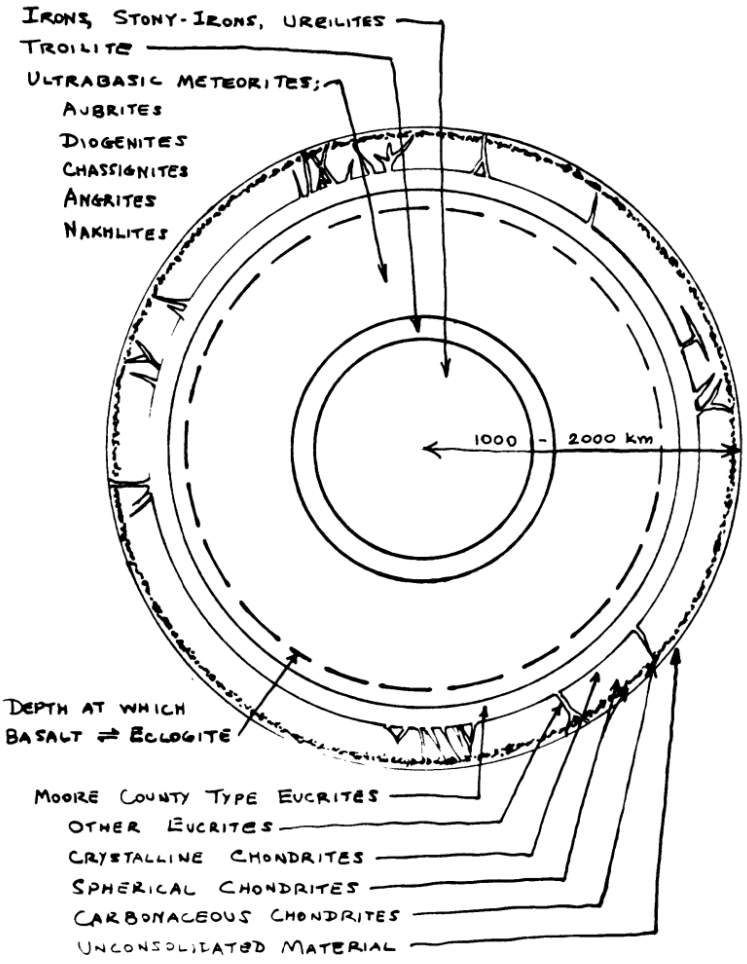


Figure 1.2: An early diagram for "The Proposed Parent Meteorite Planet", from Wood (1958). This sketch is of a single moon-sized planetesimal from which many meteorite groups could have originated as metamorphism varies radially in layers.

1.3.3 Chondrites from the planetesimal interior

To allow for the existence of a thin, unmelted crust on an otherwise differentiated asteroid, accretion onto the parent body is proposed to have occurred through impacts of ∼50 km chondritic-like asteroids that formed around 0.75 Myr after CAI formation (Hevey and Sanders, 2006). In this model, highly efficient convective heat transport from the molten planetesimal interior would effectively preserve a $\sim$ 2 km chondritic crust (Weiss and Elkins-Tanton, 2013) while the core and mantle cooled. A conductively cooled chondritic crust, as suggested in the planetesimal model, would require progressive heating of the newly accumulated chondrite-like material, which is not evident in the thermal records of C-type chondrite samples (Ganino and Libourel, 2017). In contrast, there is evidence to support undifferentiated planetesimal bodies.

The discovery of the CV3 chondrite Northwest Africa (NWA) 2086 (Russell et al., 2005) provides evidence for an undifferentiated CV parent body: NWA 2086 is understood to be a sample from the interior of the CV parent body. The sample bears a high fragmented-to-intact chondrule ratio (compared to similar CV3 chondrites Mokoia and Bali), has led to the conclusion this object likely originated deeper within the interior of the parent asteroid (Kereszturi et al., 2014), yet the samples remain undifferentiated and unmelted.

1.3.4 The chondrite parent dynamo

Given the presence of a large ($\sim$ 100 km) iron-metallic core, thermal convection within the core would result in a stable dynamo field < 2 μT (Nichols et al., 2021) and a planetesimal similar in structure to Earth's geodynamo (Weiss et al., 2008a,b; Elkins-Tanton et al., 2011; Weiss and Elkins-Tanton, 2013). Similar to terrestrial crustal rocks, the magnetisation present in chondritic meteorites would be acquired over a million-year stay on the surface of the planetesimal as a mixture of viscous remanence and thermoremanent magnetisation. In this model, chondrites then a hold direct record of the dynamo present within the parent body, with palaeointensity measurements suggesting a possible core magnetic field strength across a wide range, between $100 - 2600$ μT (Weiss et al., 2010b).

An internal dynamo field also supports the observation that the acquisition of the magneti-

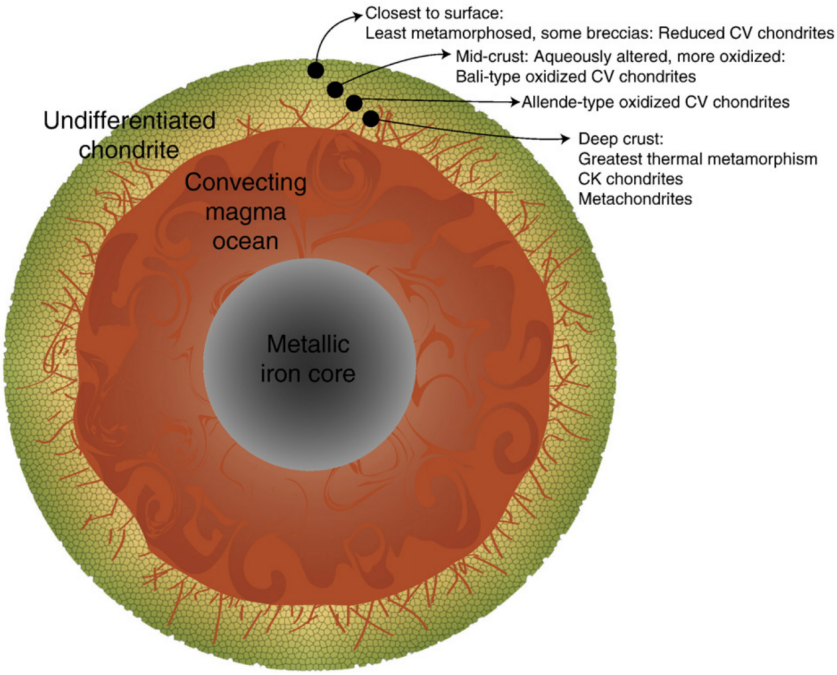


Figure 1.3: Division of the proposed meteorite parent planetesimal into a metallic core, magma ocean and undifferentiated chondritic crust (Fig. 1, from Elkins-Tanton et al. (2011)). Convection in the metallic iron core would then generate a planetesimal dynamo field, strong enough to magnetise the adjacent stony material.

sation stored within chondrites was acquired after their accretion onto the parent body (Weiss et al., 2021). There also exists a body of work, including experimental data (Wang et al., 2015) and thermal modelling of the planetesimal body (Bryson et al., 2017, 2019; Dodds et al., 2021) that support 4-5 Myr delayed onset of an active dynamo. This would have allowed enough time for the estimated > 1 Myr accretion timescale of chondritic asteroids (Cuzzi et al., 2008) prior to their accretion onto any large, differentiated planetesimal.

1.3.5 Radioactivity in the chondrite planetesimal

Along with ^{60}Fe, the decay heat produced as ^{26}Al decays into ^{26}Mg inside stony material is thought to be the primary heat source for the differentiation of planets in our solar system (Wadhwa et al., 2007). Chondrules and CAIs recovered from chondrites have been used to determine an abundance of the short-lived radioisotope ^{26}Al in the early solar system (Lee et al., 1977).

However, chondrules from Yamato 81020, one of the most primitive CO3 chondrites, have

shown that the relative abundances of ^{26}Al and ^{60}Fe were too low during the accretion of the parent body to have produced large-scale melting (Kojima et al., 1995), implying that radioactive decay would have been an insufficient heating mechanism for large-scale differentiation. In fact, evidence from chondrules collected across the chondrite groups suggest that only a planetesimal containing the most primitive chondrules, those that accreted between 0.1 - 0.9 Myr of CAI condensation (Connelly et al., 2012; Bollard et al., 2019), would contain sufficient ^{26}Al and ^{60}Fe to have undergone large-scale melting (Fig. 1.1).

The lack of sufficient radioactivity in the chondrite parent bodies for differentiation is further evidenced by studies of CAIs from CV chondrites. At the time of CV parent body accretion, around 2 Myr after CAIs, the relative abundance of ^{26}Al has been estimated to have been capable of producing maximum bulk temperatures around 825°C (Kunihiro et al., 2004; Kleine and Wadhwa, 2017). This estimate is significantly lower than the accepted $1300 - 1400$°C bulk temperature required to produce large-scale melting (Taylor, 1992). More recently, evidence from uranium-corrected Pb-Pb dating using chondrules from the CV parent body and NWA 5697 (Bollard et al., 2019) which have found between 3-11 times lower [^{26}Al/^{27}Al] ratio in the early solar system than the previously accepted canonical value (Jacobsen et al., 2008). Hence, it is most likely that the chondrite parent bodies accreted too late and contained too little ^{26}Al to differentiate.

1.3.6 Chondrule ages too young for differentiated accretion

While the origin of chondrules is debated, chondrules must have formed prior to their accretion on to the chondrite parent bodies. Hence, the maximum age of chondrites can be constrained by the age of the chondrules that reside within them. The proposed accretion timescale for differentiated planetesimals is inconsistent with chondrule ages recovered from within chondrites (e.g. Connelly et al., 2017; Bollard et al., 2019). Chondrules recovered from L, CO and CV chondrites have been dated to have formed ∼1.8 - 2.5 Myr after CAIs (Doyle et al., 2015), while chondrules in CV3 chondrite Allende have been dated around 2 Myr after CAIs (Connelly et al., 2017). These chondrules ages are significantly older than the 0.9 Myr post-CAI condensation maximum chondrule age required differentiated-asteroidal accretion (Bollard et al., 2019),

implying the accretion of the chondrite parent bodies was too late for global melting.

1.3.7 Chondrite groups: a product of burial or different parents?

Variability between lithic fragments of CV3 chondrites Vigarano, Bali and Allende display different porosities and permeabilities, in conjunction with different quantities of secondary mineral assemblages within their matrix (Brearley and Krot, 2013), has previously been used as evidence for meteorite formation at a variety of depths within a differentiated parent body (Elkins-Tanton et al., 2011). However, an explanation that is more consistent with this evidence, as well as the relatively low abundance of $^{26}Al/^{60}Fe$ in chondrites (Kleine and Wadhwa, 2017), is that fragments were variably altered from one heterogeneously Darcy flow percolated asteroid(Ganino and Libourel, 2017), comparable to terrestrial aquifers. This scenario, one where the physiochemical differences between CV3 chondrites can be explained by a single hydrothermal process in a chondritic environment, means that there is no requirement for the CV parent body to have been a differentiated object, or possess an 'onion shell' structure.

1.4 Impact-induced lithification of chondrites

Chondrites accreting onto a differentiated planetesimal as pre-lithified rocks and the resultant thin chondritic crust has presented a number of conflicting pieces of evidence. As palaeomagnetic evidence over the last decade continues to support a nebula origin for chondrite magnetism (e.g., Fu et al., 2014; Cournede et al., 2015; Muxworthy et al., 2017; Bryson et al., 2020a), recent studies have turned to look for an accretion mechanism that is able to explain the physiochemical nature of chondrites and may explain the origin of their magnetisation (e.g., Bland et al., 2011, 2014; Forman et al., 2016, 2017). This accretion mechanism must be able to reconcile the differences in shock stage classification, porosity and physiochemistry that is observed between recovered chondritic meteorites.

Impact-generated shock textures have been observed in both chondrules and matrix material in chondrites (e.g., Trigo-Rodriguez et al., 2006; Weidenschilling and Cuzzi, 2006; Bland

et al., 2011, 2014; Forman et al., 2016), but impacts are generally not considered as a dominant factor in their evolution; 85% of the most primitive chondritic meteorites, carbonaceous chondrites(CCs), are ranked as either S1, 'unshocked' (< 5GPa), or S2, 'very weakly shocked' (5 − 10GPa) (Stöffler et al., 1991; Scott et al., 1992). However, these shock classifications were calibrated using impact experiments on non-porous or low-porosity targets (Stöffler et al., 1991), which have a different mechanical and thermal response when shocked compared to porous targets (Kieffer et al., 1976; Davison et al., 2010, 2016).

Recovered CCs have present-day porosities (ϕ_{bf}) between 0-41%, with an average bulk porosity of $\phi_{bf} \sim 17\%$ across all groups (Macke et al., 2011). As chondrules are igneous, zero-porosity inclusions, the porosity is entirely derived from within the stony matrix. Measurements of CC matrix materials have shown present-day porosity (ϕ_{mf}) to be as high as 60% in CV chondrites (Bland et al., 2011) and between 66-70% in the most porous COs (Watt et al., 2006). During impacts on porous targets, the crushing out of pore space attenuates the strength of the shock wave and releases excess work done as heat into local material, generating temperatures much greater than a similar impact on non-porous target (Melosh, 1989). This means that the strength of an impact on a porous target can be measurably lower than on a non-porous target to produce the same post-shock temperature increase.

Precursor material for CCs has been shown to have been highly porous; for CV chondrite Allende, pre-compaction bulk porosity (ϕ_{bi}) estimates are in the range 38 - 61%, where the matrix was likely 70 - 80% porous (Bland et al., 2011). The mechanism for the densification of chondrites is likely a result of low-velocity, 0.75 - 2 km/s, impacts on planetesimals, corresponding to bulk shock pressures between 0.6 - 3.7 GPa (Bland et al., 2014). Extensive modelling of such impacts has enabled these constraints to be tightened further, such that the initial pre-impact bulk porosity to lie within $\phi_{bi} \sim 45$ - 57% (Davison et al., 2016), producing post-impact porosities between $\phi_{bf} \sim 4$ - 28% in CCs, consistent with natural samples (Macke et al., 2011). This method of densification has also been verified in meteorite-analogue laboratory experiments (Rutherford et al., 2017), which have provided some of the first evidence that chondrite parent bodies can be consolidated in this way.

1.4.1 An impact mechanism for recording remanent magnetisation

Depletion in the porosity of the chondrite parent bodies resulted in greater thermal energy absorbed into the matrix than would be expected for a non-porous target. However, due to the bimodal mixture of chondrules and aggregate matrix material, heat released from the crushing out of pore space would then be rapidly removed ($<$ 10s), as chondrules have been shown to act as heat-sinks (Davison et al., 2016). These results suggest that the temperature in localised sub-volumes of the chondrite matrix experience a post-shock temperature increase of more than $\sim$ 300°C which is consistent with temperature estimates based on palaeomagnetic data (Muxworthy et al., 2017; Wang et al., 2017; Bryson et al., 2020a). Moreover, these temperature elevations do not require the large pressures (30 - 35 GPa) that they have been historically associated with (Stöffler et al., 1991). Similarly, low-velocity impacts would not have produced the shock textures or faults and fractures that would be expected of a 30 - 35 GPa impact and subsequent S4/S5 shock classification (Stöffler et al., 1991; Scott et al., 1992). The rapid cooling of the matrix means that the consequences of extensive thermal heating on stony material, such as mineral decomposition or even localised melting, would also have been minimised.

Localised heating within chondrites as detailed above would have been capable of raising the temperature of magnetic material (iron oxides and sulphides) within the matrix sufficiently close to, or above, their Curie temperatures (for iron oxides, $T_C \sim 580$°C, while for iron sulphides $T_C \sim 320$°C Dunlop and Özdemir, 1997). The rapid cooling observed in numerical modelling of impacts on porous chondrites (Davison et al., 2016) opens an opportunity for these magnetic carriers to have recorded a transient or unstable background magnetic field over a very brief duration (Muxworthy et al., 2017). A stable, internally generated magnetic field has previously been thought of as the only way chondrites can have acquired their stable remanence. However, as impact-induced heating events have been shown to be short-lived, there exists a window of opportunity to have recorded a 'snapshot' of a sufficiently strong and unstable background field present at the time of the impact.

Using available data, it is possible to estimate a likely time frame for when impact-induced

compaction could have facilitated recording the Solar Nebula field in chondrites (Fig. 1.1). The theoretical ability of impact-induced compaction to record a palaeofield occurs during the overlap between chondrite parent body accretion and the persistence of the Solar Nebula field. However, there is significant difficulty in constraining the lifetime of the field due to a lack of understanding with regards to (1) the decay in field intensity over time and (2) the decay in field strength with increasing distance from the Sun. The epoch of chondrite formation is largely well-constrained from Pb-Pb dating investigations (Connelly et al., 2012). However, data on the lifetime of the nebula field is poorly constrained due to a lack of understanding surrounding the origin of the magnetisation. The Solar Nebula field is understood to have diminished to < 1 μT around ~ 3.8 Myr after CAI condensation (Wang et al., 2017), though in contrast, CV chondrite Allende has a remanence corresponding to a nebula field around 11 μT 3.2 Myr of CAIs at an unknown distance from the Sun (Muxworthy et al., 2017), while the ungrouped C2 chondrite WIS 91600 experienced a nebula field of ~ 4.4 μT at a distance of 10 AU, between 3-4 Myr after CAIs.

1.4.2 A synopsis of chondrite magnetism

Chondrite magnetism can be split into two broad categories: the first is chondrule magnetism, and the second is matrix magnetism. Chondrule magnetisations are generally found to be heterogeneously aligned, suggesting the origin of their magnetisation predates their accretion onto the parent body, likely reflecting the nebular conditions they formed in (Shah et al., 2017). On the other hand, the magnetisation in chondrite matrix material is uniaxial, indicative of an origin during the accretion process onto the parent body (Muxworthy et al., 2017).

Impact-induced compaction has been identified as the most promising mechanism for early fabric development in chondrites in a number of studies (e.g., Gattacceca et al., 2005; Bland et al., 2011, 2014; Davison et al., 2016), supported by magnetic evidence of a strong, planar magnetic fabric that is aligned with the magnetisation direction (Muxworthy et al., 2017). Finding a shared alignment between the magnetic fabric and magnetisation direction has lead to the conclusion that the magnetising event responsible for the magnetic fabric and the remanence of chondrites are most likely the same. There are three explanations that satisfy

this observation: (1) The magnetisation was present pre-impact and rotated into the plane, (2) the magnetisation was recorded at the same time as impact or (3) the magnetisation was recorded following an impact, and the magnetic remanence direction was strongly controlled by the existing fabric.

The first of these scenarios can be dismissed as results from numerical modelling have shown that even in low-velocity impacts, the post-shock temperature increase ($300 - 400$°C; Davison et al., 2016) would be great enough to entirely reset an NRM carried by iron sulphides ($T_c = 320$°C; Dunlop and Özdemir (1997)) present in CCs, which have been identified as the primary remanence carrier in CV chondrite Allende (Muxworthy et al., 2017). Moreover, the CV parent body is understood to have had a peak metamorphic temperature of $\sim$ 300°C (Rietmeijer and Mackinnon, 1985; Weinbruch et al., 1994; Bonal et al., 2007), which would also reset any pre-accretional remanences in iron sulphides.

The second conclusion has deeper implications for the nature of the chondrite parent bodies; should the chondrite parent body have been a differentiated planetesimal, it would have cooled from very high temperatures, greater than the Curie temperatures of magnetite and pyrrhotite, over a period of millions of years, and generated a stable magnetic field from an internal convecting dynamo (Weiss and Elkins-Tanton, 2013). Rotation of the parent body with respect to a Solar-generated magnetic field and decay of the nebula field estimated to be $\sim$3.8 Myr after CAIs (Wang et al., 2017) has previously reinforced these assumptions as this type of field would be unstable, unable to have imparted a unidirectional remanence over several Myr. However, very brief temperature excursions due to the chondrule heat-sink mechanism, means the magnetisation recorded within the matrix could be a 'snapshot' of an unstable field in the Solar nebula. Palaeointensity measurements are consistent with MHD affects that are expected to have been present in the Solar nebula (Fu et al., 2014; Weiss et al., 2021). Moreover, nebula palaeofield estimates from meteorites range from 2-54 μT (Fu et al., 2014; Cournede et al., 2015; Muxworthy et al., 2017) which agrees with a magnetically-governed protoplanetary disk (Crutcher, 2012; Cournede et al., 2015) and is considerably lower than the > 1000 μT estimates of the field strength produced by a planetesimal dynamo (Weiss et al., 2010b).

Thirdly, in the case that the remanent magnetisation was controlled by an already present

magnetic fabric, then the magnetisation is highly likely to be of chemical/crystalline origin (Fu et al., 2014). The likelihood of this scenario occurring remains unclear and requires a deeper understanding of the chemical alteration of magnetic carriers. In order to distinguish whether the remanent magnetisation has been contaminated by crystalline alteration would require knowledge of both the age of the crystals and how they are able to alter the magnetic fabric.

In any case, the mechanism for the magnetisation of chondrites remains uncertain, as does the field that has been recorded. The impact-induced compaction hypothesis of Bland et al. (2014) and Davison et al. (2016) has been partially confirmed by low-velocity impact experiments on porous silica targets (Rutherford et al., 2017; Davison et al., 2017; Derrick et al., 2019), as well as from electron backscatter diffraction mapping (Forman et al., 2016, 2017). However, the hypothesis that low-velocity impacts can produce localised thermal anomalies, capable of recording snapshots of an ambient magnetic field (Bland et al., 2014; Muxworthy et al., 2017), is almost entirely based on simulations and needs experimental confirmation. This is one of the hypotheses that are to be tested in this thesis.

1.4.3 Planetary migration from chondrite magnetism

When investigating impacts on chondrites, a major consideration is the 'speed-limit' at which collisions are able to impart remanence while still producing asteroids consistent with chondrites. Collisions above $\sim$ 3 km/s do not produce asteroids consistent with chondrites as melting begins to occur at these velocities (Davison et al., 2016). Instead, impacts in the range 0.75 - 2 km/s are capable of producing both ordinary chondrites (OCs) and CCs, consistent with impact velocity estimates obtained from collisional evidence in meteorites (Beitz et al., 2013). Constraining the velocity to this range, there are significant implications for astrophysical processes in the young solar system. Models such as The Grand Tack (Walsh et al., 2012) that predict an early inward migration of Jupiter predict even higher velocities; Bland et al. (2014) find these velocities inconsistent with their simulations as well as evidence in natural samples. If impact-induced compaction can indeed be shown as the most promising mechanism for recording remanence in chondrites, it would support models that include a 'late phase'

collisional evolution of planetesimals (Bland et al., 2014).

More recently, very low palaeointensities ($< 0.15\mu$T) measured from the Tagish Lake chondrite have been used to directly determine the distances small bodies travelled across the solar system in the first few Myr after CAI condensation (Bryson et al., 2020b). Their study found the Tagish Lake chondrite to contain CAIs and chondrules from the inner solar system, while the meteorite itself formed in the distal solar system, around where present-day Saturn lies (8-13 AU). These examples demonstrate the importance of understanding chondrite magnetism to understanding the evolution of the solar system.

1.5 Thesis objectives

This thesis aims to develop an understanding of the role of impacts in meteorite magnetism. I investigate how impacts may operate as a mechanism in which magnetic remanence is recorded in primitive meteorites. In particular, the cases where (1) remanence is recorded during impact-generated heating on porous meteorite precursor material and (2) the case where the state of the remanence is altered or recorded due solely to the pressure exerted during an impact. Historically, studies have looked at the bulk pressure produced in impacts that leads to large scale cratering without an appreciation for the effects on the scale of the often millimetre-sized samples being studied. This work will focus on the sub-millimetre 'mesoscale' and the submicron-scale response of ferromagnetic grains to an induced stress. This is a novel idea and aims to shed new light on the way the thermal and shock histories of meteorites are interpreted through palaeomagnetism.

1.5.1 Overview

The thesis is divided into the following chapters:

Chapter 2 outlines the core physics principles this work is based on. The necessary background includes a comprehensive summary of the fundamentals of rock and meteorite magnetism. The key aim of the thesis is to develop an understanding of how impact-generated

shock waves enable meteorites to record magnetism, right down to the nanoscale.

Chapter 3 outlines the usage and functionality of the iSALE shock physics code that has been used for the numerical modelling of impacts throughout this thesis. iSALE is a highly capable tool that uses a finite-difference approach to solve the fundamental physics conservation laws. Combined with a set of material-specific expressions, iSALE is able to model the deformation and thermal evolution through time experienced by multiple materials in impacts.

Chapter 4 contains a detailed explanation of an experiment designed to test whether impact-induced compaction of primitive solar system solids was capable of recording a magnetic field. To do this, a synthetic chondrite contained within a recovery fixture was subjected to 1-2 GPa impacts by a projectile. The investigation used numerical models to design a bespoke recovery fixture for the experiments and assess the likely conditions that would be experienced within the samples. The capsules were then manufactured according to specification and I performed the experiments using a high-pressure gas gun at the University of Oxford inside a controlled magnetic environment. Once recovered, samples were examined back at Imperial College London to recover the remanent magnetisation in the sample and build an understanding of how primitive meteorites came to be magnetised.

Chapter 5 presents a suite of numerical simulations that were designed to test the thermodynamic response of a Martian meteorite to planar shock. Using thermal constraints from a mixture of palaeomagnetic, petrologic and mineralogical studies, we have been able to reconcile a number of independent observations about a particular Martian Meteorite and explain its complex history through a suite of impacts. This work can be seen in the wider context of any meteorite impact investigation whereby we have developed a workflow that allows the user to pass a planar shockwave through a real meteorite sample and analyse the thermal and mechanical effects. This is a work that I am the first-author of and is a collaboration between our group at Imperial College and a group at Harvard University. This chapter has been published in the planetary sciences journal Icarus (`https://doi.org/10.1016/j.icarus.2022.115322`).

Chapter 6 details a numerical investigation into the acquisition of residual magnetisation in single grains of magnetite as they are subjected to stress. Stress was applied to a number of magnetite grains of different sizes which were initialised with a remanent magnetisation in a

known domain state. The aim of this work was to explore how, across a variety of stresses and stress axes applied to different remanences, the magnetisation changes and is recorded. This is pertinent in building an understanding of how in both meteorites and terrestrial samples the cause of the remanence is not thermal nor chemical, but instead a shock remanent magnetisation

Chapter 7 is a conclusions chapter and describes how I have achieved the motivations and aims of the project. Finally, I also comment on the limitations of the work done and suggestions for future work.

Chapter 2

Background to Meteorite Magnetism

2.1 Introduction

In this chapter, I outline the fundamental principles of rock magnetism and how an understanding of the magnetisation of natural samples can be used to decipher information about the thermal, metamorphic and impact histories of meteorites.

2.2 Fundamentals of rock magnetism

Here, I describe the fundamental physics that governs magnetisation from the atomic level to the grain scale, and how rocky material is able to carry a measurable, *remanent* magnetisation, that persists in the rock material following a magnetising event. Developing an understanding of the how rocks and meteorites respond when subjected to an external magnetic field, as well as how they are able to acquire a magnetisation, enables palaeomagnetic techniques to recover meaningful information about the nature of the magnetising field.

2.2.1 Magnetic moment

Fundamental to the types of magnetism described in this thesis is the atomic magnetic moment. Magnetic properties of materials originate at the atomic level and are a net affect of

the alignment of many atomic magnetic moments (Néel, 1949). The atomic magnetic moment is made up from a contribution of both the quantum mechanical spin and the orbital angular momentum of its electrons; while atoms with entirely full electron shells have a net magnetic moment of zero, atoms with partially-filled electron shells have a non-zero net magnetic moment (Pauli, 1927).

2.2.2 Diamagnetism and paramagnetism

Faraday's discovery that all materials have diamagnetic properties set a foundation for developing an understanding of magnetism (Faraday, 1846). In a magnetic field $\boldsymbol{B}$, an electron moving with velocity $\boldsymbol{v}$ in orbit around a positively charged nucleus will experience a Lorentz force equal to $e\boldsymbol{v} \times \boldsymbol{B}$, where e is the elementary charge. The Lorentz force causes electron orbits to precess about $\boldsymbol{B}$, equivalent to an electric current, resulting in a negative induced magnetic moment known as the diamagnetic force (Knudsen, 1976). This results in diamagnetic materials being repelled by an applied magnetic field (Fig. 2.1). While a weak effect in most materials, superconductors are an example of strongly diamagnetic materials. Diamagnetism is much stronger in materials where there are no unpaired electrons in the outer shell.

On the other hand, paramagnetism is the temporary partial alignment of atomic magnetic moments in the direction of an applied field, $\boldsymbol{B}$ (Faraday, 1846). In paramagnetic materials, the weak diamagnetic force is overcome by attractive magnetic dipoles which couple to an applied field. Paramagnetic materials have at least one unpaired electron in their atomic structure. The resistance of a paramagnetic material to aligning in parallel with an applied field is known as *magnetic susceptibility* and is a measurable quantity (Tauxe et al., 2010).

2.2.3 Magnetic susceptibility

Magnetic susceptibility is a quantifiable property that describes the ease of a material to becoming magnetised while under the application of an external magnetic field. The magnetic susceptibility of a particular material is not a constant and can be a complicated function of temperature, pressure, orientation and strength of the applied field (Tauxe et al., 2010). To

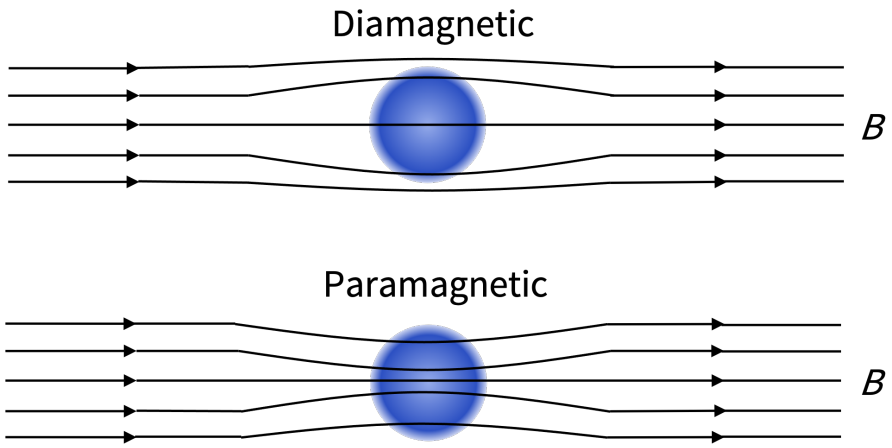


Figure 2.1: Schematic demonstrating the response of a diamagnetic and paramagnetic material on some external field, $\boldsymbol{B}$. The field lines bend slightly away from the diamagnetic material, while they bend towards the paramagnetic material.

better understand the physical meaning of susceptibility, consider the simple case whereby a magnetic field arises from a current loop or dipole. A dipole produces a magnetic field, $\boldsymbol{H}$. The magnetostatic definition of $\boldsymbol{H}$ is the observed alignment of an object in the same direction (such as a compass needle). However, there is a subtle distinction between $\boldsymbol{H}$ and the 'magnetic induction' or total field, $\boldsymbol{B}$.The induction field $\boldsymbol{B}$ can be defined as an augmented field:

$$\boldsymbol{B} = \mu_0(\boldsymbol{H} + \boldsymbol{M}) \tag{2.1}$$

where $\boldsymbol{M}$ is the macroscopic magnetisation and μ_0 is a constant, the permeability of free space. Outside of a magnetic material, $\boldsymbol{M}$ is zero and this equation simply becomes $\boldsymbol{B} = \mu_0\boldsymbol{H}$. This is where the distinction is made apparent; as $\boldsymbol{M}$ is a macroscopic quantity, $\boldsymbol{B}$ can only be defined on a macroscopic scale. However, $\boldsymbol{H}$ can be thought of a local (or internal) magnetic field, defined on any scale, down to the atomic.

Magnetic susceptibility, χ, is a dimensionless quality, defined as the ratio between magnetisation, $\boldsymbol{M}$, and the applied magnetic field intensity, $\boldsymbol{H}$:

$$\boldsymbol{M} = \chi\boldsymbol{H} \tag{2.2}$$

Hence, magnetic susceptibility can be described as a direct measure of how much of a material

is magnetised when subject to an externally applied field (Dunlop and Özdemir, 1997). Additionally, equation 2.2 can be used to quickly determine whether a material is diamagnetic or paramagnetic: if $\chi < 0$ then a material is diamagnetic, whereas when $\chi > 0$ the material is paramagnetic.

2.3 Ferromagnetism

Diamagnetic and paramagnetic materials only experience a temporary or induced magnetisation: the magnetisation $\boldsymbol{M}$ disappears when the external field $\boldsymbol{B}$ is removed. However, when the alignment of magnetic moments in a material exists long after the removal of an applied field, a permanent, remanent magnetisation (or *remanence*) remains. This is an effect that arises from a material having unpaired electrons in their outermost atomic shell (Stacey, 1976). These unpaired electrons cause the atomic magnetic moments to align spontaneously, giving rise to a spontaneous magnetisation, even in the absence of an external field (Néel, 1949). Materials that behave in this way are described as ferromagnetic (Bozorth, 1951).

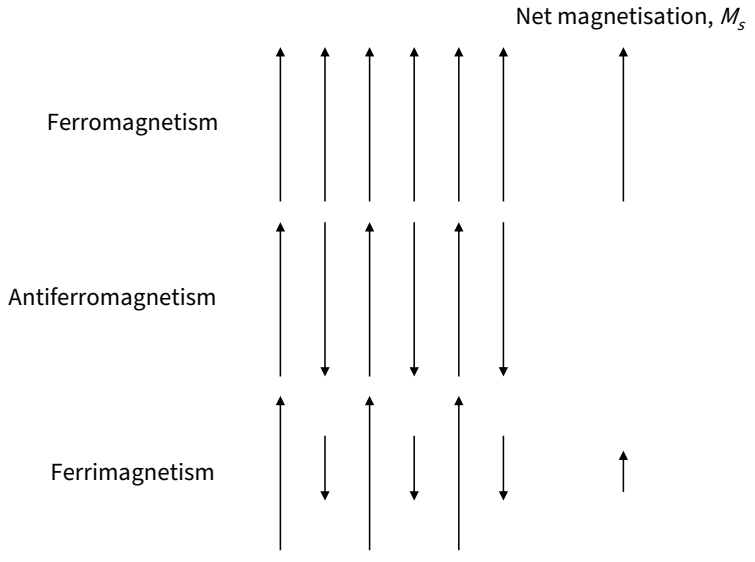


Figure 2.2: Different possible exchange-coupled spin structures of and the net spontaneous magnetisation, M_S, of each. Ideal ferromagnetic coupling is the parallel alignment of spins, while antiferromagnetism is the result of antiparallel coupling. In the case that coupling is antiparallel but one layer is stronger than the adjacent layer, the result is ferrimagnetism which still results in a non-zero net spontaneous magnetisation.

2.3.1 Ferrimagnetism and antiferromagnetism

Ferromagnetic interactions are a result of the parallel coupling between neighbouring atomic magnetic moments, but atomic magnetic moments can also couple in antiparallel (Fig. 2.2). Antiparallel coupling occurs in crystalline structures where the magnetic moments within layers of atoms align with one another, but in the opposite direction to adjacent layers. The strength of the magnetic moments between layers affects the classification of the coupling; layers with equal and opposite magnetic moments are declared antiferromagnetic, and those where the magnetic moment of one layer is greater than the next are ferrimagnetic (Néel, 1948, 1952). This means that the net magnetic moment of ferrimagnetic materials is non-zero, while the net magnetic moment of antiferromagnetic materials is zero.

2.3.2 Exchange coupling

Although on the atomic scale ferromagnetism is the result of unpaired electrons, electronically neutral materials (those which share electrons through chemical bonds) and ions within molecular compounds (e.g., Fe^{2+} and Fe^{3+} in magnetite, Fe_3O_4) are ferromagnetic and also much more common in nature. In these materials, it is spin-dependent interaction between neighbouring atoms that gives rise to magnetic behaviour (Compton, 1921).

Electrons that exist in overlapping 3d (or 4s) atomic shells between neighbouring atoms are found to spend time in either state, and can effectively be exchanged between these neighbours (Kittel, 1976). The degree of overlap between these neighbouring atomic shells dictates whether the coupling is parallel (the exchanged electrons are found to have the same spin value, S) or antiparallel (electrons are found to have opposite spin). A large overlap between 3d atomic shells results in antiparallel (negative exchange or antiferromagnetic) coupling, while less overlap results in parallel (positive exchange, or ferromagnetic) coupling (Dunlop and Özdemir, 1997). For values where the overlap is extremely small, the exchange coupling is lost and materials begin behaving paramagnetically. Chromium and manganese are examples of elements that are antiferromagnetic, while iron, cobalt and nickel are ferromagnetic and copper is paramagnetic.

Exchange coupling acts over long-ranges through solids in *spin waves* (Fig. 2.3). Neigh-

bouring spins form a cone that share a spin component (S_z) along a magnetic field $\boldsymbol{H}$, while the spin wave traces along the neighbouring atomic magnetic moments of the exchange-coupled atoms (Kittel, 1976). The exchange energy between coupled atomic magnetic moments is:

$$E_{ex} = -2J_e \boldsymbol{S_i} \cdot \boldsymbol{S_j} = -2J_e S_i S_j \cos\theta_{ij} \tag{2.3}$$

where θ_{ij} is the angle between the spins of neighbouring atoms i and j, $\boldsymbol{S}$ is the spin vector and J_e the angular momentum (Dunlop and Özdemir, 1997).

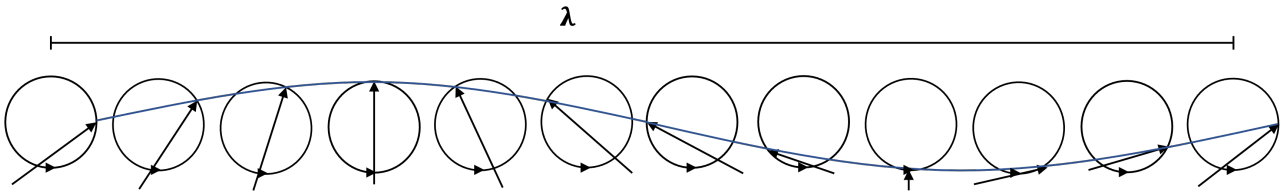


Figure 2.3: A sketch one full wavelength, λ, of a spin wave. A series of exchange-coupled spins in a line form a spin wave that is able to act over long-distances throughout a solid material. The coupled spin component S_z is the circular base of the cone which is shown in this two-dimensional view. As spin waves act over a large number of n atoms, the angle between neighbouring atomic magnetic moments can be as small as π/n.

2.3.3 Curie temperature and Néel point

The Curie temperature describes the point at which ferromagnetic and ferrimagnetic materials undergo a phase transition and exhibit paramagnetic behaviour. Above the Curie temperature, atomic excitation leads spin orientations to become randomised (erasing any remanent magnetisation), although they can be realigned under an applied field. The Néel point is analogous to the Curie temperature, but describes the temperature at which antiferromagnetic materials transition to paramagnetic behaviour (Néel, 1948).

The Curie temperature is a quantity derived from Curie's law. Curie's law is a calculation of the magnetic susceptibility of a paramagnetic material, χ_p. Using the expression of magnetic susceptibility in equation 2.2:

$$\chi_p = \frac{M}{H} = \frac{M\mu_0}{B} = \frac{1}{3}\frac{n\mu^2\mu_0}{k_B T} = \frac{C}{T} \qquad \text{Curie's Law} \qquad (2.4)$$

where there are n atoms per unit volume with magnetic moments μ, T is the temperature and C is the material-specific Curie constant which describes the strength of the atomic magnetic moments (Dunlop and Özdemir, 1997).

In the quantum mechanical expression of Curie's law, there are $2J + 1$ states with corresponding energies $E = -m_J\mu_B$ $(-m_J = -J, ..., J)$. Using this expression, the magnetisation can be written as:

$$M = ng_J J\mu_B B(x) \qquad (2.5)$$

where J is the total angular momentum given as an integer or half-integer, g_J is the Landé g factor (Landé, 1921) and $B(x)$ is the Brillouin function, a special function that describes ideal paramagnetic behaviour, where $x = g_J J\mu_B B/k_B T$ (Darby, 1967). Substituting this expression for M into equation 2.4:

$$\chi_p = \frac{ng_J^2 J(J+1)\mu_B^2\mu_0}{3k_B T} = \frac{C}{T} \qquad (2.6)$$

Curie's law applies in the case that $\chi_p << 1$ and $T > T_C$, where T_C is the Curie temperature and describes the temperature above which a material behaves paramagnetically. This can be further generalised for an expression of the spontaneous magnetisation, M_S, as a function of temperature. It can be shown from these expressions that $M_S(T) \propto (T - T_C)^\gamma$, with $\gamma = \frac{1}{2}$ from the molecular field approximation (Weiss, 1907). Experimentally, this has been shown to describe spontaneous magnetisation as a function of temperature well, with $\gamma = 0.34$ for iron and $\gamma = 0.43$ for magnetite (Dunlop and Özdemir, 1997).

Equation 2.6 shows that the Curie temperature is a material-specific and well-defined transition temperature, which when exceeded in zero field will effectively randomise the magnetic

moments of a material (i.e., paramagnetic behaviour). In the presence of an external field, a ferromagnetic material that is heated above its Curie temperature will lose the record of its previous magnetisation, obtaining a new remanent magnetisation that reflects the strength and orientation of the applied field as it cools back down.

The Curie temperature can also be shown to be a measure of the strength of the exchange coupling. Consider a simple molecular structure where all atomic magnetic moments, μ, are aligned such that the total magnetic moment, M, becomes $M = n\mu$ for n atoms. The energy of the magnetic field ('Zeeman energy') is $E_m = -kT_C$, where $k = \mu_0\mu\lambda$ and λ is the Weiss molecular field constant, such that $\lambda = \frac{T_C}{C}$ at $T = T_C$ (Levy, 1968). In this scenario, the molecular field arises from exchange coupling with the nearest z neighbours, hence, the exchange energy (from equation 2.3) is given by $E_{ex} = -2zJ_eS^2$ (Dunlop and Özdemir, 1997). Equating E_{ex} and E_m, the Curie temperature can finally be shown to be a measure of the exchange interaction:

$$J_e = \frac{k}{2zS^2}T_C \tag{2.7}$$

2.4 Magnetic domain theory

Neighbouring atoms form 'grains' within ferromagnetic materials. Within these grains, the atomic magnetic moments are organised into energetically-favourable groups called domains (Kittel, 1949). Grains may divide themselves into one or many domains in order to minimise the total magnetostatic energy of the grain (Butler, 1992), and can be broadly categorised into one of three basic domain structures: single domain (SD), pseudo-single domain (PSD) or multi-domain (MD) states (Figure 2.4).

Grains are inclined to transition from one domain state to another depending on their size (volume) in order to minimise magnetostatic energy. Larger grains favour a scenario where regions within the grain are split into multiple domains, divided by 'domain walls', giving rise to MD and PSD states, whereas smaller grains prefer a SD state. In SD, PSD and MD grains, it is the total sum of the constituent domains that result in a net magnetisation.

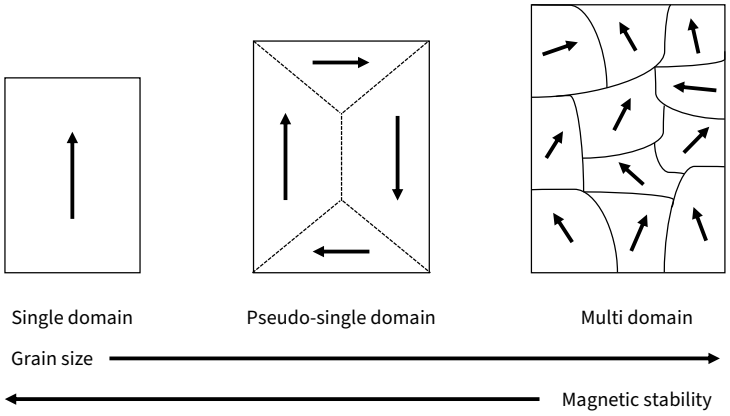


Figure 2.4: 2D representation of the three general magnetic domain states. Past a certain size/volume, grains divide into a subset of energetically-favourable regions called domains. The sum of the magnetisation of these domains results in a net magnetisation of the grain. This figure shows a basic schematic of single domain (SD), pseudo-single domain (PSD) and multi-domain (MD) states. As grain size increases, domain heterogeneity increases and consequently magnetic stability decreases. For magnetite, SD grains are typically < 100 nm in size (Muxworthy and Williams, 2006), PSD 80 - 1000 nm and MD grains > 1000 nm, though grain sizes are flexible due to the nature of the magnetising event(s) (Nagy et al., 2017).

2.4.1 A balance of energies

The domain structures that exist within magnetic grains are a result of multiple local minimum-energy (LEM) state. The requirement for LEM states arises from a balance between four energies. The first of these energies is the exchange energy (equation 2.3) which arises due to neighbouring coupled atomic magnetic moments, while the remaining three, the anisotropy, Zeeman and demagnetising energies, are described below.

Anisotropy energy

The energy required to magnetise a ferromagnetic material depends on the specific crystal direction or 'axis' along which it is being magnetised (Honda et al., 1926). For example, cubic magnetite is most easily magnetised along the [1 1 1] 'easy' direction, the diagonal which connects opposite cubic corners, while it is most difficult to magnetise in the 'hard' [1 0 0] direction, the shortest distance which connects the two closest vertices (Daalderop et al., 1990). When a magnetisation $\boldsymbol{M}$ is established within a ferromagnetic grain, there is a potential energy required to set up the associated field $\boldsymbol{H}$, which in an initially unmagnetised sample is defined as:

$$\int \boldsymbol{H} \cdot d\boldsymbol{B} = \mu_0 \int H dH + \mu_0 \int \boldsymbol{H} \cdot dM = \frac{1}{2}\mu_0 H^2 + \mu_0 \int H dM \tag{2.8}$$

The difference in the potential energies required to saturate a material along its easy axis versus its hard axis is a measure of the crystalline anisotropy and is known as the anisotropy energy.

The Zeeman and demagnetising energies

Leftover is the Zeeman energy which is the potential energy a magnetised particle experiences in an external magnetic field, while the final energy is the internal or 'demagnetising' energy, an energy term that emerges due to the polarisation of charges caused by the internal magnetisation, $\boldsymbol{M}$ (Tauxe et al., 2010). The demagnetising energy arises due to the associated internal or 'demagnetising' field, $\boldsymbol{H}_d$, whose field lines flow from the positive to negative charge within a magnetically-polarised material—analogous to Maxwell's electrostatic equations.

These two energies can be derived from a simple test case. Consider a test dipole with some magnetic moment $\boldsymbol{\mu}$, being acted on by a magnetised grain which has some internal demagnetising field, $\boldsymbol{H}_d$. This will introduce a torque, $\boldsymbol{\tau}$, between the magnetic moment and the demagnetising field, such that:

$$\boldsymbol{\tau} = \boldsymbol{\mu} \times \boldsymbol{B} \tag{2.9}$$

which yields an expression for the magnetostatic potential energy of the grain:

$$E_m = -\boldsymbol{\mu} \cdot \boldsymbol{B} \tag{2.10}$$

where $\boldsymbol{B}$ consists of both the internal demagnetising field and the external field.

A ferromagnetic material with some magnetisation $\boldsymbol{M}$, that is also subject to an external magnetic field $\boldsymbol{H}_0$, experiences a total internal field ($\boldsymbol{H}_i$) that is a sum of the external magnetic field and the internal demagnetising field, $\boldsymbol{H}_d$, hence:

$$\boldsymbol{H}_i = \boldsymbol{H}_0 + \boldsymbol{H}_d \tag{2.11}$$

The *demagnetising tensor*, $\boldsymbol{N}$, relates the magnetisation to the internal demagnetising field and is defined by:

$$\boldsymbol{H}_d = -\boldsymbol{N} \cdot \boldsymbol{M} \tag{2.12}$$

Using the expression for the magnetostatic potential energy (equation 2.10), with equations 2.11 and 2.12, it can be shown that:

$$E_m = -\mu_0 V \boldsymbol{M} \cdot \boldsymbol{H_0} + \frac{1}{2}\mu_0 V \boldsymbol{M} \cdot \boldsymbol{N} \cdot \boldsymbol{M} \tag{2.13}$$

where $\boldsymbol{H_0}$ is the externally applied field and V the volume of the grain. This equation forms a fundamental expression for the magnetostatic potential energy of the grain and can be separated into two competing terms; these are the Zeeman energy:

$$E_H = -\mu_0 V \boldsymbol{M} \cdot \boldsymbol{H_0} \tag{2.14}$$

and the demagnetising energy (sometimes called the magnetostatic self-energy):

$$E_d = \frac{1}{2}\mu_0 V \boldsymbol{M} \cdot \boldsymbol{N} \cdot \boldsymbol{M} \tag{2.15}$$

The demagnetising field, H_d, is a field that begins on positive magnetic charges and ends on negative magnetic charges inside a magnetised material and it is nearly always antiparallel to the magnetisation (i.e., $\boldsymbol{H}_d || -\boldsymbol{M}$). Hence, the demagnetising energy takes a general form $E_d = \frac{1}{2}\mu_0 V N M^2$ (Dunlop and Özdemir, 1997).

Magnetic grains naturally work to try to minimise the demagnetising energy, E_d, in an effort to minimise the overall magnetostatic energy and 'relax' into a stable equilibrium state. In SD grains, there is often large magnetostatic energy which is associated with both the internal

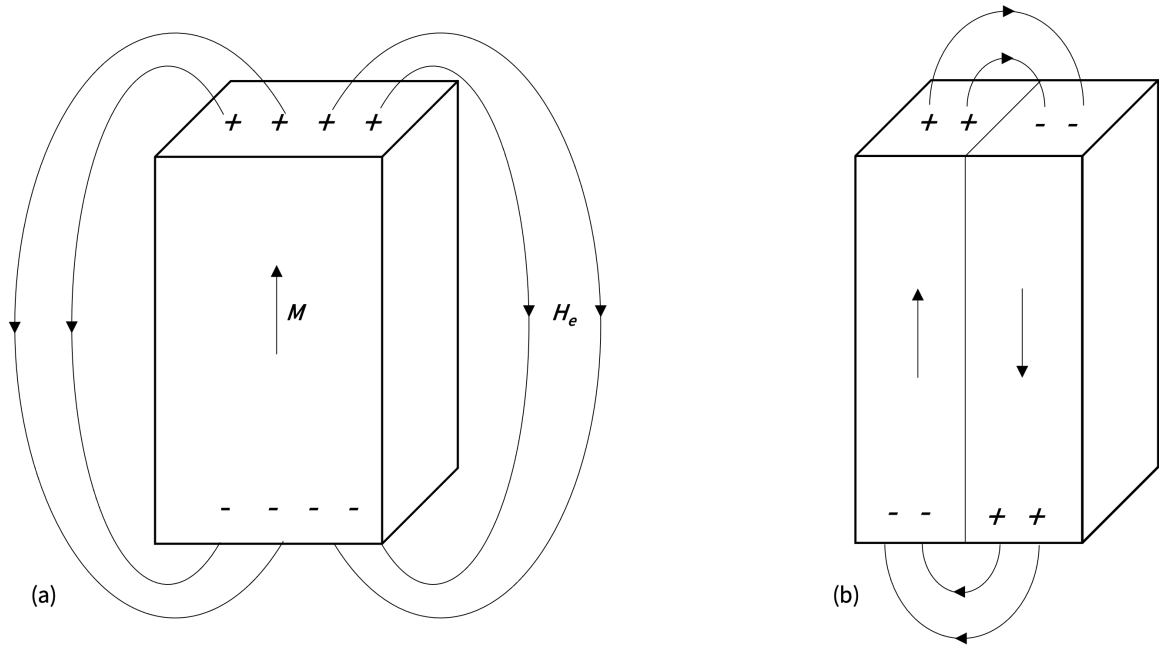


Figure 2.5: A schematic representing two different possible domain structures for the same grain. Shown here is a single domain (SD) grain (a) alongside a two domain structure (b). Labelled are the external field, $\boldsymbol{H}_e$, generated at the poles of each grain, along with the charges experienced due to polarisation by the magnetisation of the grain, $\boldsymbol{M}$. This schematic is inspired by Figure 5.2 from Dunlop and Özdemir (1997).

demagnetising field, $\boldsymbol{H}_d$, and the external field, $\boldsymbol{H}_e$, produced at the poles either end of grain (Fig. 2.5a). If an SD state is divided into a two-domain state, the resultant structure would retain the same surface pole densities, reduce the stray field $\boldsymbol{H}_e$ and reduce the demagnetising energy by about a factor of 2. However, the creation of a domain wall adds exchange energy, E_{ex}, as well as the anisotropy energy, E_k.

Both domain states shown in Fig. 2.5 are possible low-energy equilibrium states for that grain. However, deciding which of these equilibrium states has the lowest absolute energy is dependent on its magnetic history (Dunlop and Özdemir, 1997). Ferromagnetic grains require energy to transition between domain states such as thermal energy from heating events or elastic energy from impact stress, hence, similar sized grains within similar compounds are often found to have different numbers of domains.

2.4.2 Magnetic hysteresis

When placed in an external field $\boldsymbol{H}_0$, some (or all) of the magnetic moments within a ferromagnetic material will align parallel to $\boldsymbol{H}_0$. This increases the strength of the total field, $\boldsymbol{B}$, in the direction of the applied field. However, even after the field is removed, there will still be some residual magnetostatic energy in a fraction of the ferromagnetic grains which remain aligned to the now absent field. It is this effect that gives rise to remanent magnetisation. To coerce the magnetisation of the grain back to zero, either heat ($T > T_C$) or a field with sufficient *coercive* force, H_c, must be applied in the opposite direction. The name given to the effect whereby an external field leaves a material with a residual internal magnetisation once that field has been removed is magnetic hysteresis (Ewing, 1886).

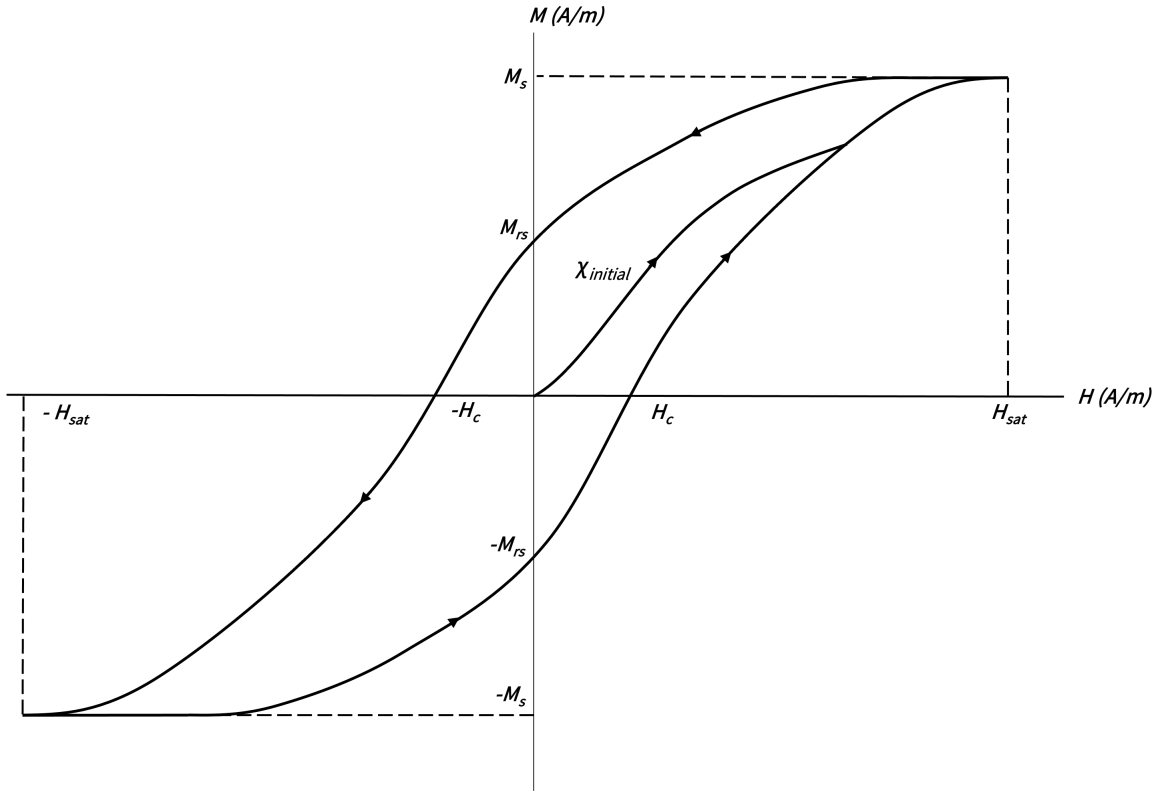


Figure 2.6: An ideal hysteresis loop for a single domain (SD) ferromagnetic grain. The loop is formed by the application of some magnetic field, H, to a SD grain with an initial susceptibility, $\chi_{initial}$, up until a saturating field, H_{sat}, where the sample magnetisation becomes saturated, M_s. The loop is then removed and the same field is applied in the opposite direction. Additionally labelled are the points of crossing at the x and y axes, which reveal the coercive force (or *coercivity*), H_c, and saturation remanence, M_{rs}, respectively.

Hysteresis in single domain grains

Induction of hysteresis in magnetic grains is used to measure a number of magnetic quantities. In practice, this is done by placing a sample between two coils and applying an increasing field, $\boldsymbol{B}$, up to a very high strength (e.g., $>$ 200 mT for magnetite) in order to saturate the magnetisation carried within the sample. This is a process called *domain rotation*, describing the complete parallel alignment of the magnetisation vector with the applied field (Néel, 1955). When a sample becomes magnetically saturated, the applied field no longer increases the magnetisation within the sample. The magnetisation in this state is known as the saturation magnetisation, M_s, and is induced by the saturating field, H_{sat}.

The field is then returned to zero and applied in the opposite direction until again the sample becomes saturated at $-H_{sat}$. The field is then increased a final time up to H_{sat} and a plot of magnetisation against the applied field (M versus H) can be made to form a hysteresis loop (Fig.2.6).

As the field is applied in the first instance to the sample, it traces a line within the hysteresis loop up until M_s is reached. As the field is then removed, ferromagnetic grains retain some of the magnetisation and the magnetisation has a positive value as the field is returned to zero. This is known as the saturation remanence, M_{rs}. The field then has to be applied to a certain value to remove M_{rs} and return the magnetisation back to zero. This field is the coercive field, or coercive force, H_c. Magnetic particles with high coercivities are referred to as 'hard' as they require a strong coercive field to reduce their magnetisation to zero, while magnetic particles with low coercivities are referred to as 'soft' (Snoek, 1947).

Hysteresis in multidomain grains

Multidomain (MD) grains are subject to hysteresis using exactly the same process as described above for single-domain grains. However, the response of MD grains to an external field is different. Individual domains whose orientation is close to the applied field $\boldsymbol{H}_0$ will be energetically favoured over others and the volume of the domain is increased in a process called *domain wall displacement* (Dunlop and Özdemir, 1997). This process is often reversible as the

exchange-coupled spins that form the domain wall rotate to align with the field. In some cases, the energy supplied by increasing the applied field will not return domains to their starting position in a process known as *domain wall pinning*. In other cases, the additional energy may cause the formation of new domains in a process called *nucleation*.

Similar to the single-domain case, the final possible response of an MD grain to an applied field is domain rotation, although this is typically a higher-energy process than both wall displacement and nucleation (Dunlop and Özdemir, 1997). As MD grains have a number of processes available to change their magnetisation at lower energy cost than SD grains, it often requires a significantly greater field to alter the magnetisation of an SD grain than an MD grain. Hence, SD grains are more magnetically hard than MD grains.

2.4.3 Recording fidelity of different domain states

The domain state is directly linked to the magnetic stability of the grain, meaning the fidelity for recording magnetic fields is affected by domain state. When an external field is applied to a ferromagnetic grain, the magnetisation $\boldsymbol{M}$ rotates towards the direction of the field. As previously mentioned, if this rotation persists once the field has been removed then the grain is said to be left with a remanent magnetisation or remanence, a record of the magnetisation 'frozen-in' that grain by the applied field. This can be considered an irreversible effect of being subject to an external field, i.e., the grain has not returned exactly to its former state.

For irreversible changes to be made to the magnetisation of a grain, the applied field must reach some critical strength, H_{crit} (sometimes called the microscopic coercive force, H_K). In general, this is known as the anisotropy field and it describes the field strength at which the magnetisation vector will switch from one easy direction to another (Dunlop and Özdemir, 1997). In general, this field can be calculated by:

$$H_K = \frac{2K_u}{\mu_0 M_s} \tag{2.16}$$

where K_u is an anisotropy constant that is magnetoelastic (controlled by mechanical stress) or shape-controlled, with units of J/m^3.

To put this in physical context, consider this for an ideal grain of magnetite: the anisotropy constant is $K = 1.35 \times 10^4$ J/m^3 and $M_s = 480 \times 10^3$ A/m (Fletcher and O'Reilly, 1974). Substituting in these values, the critical field is $H_k = 37.5$ mT (approximately 1000 times stronger than Earth's geodynamo field), which represents the minimum required field to cause an irreversible rotation of M_s.

2.4.4 Domain state observations from hysteresis parameters

In Earth sciences, magnetic domain states have historically been identified using methods like the Day diagram (Day et al., 1977). Day diagrams follow a coordinate system that compare the ratio of the saturation remanent magnetisation to the saturation magnetisation (M_{rs}/M_s), to the ratio of the coercivity of remanence to coercivity (B_{cr}/B_c). For example, for a random assemblage of SD magnetite particles, $M_{rs}/M_s > 0.866$, and $M_{rs}/M_s < 0.1$ for MD particles, due to the intra-grain conflicts between magnetic moments of the multiple domains (Muxworthy and Williams, 2006). Hence, M_{rs}/M_s can be used to determine the mean domain state of magnetic particle assemblages.

However, Day diagrams have been shown to be becoming increasingly ambiguous as the understanding of particle distributions and their magnetic responses in natural samples has improved (Roberts et al., 2018). Parameters such as the magnetic anisotropy, mineralogy, magnetostatic interactions and grain shape are not taken into account in the Day diagram, but are all intrinsically linked to the domain state of magnetic carriers. This has led to the development of new methods of domain state analysis that move away from the Day protocol.

First-order reversal curves (FORCs)

Pike et al. (1999) proposed an alternative method whereby a set of partial hysteresis loops can be processed to yield definitive domain state distributions, named first-order reversal curves (FORCs). Similar to the major hysteresis method described in the previous section, FORC measurements are obtained by magnetising a sample in a saturating field, B_S, which yields an associated magnetisation M_S. The process differs where periodic back-sweeps along the major

hysteresis loop are performed by reducing the applied field to some *reversal* field, $B_r < B_S$. Between each increasingly strong reversal field applied, the saturating field is then applied again, generating a minor hysteresis loop and the magnetisation of the sample is recorded at intervals during the measurement. Repeating this process and combining many FORCs from different reversal fields allows the construction of FORC diagrams, typically consisting of hundreds of individual curves (Muxworthy and Roberts, 2007). Features of FORC diagrams include the determination of magnetic domain state, but also extend to offer insight into the magnetostatic interactions between grains and source discrimination (Pike et al., 2001; Roberts et al., 2004; Carvallo et al., 2006; Muxworthy and Roberts, 2007; Roberts et al., 2014, 2022).

2.5 Natural remanent magnetisation

The total remanent magnetisation of an assemblage of magnetic carriers in a rock in the absence of an external magnetic field is known as the natural remanent magnetisation (NRM). The NRM of a sample can be analysed to reveal the orientation and strength of the remanence which are intricately linked to the nature of the magnetising event. The NRM may be comprised of a single or multiple components, depending on the number and relative strengths of the magnetising events that the rock has experienced.

2.5.1 Characteristic remanent magnetisation

In palaeomagnetic studies, the most important component of the NRM is usually the one which was acquired first, when the rock was formed. This is referred to as the primary or characteristic remanent magnetisation (ChRM). Components recorded after the acquisition of the ChRM are then known as secondary components. Distinguishing the ChRM from secondary components can be challenging, but essential to determine the nature of the most ancient magnetising field recorded within a sample.

In the case that a material is completely reset during a magnetising event, the ChRM may actually be indistinguishable as a secondary magnetisation. Total resetting of a material could

occur if magnetic carriers are subject to extremely large shock pressures or temperatures which exceed their Curie temperature.

2.5.2 Magnetic relaxation

Magnetic systems are always acting to minimise their magnetostatic energy. Both individual grains and assemblages of grains do this by reaching equilibrium states. Over very long periods of time, thermal energy from a rock's environment will contribute towards 'relaxing' grains into new and more energetically-favourable equilibrium states and this is a process known as magnetic relaxation (Néel, 1949). Magnetic systems also relax into new equilibrium states as the environment changes. For example, this might be due to temperature fluctuations, or because the angle between an external field and the internal magnetisation changes.

Magnetic relaxation is governed by Maxwell-Boltzmann statistics and describes the time it takes for the magnetisation to decay to $1/e$ of its initial value (Néel, 1955). The *relaxation time*, τ, describes the time over which the remanent magnetisation of a grain decays:

$$\tau = \frac{1}{\tau_0} \exp\left(\frac{\Delta E_b}{k_B T}\right) \tag{2.17}$$

where E_b is the energy barrier between different magnetisation states, k_B is the Boltzmann constant, T is the temperature and τ_0 is the atomic reordering time, typically on a scale of $\sim 10^{-9}$s (Néel, 1949). As such, τ_0 describes the time interval between consecutive thermal excitations on an atomic scale. This equation can be rearranged to form an expression just for the energy barrier between magnetisation states:

$$E_b = k_B T \ln\left(t/\tau_0\right) \tag{2.18}$$

where T is the temperature and t represents some wait time. At temperatures close to the Curie temperature, T_C, E_b is small and equilibrium is achieved almost instantaneously ($t \sim \tau_0$).

2.5.3 Types of remanence in rocks and meteorites

Examples of magnetising events include high-temperature excursions, chemical alterations and strong shock waves, and the NRM is characterised accordingly:

Thermoremanent magnetisation Meteoritic materials are known to have experienced very high temperatures during both their metamorphic formation and impact events. Igneous rocks have experienced high temperatures that exceed the Curie temperature of their magnetic carriers. As they cool down through their Curie temperature, the domains within grains align with and record any present external magnetic field (Dunlop and Özdemir, 1997). An NRM acquired in this way is known as a thermoremanent magnetisation (TRM). When an NRM is suspected to be a TRM, typically samples are heated to observe the thermal stability of the magnetisation. In the case that magnetic carriers are heated and cooled in the presence of a magnetic field but the Curie temperature is not reached, samples are said to have recorded a partial-TRM (pTRM).

The 'blocking temperature', T_B, is the temperature below which there is not enough thermal energy to overcome the locked-in magnetostatic energy barrier, E_b. Hence, T_B indicates the point at which a ferromagnetic grain had its magnetic moment frozen-in due to the thermal excitation from one magnetic state to another (Néel, 1949). For a particular ferromagnetic grain, the blocking temperature describes the temperature at which the transition from paramagnetic to ferromagnetic behaviour occurs.

As natural samples are assemblages of many magnetic grains, there exists a distribution of blocking temperatures, or 'blocking spectra'. The successive heating during a thermal demagnetisation measurement means the total TRM is able to be broken up into partial-TRM (pTRM) components (Fig. 2.7), hence, the TRM can be thought of as a vector sum of all pTRM's (Tauxe et al., 2010). For ideal SD grains, the blocking temperature has a reciprocal 'unblocking temperature'—the temperature at which the remanence becomes 'unblocked' (Néel, 1949). However, this fails for MD grains and vortex domain states.

Shock remanent magnetisation Shock remanent magnetisation (SRM) is typically observed following hypervelocity impacts (> 3 km/s), where the impact-induced pressure exceeds

several GPa (Nagata, 1971; Tikoo et al., 2015). In the presence of an ambient field, the induced stress from due impact can supply sufficient energy to exceed the anisotropy energy in SD grains, and even rearrange domain walls in MD grains, remagnetizing the sample (Cisowski and Fuller, 1978). The efficiency of SRM compared to TRM acquisition is lower and has been shown to increase with a decrease in coercivity (Gattacceca et al., 2008). However, this can be helpful when attempting to distinguish between whether an NRM is a TRM or an SRM, which in turn affects the interpretation of the palaeointensity of the sample.

Chemical remanent magnetisation Phase change, chemical action or crystal growth are able to record external magnetic fields in natural samples and are categorised as chemical remanent magnetisation (CRM; Merrill, 1975). Newly crystallising ferromagnetic grains may inherit remanence from the parent (Craig and Vokes, 1993; Barrie et al., 2010), as well as acquiring a new remanence, biased by some ambient field at the time of formation (Fu et al., 2014). However, CRM is generally considered contamination of remanence as it is often difficult to separate the inherited and acquired magnetisations (Cournede et al., 2015).

Viscous remanent magnetisation Over time and at a constant temperature, the magnetisation of a material can change to align with even a weak external field, such as a planetary dynamo. The fraction of grains that exist in a material above a given size will gradually acquire a viscous remanent magnetisation (VRM) in the direction of the external field (Dunlop and Özdemir, 1997). This phenomenon is particularly important for meteorite samples collected on Earth that have been subject to the geodynamo field for many years.

2.6 Palaeomagnetic methods

Often, there are multiple magnetisations recorded within a sample that contaminate the desired characteristic magnetisation. In such cases, samples require the contaminant component(s) of the magnetisation to be removed before the desired component can be measured. Recovering palaeomagnetic information from a sample can be a magnetically-destructive process. Some techniques require the use of intense fields that cause irreversible rotation of magnetisations, some require exposure to extreme temperatures that reset the magnetisation of a sample al-

together. In this section, I discuss different methods for extracting palaeomagnetic data from samples and the advantages of choosing a certain technique over others.

2.6.1 Thermal demagnetisation

Thermal demagnetisation involves heating samples and recording their response to an applied magnetic field as they are progressively heated in order to recover information about a thermoremanent magnetisation (TRM). These tests are highly effective, although destructive, as they erase the magnetisation in the sample once the measurement is completed. When raised above the temperature they were originally magnetised at, or above their Curie temperature, the magnetisation of an ideal magnetic grain hosting a TRM will fall to zero. Natural samples, however, are typically composed of a distribution of grain sizes and shapes, which means there is a distribution of magnetic properties (e.g., coercivities, shape anisotropies, volumes), and so in practice a steep drop-off to zero is rarely observed.

Laboratory thermal demagnetisation measurements consist of successively heating samples between blocking temperature intervals, up until the Curie temperature (Fig. 2.7). As the particles are heated, their magnetisations are randomised due to thermal energy and become 'unblocked'. In addition to the destructive nature of erasing remanent magnetisation, some thermally unstable materials are unsuitable for thermal demagnetisation as there is a potential for chemical alteration to occur (Cournede et al., 2015). Some samples, in particular meteorites which contain iron sulphides, have been shown to be thermally unstable upon heating. The nature of applying a field during these measurements means that thermal alteration of the magnetic carriers can either inherit a magnetic fabric from the previous mineralogy (Craig and Vokes, 1993) or record a new CRM.

2.6.2 Alternating field demagnetisation

Applying a decaying magnetic field that alternates in direction to a sample can 'clean' it of any remanent magnetisation with a coercivity that is below the peak intensity of the applied field (Collinson, 1983). This process removes less stable (low-coercivity), non-primary magnetisa-

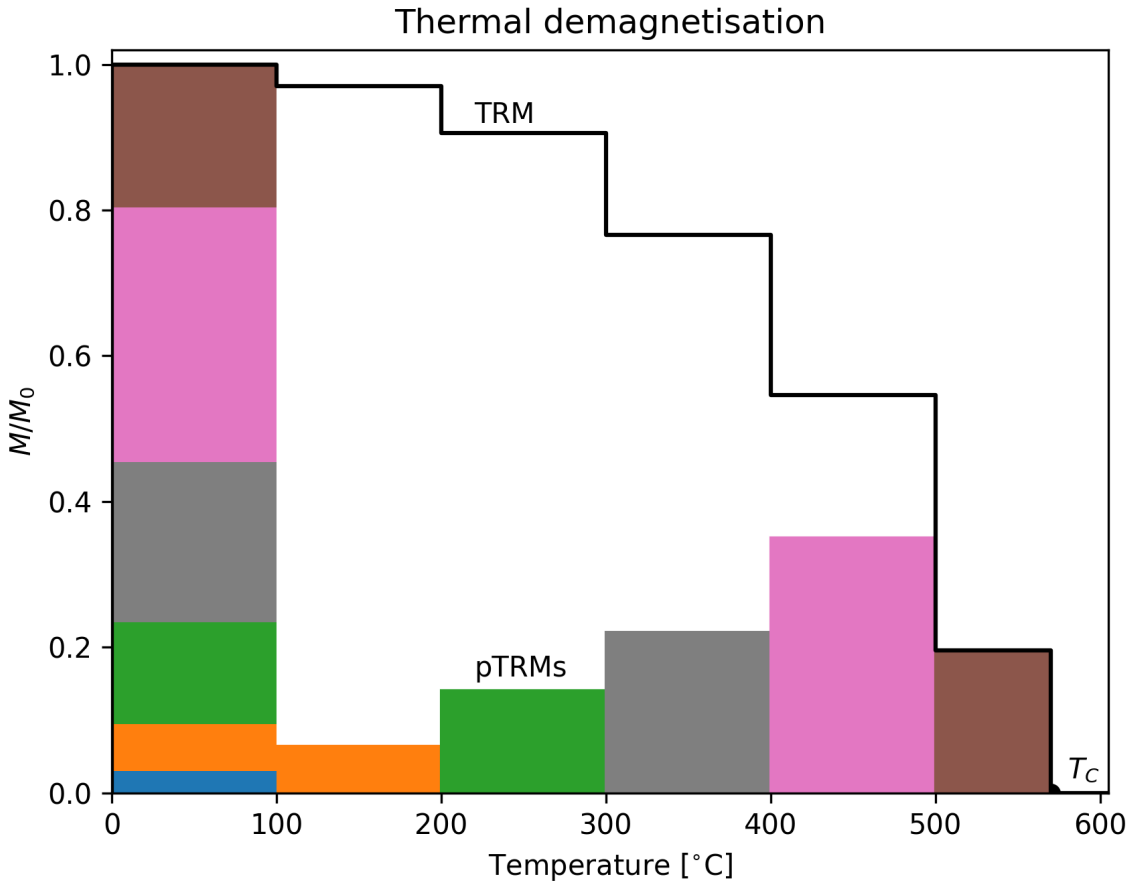


Figure 2.7: Schematic demonstrating thermal demagnetisation and the contribution of pTRM to the total TRM. The solid black line represents the total TRM remaining after some temperature, while the coloured bars show the pTRMs that are 'blocked' between successive temperature intervals (Tauxe et al., 2010). The magnetisation subsequently falls to zero at the Curie temperature, T_C (580°C here, for magnetite).

tion(s) that might be hosted within a sample, while the higher-coercivity NRM remains. This process is called alternating-field (AF) demagnetisation. Samples typically consist of a large assemblage of grains that have a distribution of sizes and consequently magnetic coercivities, H_c. Hence, applying AF demagnetisation to such a sample reveals a spectrum of coercivities.

For example, if an alternating-field, $\tilde{\boldsymbol{H}}$, with a peak field strength of 10 mT is applied to an assemblage of grains, those with coercivities $H_c \leq 10$ mT have their magnetisations randomised (i.e., remanences erased). This can be similarly repeated at higher steps, applying $\tilde{H} = 20$ mT will then erase the magnetisations of grains where $H_c \leq 20$ mT, and so on. This process reveals the *coercivity spectrum* for an assemblage of ferromagnetic grains. The median value of H_c for which half of the original NRM is randomised is called the median destructive field and is a

measure of the magnetic hardness of the sample (Dunlop and Özdemir, 1997).

2.7 Interpreting palaeomagnetic data from meteorites

Ancient magnetic data recoverable from meteorites holds a unique insight into the physical processes that occur in extraterrestrial environments. However, meteorites are prone to producing unreliable remanence measurements of remanence due to the uncertain nature of their origin and formation. This stems from several factors, including terrestrial weathering (Krähenbühl et al., 1998), acquisition of viscous magnetisation (Nagata et al., 1972), aqueous alteration (Doyle et al., 2015) and vulnerability to chemical alteration (Cournede et al., 2015). This means that determining the primary magnetisation in meteorites can be highly challenging, as can deciphering their chemical, shock and thermal alteration histories. Depending on their origin, recovered meteorites have been found to vary in age across several orders of magnitude, from thousands to billions of years old (Nyquist et al., 2001). The ages of meteorites are typically calculated from cosmic ray exposures using noble gas concentrations (e.g. Eugster et al., 1997) and they are able to be broadly classified based their mineralogy and structure (stony versus metallic content). This has led to the interpretation that meteorites that share similar mineralogy, structure and ages are likely from the same parent bodies; for example, Martian meteorites were initially identified by comparing their chemical composition to the thin Martian atmosphere (Mittlefehldt, 1994).

Palaeomagnetic studies of meteorites often use relatively small sample sizes to draw conclusions about the nature of magnetising events. When combined with palaeomagnetic results, non-magnetic measurements can be used to determine the likely thermal, metamorphic and shock histories for a meteorite. For example, mineralogical studies that have identified the presence of certain minerals attributed to high-temperature decomposition processes (e.g. Steele et al., 2016) can be reconciled with peak temperatures measured from thermal demagnetisation (Antretter et al., 2003) and numerical shock-modelling (North et al., 2023) to form a more complete history.

2.7.1 Magnetic meteorite mineralogy

This section provides a brief overview of the main magnetic minerals that are found in meteorites and discussed over the course of this thesis. These are magnetite, arguably the most important magnetic mineral in existence, the iron sulphides group and the iron-nickel alloys kamacite and taenite.

Iron-Nickel alloys

Iron-nickel (FeNi) alloys are common throughout iron meteorites. From a palaeomagnetic point of view, there are two FeNi alloys of interest: the nickel-poor alloy kamacite, α-FeNi, and the nickel-rich alloy, taenite, γ-FeNi (Paulevé et al., 1962; Ramsden and Cameron, 1966). The Curie temperature of kamacite is shared with iron, around 765°C, while for taenite this is significantly lower, around 550°C (Nagata et al., 1972). The NRM stored within Lunar rocks is often found to be carried by α-FeNi and/or γ-FeNi which are typically identified using thermal demagnetisation techniques. The iron and nickel atoms in taenite have a random or disordered arrangement, but can become ordered over long periods of time while below a critical temperature of 320°C, forming tetrataenite (Wasilewski, 1988). Tetrataenite has much higher coercivities than taenite ($30-600$ mT) and is commonly found in chondritic meteorites (Nagata and Funaki, 1982).

Magnetite

Magnetite (Fe_3O_4) occurs throughout continental rocks and the oceanic crust on Earth and is often found in extraterrestrial samples, such as Martian meteorites (e.g., McKay et al., 1996; Treiman, 1998) and in some of the oldest ($>$ 4 Ga), most primitive meteorites that have ever been recovered (e.g., Stacey, 1976; Sugiura, 1977; Krot et al., 1995). With a Curie temperature of 580°C (Dunlop and Özdemir, 1997), it is an excellent candidate for recording TRMs in extraterrestrial and terrestrial geologic processes, capturing the magnetic fields that many igneous rocks record as they cool on planetary surfaces.

Although magnetite has been identified as the primary magnetic carrier in some of the oldest

meteorites on record, many primitive meteorites are understood to have remained below $\sim 300-400$°C since their formation (McSween, 1979). This would suggest that the extraterrestrial field they have recorded is not a pure TRM (where the meteorite recorded a field as it cooled through its Curie temperature) but instead could consist of pTRM, SRM and/or CRM components (Cournede et al., 2015; Muxworthy et al., 2017).

Iron sulphides

The iron sulphides most commonly found in meteorites are pyrrhotite ($Fe_{1-x}S$, $x = 0-0.2$) and troilite (FeS), though it is pyrrhotite that is most typically identified as the primary magnetic carrier due to its relative iron deficiency (Butler, 1992). Pyrrhotite has a much lower Curie temperature than magnetite, $T_C = 320$°C (Dunlop and Özdemir, 1997), and is susceptible to chemical alteration when heated (Cournede et al., 2015). It is a relatively large ferrimagnetic mineral; single-domain grains are typically $< 3\mu$m, whereas multidomain grains are $\sim 80\mu$m (Clark, 1984). These grain volumes per domain state are considerably larger than those for magnetite (Fig. 2.4).

Chapter 3

The iSALE Shock Physics Code

3.1 An introduction to iSALE

The iSALE (impact-SALE) shock physics code (Collins et al., 2004; Wünnemann et al., 2006) is a multi-rheology, multi-material extension of the SALE (Simplified Arbitrary Lagrangian Eulerian) hydrodynamic computer code or 'hydrocode' (Amsden et al., 1980). The SALE hydrocode was developed to model Newtonian fluid flow of a single, strengthless material. Between the original version of SALE and the present version of iSALE, there has been a number of updates and improvements made to the underlying algorithm and code (Melosh et al., 1992; Ivanov et al., 1997; Collins and Melosh, 2002; Wünnemann and Ivanov, 2003; Wünnemann et al., 2005).

With some limitations, the iSALE solution algorithm is able to solve the governing equations of continuum mechanics in a Lagrangian reference frame, an Eulerian reference frame or an arbitrary frame of reference, achieving what is known as the Arbitrary Lagrangian Eulerian (ALE) solution. The choice of whether to approach a problem using either the Lagrangian or Eulerian description is circumstantial. In Lagrangian mode, the frame of reference of the computational mesh is defined to represent the geometry of the problem, deformation is described relative to the material and the degree of deformation of the mesh itself. In contrast, in Eulerian model a fixed frame of reference is employed where the material moves through a static mesh, and deformation is described relative to a fixed point in space.

Calculations using the Lagrangian description tend to be faster than in Eulerian because material fluxes between cells are computationally expensive. Similarly, there are many cells that require resolving which contain empty space in Eulerian mode compared to Lagrangian. However, the Lagrangian description encounters problems in simulations where cells experience high levels of deformation. In Lagrangian mode, cells can become extremely elongated to the point where cell vertices become inverted and the calculation is forced to stop. This problem is avoided in Eulerian calculations as the mesh remains fixed and the issues caused by highly deformed cells in Lagrangian calculations are omitted. For this reason, the Eulerian description is typically preferred over the Lagrangian for impact modelling. Where iSALE is used in this thesis, I have only used it in Eulerian mode.

iSALE is also able to be run in two-dimensional (iSALE-2D) and three-dimensional (iSALE-3D; Elbeshausen and Wünnemann (2011)) modes. iSALE-3D is significantly more computationally expensive than iSALE-2D. For this reason and the number of simulations that I have ran over the course of the work presented in this thesis, I have used iSALE-2D exclusively.

3.2 Fundamental equations

The fundamental equations that are solved by iSALE are those described by Anderson (1987) and Pierazzo and Collins (2004). These equations describe the dynamics of compressible, continuous material and include a set of material-specific expressions. The first of these are three differential equations that describe the fundamental conservation laws of physics - the conservation of momentum, conservation of mass and conservation of energy.

iSALE-2D consists of a two-dimensional grid of quadrilateral cells and uses either a Cartesian or cylindrical coordinate system. Hence, iSALE-2D is able to solve problems that are demonstrably two-dimensional or symmetrical about a central axis. The first of these equations that are implemented in iSALE-2D are those which describe the conservation of momentum:

$$\frac{\partial \rho u}{\partial t} = \frac{\partial (P+q)}{\partial x} + \frac{1}{r}\frac{\partial r s_{xx}}{\partial x} + \frac{\partial s_{xy}}{\partial y} - \frac{s_\theta}{r} + \rho \mathbf{g_x} \tag{3.1}$$

$$\frac{\partial \rho v}{\partial t} = \frac{\partial (P+q)}{\partial y} + \frac{1}{r}\frac{\partial r s_{xy}}{\partial x} + \frac{\partial s_{yy}}{\partial y} + \rho \mathbf{g_y} \tag{3.2}$$

where q is an artificial pressure, required to stabilise the calculation during shock wave propagation, r is a radial distance component, ρ is material density, t is time and the velocities u and v describe the horizontal and vertical velocity components, respectively. When used in cylindrical geometry (this is implemented in iSALE by setting the input parameter `CYL`=1), the coordinate system is $[r, \theta, z]$ such that $x = r$, $y = z$. Whereas when using the Cartesian system (i.e., $[x, y]$ and `CYL`=0), radii are set to unity ($r = 1$). Factors of π are able to be omitted from all equations, even when using cylindrical geometry, as calculations are scaled to unit azimuthal angle.

Solving the remaining two equations in 2D, the conservation of mass is simply:

$$\frac{\partial \rho}{\partial t} = -\rho \left(\frac{1}{r}\frac{\partial r u}{\partial x} + \frac{\partial v}{\partial y} \right) \tag{3.3}$$

and finally, the specific internal energy, E, is calculated using:

$$\frac{\partial \rho E}{\partial t} = -(P+q)\left(\frac{1}{r}\frac{\partial r u}{\partial x} + \frac{\partial v}{\partial y} \right) + s_{xx}\frac{\partial u}{\partial x} + s_{xy}\left(\frac{\partial v}{\partial x} + \frac{\partial u}{\partial y} \right) + s_y \frac{\partial v}{\partial y} + \frac{u s_\theta}{r} \tag{3.4}$$

To complete the full set of equations that form the Eulerian solution, iSALE requires material-specific equations that are able to account for density, internal energy, pressure and velocity components. These are known as an *equation of state* and a *constitutive (strength) model*:

$$P = P(\rho, E) \qquad \text{Equation of state} \tag{3.5}$$

$$s_{ij} = g(\epsilon_{ij}, \dot{\epsilon}_{ij}, P, T, D) \qquad \text{Strength model} \tag{3.6}$$

where P represents pressure, T represents the temperature and D the damage, which is a measure of the degree of fracturing in a computational cell. Other variables follow the same nomenclature as equations 3.1 - 3.4. The equation of state describes the response of a material to a change in volume while the strength model describes the resistance to changes in shape. The different equations of state and strength models that are used throughout this thesis are discussed later on in this chapter.

As an extension of the SALE hydrocode (Amsden et al., 1980), iSALE shares the same underlying solution algorithm. That is, the model solves the Lagrangian version of the governing equations and then transposes these solutions onto an Eulerian grid, should the Eulerian description be specified.

iSALE solves these governing equations using a finite-difference approximation. The main purpose of doing this is to spatially and temporally discretise the partial differential equations in order to be solved using a computer. This allows for the calculation of physical parameters to occur at each timestep of the calculation.

3.3 Material models

As mentioned previously, iSALE uses two material-specific equations as part of the fundamental equations that are solved by the code: the equation of state and the constitutive or strength model (equations 3.5 and 3.6, respectively). In this thesis, I have used a number of the available equation of state regimes and strength models that are supported by iSALE. In this section, I describe these equations in detail and also address how iSALE describes pore space compaction.

3.3.1 Equations of state

An equation of state takes the general form of equation 3.5. It describes the relationship between the three thermodynamic variables, pressure, P, density, ρ and specific internal energy, E (or temperature, T). Within iSALE, the purpose of the equation of state is to calculate the physical response of a material to a change in volume. Consequently, it is the equation of state that

dictates to a large degree the material response to shock heating during an impact. In all cases throughout this thesis, I have tried to use the most relevant and advanced equation of state possible.

For meteoritic materials, shock data is often very limited, and so in some cases materials have been described using more simplified equations of state. Where there has not been a suitable equation of state already determined, I have created a new equation of state using shock data that has been made available on the Rusbank shock database (`http://www.ihed.ras.ru/rusbank`). Where a new equation of state for a material has been created, it is explained in detail in place in the thesis. In this section, I present the mathematical form of the equations of state used throughout this thesis, in order of increasing complexity.

Mie-Grüneisen equation of state

Of the three equations of state used in this thesis, the Mie-Grüneisen equation of state (Heuzé, 2012) is the most simple. In this descriptor, the pressure is divided into two components: the 'cold' term, P_C, also called the reference pressure, which depends on density, and the thermal term, P_T, which depends on both the density and energy:

$$P = P_C + P_T = P_C + \Gamma(\rho)\rho(E - E_C(\rho)) \tag{3.7}$$

where the reference pressure, P_C, reference energy, E_C, and Grüneisen parameter, Γ, are purely functions of the material density, ρ.

Terms P_C, E_C and Γ can be derived by defining the reference state as the shock Hugoniot, a locus of all the possible thermodynamic states a material can occupy following a shock. This then redefines $P_C = P_H$, $E_C = E_H$, and assumes the relationship between shock velocity, u_s, and particle velocity, u_p, is linear (i.e., $u_s = Su_p + c_0$, where S is the 'slope coefficient'). Under these assumptions, the Mie-Grüneisen equation of state can be rewritten in terms of the Hugoniot energy as:

$$P = P_H + \Gamma_0\rho_0(E - E_H) \tag{3.8}$$

where the Mie-Grüneisen parameter is inversely proportional to the density, ρ, such that $\Gamma\rho = \Gamma_0/\rho_0$. Defining two new parameters, $\eta = \rho_0/\rho$, and $\mu = 1 - \eta$, along with assuming that $P_0 = E_0 = 0$, the equation of state is able to be redefined in terms of the slope coefficient (S) that describes the relationship between the particle velocity and shock velocity:

$$P = \frac{\rho_0 c_0^2}{(1 - S\mu)^2}\left(\mu - \frac{\Gamma_0}{2}\mu^2\right) + \Gamma_0\rho_0 E \tag{3.9}$$

Finally, differentiating equation 3.15 with respect to density, ρ, and rearranging yields an expression for the sound speed, c, squared:

$$c^2 = \left(\frac{c_0\eta}{1 - S\mu}\right)^2\left(\frac{1 + \mu(S - \Gamma_0)}{1 - S\mu}\right) + \frac{P}{\rho}\Gamma_0\eta \tag{3.10}$$

valid for compression where $\rho/\rho_0 \leq S/(S - 1)$. This form of the Mie-Grüneisen equation of state is able to be used within iSALE.

Tillotson equation of state

Improvements to the SALE code by Melosh et al. (1992) provided the inclusion of the Tillotson EoS (Tillotson, 1962), which describes the response of a material to a change in volume.

The empirical Tillotson equation of state (Tillotson, 1962) is suitable for a wider range of pressures and considers more material parameters than the Mie-Grüneisen description. The equation extrapolates the linear, low-pressure shock-particle velocity relationship ($u_s = Su_p + C$) to the Thomas-Fermi limit at high pressures (Tillotson, 1962).

When a material is compressed to a higher density than its reference, zero-pressure density (i.e., $\rho \geq \rho_0$), the Tillotson equation of state takes the form:

$$P_c = \left[a + \frac{b}{E/(E_0\eta^2) + 1}\right]\rho E + A\mu + B\mu^2 \tag{3.11}$$

where $\eta = \rho/\rho_0$ and $\mu = \eta - 1$. The remaining values, a, b, A, B and E_0 are the Tillotson parameters, while the initial energy density, E, must be equal to zero to ensure $P = 0$ in the

initial state. In this description, E_0 is not the initial energy, but instead is a value that is typically close to the vaporisation energy of the material. This equation is true any material state where the internal energy density E is less than the energy of incipient vaporisation, i.e., $E < E_{iv}$.

In the case of a material expansion whereby the new material density following a shock is less than the reference density (i.e., $\rho \leq \rho_0$) and the material is in an expanded state (the internal energy density is greater than the energy of complete vaporisation, $E > E_{cv}$), the equation of state becomes:

$$P_h = a\rho E + \left[A\mu e^{-\beta\mu} + \frac{b\rho E}{E/(E_0\eta^2) + 1} \right] e^{-\alpha\mu^2} \tag{3.12}$$

where α and β are constants that control the rate of convergence of equation 3.18 to the ideal gas law.

To make the transition between the compressed to expanded descriptions, in a state of partial vaporisation where the internal energy is between the energy of incipient vaporisation and complete vaporisation ($E_{iv} < E < E_{cv}$ and $\eta < 1$), the pressure can be calculated using a composite formula:

$$P_m = \left(\frac{E - E_{iv}}{E_{cv} - E_{iv}} \right) P_h + \left(\frac{E_{cv} - E}{E_{cv} - E_{iv}} \right) P_c \tag{3.13}$$

ANEOS

Ivanov et al. (1997) later modified the SALE hydrocode to included support for the Analytical Equation of state, *ANEOS* (Thompson and Lauson, 1972; Melosh, 2007). This modified version of SALE was known as the SALEB hydrocode and was capable of modelling entire impact events (e.g., Ivanov and Deutsch, 1999; Ivanov and Artemieva, 2002)

ANEOS is a semi-analytical model that is capable of complex material description across a broad range of pressures. This model derives densities, temperatures and pressures from the Helmholtz free energy, making them thermodynamically consistent. This is done by separating

the Helmholtz free energy, F, into three components: F_c the 'cold' component, controlled by inter-atomic forces, F_t the thermal component, arises from atomic vibrations and thermal motion, and an electronic component, F_e, which describes high-temperature ionisation gaseous behaviour.

While a superior equation of state to the previous descriptions, the derivation of ANEOS tables for materials is complex and constantly being improved. A large amount of shock data is required to accurately represent a material using an analytical model such as ANEOS. In this thesis, while I have used ANEOS-derived tables where possible, only those that exist in the publicly-available Dellen release of iSALE have been used.

3.3.2 Strength models

Improvements made to the original SALE code (Melosh et al., 1992; Ivanov et al., 1997) to include better modelling of deformation features and an improved range of rheologic models were released as SALES-2 (Collins and Melosh, 2002). The inclusion of a modified strength model was the final update before the previous SALES-2 release was released as the iSALE shock physics code (Collins et al., 2004).

While the equation of state describes the response of a material to a change in volume, the fifth fundamental equation that iSALE solves, the constitutive (or strength) model, describes the resistance of a material to a change in shape. In this thesis, I have used three of the available strength models in iSALE to describe a number of different materials. The choice of strength model is made based on available shock and material data, as well as the suitability of the model for that material. Here, the governing equations of these three strength models are outlined and the parameters required for the calculation are defined.

Drucker-Prager strength model

The Drucker-Prager strength model (Drucker and Prager, 1952) defines the yield strength, Y, as:

$$Y = min(Y_0 + \mu P, Y_m) \tag{3.14}$$

where P is the applied pressure, Y_0 describes cohesion, the yield strength at zero pressure, μ is the coefficient of internal friction and Y_m is the limiting strength at high pressure.

ROCK strength model

The ROCK strength model (Ivanov et al., 1997; Collins et al., 2004) incorporates a damaged material strength, Y_d, and intact material strength, Y_i, into the calculation. In this model, yield strength, Y, is defined by:

$$Y = Y_d D + Y_i(1 - D) \tag{3.15}$$

where D is a measure of damage such that $D = 0$ represents an intact material and $D = 1$ a damaged material. In the work throughout this thesis, the damage is described as a function of plastic strain using the `IVANOV` model within iSALE:

$$D = min\left(\frac{\epsilon_p}{\epsilon_f}, 1\right) \tag{3.16}$$

where ϵ_p is a measure of the total plastic strain ($\epsilon_p > 0$ in all cases), while ϵ_f is the plastic strain at failure and is a function of pressure (Ivanov et al., 2010):

$$\epsilon_f = max(\epsilon_{fb}, B(P - P_c)) \tag{3.17}$$

where ϵ_{fb} is the minimum failure strain at low pressure, B is a positive constant, P is again pressure and P_c is the pressure above which failure becomes compressional.

The damaged material strength, Y_d, is calculated by:

$$Y_d = min(Y_{d0} + \mu_d P, Y_{dm}) \tag{3.18}$$

where P is pressure, Y_{d0} is the cohesion of damaged material, μ_d is the coefficient of internal friction for damaged material and Y_{dm} is the limiting strength at high pressure for damaged material. On the other hand, the intact material strength, Y_i, is defined as:

$$Y_i = Y_{i0} + \frac{\mu_i P}{1 + \frac{\mu_i P}{Y_{im} - Y_{i0}}} \tag{3.19}$$

where Y_{i0} is the cohesion of the intact material, μ_i is the coefficient of internal friction for intact material and Y_{im} describes the limiting strength at high pressure for intact material.

Johnson-Cook strength model

The Johnson-Cook strength model (Johnson and Cook, 1983) adds additional complexity to the previous strength models described. The complete Johnson-Cook description of the yield strength is defined as:

$$Y = (A + B\epsilon^N)(1 + C \ln \dot{\epsilon}) \left[1 - \left(\frac{T - T_{ref}}{T_m - T_{ref}}\right)^M\right] \tag{3.20}$$

where ϵ represents the plastic strain, $\dot{\epsilon}$ the strain rate and T temperature. A is the yield strength in the reference state, a state when $T = T_{ref}$, $\epsilon = 0$ and $\dot{\epsilon} = 1$, while T_m defines the melting temperature. B, C and N are constants, set with iSALE input parameters.

The Johnson-Cook model also has an associated damage model that differs from that as described by Ivanov et al. (2010) (equation 1.16). The damage equation takes the same form as equation 1.16, but the plastic strain at failure, ϵ_f, takes the form:

$$\epsilon_f = [D_1 + D_2 \exp(D_3 \sigma^\star)][1 + D_4 \log \dot{\epsilon}^\star][1 + D_5 T^\star] \tag{3.21}$$

where $\dot{\epsilon}^\star$ is the total strainrate, $T^\star$ is the homologous temperature, $T^\star = (T - T_{ref})/(T_m - T_{ref})$, and $\sigma^\star$ is the ratio between pressure and stress ($\sigma^\star = -P/\sigma$). D_1 through D_5 are constants.

3.3.3 The OHNAKA thermal softening model

Many materials experience a reduction in stiffness due to heating in a process called 'thermal softening'. In rocks, increasing temperatures result in a decrease in shear strength. iSALE is able to approximate the thermally-softened strength of rocks as a function of temperature, using the `OHNAKA` thermal softening model (Ohnaka, 1995; Collins et al., 2004):

$$Y = Y_c \tanh\left(\xi\left(\frac{T_m}{T} - 1\right)\right) \tag{3.22}$$

where the thermally-softened strength, Y, is a function of the 'cold' yield strength, Y_c, temperature, T, melt temperature, T_m and a material constant, ξ.

3.3.4 The Simon approximation

The Simon approximation is used to define melt temperature, T_m, is defined as a function of pressure, P, in iSALE:

$$T_m = T_{m0}\left(\frac{P}{a} + 1\right)^{1/c} \tag{3.23}$$

where T_{m0} is the melt temperature at zero pressure and a and c are material constants.

3.3.5 The $\epsilon - \alpha$ porosity compaction model

The porosity depletion or compaction model used in iSALE relates volumetric strain, ϵ_v, to the distension, α, which is the ratio between the solid material density, ρ_s, and the bulk density, ρ ($\alpha = \rho_s/\rho$) (Wünnemann et al., 2006; Collins et al., 2011). Porosity, ϕ, is related to distension and consequently the solid and bulk densities by:

$$\phi = 1 - \frac{1}{\alpha} = 1 - \frac{\rho}{\rho_s} \tag{3.24}$$

Hence, for a non-porous material where $\phi = 0$, the distension would be unity, $\alpha = 1$.

Initial distension, α_0, is quantity that is able to be passed directly to iSALE as an input parameter to declare the initial porosity of a given material. Following the complete $\epsilon - \alpha$ model by Wünnemann et al. (2006); Collins et al. (2011), the new distension of a material, α, is then updated according to one of four regimes that describe the densification of a porous material, from its initial state, up to and beyond its fully compacted state:

$$0 > \epsilon > \epsilon_e \qquad \alpha = \alpha_0 \qquad \text{Elastic compaction} \tag{3.25}$$

$$\epsilon_e > \epsilon > \epsilon_x \qquad \alpha = \alpha_0 \exp\left(\kappa(\epsilon - \epsilon_e)\right) \qquad \text{Exponential compaction} \tag{3.26}$$

$$\epsilon_x > \epsilon > \epsilon_c \qquad \alpha = 1 + (\alpha_x - 1)\left(\frac{\epsilon_c - \epsilon}{\epsilon_c - \epsilon_x}\right)^2 \qquad \text{Power-law compaction} \tag{3.27}$$

$$\epsilon_c > \epsilon \qquad \alpha = 1 \qquad \text{Compression} \tag{3.28}$$

where ϵ represents the volumetric strain and the subscripts c, x, e denote the compaction regime. The parameter κ accounts for different material behaviour and types of porosities (see below). In iSALE, α is not calculated directly using these equations. Instead, the rate of compaction ($\frac{d\alpha}{d\epsilon}$) is calculated for each regime and subsequently α is updated:

$$\alpha_{n+1} = \alpha_n + \frac{d\alpha}{d\epsilon}\frac{d\epsilon}{dt}\Delta t \tag{3.29}$$

When under elastic compaction, the porosity remains unchanged and hence $\alpha = \alpha_0$. The majority of compaction occurs during the exponential compaction regime where $\epsilon_e > \epsilon > \epsilon_x$.

In this case, the rate of compaction for a volumetric strain ϵ_v is:

$$\frac{d\alpha}{d\epsilon_v} = \kappa\alpha = \kappa\alpha_0 \exp(\kappa(\epsilon_v - \epsilon_e)) \tag{3.30}$$

In the idealised case where $\kappa = 1$, all pore space is crushed out before material compression begins. In the case where $\kappa < 1$, the removal of pore space occurs simultaneously with material compression.

Following on from exponential compaction, when $\epsilon_x > \epsilon > \epsilon_c$ the material enters the power-law compaction regime where compaction occurs at a slower rate. In the power-law regime, the rate of compaction becomes:

$$\frac{d\alpha}{d\epsilon_v} = 2(1 - \alpha_x)\left(\frac{\epsilon_c - \epsilon_v}{(\epsilon_c - \epsilon_x)^2}\right) \tag{3.31}$$

Finally, once all pore space has been removed and $\epsilon_v < \epsilon_c$, both the distension and rate of compaction fall to zero ($\alpha = 0$ and $\frac{d\alpha}{d\epsilon_v} = 0$) and the compaction regime becomes entirely compressive.

When using iSALE, there are a total of five material input parameters for the $\epsilon - \alpha$ porosity compaction model. These include α_0, α_x and κ, which share the same definition as in the compaction regimes described here. In addition, there are two more variables, the first being χ which describes the ratio between sound speed of porous material relative to solid matrix ($\chi = c_0/c_{s0}$), and ϵ_{e0}, which is the elastic volumetric strain threshold.

3.4 Mesoscale modelling

In this thesis, I use iSALE to resolve localised pressure and temperature experiences of millimetre-sized meteorites and synthetic meteorite analogues. While historically used for impact crater-scale studies (e.g., Goldin et al., 2006; Potter et al., 2013; Johnson et al., 2015), iSALE can also be employed to study the thermodynamic and mechanical sub-millimetre interactions between materials on the so-called 'mesoscale'. With an arbitrary meaning describing the intermediate

stage between the micro- and macroscale (e.g., Nesterenko, 2001; Borg and Vogler, 2008), the mesoscale can be defined as the resolution of a single pore, $\sim 1 - 10$ μm (e.g., Williamson and Berry, 1986; Güldemeister et al., 2013), or in meteorite studies, the mesoscale is often defined as the scale of one chondrule, $\sim 10 - 100$ μm (e.g., Bland et al., 2014; Davison et al., 2016).

Eulerian finite-element shock physics codes used for mesoscale simulation have been verified against laboratory experiments with shock experiments on granular materials (Benson, 1994; Benson et al., 1997). Recent studies using iSALE have explored the chondrule-matrix interaction of chondritic meteorites in low-velocity impacts (Bland et al., 2014; Davison et al., 2016), while others have explored the extreme shock pressures (> 70 GPa) that have been recorded in partially melted meteorites (Moreau et al., 2019).

When using iSALE, the spatial resolution is simple to set in the input file. In Eulerian mode, the fidelity with which the free surface and material boundaries are modelled depends on the spatial resolution of the mesh, hence, the higher the resolution the more accurate the simulation is likely to be. Typically, the resolution of the mesh can be quantified using a measure called the cells per particle radius (CPPR).

3.4.1 Lagrangian tracers

When using iSALE in Eulerian mode, the history of a material cannot be tracked directly. Instead, iSALE uses non-interacting, massless 'Lagrangian' tracer particles (tracers hereafter) to record the experience of materials through the mesh (Ivanov et al., 1997; Ivanov and Artemieva, 2002). Tracers are capable of recording a number of physical parameters of the material to which they have been assigned, including temperature, pressure, distension, velocity and strain. The assignment process uses a cell coordinate system, i, j, where the computational mesh is i cells across and j cells tall.

One recent improvement to the iSALE code includes the `MATERIAL` algorithm, allowing Lagrangian tracers to be moved through the Eulerian computational grid according to material volume fluxes (Davison et al., 2016). In this thesis, I have used the `MATERIAL` algorithm in all tracer assignments. Tracers are assigned as one tracer per computational cell of the mesh,

recording the history of the material in that cell as it moves through the mesh according to the velocity field. The algorithm works by defining fractional distances across the cell the tracer occupies, ξ_x^n and ξ_y^n. This means that the horizontal and vertical velocity components can be defined by:

$$v_x = \left(\frac{(1-\xi_x^n)F_L}{\alpha_L} - \frac{\xi_x^n F_R}{\alpha_R} \right) \frac{x_{i+1} - x_i}{V_{ij} dt} \tag{3.32}$$

$$v_y = \left(\frac{(1-\xi_y^n)F_B}{\alpha_B} - \frac{\xi_y^n F_T}{\alpha_T} \right) \frac{y_{j+1} - y_j}{V_{ij} dt} \tag{3.33}$$

where F is the net volume of the material fluxing between adjacent cells, α is the ratio of the material fluxing between cell interfaces and the total material volume (i.e., $F_{material}/F_{tot}$), V_{ij} is the total volume of the cell i, j, while dt is the length of the current timestep and subscripts L, R, T, B are cell interfaces left, right, top and bottom, respectively.

3.4.2 pySALESetup

Complex mesh geometries have been made possible thanks to James Derrick who recently developed the publicly available python module `pySALESetup` (`https://github.com/jgd10/PySALESetup`). This module is able to create iSALE mesh files from bitmap images. Moreover, it is able to assign different materials to cells in the computational mesh, meaning mineralogically heterogeneous rock geometries can be directly imported into the iSALE setup. The spatial resolution chosen within the iSALE input file is mapped directly onto the pixels of the bitmap file and materials are assigned according to pixel colouration. The `pySALESetup` module is used extensively in Chapter 5, where a workflow for calculating the heterogeneous mesoscale response of synthetic meteorite thin sections to planar shock has been developed.

Chapter 4

Recording Magnetic Fields During Impact-induced Compaction

4.1 Introduction

The lithification of bodies within the Solar System, from primordial "rubble piles" (Weidenschilling and Cuzzi, 2006) to rocky asteroids and ultimately planets, is an area of active debate (e.g. Cuzzi and Weidenschilling, 2006; Weiss et al., 2010b; Bai and Stone, 2013; Bland et al., 2014; Turner et al., 2014; Matsumoto et al., 2017) that may be answerable by the palaeomagnetic evidence contained within a group of the oldest, most pristine and unaltered meteorites on record: carbonaceous chondrites (CCs). Recovered CCs are often found to contain a remanent magnetisation of uncertain origin. The most likely candidate for the inducing palaeofield that magnetised CCs was either the Solar Nebular field (Bland et al., 2014; Fu et al., 2014; Wang et al., 2015) or a planetesimal dynamo (Weiss et al., 2010b; Elkins-Tanton et al., 2011) from within the parent body on which they formed.

From the literature, there are generally thought to be three mechanisms which may be responsible for the acquisition of remanence by chondrites: (1) chemical action or crystallisation from aqueous alteration which would mean the NRM is in fact a chemical remanent magnetisation (CRM) (McSween, 1979; Cournede et al., 2015), (2) a thermoremanent magnetisation (TRM), recorded following the metamorphic heating and differentiation of the parent

body (Weiss et al., 2010b; Elkins-Tanton et al., 2011; Carporzen et al., 2011; Gattacceca et al., 2016), or (3) an impact-induced TRM, whereby low-velocity impacts cause transient heating (Davison et al., 2016). The first two mechanisms require stable magnetic fields, whereas the third mechanism is sufficiently brief ($\sim$ 10s) to have also recorded snapshot of an unstable background field, such as those in the Solar Nebula (Nagata, 1979; Bland et al., 2014) or the Solar wind (Tarduno et al., 2017; O'Brien et al., 2020), as this is much longer than the $\sim$nanosecond magnetic reordering time (Néel, 1949).

This chapter focuses on testing the third of these hypotheses, namely whether shock-induced heating could be the mechanism responsible for the observed TRM within CCs. Carbonaceous chondrites show little evidence for high shock pressures (Stöffler et al., 1991; Scott et al., 1992), hence impacts have generally not been considered a significant factor in their history. However, recent studies have proposed that these and other chondrites originated from highly porous asteroids that were compacted and lithified by low-velocity impacts (Bland et al., 2014; Lindgren et al., 2015). Recent numerical models have further shown that in such high porosity precursor materials, the low velocity collisions consistent with the shock state of CC meteorites can produce significant shock heating of the compacted matrix raising it to temperatures $>$ 300 K higher than the bulk temperature of the material (Davison et al., 2010; Bland et al., 2014; Davison et al., 2016). This has led to the hypothesis that low-velocity collisions between primitive chondritic objects can provide a mechanism for recording palaeomagnetic fields in matrix material Bland et al. (2014). This hypothesis has been supported by recent palaeomagnetic evidence from CV chondrite Allende, where the NRM was confirmed to be a TRM with behaviour and intensity consistent with an impact-induced origin (Muxworthy et al., 2017). It has also been suggested that the same mechanism was responsible for the pTRM recorded in the ungrouped C2 chondrite WIS 91600 (Bryson et al., 2020a).

However, there is a lack of experimental evidence that confirms the ability of highly-porous ferromagnetic materials to record an external magnetic field. While the lithification of high porosity materials consistent with CCs has been shown experimentally (Beitz et al., 2013; Forman et al., 2016; Rutherford et al., 2017), the temperature experienced in the matrix has not been determined, nor was the potential to record a magnetic field tested. In this study, I am

to reconcile this missing evidence with the conditions that are inferred to have been experienced by recovered chondrites.

4.1.1 Motivation and aims

Chondrites are now understood to have originated from highly-porous precursor material, undergoing a gentle accretion process where they were lithified by multiple low-velocity impacts (Bland et al., 2014; Lindgren et al., 2015; Forman et al., 2017). During these low velocity impacts, heating was brief (∼seconds-minutes) and sufficiently intense (> 300°C; Davison et al. (2016)) to have recorded a magnetic field (Muxworthy et al., 2017). In this chapter, I aim to experimentally test whether the impact-induced compaction of highly-porous chondritic material is capable of recording a thermoremanent magnetisation. To test my hypothesis, this work details an experiment in which a planar shock wave is driven into a porous, synthetic material, with mechanical properties comparable to natural chondrite samples. By carefully choosing materials that share mechanical properties similar to chondrite precursor material, these experiments should heat magnetic carriers within the sample to sufficiently high temperatures to record a magnetic field, meanwhile reaching pressures that are similar to those experienced by recovered chondrites (Stöffler et al., 1991; Scott et al., 1992).

4.1.2 Experiment overview

The experiment comprised of three distinct phases: numerical modelling, physical shock experiments and magnetic measurements. The project was initiated with extensive numerical modelling of the sample capsule. The projectile size, shape and weight, cooperatively with the capsule design were thoroughly investigated using iSALE to configure a scenario where the sample material would experience a planar shock wave close to the natural conditions expected for a low-velocity impact (a bulk shock pressure between 1-2 GPa; Bland et al. (2014)) and also where the matrix would experience a temperature excursion consistent with measured palaeomagnetic data from CCs (peak matrix temperatures recorded in CV chondrites have been found to be between 300-350°C; Muxworthy et al. (2017)). Results of the modelling are outlined in

the next section.

Secondly, the experiments required a magnetically-controlled environment for the impact apparatus to be contained within. The target chamber—the sealed aluminium box used as the collision site for the shock experiments—was placed inside a Helmholtz cage. Three pairs of Helmholtz coils were arranged in perpendicular planes that allowed the strength and direction of the magnetic field to be controlled. I built the cage at Imperial College, custom designed for the light-gas gun apparatus in the shock physics laboratory at the University of Oxford. Using this Helmholtz cage, the magnetic field around and within the shock apparatus could be controlled, both in terms of nullifying Earth's background field as well as generating desired field strengths.

Samples were then prepared to have similar initial porosity and density to chondritic precursor material which required compaction of the sample (see §4.5.4) to a desired porosity, $\phi \sim 70\%$. Shock experiments were then performed using the light-gas gun apparatus at the University of Oxford. The shots were performed over three days which included assembly, velocity testing and capsule recovery (see §4.5 for full detail).

Finally, the recovered capsules were taken to the Natural Magnetism Group laboratory at Imperial College where the remanent magnetisation could be measured. This collaborative project took place over the course of my PhD and facilitates a proof-of-concept study that impact-induced compaction is a viable mechanism for recording magnetic fields in the early Solar System. This chapter presents the preparatory phases of this experiment in full detail, as well as a discussion of the results from the magnetic measurements and their implications for the meteorite record.

4.2 Numerical modelling an impact experiment

To predict the physical conditions experienced during the impact experiments, the response to shock of the projectile, capsule and sample was modelled using shock physics code iSALE (Collins et al., 2004; Wünnemann et al., 2006). This provided a framework to estimate the shock

pressure and temperature experienced by the sample and how these change with alterations to the capsule design.

Ultimately, the aim of the modelling was to determine an experimental configuration whereby the estimated temperatures and pressures experienced across the sample are consistent with those inferred from palaeomagnetic studies (e.g., Carporzen et al., 2011; Shah et al., 2017; Muxworthy et al., 2017) and estimates from previous numerical investigations (Bland et al., 2014; Davison et al., 2016). Using iSALE also allows for adjustment of the experiment to minimise any spatial pressure and temperature variation and improve the homogeneity of the pressure and temperature experience in the sample.

4.2.1 The recovery fixture criteria

The design of a recovery fixture suitable for the experimental aims had to fulfil a number of criteria:

1. The sample must be recoverable and not destroyed during the experiment.
2. The capsule must be capable of withstanding shock pressures ~ 2 GPa.
3. The capsule must be made of a non-magnetising material.
4. The design should reduce intra-capsule reflections as much as possible.
5. The design should reduce heterogeneity of pressures and temperatures in the sample.

Using the above criteria, some parts of the design were able to be predetermined. Firstly, the sample must be secured within a sealed capsule as it needs to be recovered and this capsule should be similar in size to the circular 25 mm gun barrel. This way, the shock wave can be generated at a collision site that is separated a small distance from the sample itself, and the sample is not subject to direct impact damage. Secondly, the capsule could not be manufactured from iron or any other ferromagnetic material. This eliminates widely used iron alloys, such as steel, which are strong, cheap and easily manufactured. To address these realisations, the

capsule would be cylindrical, with the sample contained inside, and be made from an a non-magnetic metal. Aluminium alloys are well known to be rugged and non-magnetic. Aluminium-6061, which uses magnesium and silicon as its major alloying elements, was determined to be suitable as it is non-magnetising, non-brittle and malleable, making it suitable for capsule manufacture (Nunes et al., 1990).

The only physical constraint placed on the capsule design was that the diameter should be 25 mm, matched to the size of the light-gas gun barrel and projectiles at the University of Oxford. Advised by Dr. Daniel Eakins, the lead researcher at the Department of Engineering Science at Oxford and his laboratory staff, I determined a suitable diameter for the sample contained within the capsule should be 9 mm, while the height of the sample was chosen to be 3 mm as to ensure the sample would be large enough after compaction to host a strong magnetisation. The final constraint was to determine the velocity of the projectile fired by the single-stage light-gas gun used in the experiments. Following advice from the laboratory operators, a 6 mm flyer plate was used, also made from aluminium-6061, mounted on a 36 mm polycarbonate sabot, which was a suitable size and mass to reach a consistent target velocity of 800 ms^{-1}. This velocity was within the working limits of the apparatus and, based on previous experiments using similar-sized aluminium targets, would be capable of generating peak shock pressures in the 1 - 3 GPa range on an aluminium target (Dr. Daniel Eakins, personal communication).

4.2.2 The Sawaoka capsule

The *Sawaoka* capsule architecture was designed to be used in experiments that produce a planar shock on several targets at once (e.g. Song and Thadhani, 1992; Eakins and Thadhani, 2009). The original design consisted of multiple cylindrical sample containers embedded in a large plate, cushioned by a momentum trap (Sawaoka, 1993). I have adapted the design of one of these sample containers into a standalone recovery fixture, suitable for an impact-recovery experiment using a light-gas gun (Fig. 4.1).

The iSALE modelling of the experiment involved adjusting the sample depth from the impact face of the capsule, the height of the capsule as well as exploring the inclusion of an

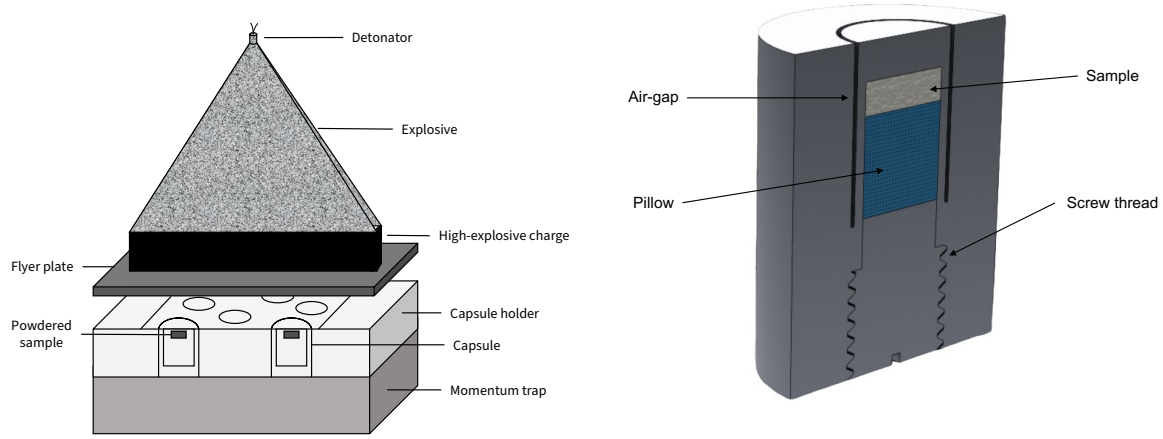


Figure 4.1: (a) The original Sawaoka capsule design was used in a plate, engineered to produce a uniform shock wave in multiple powdered samples simultaneously (Song and Thadhani, 1992). (b) I have taken the architecture of one individual capsule to design the recovery fixture suitable for the experiments presented in this chapter. The design presented here includes major architectural modifications, including an air-gap and shock-absorbing 'pillow'.

intra-capsule air-gap to control the shock front passing through the sample and a low-impedance shock attenuation 'pillow', to reduce the amplitude of the shock wave after it passed through the sample. Adaptations made to the model are explained below in detail.

4.2.3 Material models

A total of three material models have been used to describe (1) the capsule and flyer plate, (2) the sabot and fixing plate and (3) the sample material materials. In iSALE, the material model is defined by an Equation of State (EoS), which describes the response of a material to a change in volume, and a strength model, which describes the resistance of a material to changes in shape (these are explained in detail in Chapter 3). Each of the materials were described using a material model with the greatest level of complexity possible based on the shock data that was available.

Equations of state

Due to shock data for meteoritic materials (and subsequently their experimental analogues) being limited, the bulk sample was represented by a Tillotson EoS for fused quartz (Borg et al., 2005), a non-crystalline silica, while both the capsule and flyer plate were to be made

Table 4.1: Tillotson parameters (see §3.3) for the materials fused quartz (Borg et al., 2005) and aluminium (Tillotson, 1962). The model for aluminium was used to model the capsule and flyer plate, while the fused quartz was used to model the silica sample material. The fused quartz material model is taken from a non-porous model developed by Borg et al. (2005). For this study, the initial porosity was then added using the iSALE $\epsilon - \alpha$ porosity model — this was chosen to be 70%, consistent with chondrite precursor material estimates (Bland et al., 2014; Davison et al., 2016).

Parameter	Fused Quartz	Aluminium
a	0.90	0.50
b	0.00	1.63
α	0.00	5.00
β	0.00	5.00
A (Pa)	5.78×10^{10}	7.52×10^{10}
B (Pa)	0.00	6.50×10^{10}
E_0 (J/kg)	0.00	5.00×10^{6}
E_{IV} (J/kg)	4.72×10^{16}	3.00×10^{6}
E_{CV} (J/kg)	1.82×10^{17}	1.39×10^{7}
ρ (kg/m^3)	2.20×10^{3}	2.70×10^{3}
C_p (J/kg·K)	1.00×10^{3}	8.96×10^{2}

Table 4.2: Mie-Grüneisen parameters for the polycarbonate material model (Heuzé, 2012): the reference density, ρ, the sound speed, c_s, specific heat capacity at constant volume, C_p, the slope constant from the linear shock-particle velocity relationship, S and the Grüneisen parameter, γ.

Parameter	Polycarbonate
S	2.04
γ	0.61
c_s (m/s)	1.93×10^{3}
ρ (kg/m^3)	1.19×10^{3}
C_p (J/g·K)	1.21×10^{3}

from aluminium-6061, for which a robust equation of state already exists (Tillotson, 1962). The Tillotson parameters for the fused quartz (silica) and aluminium EoS are summarised in Table 4.1. It should be noted that the material model for the silica technically simplifies to a Mie-Grüneisen EoS—the Tillotson parameters (see §3.3) b, α, β, B and E_0 are all zero and E_{IV} and E_{CV} are very large. However, the data that was available has meant that the Tillotson EoS was used for the modelling.

The fixing plate that attached the capsule to the apparatus was made from Lexan polycarbonate. The polycarbonate was described according to the Mie-Grüneisen EoS (Heuzé, 2012) and the parameters are summarised in Table 4.2. All of these EoS are available in the public iSALE Dellen release (`https://isale-code.github.io/`).

Table 4.3: $\epsilon - \alpha$ porosity parameters used for the fused quartz (silica) material model. To achieve the desired porosities ($\phi = 70 - 95\%$) and test the model parameters, the initial distension, α_0, was chosen to be between $3.3 - 10$ ($\phi = 1 - 1/\alpha_0$). These parameters are described in detail in §3.35.

Parameter	Silica
α_0	$3.3 - 10$
ϵ_0	0.00
α_x	1.29
κ	0.80
χ	0.33

Strength models

The silica and polycarbonate material models use a Drucker-Prager strength model (Drucker and Prager, 1952) which is a linear pressure-dependent strength model. For the silica, I have used the `OHNAKA` thermal softening model (Ohnaka, 1995; Collins et al., 2004) to describe the temperature-dependent strength behaviour, and the $\epsilon - \alpha$ porosity compaction model (Wünnemann et al., 2006; Collins et al., 2011) to calculate the crushing of pore space in the high-porosity silica (Table 4.3).

Meanwhile, the aluminium uses the more sophisticated Johnson-Cook strength model (Johnson and Cook, 1983) which has been made possible by the extensive shock research and data available for this metal. The Johnson-Cook strength model was developed for metals and accounts for pressure-, strain- and temperature-dependence of the yield strength. The Drucker-Prager (Drucker and Prager, 1952) and Johnson-Cook strength models and the $\epsilon - \alpha$ porosity compaction model (Wünnemann et al., 2006) are described in detail in Chapter 3.

4.3 Capsule optimisation using iSALE-2D

Both the capsule and flyer plate are cylindrical and hence symmetrical about a shared central axis. Using two-dimensional simulations, the models are able to be translated into cylindrical space which allows for significant savings on computational expense. This is supported by iSALE which is capable of performing the calculations using cylindrical geometry.

In order to determine the optimal capsule configuration for the experimental criteria, I have produced a suite of simulations using iSALE that explore a number of different capsule

architectures. The ideal capsule design aims to minimise unwanted reverberations at the capsule and material boundaries and achieve uniform thermal and mechanical experience throughout the sample. In practice however, this ideal scenario is unachievable, but using iSALE as an optimisation tool will inform the best design of the capsule.

The simulations in this section maintain a number of control variables. These are (1) the impact velocity, which was set to 800 m/s, (2) the capsule outer dimensions, which were set to be a 25 mm diameter, 30 mm tall cylinder and (3) the sample dimensions, which were set to be a 9 mm diameter, 3 mm tall disc. In this section, I present the designs that have been explored prior to the manufacture of the capsule, outline their benefits and issues and their influence on the final capsule design.

4.3.1 Solid capsule simulations

The simplest design, a solid aluminium cylinder with the sample contained inside, was the first architecture explored (Fig. 4.2). This initial suite of models were used to determine the thermal and pressure conditions that the sample would experience in an effectively worst-case scenario, a solid capsule, allowing modifications to the capsule architecture to be compared to this simple architecture.

In the solid capsule, the shock wave was generated at the collision site between the capsule surface and the flyer plate attached to the projectile. The shock wave then travelled through the aluminium buffer between the projectile and the sample and entered the sample (Fig. 4.3). As the wave entered the sample it slowed down, due to the much lower impedance of the porous sample. However, the wave in the capsule continued to travel much faster such that it 'wrapped around' the sample chamber before entering the chamber from the sides as well. This produced a convergent shock wave into the sample from the side. Finally, once the wave through the sample reaches the back of the sample chamber ($\sim$ 2.4μs after impact), the high impedance contrast between the sample and capsule generates a reflected wave that re-shocks the sample. The reflected wave travels back up through the sample and can also reverberate in the sample.

Peak temperatures recorded by tracers (see §3.4.1) which were placed in each material cell

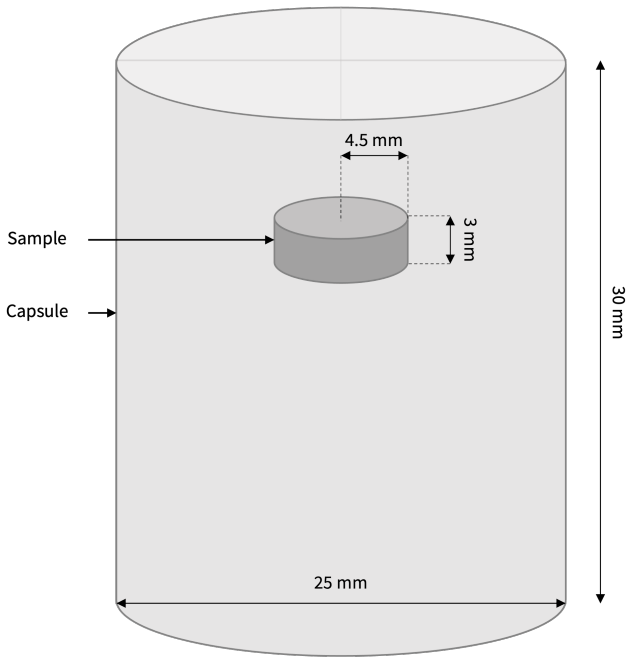


Figure 4.2: Schematic of the solid capsule. This is the most simple architecture that I have explored in the iSALE simulations whereby the sample, a small 3 mm tall, 9 mm wide disc was encased within a solid aluminium 25 mm wide, 30 mm tall capsule. An aluminium impactor then collided with the top face of the capsule and generated a planar shockwave that travelled through the entirety of the capsule.

throughout the sample were in excess of 3000°C while average peak temperatures were around 2000°C (Fig. 4.4). These temperatures are above the melting point of silica (1710°C) and therefore inconsistent with the thermal histories and material properties of unmelted chondrites (Scott et al., 1992; Macke et al., 2011). Moreover, the statistical spread of data present in these results was very large. Temperatures were spread across an $\sim$ 1100°C interquartile range (IQR), while the peak pressure was centred around an average of 6.5 GPa and had an IQR = $\sim$ 4 GPa. This pressure would not normally produce $\sim$ 3000°C temperatures (Stöffler et al., 1991; Scott et al., 1992), however, the extreme temperatures were due to a very complex shock-loading pattern which involved multiple shock reverberations and convergent shock waves. While this did not lead to excessive pressures, the sample was heated much more than intended.

In addition to the inconsistencies outlined above, the minimum peak temperature ($\sim$ 950°C) was also much higher than the typical Curie temperatures of magnetic carriers that have been found in chondritic meteorites (such as pyrrhotite, T_C = 320°C, and magnetite, T_C = 580°C; Dunlop and Özdemir, 1997). Upon viewing the simulation (Fig. 4.3), the wide spread of data, coupled with extreme peak temperatures and pressures, can be attributed entirely to

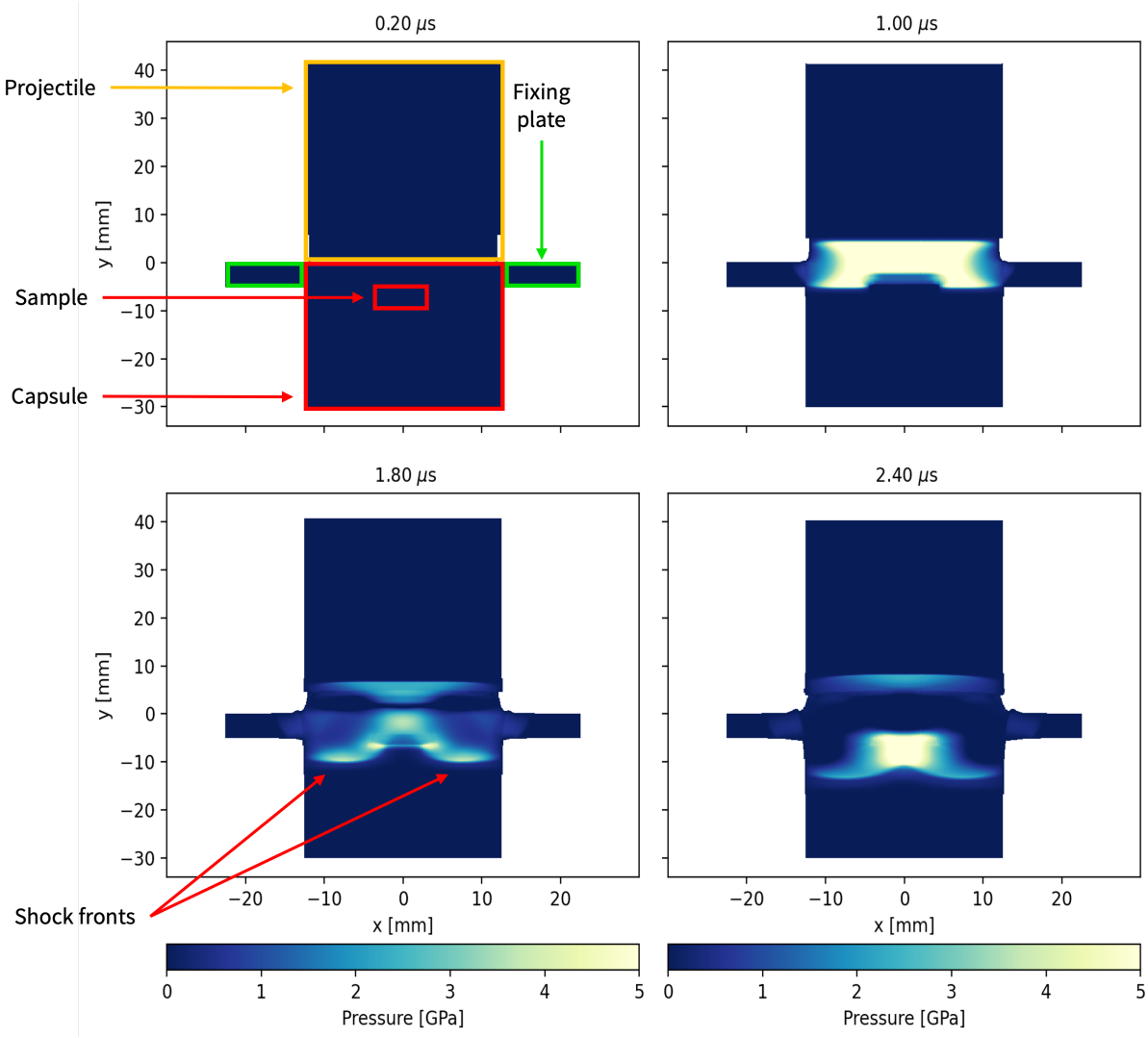


Figure 4.3: Images taken from the two-dimensional cylindrical simulation of the solid capsule. These show the shock wave moving into the sample and converging through the sides and at the back of the sample chamber. The shock wave entered the sides of the sample within $\sim$ 1.8 μs and began to converge on the back of the sample chamber around $\sim$ 2.4 μs after the beginning of the simulation.

unwanted reverberations and convergent shock waves. As reflections were numerous throughout the capsule, the sample was not released from a shocked state for the duration of the simulation, which further increased the stress it was put under. Following these observations, it was clear that the pressures and temperatures had to be reduced. An obvious way to do this would be to reduce the projectile velocity, however, it was preferable to change the capsule design. This was both to simplify the loading pattern and because low impact speeds are not as reproducible over multiple experiments with the light-gas gun. The ideal experiment would feature a simple one-dimensional shock loading and unloading pattern. To achieve this, two modifications to the capsule architecture were introduced, the first to reduce the effect of convergent shock waves,

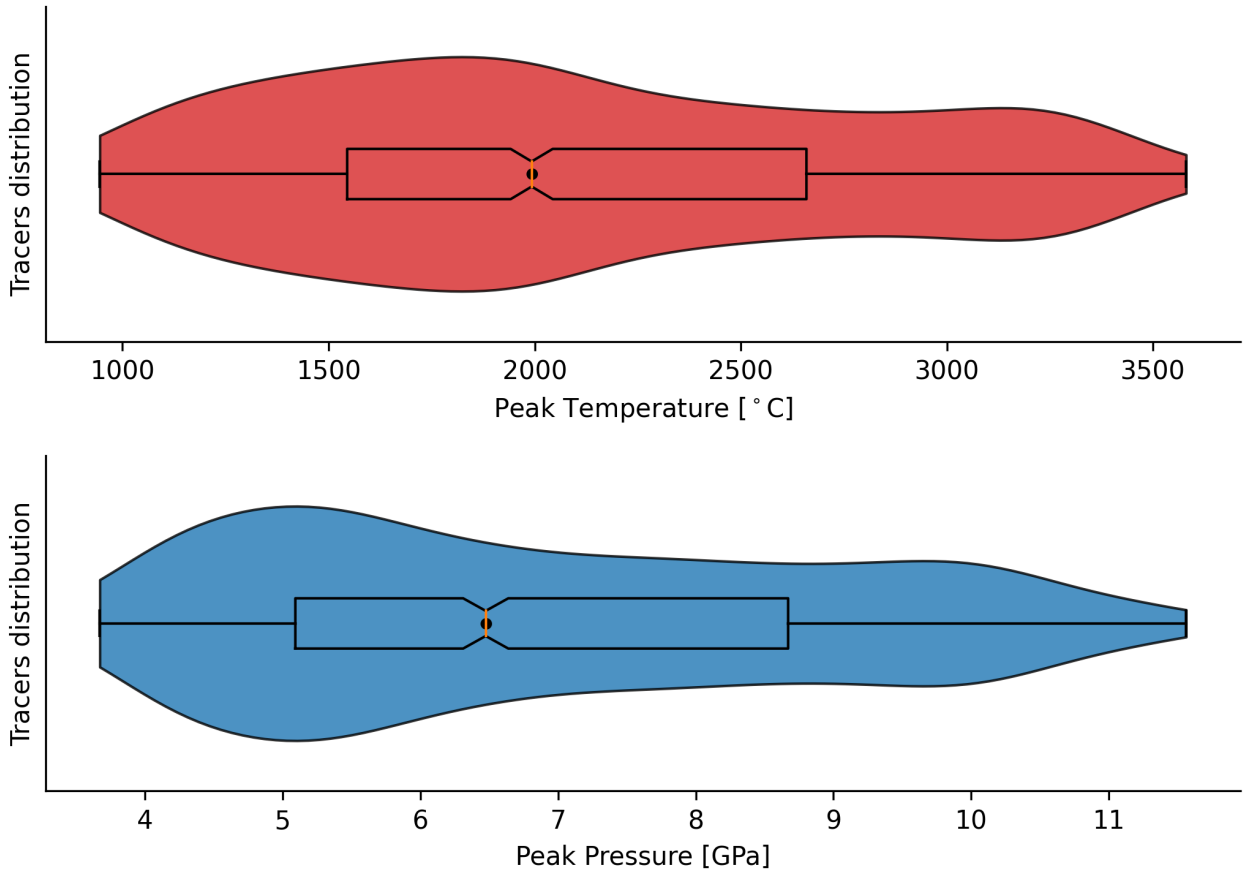


Figure 4.4: These results show the peak temperature and peak pressure experienced by the 1200 Lagrangian tracers that were placed into of the sample material. The hottest tracers experience peak temperatures in excess of 3000°C and peak pressures across a wide range, centred around 6.5 GPa. Average peak temperature (2000°C) and average peak pressure (6.6 GPa) are shown by black dots.

and the second to attenuate the energy of the shock wave after it passed through the sample.

4.3.2 An 'air-gap' to reduce shock wave interference

Relative to the initial impact-induced shock wave, reflections at material boundaries were strong and re-shocked the sample multiple times while it was in a stressed state. The complex loading pattern and 'wrap-around' effect described in the previous section made reliably predicting the mechanical conditions experienced by the sample challenging, and led to undesirable peak temperature and pressure experiences. To combat these unwanted effects, the capsule architecture was modified to include an air-gap around the sample and tested to observe whether it would sufficiently mitigate intra-capsule reflections (Fig. 4.5).

As the shock wave moved much faster through the solid aluminium capsule than it did

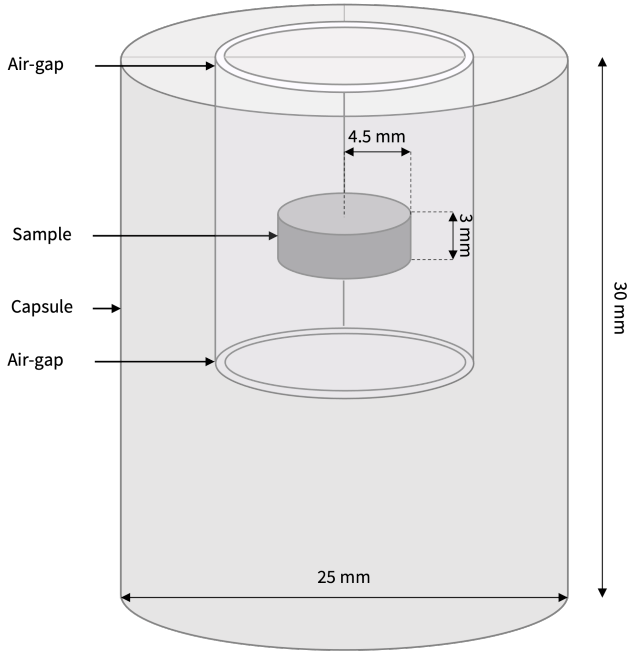


Figure 4.5: Schematic of the air-gap within the capsule. The depth of the air-gap here is arbitrary and not drawn to specification. Essentially a hollow annulus at a distance from the centre goes down the capsule to a chosen depth. There is solid aluminium material on either side of the annulus which itself acts as a void space. This prevents the part of the shock wave travelling close to the edge of the capsule from reflecting at the capsule boundary and inwards towards the sample.

through the porous sample, the air-gap should allow the shock wave that travels into the sample enough time to fully pass through and enter the rear of the capsule before the shock waves converge on the sample chamber. Meanwhile, the shock wave that travelled around the edges would wrap-around the rear of the capsule (Fig. 4.6) where it encounters the shock wave exiting the sample chamber in the opposite direction, reducing the strength of any further reflections.

When approaching this problem, the location, depth and width of the air-gap were cooperatively tested throughout a reasonable parameter space within the capsule. I have determined 'reasonable' to be within one half of the capsule radius from the centre (7.5 mm) and no deeper than two thirds of the capsule height (20 mm). Parameter space was explored thoroughly using a systematic approach that included adjusting the distance of the air-gap from the centre, its depth within the capsule and the gap-width (a subset of these results are shown in Fig. 4.7). The simulations found the air-gap would collapse during the impact, given the pressure range that was being investigated, so an additional factor was to verify the sample was still contained within the capsule once the shock wave had dissipated.

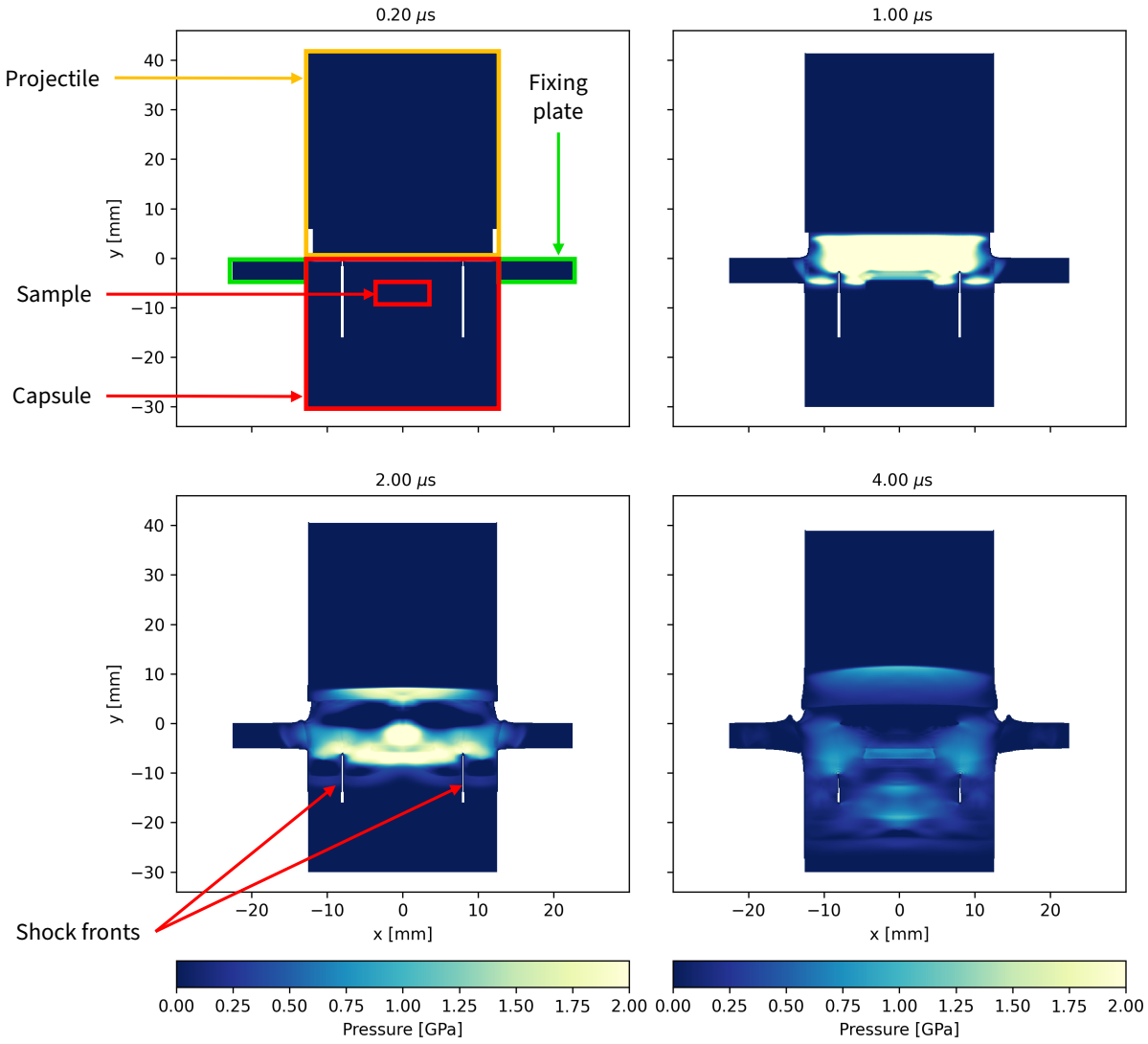


Figure 4.6: An example simulation where the air-gap is reducing the 'wrap-around' convergent effect of the shock waves moving through the outside of the aluminium capsule. This is typical of how the simulations were setup, where the projectile (which consists of a 36 mm polycarbonate sabot and 6 mm aluminium flyer plate) is given an 800 m/s velocity in the negative y-direction, colliding with the capsule. The polycarbonate fixing plate was also included to account for any affect on the shock propagation.

The optimal setup for the modified capsule was found where the air-gap was placed 8 mm from the central capsule axis, 0.4 mm wide, 16 mm deep. Compared to the solid capsule, the results for the inclusion of an air-gap significantly reduced the spread of peak temperatures and pressures experienced in the sample (Fig. 4.8). With the air-gap modification, the average peak temperature was $\sim$ 990°C with an IQR around 280°C, while average peak pressure was 3.5 - 3.6 GPa with an IQR of $\sim$0.8 GPa. This meant the pressure range was now consistent with an S1 categorised 'unshocked' meteorite (Stöffler et al., 1991), in addition to the temperatures

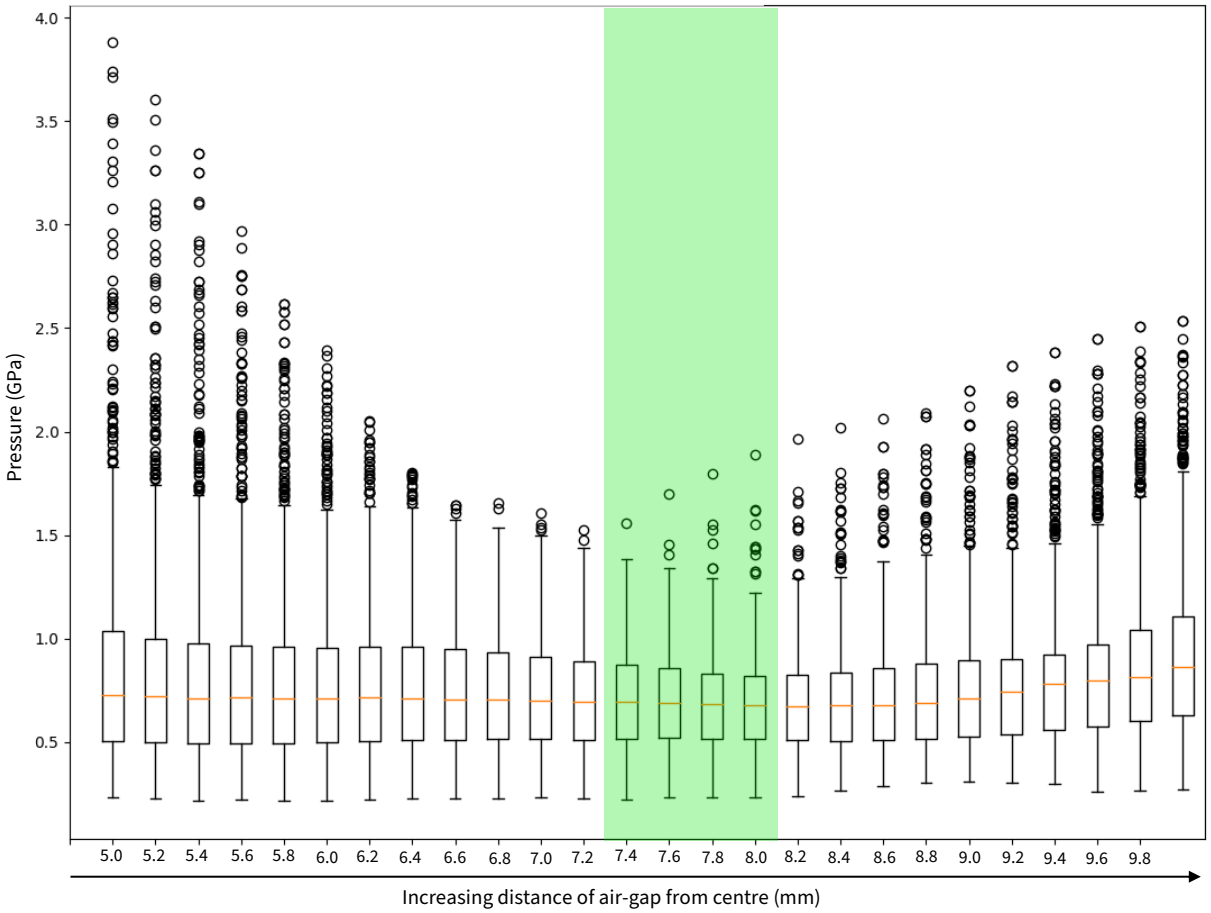


Figure 4.7: Statistical variation in peak pressure experienced by tracers inside the sample as, for a given width and depth, the air-gap was moved from the centre of the capsule outwards. Statistical outliers are shown by black circles. The median average is plotted using a horizontal orange line inside the box plot. In addition, the best results for this particular subset of simulations have been highlighted in green. In this example, the best results stretch from the simulation with the least outliers to the simulation with the smallest IQR.

now being far below the silica melting point and consistent with an unmelted sample. However, the temperatures reached inside the sample were still well in excess of the reported $300-400°C$ temperatures recorded in chondrites.

Although there was less variance between peak pressures with the air-gap modified capsule compared to the solid capsule, the elevated temperatures within the sample suggested that the sample was being shocked again before it had released from its initially shocked state. In this new capsule architecture, it was apparent that the most significant reflections were now coming from the rear of the chamber where the sample was contained (Fig. 4.6). Once the shock wave has moved through the porous sample, the shock front would have seen a steep increase in impedance at the sample-aluminium boundary. This caused the shock wave inside the sample

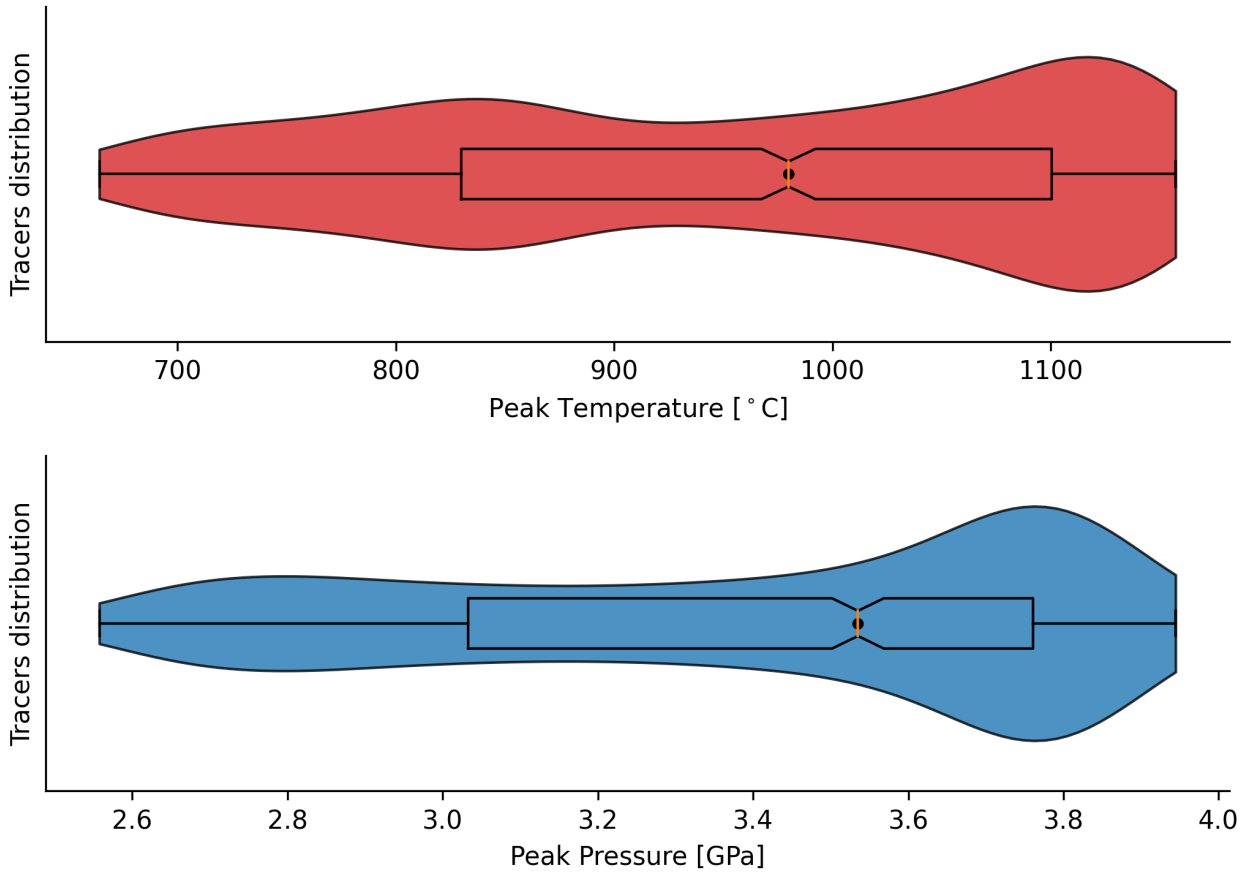


Figure 4.8: The peak temperature and peak pressure variation as recorded by tracers throughout the sample for the optimal air-gap placement. In contrast to the solid capsule, there are no outliers in this data. The average peak temperature was 990°C while the average peak pressure was 3.55 GPa.

chamber to be reflected, effectively re-shocking the sample before it had time to release from its shocked state, resulting in the high temperatures observed (Fig. 4.8). This meant that while the air-gap significantly reduced shock wave reflection from the capsule edge compared to when it was absent, the boundary of the sample chamber was still a prominent source of unwanted reflections.

4.3.3 Capsule with low-impedance shock attenuation 'pillow'

The complex reflections would make the conditions experienced in the sample difficult to predict. To mitigate the reflection at the rear of the sample chamber as much as possible, I tested whether the inclusion of a low-impedance 'pillow' material immediately behind the sample would sufficiently absorb the energy of the shock front (Fig. 4.9). This required expanding the

length of the sample chamber from 3 mm to 12 mm to accommodate for the pillow.

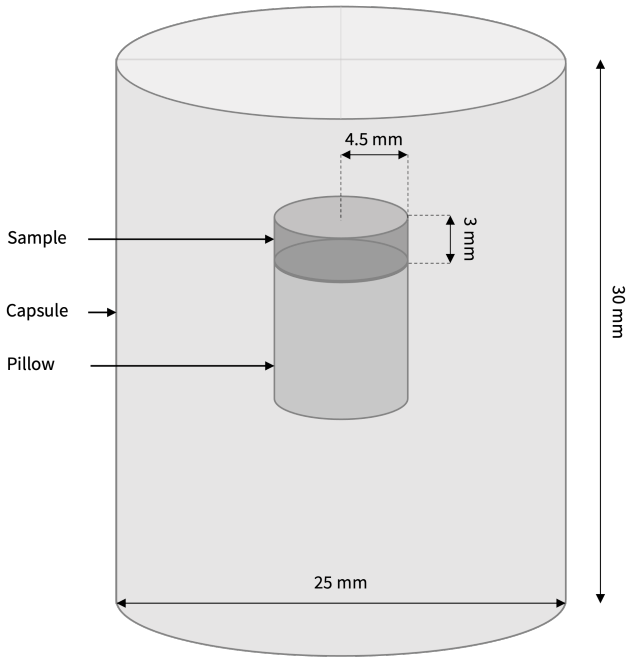


Figure 4.9: Schematic of the capsule, modified to include a low-impedance shock attenuation 'pillow' behind the sample. The pillow material was highly-porous silica ($\phi > 90\%$) while the sample was modelled a less-porous silica ($\phi \sim 70\%$). The capsule was again made from aluminium-6061, modelled using the Tillotson EoS for aluminium (Tillotson, 1962) and the dimensions were unchanged.

In these simulations, the air-gap described in the previous section was omitted to determine only the contribution from reducing the impedance between the sample and the adjacent capsule. In a practical experimental setup, the sample would first be loaded into the chamber and then compacted to the correct porosity, then the remainder of the empty chamber would be filled with uncompressed silica ($\phi > 90\%$) which would act to attenuate the energy of the shock wave directly. This should also reduce the effect of shock waves reflected at the capsule boundary from re-entering the sample and creating a complex, unpredictable experience.

Lower average peak temperatures and peak pressures were measured in the sample when compared to the previous solid capsule and modified air-gap simulations. In addition, the pressure and temperature of the sample was more homogeneous, making the thermal and mechanical experience in the sample more uniform. The parameter space explored for the pillow depth was simpler than the previous air-gap placement investigation. The depth of the pillow was varied from 3 mm to 20 mm while the diameter remained constant at 9 mm, matched to the diameter of the sample. The depth of the pillow was tested in 0.5 mm increments.

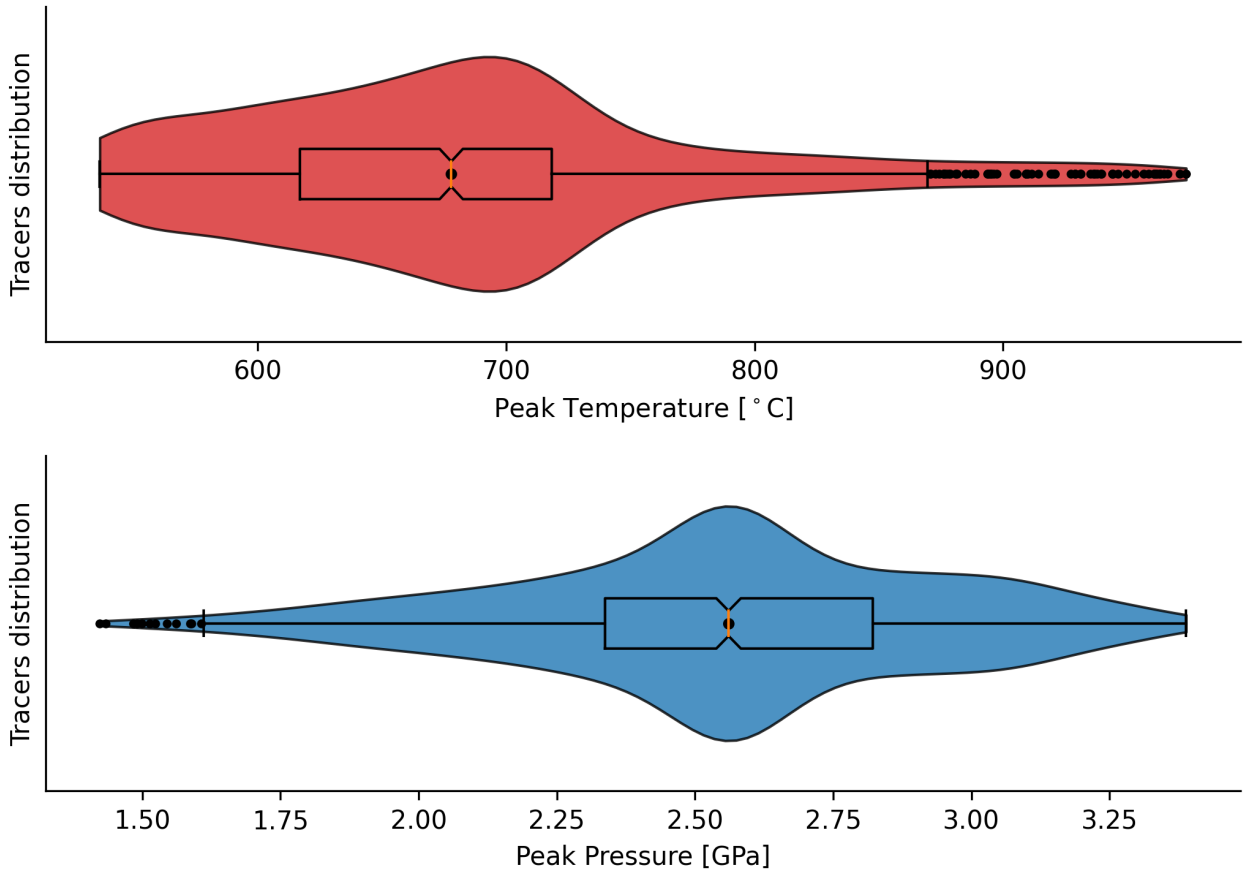


Figure 4.10: Statistical data for peak temperature and peak pressure experienced within the sample when a high-porosity 'pillow' was included in the capsule design. Attenuation of the shock wave from the uncompressed sipernat pillow reduced the average peak temperature and pressure recorded in the sample, compared to the previous architectures explored. This is shown as the temperature and pressure are once again reduced compared to previous designs; average peak temperature is around 680°C while the average peak pressure experience was 2.6 GPa.

The optimum depth for the pillow was found to be 16.5 mm, requiring a 9 mm extension of the sample chamber. In this model, the peak temperature in the sample was reduced to 680°C and the tracers were contained within a much smaller IQR, around 110°C, while the peak pressure was reduced between 2.5-2.6 GPa, with an IQR 0.5 GPa (Fig. 4.10). This put the sample further into the S1 meteorite shock classification band (Stöffler et al., 1991) and more consistent with the desired pressure and temperature conditions than when the capsule had only been modified to include only the air-gap.

4.3.4 Final capsule design

A combination of the air-gap and highly-porous pillow proved to be the best solution for the capsule. In this combined architecture, data recorded in tracers showed that the peak temperatures and peak pressures shared the least variance from the mean value and were consistent with conditions that match recovered chondrites. The average peak temperature was ~ 340°C (Fig. 4.12), which is in good agreement with the peak temperatures found in CV chondrite Allende (Weiss et al., 2010b), and an IQR of 40°C, which meant the data was less variable than the previous capsule architectures. Similarly, the peak pressure was less variable than previous capsule designs, with an IQR of 0.4 GPa, centred around a median average between $\sim$1.55 GPa. Once again, this is in good agreement with measured the pressures in carbonaceous chondrites (Scott et al., 1992; Macke et al., 2011).

Comparing the four variations of the capsule architecture, each modification has decreased the spread of data, reduced the IQR and brought the average peak temperature and pressures closer to values inferred from recovered chondrites (Fig. 4.13). This suite of simulations have informed a capsule design that should minimise unwanted intra-capsule reflections and expose samples to pressure and temperature conditions that are representative of the low-velocity impacts that have been proposed to have lithified chondritic meteorites. With the modifications to the simple design that were made during the modelling, the final capsule design, when impacted, should experience a single strong, predictable shock wave through the sample.

4.4 Capsule manufacture

The capsule was manufactured in accordance with the simulation outcomes. The optimal capsule parameters found are summarised in a technical sheet that was used as a blueprint for the manufacture (Fig. 4.14). The capsule was manufactured from aluminium-6061 by AE Precision in the UK (Fig. 4.15): the outer dimensions of the capsule were a 25 mm diameter by 30 mm height fixture. The air gap was placed 5.5 mm from the centre of the capsule and was 0.4 mm wide. The sample chamber was offset by 3.5 mm from the impact face of the capsule and measured a total of 9 mm diameter by 16.5 mm in length: 3 mm height for the sample and

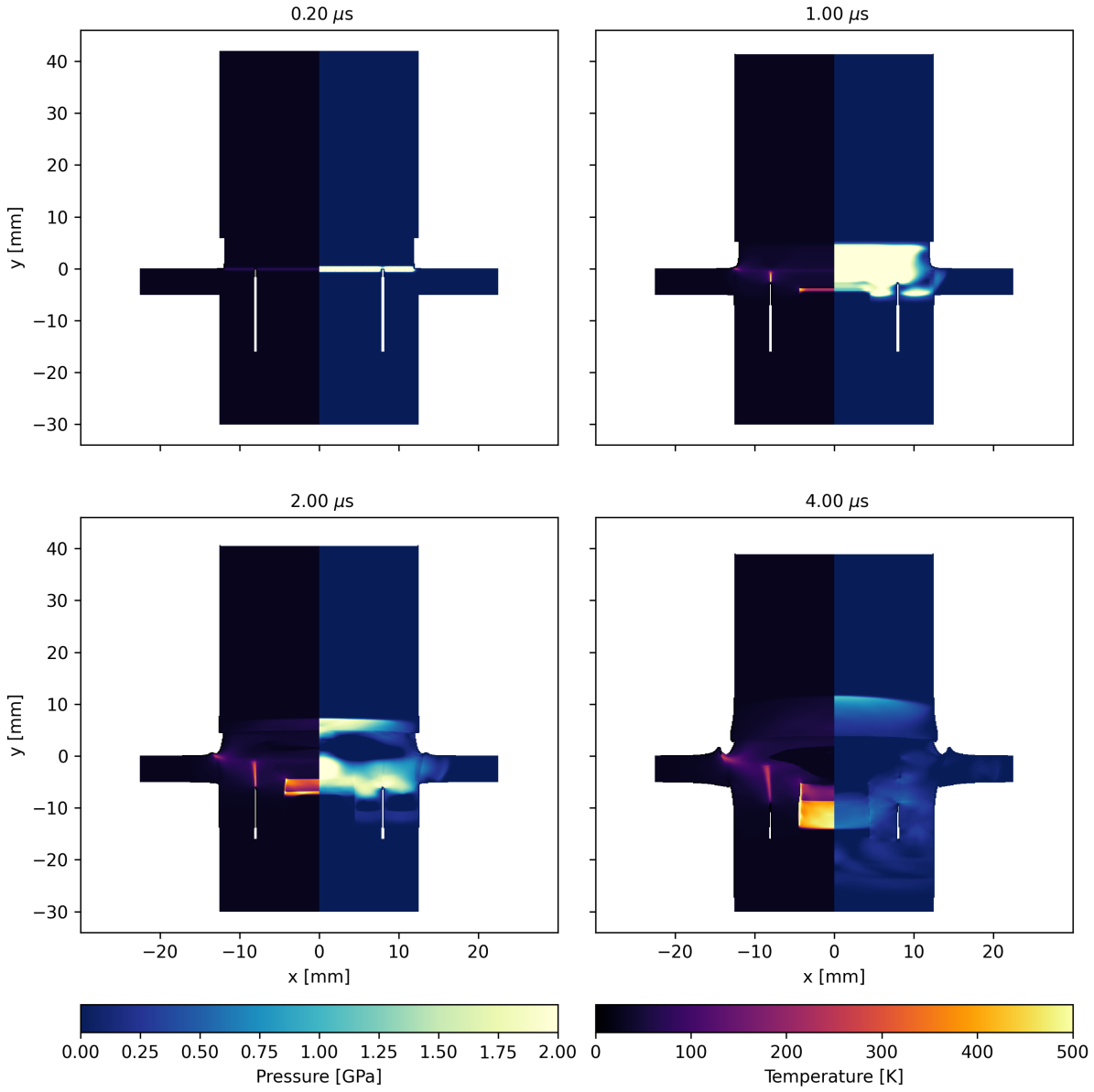


Figure 4.11: Still images from the final simulation which is used to predict the in-situ experience of the sample during the shot experiments. Temperature and pressure distributions of the tracers placed inside the sample material are shown in Fig. 4.12.

9 mm for the pillow. The additional 4.5 mm was to accommodate a plug attached to the end of the M12 screw thread that was used to secure the sample and pillow mixtures in place once they had been put inside the capsule.

The capsule was manufactured in two sections that were fixed together: a cylindrical shell or 'skirt' that made the outer shell of the capsule, and the T-shaped main body or 'core' of the capsule which contained the sample chamber. The skirt was 16 mm tall with an inner diameter of 11.8 mm and an outer diameter of 25 mm which fit on top of the main capsule body (this can

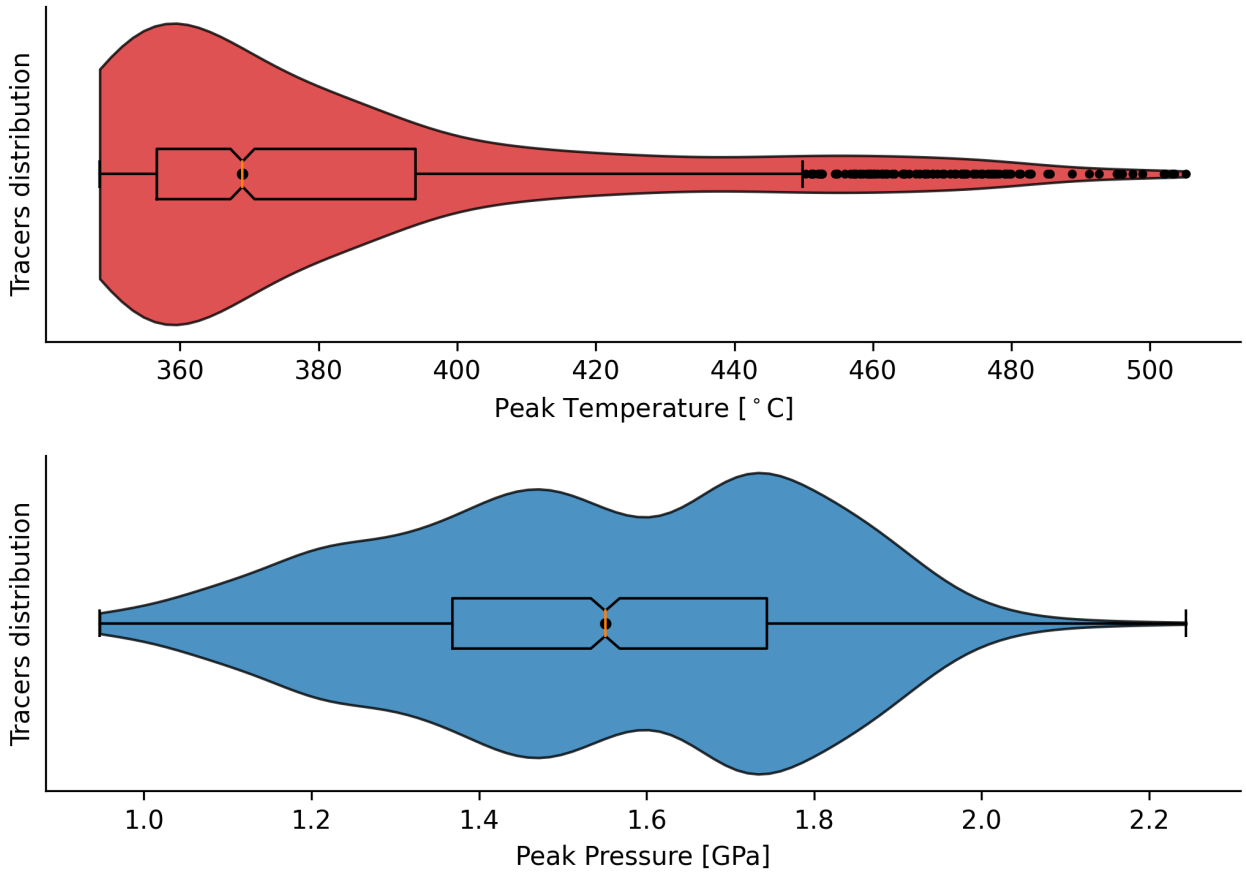


Figure 4.12: iSALE modelling of the optimal capsule design predicts median average peak temperatures of 370°C and median average peak pressure around 1.55 GPa. A small sub-volume of the sample is represented as outliers on the peak temperature plot, indicating these fractions of the sample may experience intense temperatures in excess of 450°C.

be seen in Fig. 4.15). The split-section manufacturing was necessary to accommodate the air-gap. The skirt fit closely to the main capsule body so the simulation results were not adjusted to account for the interface between the two pieces. However, future experiments may investigate the skirt-body interface further in the case of inconsistent simulation and experimental results.

4.5 Experiments: manufacturing chondrites

The experiments were performed at the University of Oxford under supervision of Dr. Daniel Eakins and his lab staff. Using a single-stage gas gun powered by compressed helium, the apparatus is capable of achieving projectile velocities in excess of 1000 ms^{-1}. As discussed above, the desired projectile velocity was 800 ms^{-1} as this was the speed used in the simulations

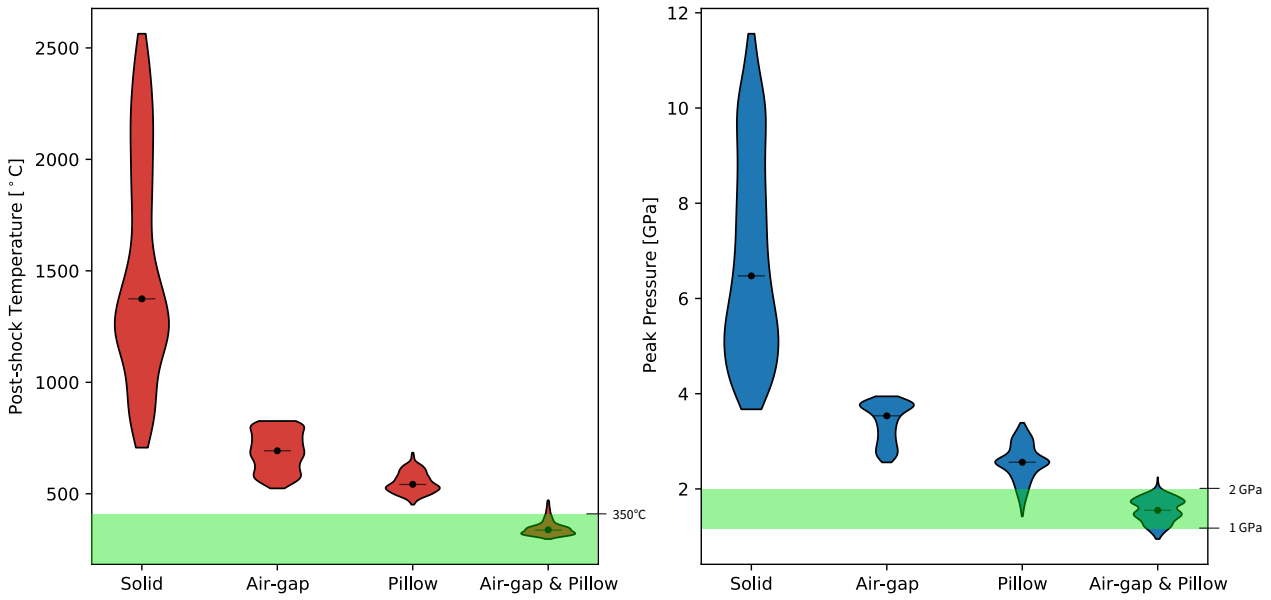


Figure 4.13: Summary of the comparison of the peak pressures and the post-shock temperatures recorded by tracers in the sample for each capsule architecture. The bodies of each violin plot represent the frequency of tracers at a given value. Regions highlighted in green are the desired temperature and pressure ranges, consistent with recovered chondrites and the experimental criteria that were determined in §4.1.2.

to parameterise the capsule architecture. This was a conservative velocity to choose for the apparatus and projectile setup that was typically able to be well controlled, according to the operating guidelines.

4.5.1 Sample material composition

Consistent with recovered chondrite matrix material, the sample was prepared as a porous mixture of fine-grained silicate and iron oxides. The initial sample properties were based on the reconstruction of a pre-compaction matrix of CV chondrite Allende (Davison et al., 2016). Their work showed a pre-compaction matrix with an initial porosity (ϕ_{mi}) of 70% that, when subject to sample-wide peak pressures around 1.5 GPa, produced a final bulk and matrix porosity consistent with measurements of Allende. Other than silicate material, iron sulphides (troilite, pyrrhotite), iron-nickel sulphides (pentlandite) and iron oxides (magnetite) have been found in a number of chondrite groups (Krot et al., 1995). It is the ferromagnetic iron-sulphides and iron-oxides that host the remanent magnetisation in chondrites and when creating these samples was a key consideration in which would most reliable record a remanence in these shock

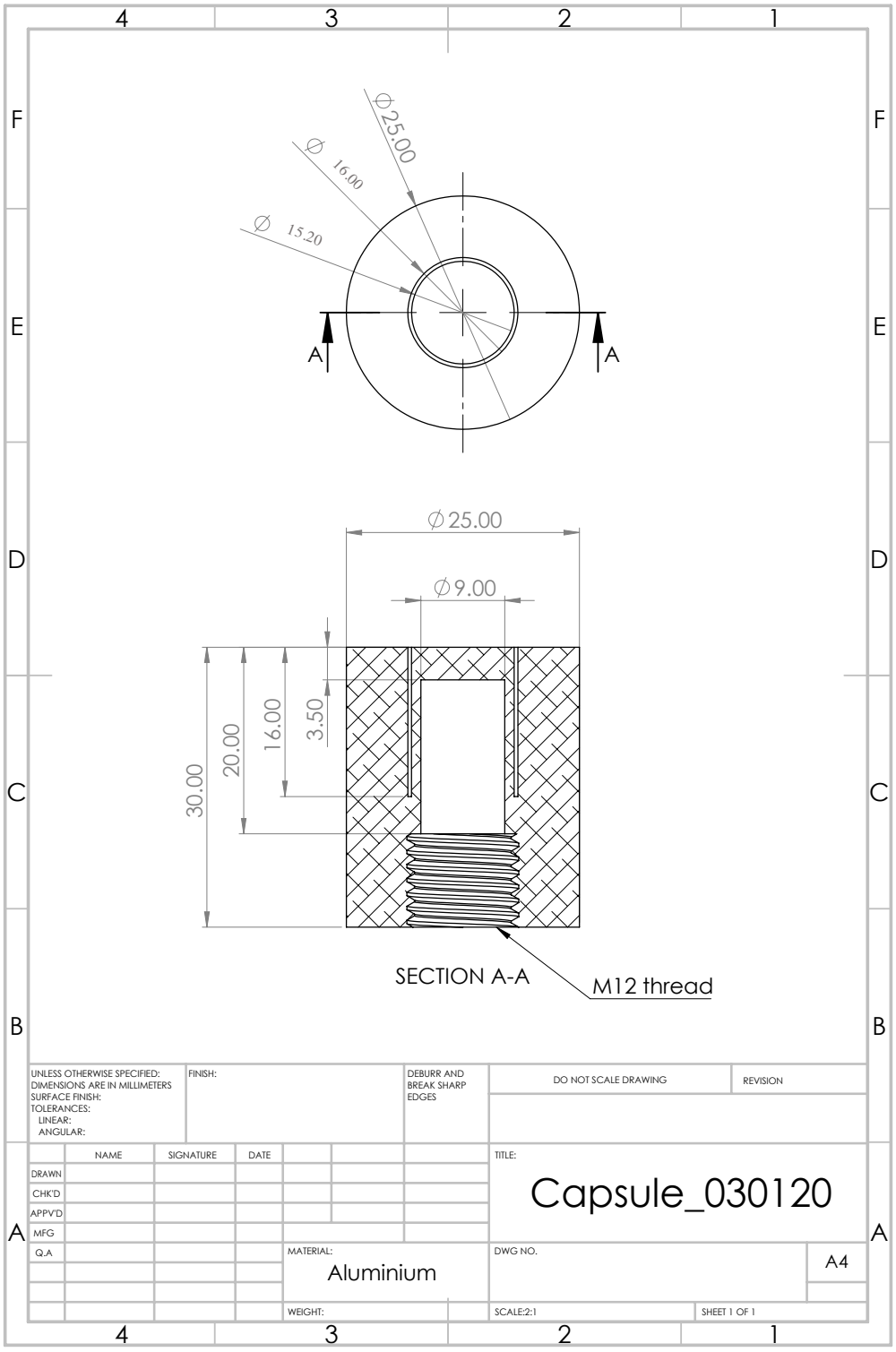


Figure 4.14: Technical sheet describing the capsule that was to be manufactured in accordance with the optimised simulation parameters. The four capsules were made of aluminium-6061, containing a small air-gap on the impact face which would act to reduce the intra-capsule reflections experienced during the shock experiments. The sample chamber measured 16.5 mm deep by 9 mm wide, however the thread had a 4.5 mm plug on the end (not pictured here; see Fig. 4.1), meaning there was a total of 12 mm for the sample and pillow material to occupy.

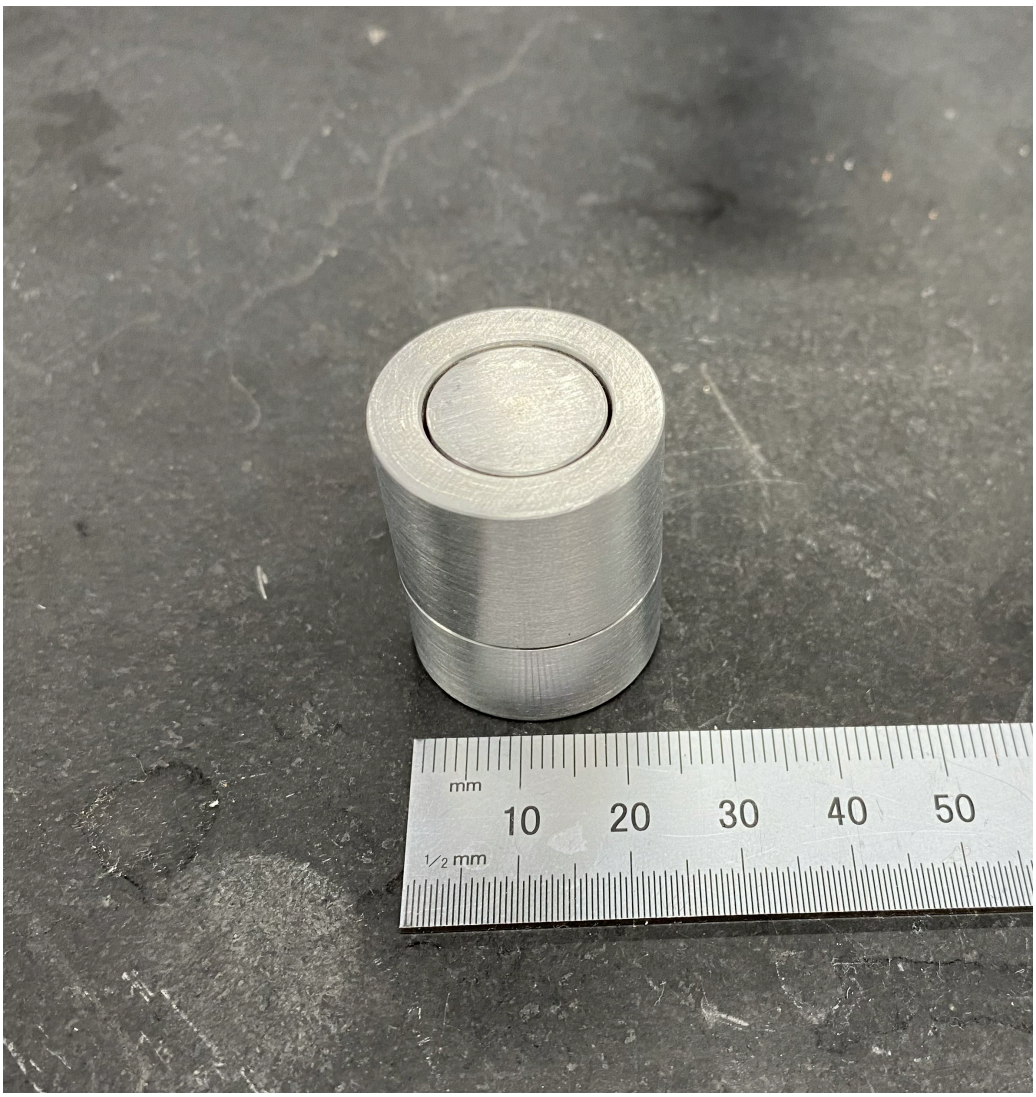


Figure 4.15: The aluminium Sawaoka capsule as manufactured at AE precision. The capsule is entirely made from high-purity aluminium-6061 to avoid any iron contamination. The capsule was manufactured according to the technical sheet (Fig. 4.14).

experiments.

As a mechanical analogue to chondritic silicate rock, I have used SIPERNAT 320 DS (sipernat hereafter), a highly-porous (ϕ = 90-95%) silica powder (SiO_2; average grain diameter $\sim$ 7.5μm). Sipernat was then mixed with 8% by volume (vol%) hematite (α-Fe_2O_3; average grain diameter $<$ 1μm) and 2 vol% magnetite (Fe_3O_4; average grain diameter $<$ 1μm)—a composition similar to iron oxide-bearing chondrites. The choice of magnetite and hematite was deliberate: these iron oxides are known to behave as excellent magnetic recorders (Dunlop and Özdemir, 1997) and have significantly different Curie temperatures; the Curie temperature of magnetite is 580°C, around 100°C lower than that of hematite (Dunlop and Özdemir, 1997).

This intrinsic difference meant that if the pre-experimental modelling had falsely predicted the peak temperatures and the sample temperature exceeded the Curie-point of magnetite, a pTRM should still be recorded in the hematite which would enable the measurement of the true peak experiment temperature using thermal demagnetisation. The choice of hematite, a non-naturally occurring mineral in chondrites (Krot et al., 1995), over a naturally occurring abundant mineral such as pyrrhotite for these experiments, is specifically for (1) demonstrating that impact-induced compaction can lead to a magnetic field being recorded in porous rocky material and (2) the calibration of these experiments to the iSALE modelling.

4.5.2 Working in a controlled magnetic field

Key to the success of this experiment is controlling the magnetic field inside the target chamber; the first experiment that was performed was in absence of any magnetic field as a control result, followed by three uniform fields at predetermined intensities that mimicked reported ranges for the Solar nebular field. The ambient field due to Earth's Geodynamo is $\sim$ 50 μT in Oxford which had to be nulled for the control experiment. Producing a space of zero field enabled excellent control of an applied field when the aim of the experiment was to leave the sample with a remanent magnetisation.

To achieve a field-free working space, I have built a series of paired square Helmholtz coils (Figure 4.16), following the methodology as documented by Collinson (1983). The coil pairs were arranged into a cage comprised of a total of six square frames: two in each plane (x, y, z). The largest two of the six coils were 84 cm in length on each side, with the frames in the remaining two planes consecutively decreasing in size by 2 cm - the width of the aluminium channel the frames were made from. Once again, aluminium was used to manufacture the frames as it is rugged, easily manoeuvrable and non-magnetic. The cage was carefully designed to be placed around the outside of the target chamber. This also ensured it is not disturbed or damaged during the experiments. To join the aluminium channel that formed the frames of the cage, I created a total of 24 3D-printed carbon fibre angle supports. These were bespoke in design, also non-magnetic and remained rigid during the experiment.

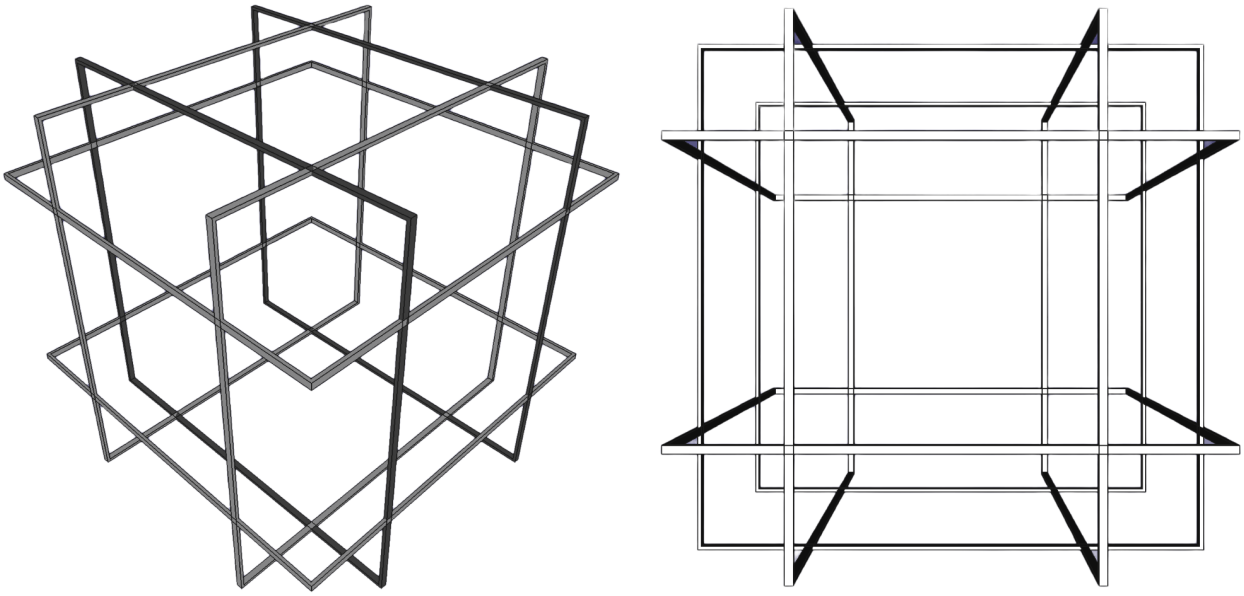


Figure 4.16: 3D render of the Helmholtz cage structure. This diagram shows the geometry of the frames, paired in three perpendicular planes. In reality, the frame was made from non-magnetic Aluminium-6061 U-channel with copper wire coiled through the channel. The brackets for fixing the frames together are 3-D printed from carbon fibre making them lightweight and durable.

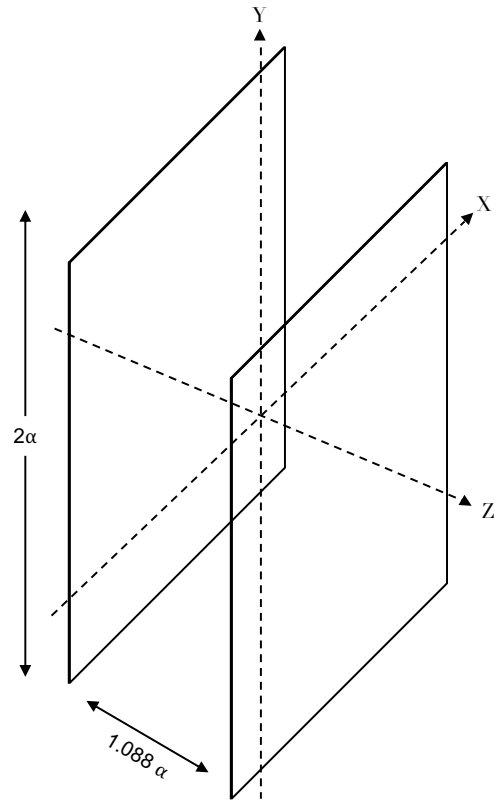


Figure 4.17: Geometry of a pair of square Helmholtz coils. Separation of coil pairs has to be equal to 1.088α, where 2α is the length of one side. The 'cage' manufactured for these experiments consisted of three pairs of these coils, one pair in each planar direction (X, Y, Z). Diagram and methodology adopted from Collinson (1983).

Coils were placed in parallel, a distance of 1.088α apart, where 2α is the length of one side (Fig. 4.17). Following the methodology by Collinson (1983) for square Helmholtz coils, the relationship between the induced central field, B_0 (μT), number of turns, N, applied current, i, and length of one half of one side of the square coil, α, is

$$B_0 = (8.148 \times 10^{-7})\frac{Ni}{\alpha} \tag{4.1}$$

Copper wire was coiled 50 times around each frame which meant the applied current could be low in order to achieve the required field. The wire was rated at 3.0 A, meaning the low current avoided heating the wire on the frame. For example, to nullify the Earth's field ($B_0 \sim 50\mu$T) required a $\sim$1.0 A current. This meant the coils were able to be operated for an extended period of time and minimise the risk of overheating.

The magnetic conditions inside the cage were tested using a handheld flux gate magnetometer, accurate to 1 nT. The instrument had two measurement settings: measurement of net magnetic field or measurements of the strength of the field vectors (X_B, Y_B, Z_B). The magnetic field strength in each vector direction was calculated as a function of the desired field. The strength of the applied field, $\mathbf{B}$, was simply:

$$\mathbf{B} = \sqrt{X_B^2 + Y_B^2 + Z_B^2} \tag{4.2}$$

Using the flux gate magnetometer at the collision site, the applied current to each coil pair was adjusted until the field strength in each vector direction was the same to maximise the applied field intensity. Effectively the sample then experiences a uniform field and should be magnetised in the [1 1 1] direction. The strength of the applied fields were 50 μT, 100 μT and 150 μT fields, in addition to the null (zero) field experiment. These values are consistent with the range of estimated palaeofield intensities that have been recovered from natural chondrites (e.g., Weiss et al., 2010a; Emmerton et al., 2011; Muxworthy et al., 2017; Wang et al., 2017), and cover a range of field strengths proposed for both nebula fields and internally-generated dynamo fields. Vector magnetisation and subsequent net magnetic field measurements taken at the collision site are shown in Table 4.4. Measurements were taken immediately prior to firing

the projectile using a small window in the side of the target chamber (Fig. 4.18). The window was unfastened and open to make the measurement, but the large aluminium lid that seals the target chamber, the momentum trap (see §4.5.5), light gates and all other apparatus were set up as they would be during the shot.

Table 4.4: Magnetic readings were taken using a flux gate magnetometer at the impact site immediately prior to the projectile being released. Readings were taken inside the target chamber with the lid sealed through a small window that was sealed during the actual experiment. **B** is the desired field for the capsule number while $\mathbf{B}^{net}$ was the actual measured field. The magnetometer measures magnetic field in Cartesian directions X_B, Y_B and Z_B which aimed to be equally strong in order to give the most uniform field experience across the chamber. This meant samples were expected to be magnetised in the **111** direction.

	B (μT)	X_B (μT)	Y_B (μT)	Z_B (μT)	$\mathbf{B}^{net}$ (μT)
Capsule 1	0	±0.014	1.52	±0.019	1.512
Capsule 2	50	28.89	-28.98	29.00	50.15
Capsule 3	100	58.14	57.51	57.89	100.19
Capsule 4	150	-87.32	-87.27	87.32	151.22

4.5.3 Magnetic mapping the target chamber

The magnetic field produced by the Helmholtz cage was used to generate a uniform field of a desired strength. For example, using equation 4.2, this meant that applying a $\sim$ 28 μT magnetic field in each Cartesian direction (X_B, Y_B, Z_B) would result in a net ∼50 μT field applied to the sample.

Using the flux gate magnetometer, I took measurements at intervals between 20-200 mm from the collision site. The capsule was expected to move between 80-120 mm from the collision site through the target chamber (this was later confirmed experimentally) and into a momentum trap, where the capsule would come to stop (see §4.5.5). These results are summarised in Table 4.5. The null field area was very small, difficult to maintain and the field inside the chamber rapidly increased with increasing distance from the impact site. This would likely be able to be improved using much larger coils in a dedicated laboratory setup. However, when a magnetic field was applied, the field was measured to be uniform on the shot axis and a stable field was able to be maintained for the duration of the shot.

Table 4.5: Magnetic mapping of the target chamber. Data for the desired magnetic field cases at 0 μT, 50 μT and 100 μT are shown, with net field measurements taken at horizontal distances 20-200 mm from the collision site. In all cases the capsule was recovered between 80 mm and 120 mm from the collision site. Results for the 150 μT field have not been included as the magnetometer was only able to measure the net field up to its upper limit, 100 μT.

Desired Field (μT)	Field strength (μT)						
	20 mm	40 mm	80 mm	100 mm	120 mm	160 mm	200 mm
0	0.4	3.3	7.9	11.4	13.7	18.4	23.5
50	49.7	49.3	49.5	49.2	48.7	49.0	49.0
100	100.0	99.5	99.3	98.8	98.5	98.7	98.1

4.5.4 Sample preparation

The sipernat-magnetite-hematite sample was initially far more porous ($\phi > 90\%$) than the target porosity $\phi_{mi} = 70\%$ as the porosity was controlled by the uncompressed 'raw' sipernat material.This meant that the zero-porosity iron-oxides and the highly-porous sipernat required compaction prior to the experiments into the capsule using a controlled loading environment. To do this, I used a universal hydraulic press machine at Imperial College London to mitigate the likelihood of producing a density gradient across the sample (Fig. 4.19).

When compacting highly porous material, there is a potential for the edges to become dense while the centre remains relatively uncompressed, forming a porosity gradient across the

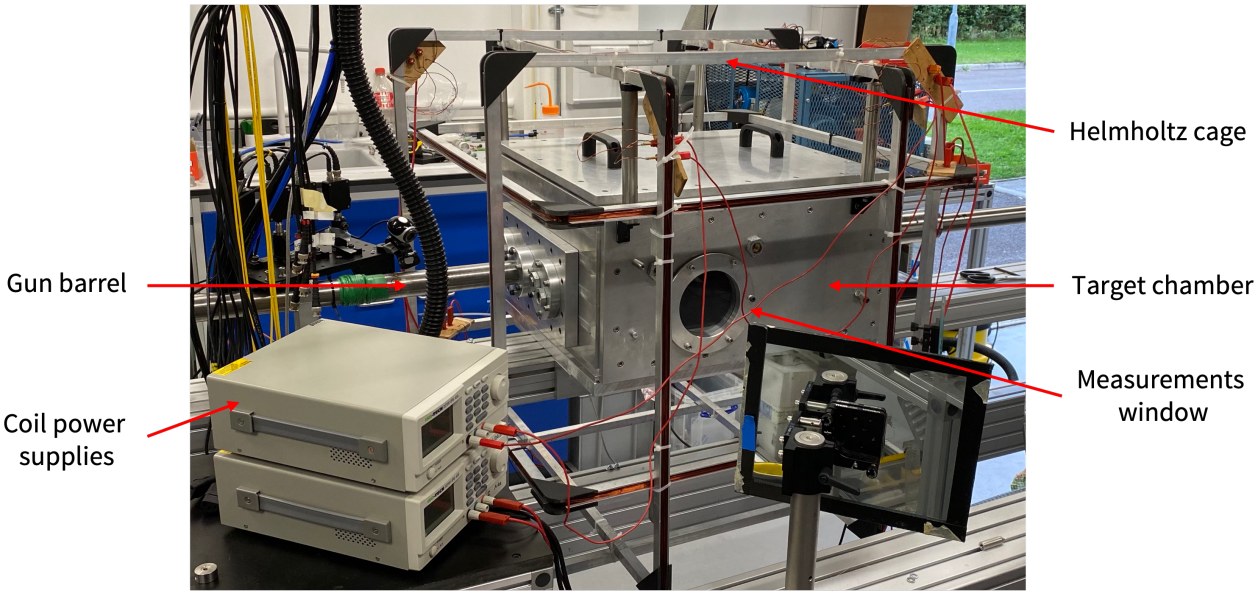


Figure 4.18: View of the shock recovery experiments. In this frame is the target chamber, Helmholtz cage and part of the light-gas gun barrel in the shock physics laboratory at the University of Oxford. Flux gate magnetometer measurements were taken through the small window in the side of the target chamber prior to the shots being fired.

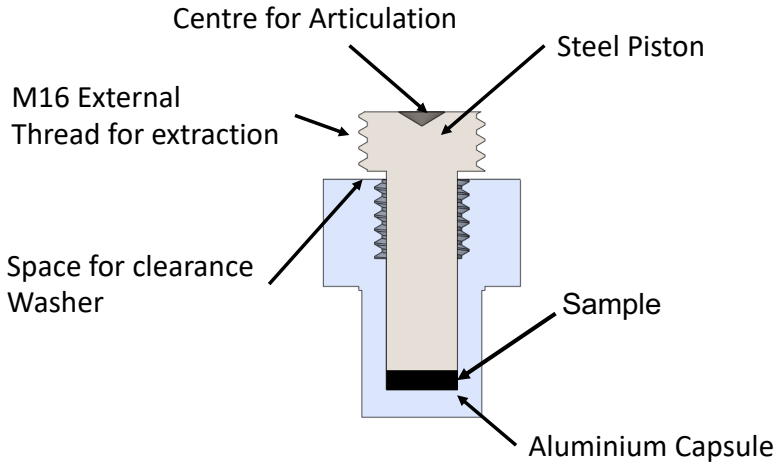


Figure 4.19: Schematic demonstrating the piston usage to compress the sample in a universal hydraulic press. The sample was compressed under a 6 kN load to reduce the sipernat porosity from $> 90\%$ to $\sim 70\%$.

compacted sample. Introduction of a density gradient in the sample was minimised using a hydraulic press. A piston was manufactured to be used in the press that was machined to fit exactly into the diameter of the capsule. The piston was manufactured after the capsules had been produced in order to measure the tolerances of the capsule sample chambers' diameters (Table 4.6). The hydraulic press was then used to load and compress the sample under a 6 kN load over the course of 1 minute. The sample was compressed inside the capsule, then the remainder of the sample chamber (volume that was left for the pillow) was filled with raw sipernat. The capsules were then sealed with the M12 screw thread and placed into magnetically shielded mu-metal boxes.

Table 4.6: Capsule sample chamber diameter measurements. Measurements were made independently 2 times using a vernier caliper with a ± 4 μm tolerance. The mean reading was 9 mm which was true to the manufacture specification.

	Read 1 (mm)	Read 2 (mm)	Average Read (mm)
Capsule 1	9.020	8.966	9.000
Capsule 2	8.966	8.992	8.990
Capsule 3	8.966	8.992	8.990
Capsule 4	8.962	8.992	9.000

4.5.5 Shot Procedure

Preparation for the suite of shot experiments included the setup and subsequent testing of the Helmholtz cage, cleaning of the inside of the gun barrel, vacuum sealing the target chamber,

projectile velocity testing and momentum trap assembly. With the team at the University of Oxford, I spent a day prior to the actual measurements preparing the apparatus (Fig. 4.20). This meant testing the firing mechanism to ensure that the projectiles were going to reach 800 ms^{-1} and planning the post-shot plan of action so that samples could be recovered quickly and efficiently from the target chamber.

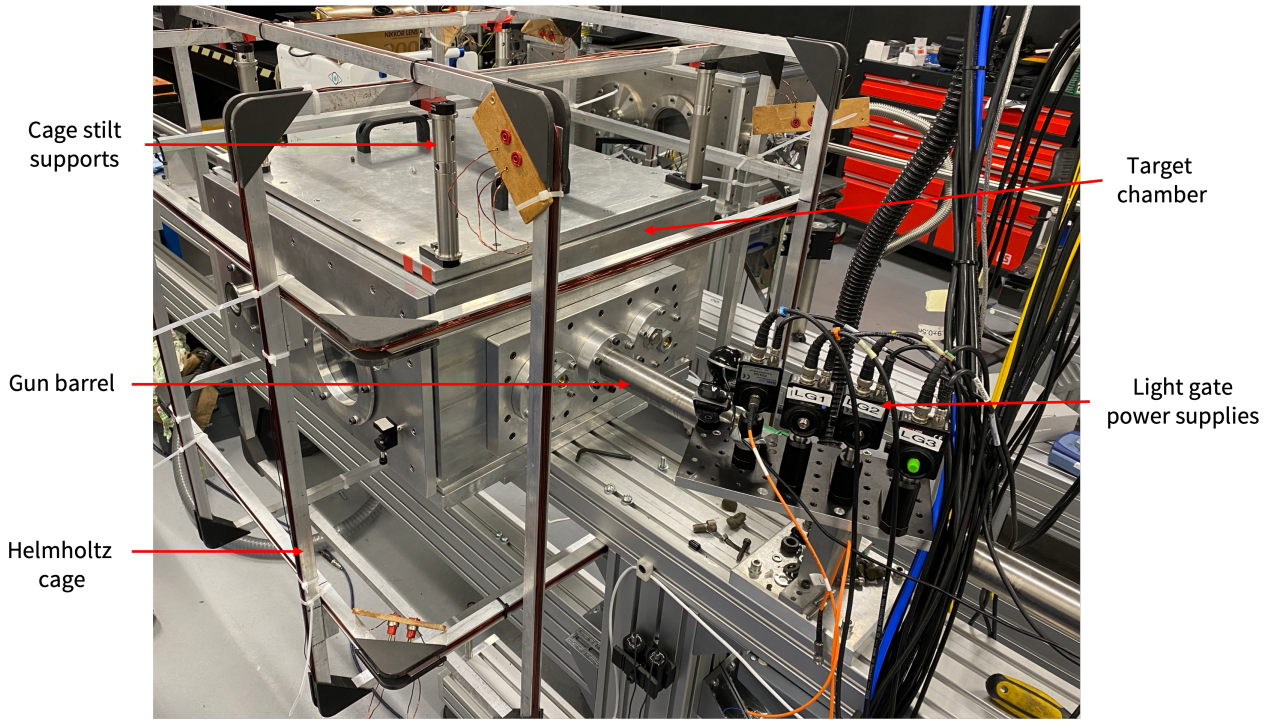


Figure 4.20: A close-up view of the the full experimental setup of the shot experiments. The Helmholtz cage was suspended above the target chamber using short aluminium stilts. The light gate power supplies are set up adjacent to the barrel entry point into the target chamber. The black corner joints on the Helmholtz cage are the carbon fibre brackets that were 3D-printed for the cage specifically. The small wooden panels with red sockets were used to connect each pair of square coils to a dedicated DC power supply.

Shot velocity

Compressed helium was used to fire the projectile - a 25 mm wide, 36 mm length polycarbonate sabot with a 24 mm wide, 6 mm height aluminium flyer plate attached to the top. The sabot stabilises the projectile through the gun barrel, while the aluminium flyer plate acts as the dominant mass and impactor. To determine both the amount of helium and the pressure required to achieve target velocity prior to firing at the samples, I performed a 'velocity shot' on an empty target chamber where the parameters were based on benchmark values from previous

experiments. This pilot investigation meant the helium compressor could be calibrated so that the velocity of the projectile was correct, however this was not necessary as the velocity shot was recorded at 800±3.3 m/s.

During the shot experiments, the velocity of the projectile was tracked immediately prior to impact using two light gates attached to the end of the gun barrel. These light gates are permanent fixtures in the chamber, spaced 12 ± 0.05 mm apart. When an object passes through the light gates they are 'tripped' and their signal goes from a high level to a nominal level (non-zero due to signal from electrical noise). Using two channels of light gates, there is time difference between the signals being tripped, which enabled the velocity of the projectile to be calculated immediately prior to impact.

Light gate trace data is shown in Figure 4.21. As the raw data was noisy, I have used a combination of two digital FIR filters, one forward and one backward, to smooth the signal. The velocities were calculated using the point in time at 50% of the trigger value (t_1, t_2, channels 1 and 2, respectively; Fig. 4.21). This meant the point of reference for each light gate (which had slightly different signal response intensities) was the same and minimised the error in measurement. Across the experiments there was a small distribution of impact velocities, from 796 - 804 m/s (Table 4.7).

Table 4.7: Impact velocities for the projectile in each of the four impact experiments. The error is consistent in each (±3.3 m/s), arising from the uncertainty in the separation between light gates. See light gate data in Figure 4.21.

	Shot 1	Shot 2	Shot 3	Shot 4	Average
Velocity	801 m/s	796 m/s	799 m/s	804 ms/s	800 m/s

Effect of velocity on generated shock pressure

In practice, the velocity is unlikely to match the desired value exactly (Table 4.7) due to variations in the vacuum produced within the apparatus, pressure fluctuations in the gas chamber and friction within the barrel as the projectile travels towards the target. As the velocity of the projectile during the actual experiments was not exactly 800 m/s, I have produced a small number of iSALE simulations where the velocity was up to 100 m/s slower than the desired

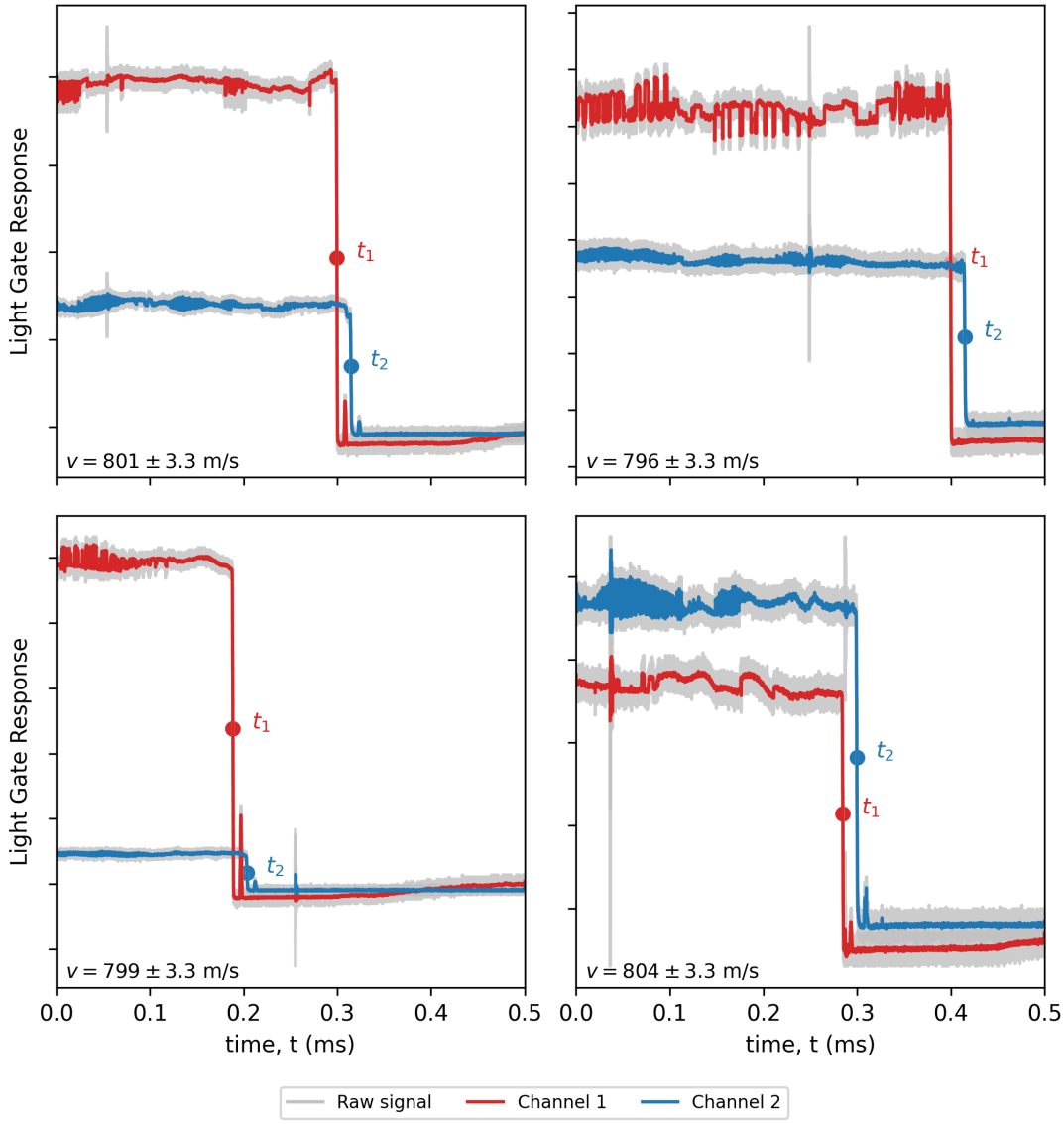


Figure 4.21: Using two light gates spaced 12 ± 0.05 mm apart, the velocity of the projectile immediately prior to impact was able to be calculated. The raw light gate data has been smoothed used two digital FIR filters in combination, one forward and one backward. For reference, the raw data is included but greyed out, while the two light gates, channel 1 and channel 2, are shown in red and blue, respectively. The difference in time was then the difference between the time the first light gate was triggered ($t1$) and the second light gate was triggered ($t2$).

value (Fig. 4.22). These simulations showed that in the case something went wrong with the apparatus and the target velocity was missed by more than 10%, the result would still yield shock pressures consistent with recovered chondrites ($\sim$ 1.3 GPa) and the average peak temperatures would be between 200-250°C.

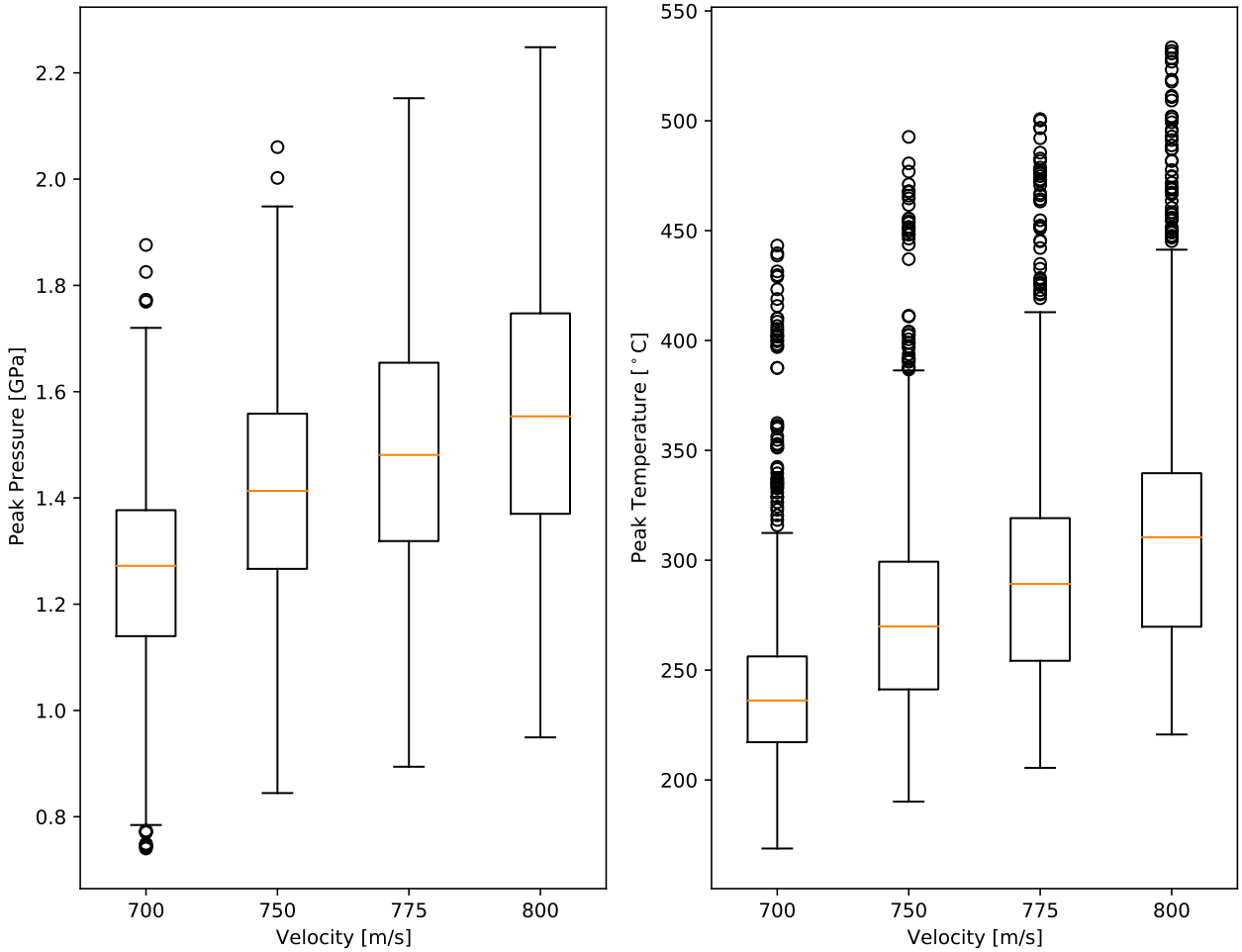


Figure 4.22: Analysis of the peak temperature and peak pressure experience across the sample in the capsule at a range of velocities between 700 - 800 m/s. Statistical outliers are represented by hollow circles, while the median average is shown by a horizontal orange line in all cases.

Momentum trap to catch capsules

Once the projectile collides with the capsule it needs to be rapidly slowed before it strikes the back of the target chamber. To brake the capsule, a 'catch can' (Fig. 4.23), a heavy steel cylinder filled with dense fabrics and aluminium honeycomb momentum traps (Fig. 4.24), was placed behind the capsule to prevent it from hitting the back of the target chamber. The main concern was generating a second shockwave from the momentum of the capsule hitting the back of the target chamber as it was not accounted for in the iSALE modelling, hence, progressive braking was a solution that minimised the effect of secondary impacts. While there would be resulting impacts as the capsule was slowed in the catch can, it would be at least an order of magnitude less than the strength of the impact from the projectile (D. Eakins, personal

communication).

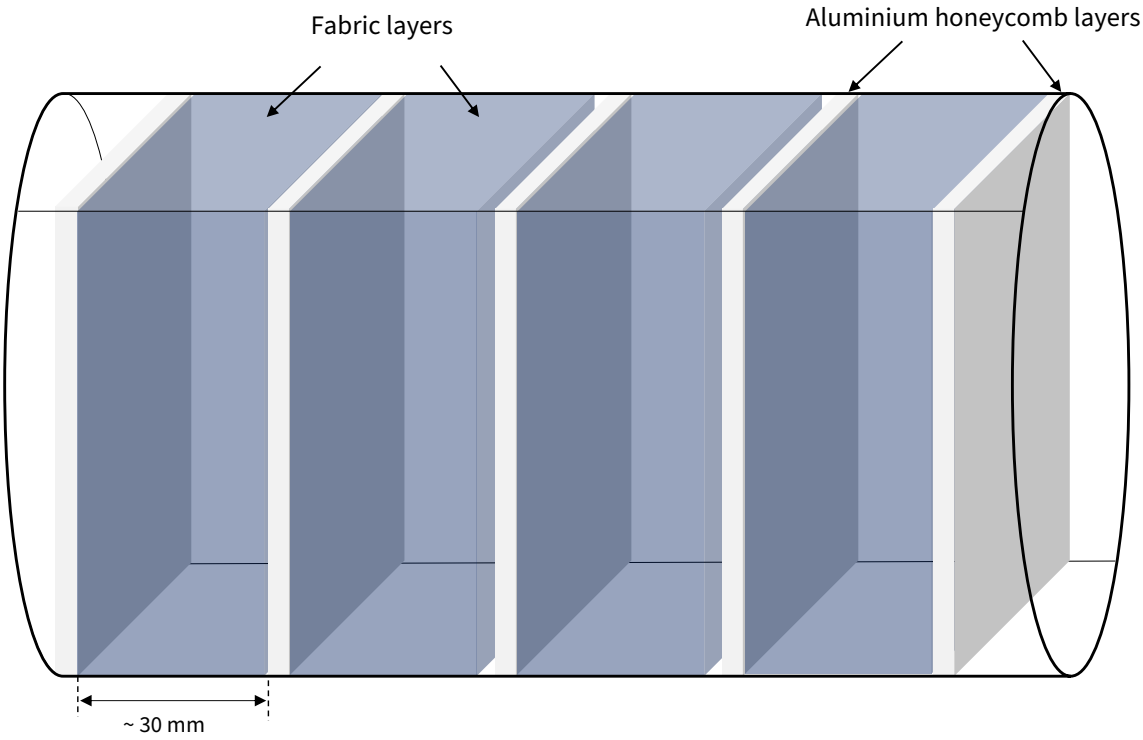


Figure 4.23: Schematic demonstrating the layering inside the 'catch can' used to slow the capsule velocity. The fabric layers were dense fabrics, sandwiched between aluminium honeycomb traps (Fig. 4.24). At the opening of the catch can, another fabric layer was used and secured using heavy duty cloth tape.

The catch can had a total of 5 aluminium honeycomb traps placed inside, separated by dense fabric, sealed with heavy duty cloth tape. In practice, I found that the capsule would pass through the first two traps entirely and begin to penetrate the third trap (Fig. 4.24), about halfway through the catch can. It is in this position, ∼100 mm from the collision site, that the sample would cool down in the applied field (that was being controlled by the Helmholtz cage) while the lid to the chamber was removed and the capsule was recovered.

Mounting the capsule

The capsule was fixed to a polycarbonate mounting plate using a thin layer of epoxy glue. The mounting plate was then attached on to the end of the gun barrel using narrow nylon screws (Fig. 4.25). Attaching the capsule directly to the barrel minimised the chance the projectile would collide with the capsule at a non-zero angle. This was to ensure parallel contact between

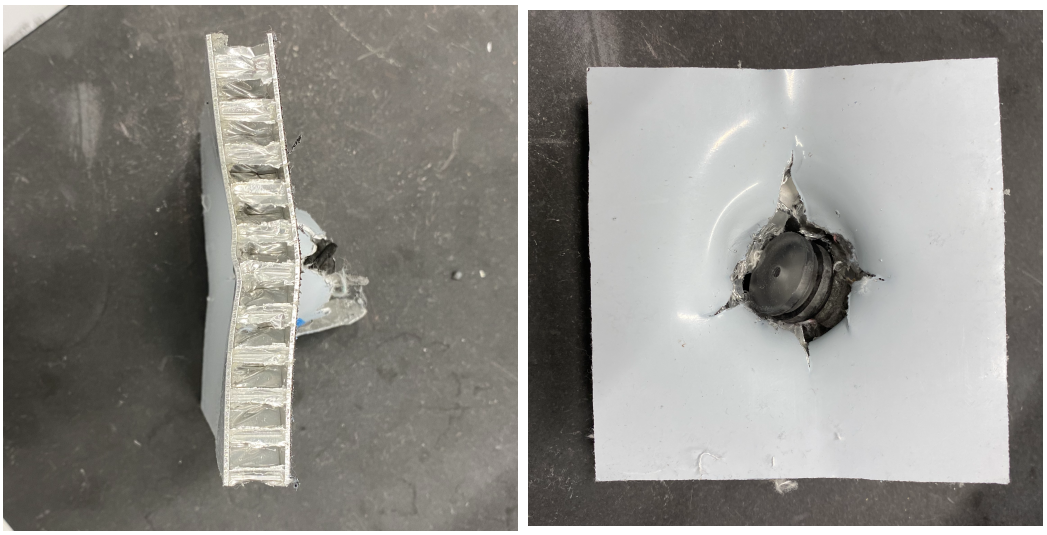


Figure 4.24: Aluminium honeycomb momentum trap after one of the shock experiments. A total of 5 of these traps were placed inside the catch can, separated by dense fabric and evenly spaced apart ($\sim$ 30 mm spacing). All of the shots completely penetrated the first two each time, typically not causing significant damage to the third trap which was approximately 120 mm from the collision site. The pierced plate shown still has the polycarbonate sabot embedded within it.

the faces of the projectile and the capsule as this was what had been modelled in iSALE. The polycarbonate plate was destroyed in all of the shots that were performed, meaning the capsule was successfully released from the mount upon impact.

Recovering capsules

Recovery of the capsules was efficient and careful. Immediately following the shot, the top of the target chamber was removed which took $\sim$ 5 minutes as it had been screwed shut prior to impact. The catch can was turned vertically for ease of access and remained inside the chamber, within the magnetically controlled environment, until the capsule was located. In all cases, the capsule was found lodged in fabrics between the second and third aluminium honeycomb momentum traps (placed at 80 mm and 120 mm from the collision site, respectively). Once recovered, the capsules were stored in a mu-metal, magnetically shielded box. Capsules had also been stored in a similar box prior to the shock experiments, since the pre-experiment

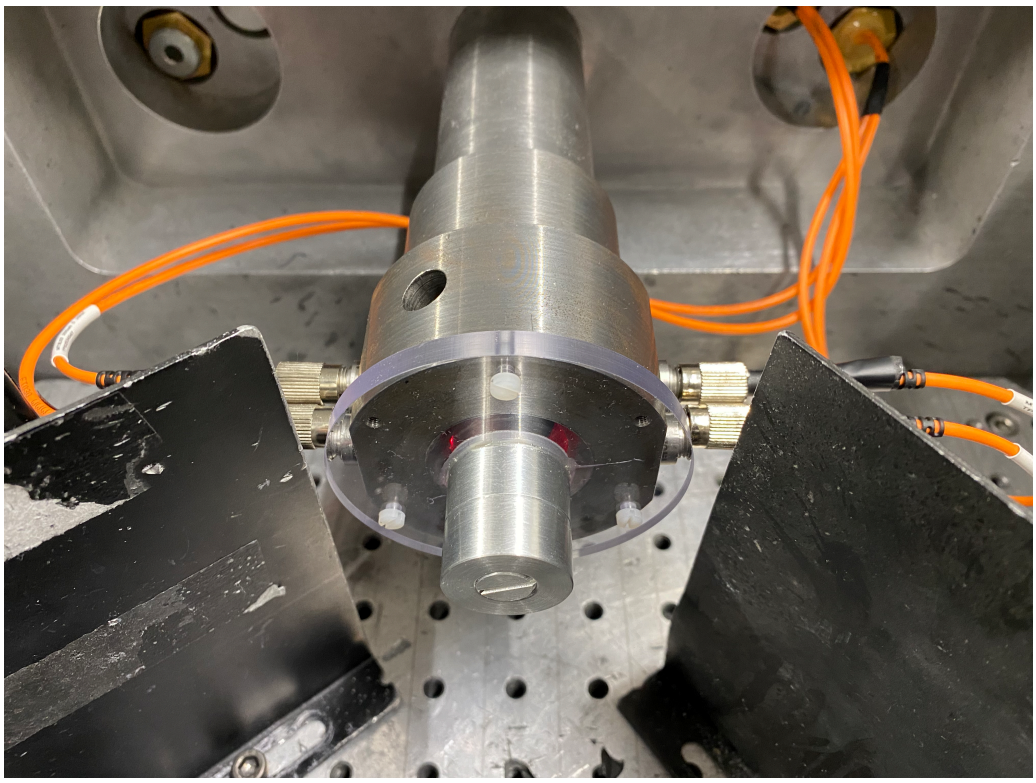


Figure 4.25: The aluminium capsule mounted onto the end of the gun barrel using a polycarbonate mounting plate. The capsule was fixed to the plate using an epoxy glue, which in turn was fixed onto the barrel mount using shallow nylon screws. The light gate equipment (connected via the orange wires in the image) was protected using two large black plates that were screwed into the bottom of the target chamber.

compaction process. Using mu-metal storage boxes ensured as little exposure to the Earth's background field as possible, minimising the chance the samples acquired a viscous remanent magnetisation from both artificial and the Earth's own magnetic field.

4.5.6 Machining of samples from recovered capsules

Following the experiments, samples were taken from the Oxford laboratory back to Imperial College where they were machined to remove the excess aluminium and expose the sample for magnetic measurements. This was necessary as the impacts had flattened the impact-face such that the capsules became conical in shape (Fig. 4.26), expanding the diameter from 25 mm to approximately 32 mm at the largest point. However, the magnetic apparatus requires a maximum sample size of 10 mm to physically fit the inside the oven.



Figure 4.26: Following the impact, the capsule had been compressed and the impact-face flattened into a conical shape. The aluminium flyer plate was loosely stuck onto the impact-face of the capsule, though this was able to be prised off with little force.

While the condition of the samples was known prior to the impact experiments (powdered, poorly consolidated), the solidity and integrity of the post-shock 'synthetic chondrite' was unknown and not determined by the iSALE simulations. The ideal outcome would have been that the synthetic chondrites were lithified, however, there was a chance the sample could have fractured or broken up while removing the aluminium casing during the machining process. In order to manage the risk of this occurring, I introduced an intermediary machining stage that involved drilling into the rear of the capsule. This meant the threaded plug could be removed and a temperature-resistant, non-magnetising (OMEGABOND CC) cement could be poured directly into the sample chamber to ensure the samples would not break up during

the remainder of the machining process. The cement was then dried out using a dehydrator at 40°C. While the cement was dehydrated, there was no way to keep the samples in a magnetically controlled environment, though they were only removed from the mu-metal shielded container for a maximum of 24 hours.

The second stage involved using a lathe to render the capsules into 10 mm diameter cylinders. The sample was turned slowly to reduce the diameter and height of the capsules suitable for the magnetic apparatus. A coolant was not used to avoid any potential chemical contamination of the samples. Samples were milled down until just a $\sim 0.5 - 1$ mm wide casing remained around the samples. Including this casing, samples remained at a 10 mm total diameter. As the aluminium was non-magnetic would be tested to ensure this was the case, the inclusion of an aluminium outer casing ensured sample integrity while not affecting the magnetic measurements.

4.6 Results: Magnetic Analysis of Recovered Samples

Following the preparation of the recovered samples, the 10 mm capsules were taken to the Natural Magnetism Group laboratory at Imperial College London. A full suite of measurements were taken to investigate (1) whether an NRM has been recorded during impacts on synthetic chondrites and (2) if the NRM recorded during impact-induced compaction is a TRM.

In addition to NRM measurements, recovering the peak temperature will enable the calibration of the modelling to the results and verify the use case for the iSALE shock physics code in simulating millimetre-scale laboratory experiments.

4.6.1 Thermal demagnetisation of the synthetic chondrites

Thermal demagnetisation measurements were made using the Orion high-temperature, low-field, three-axis vibrating sample magnetometer (VSM). The Orion includes a furnace capable of heating samples to 800°C in either a controlled DC-field or zero field (< 100 nT) and has a magnetic moment sensitivity of 5×10^{-8} Am^2.

To recover the unblocking spectra of the NRM, each of the samples were heated in zero field and the magnetisation of the sample was recorded (Fig. 4.27). If the remanence was recorded wholly in the magnetite and recorded during cooling through its Curie temperature (T_C), then the magnetic response would have been expected to have fallen to zero at T_C (580°C for magnetite; Dunlop and Özdemir, 1997). However, as the iSALE modelling predicted peak temperatures around 390°C (Fig. 4.22), the majority of the magnetisation was anticipated to be eliminated before this temperature.

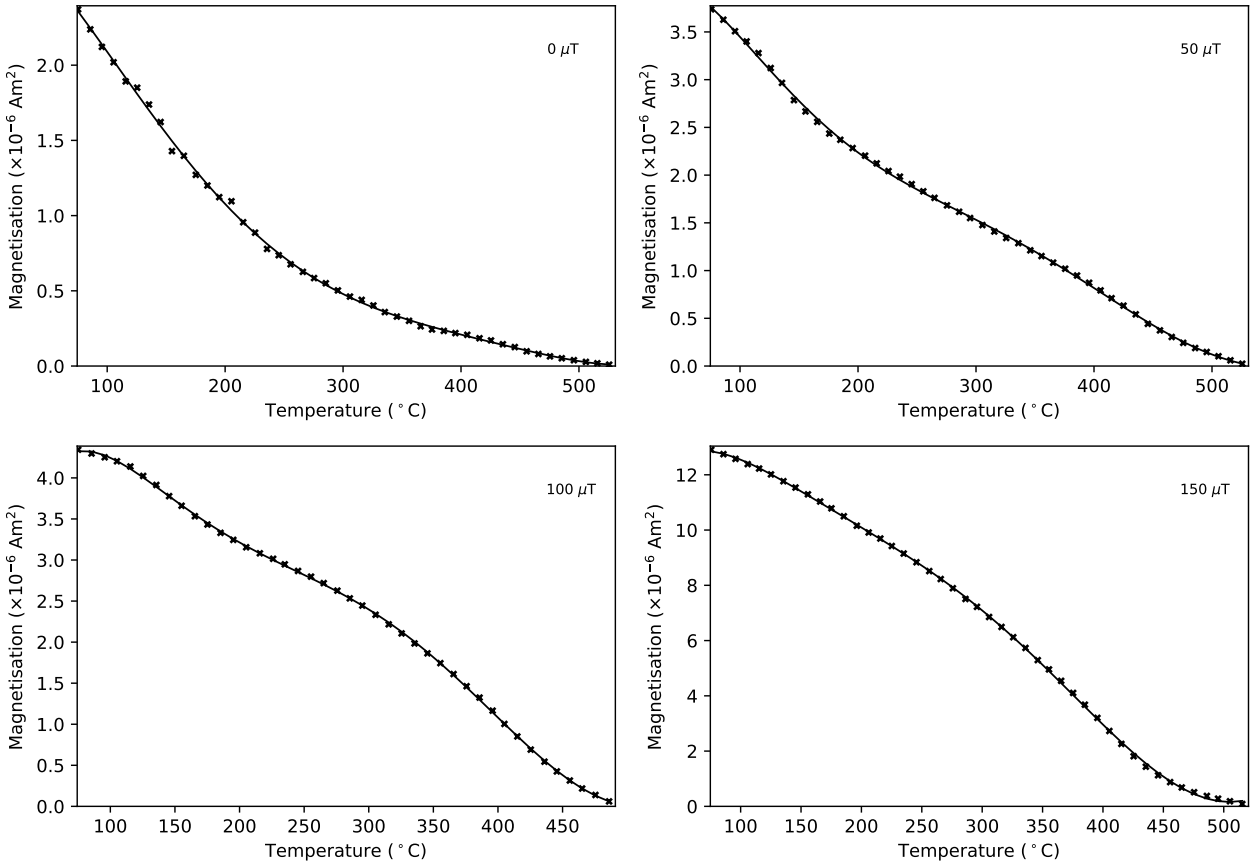


Figure 4.27: Thermal demagnetisation data for each of the four samples, experimentally shocked in magnetic fields between 0 and 150 μT (field shown in top-right of each pane). Measurements were taken using the Orion VSM apparatus continuously and data was then grouped into 10°C intervals which are shown. The solid line is a sixth-order polynomial fit to this data. Samples were heated up to a maximum of 535°C by which point all the samples appeared to have demagnetised.

The sample oscillates vertically inside the furnace where the magnetisation was measured as a function of the applied temperature. The response of the sample was measured continuously, up to 535°C, or once the magnetisation had fallen to zero. The response of the samples was not explored past 535°C as the melting point of aluminium-6061 is $\sim$ 590°C which would have

risked damaging the VSM. Measurements were then grouped into 10°C bins where the average magnetisation over the range was recorded.

4.6.2 Directional magnetic data recorded in synthetic chondrites

Directional data from each of the four samples was examined to check if the sample had tumbled during the experiment. Derived from the thermal demagnetisation data, directional magnetic data can be used to view separate magnetic components that, when combined, form the total NRM of a sample. Different components display different directions and these can be represented using Zijderveld plots and equal area projections (Tauxe et al., 2010).

As the capsules were shot on a horizontal plane, the remanent magnetisation was anticipated to have been acquired uniaxially by the magnetic carriers. However, as the capsules may have rotated or tumbled after the initial impact, this should be apparent by significant angular deviation in the directional diagrams from the initial magnetisation vector (Fig. 4.28). Zijderveld diagrams of all samples (Fig. 4.28) display shallowing in the same (E, N) direction. As all samples were initially oriented in the same direction, subject to a field in the [1 1 1] direction and experienced the same impact, the shallowing is likely due to the compaction process, where the magnetic fabric is controlled by the impact, similar to observations of Allende (Muxworthy et al., 2017).

The directional data recovered from the synthetic chondrites shocked in the 0, 100 and 150 μT fields is indicative of a well-defined NRM which appears to be largely single-component (Fig. 4.28a, c, d) and suggests low rotation during the shot. However, the 50 μT shot has two components, a high-temperature component between 405-535°C and a low-temperature component below 405°C, suggesting this shot tumbled and rotated with respect to the applied field direction. There was also some minor deviation from the main component in the 100 μT shot below 115°C (Fig. 4.28c), although this may be noise during measurement.

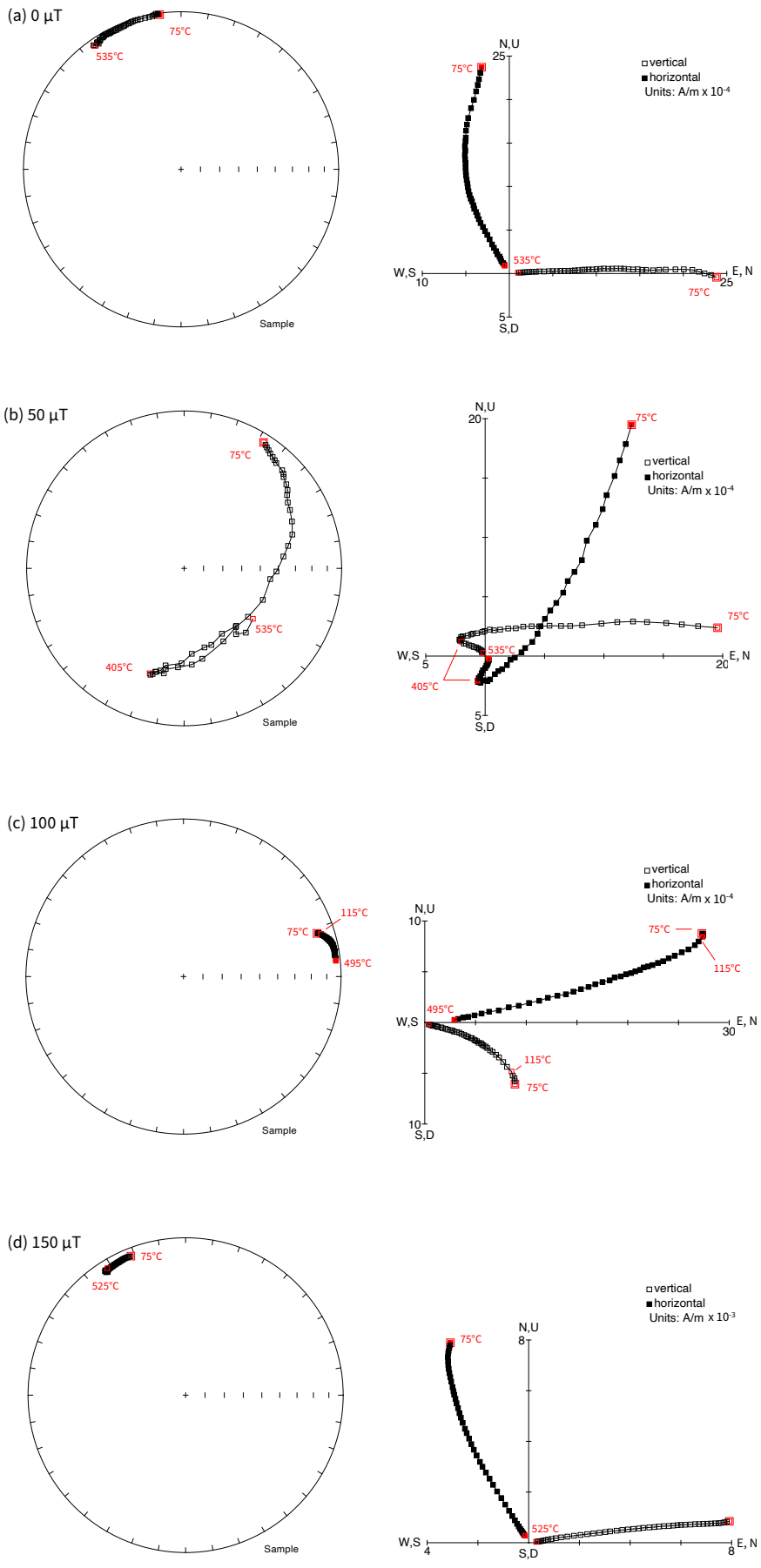


Figure 4.28: Equal area plots and Zijderveld diagrams for each of the four synthetic chondrites produced. Data was measured during thermal demagnetisation. In the cases of a strong applied field (100-150 μT) the angular deviation is very minor. Temperatures have been included at the first and last measurements, as well as at points in (b) and (c) where a change in direction was observed.

4.6.3 Unblocking spectra of synthetic chondrites

Differentiating the polynomial fit to the demagnetisation measurements (Fig. 4.27) recovers an unblocking spectra for each sample (Fig. 4.29). The unblocking spectra enables detection of the peak unblocking temperature which, in these samples, should correspond to the maximum temperature experienced during the impact experiments.

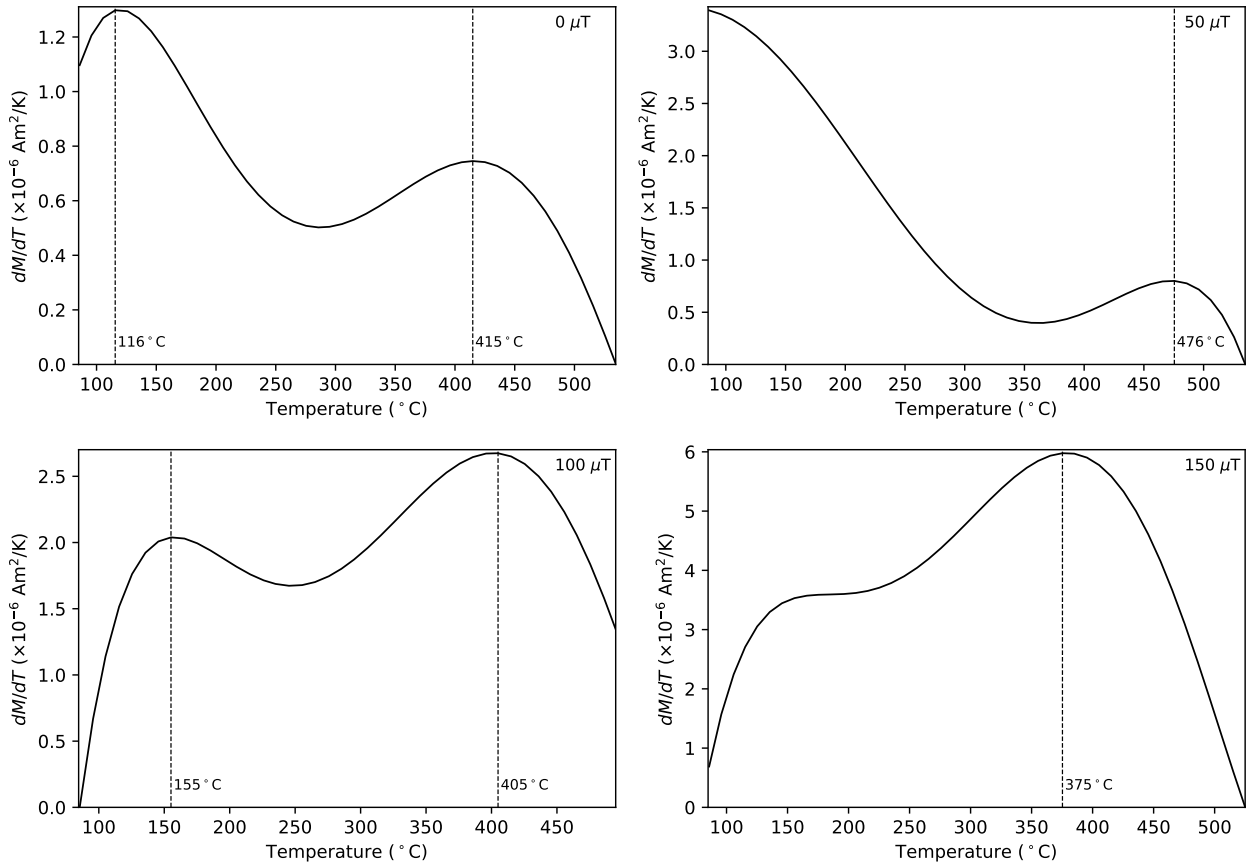


Figure 4.29: Unblocking spectra from each of the four samples where the strength of the field applied during the shot is shown on each plot. The spectra are formed by performing a discrete differentiation on the fit to the demagnetisation data (Fig. 4.27). Peaks in the spectra are representative of the peak temperature that a TRM was recorded at. The solid line is a sixth-order polynomial.

In all the samples, there were two peaks observed: the first between 100-140°C and the second between 375-410°C (excluding the tumbled 50 μT shot). The higher-temperature peaks most likely represent a TRM component acquired during the impact experiments. This higher peak temperature is also in agreement with the results from the iSALE model which predicted an average peak temperature of ∼390°C (Fig. 4.22). There will have been a distribution of coercivities within the samples, giving rise to a range of blocking and unblocking temperatures

(Özdemir, 2000). This likely also gives rise to the higher unblocking temperatures in a small fraction of the sample which demagnetise at even greater temperatures.

In the null (0 μT) field sample, the ideal result would be random behaviour due to no coherent magnetisation. However, there appears to be two magnetisation components, the more significant being a low-temperature (< 375°C) component, adjacent to a minor high-temperature (> 375°C) component (Fig. 4.29a). The high-temperature component was likely acquired during the shock experiment, similar to the other three samples, as the null field was not able to be uniformly maintained throughout the whole target chamber; samples travelled $\sim 80 - 120$ mm from the collision site, which in the case of the 0 μT shot meant the capsule cooled in an $\sim 8 - 14$ μT field (Table 4.5). While this may explain the high-temperature component, the low-temperature component is more difficult to explain. The sample possibly obtained a secondary magnetisation component over the course of the machining process, during which it was removed from its magnetically shielded enclosure.

Low-temperature peak in the unblocking spectra

An unexpected second, low-temperature peak was observed in each of the four unblocking spectra, between 100-140°C. The origin of this peak is most likely from the machining process which was the only time samples were removed from their shielded mu-metal containers between the impact experiments and magnetic measurements. A lathe was used to remove the aluminium casing from the samples and the ambient magnetic field was unable to be controlled. During this process, no coolant was used as to avoid contamination of the samples, however, this meant the temperature of the aluminium was not well regulated.

Upon producing the unblocking spectra (Fig. 4.29), the low-temperature peak, which is most well-defined in the 0 μT sample, suggests the samples have recorded an NRM component since being shocked in the impact experiments. The cutting temperature of aluminium alloys on a rotating lathe has been shown to range from 97-150°C (Kannan et al., 2013), variable depending on cutting force and depth of cut, which is consistent with the lower-peak temperatures measured in the samples.

There is also a decrease in the ratio of intensity between the lower- and higher-temperature peaks across the samples. As the applied field is increased, the intensity of the NRM component associated with the high-temperature peak also increases. However, the relative height of the lower-temperature peak decreases. This suggests a different mechanism is responsible for the two peaks and that the low temperature peak was not recorded whilst the sample was exposed to the field applied during the experiment. This hypothesis might lead to the conclusion that the two peaks in the 50 μT sample should be very similar in height as Earth's field is also ∼50 μT. However, the intensity of the remanence recorded also depends on the acquisition method and duration, which was different. The sample was machined for a significantly longer period of time (∼ minutes) than it was shocked during the experiment (∼ μs).

4.6.4 Hysteresis parameters

As the manufactured samples required a strong saturating field, the magnetic hysteresis parameters were measured using the Princeton VSM in the Natural Magnetism Group laboratory at Imperial College London. Hysteresis loops were generated using a saturating field of 0.5 T at room temperature (Fig. 4.30), which enabled the calculation of the coercivity, B_c, saturation magnetisation, M_s and saturation remanent magnetisation, M_{rs}, for each of the samples. The coercivity of remanence, B_{cr}, was then calculated from backfield (direct current demagnetisation) curves applied to each sample. The magnetisations calculated from the hysteresis data were mass normalised; each sample contained 20 ± 1 mg magnetite and 81 ± 1 mg hematite—this would suggest that each sample should have the same hysteresis parameters. The hysteresis results are summarised in Table 4.8.

Across the four samples, coercivities were found between $B_c = 18 - 21$ mT, while remanence coercivities were between $B_{cr} = 30 - 36$ mT. The average coercivity ratio was found to be $B_{cr}/B_c = 1.67 \pm 0.1$, and the average remanence ratio, $M_{rs}/M_s = 0.32 \pm 0.02$. The hysteresis parameters mean the domain state of the magnetic carriers can be identified. These M_{rs}/M_s values are too low for both SD and MD hematite (Özdemir and Dunlop, 2014). However, they are indicative of PSD magnetite (Dunlop, 2002b,a; Muxworthy and Dunlop, 2002), which is consistent with the < 1 μm grain size used in the samples (Muxworthy and Williams, 2006).

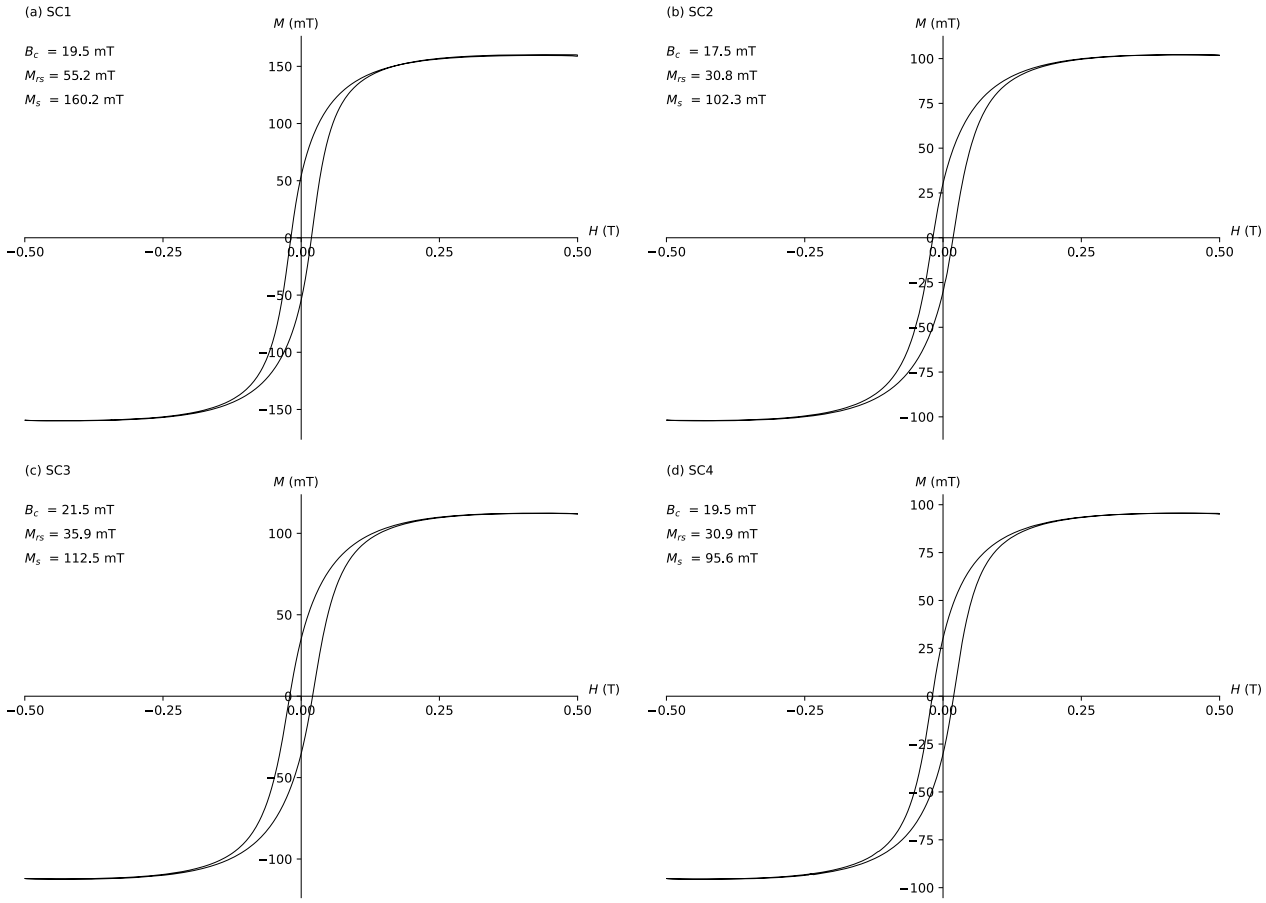


Figure 4.30: Major hysteresis loops measured using the Princeton VSM. All samples (synthetic chondrites 1-4, SC1-4) exhibit well-defined hysteresis behaviour. Included in each pain are the hysteresis parameters, coercivity, B_c, saturation magnetisation, M_s and saturation remanent magnetisation, M_{rs}. These parameters are summarised in Table 4.8.

Table 4.8: Hysteresis parameters, coercivity, B_c, coercivity of remanence, B_{cr}, saturation magnetisation, M_s and saturation remanent magnetisation, M_{rs}, for each of the synthetic chondrites (SC1-4).

B	Sample	B_c (mT)	B_{cr} (mT)	B_{cr}/B_c	M_{rs} (mAm^2)	M_s (mAm^2)	M_{rs}/M_s
0	SC1	20	30	1.54	0.84	2.42	0.34
50	SC2	18	32	1.77	0.47	1.56	0.30
100	SC3	22	36	1.67	0.55	1.70	0.32
150	SC4	20	33	1.69	0.47	1.45	0.32

4.6.5 Magnetic properties of aluminium-6061

In addition to the sample measurements, I have also measured an isolated offcut of the aluminium that was removed in the machining process. The offcut was removed from the impact face but contained none of the sample, meaning it was pure aluminium-6061 that had been subject to the same experimental process as the samples. The purpose of this was to check for any ferromagnetic impurities in the aluminium that may give rise to unanticipated magnetic

properties, influencing the results.

The aluminium offcut has been processed and measured in the same way as the samples where the Orion VSM was used to thermally demagnetise the aluminium, in conjunction with the Princeton VSM to recover the hysteresis parameters. The data measured from the post-impact, post-lathe aluminium shows no sign of magnetic coherence (Fig. 4.31); there is no coherent direction nor does the sample saturate in the intense applied field. These results give confidence that the aluminium is not an influence on the magnetic data and that any magnetic signals measured are related to the synthetic chondrite material.

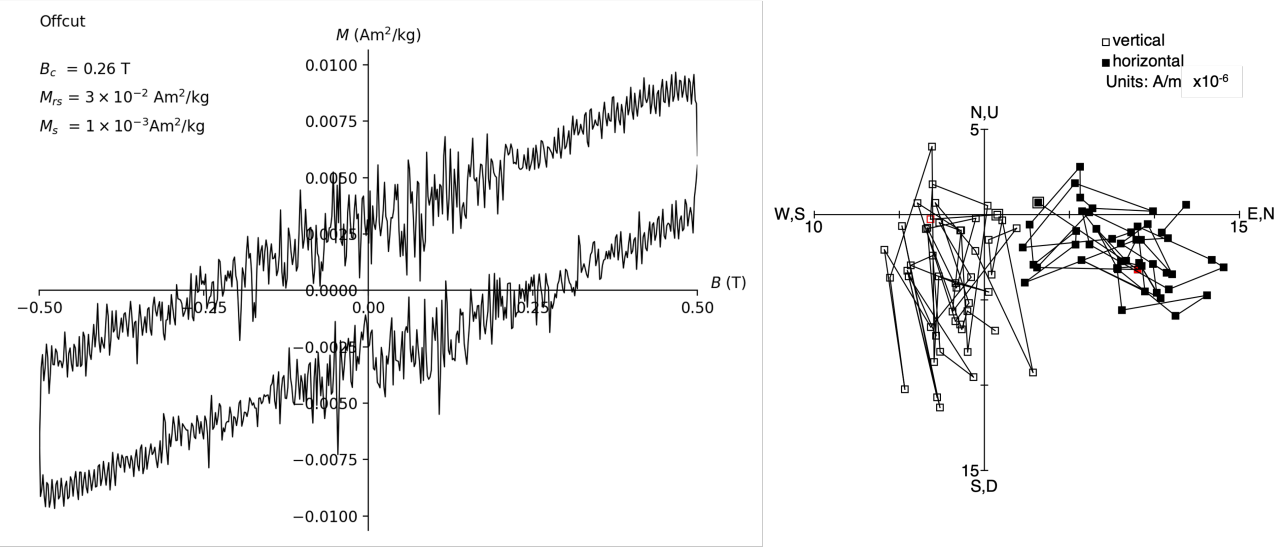


Figure 4.31: Hysteresis and directional data recorded from an aluminium offcut collected during the post-impact machining of one of the synthetic chondrites. Both the hysteresis data and Zijderveld diagram demonstrate a limited magnetic response from the aluminium.

4.6.6 Porosity calculation: SEM and Micro-CT imaging

Calculating the porosity of the post-shock synthetic chondrites was done using a scanning electron microscope (SEM). In order to use this technique, one of the samples had to be directly observed under the microscope. This meant exposing a section of one of the capsules and preparing the sample for SEM imaging.

Prior to removal of one face of the capsule, I used a Bruker Skyscan 1273 3D X-ray microscope (micro-computed tomography, or micro-CT) to examine the inside of all the capsules and locate where the sample had moved within each capsule (Fig. 4.32). After viewing the

micro-CT images of the four capsules, I chose to use the capsule that was shocked under the null field conditions for SEM analysis. This sample appeared to have maintained good integrity where the iron oxide had remained in the centre of the capsule and would be accessible after splitting the aluminium.

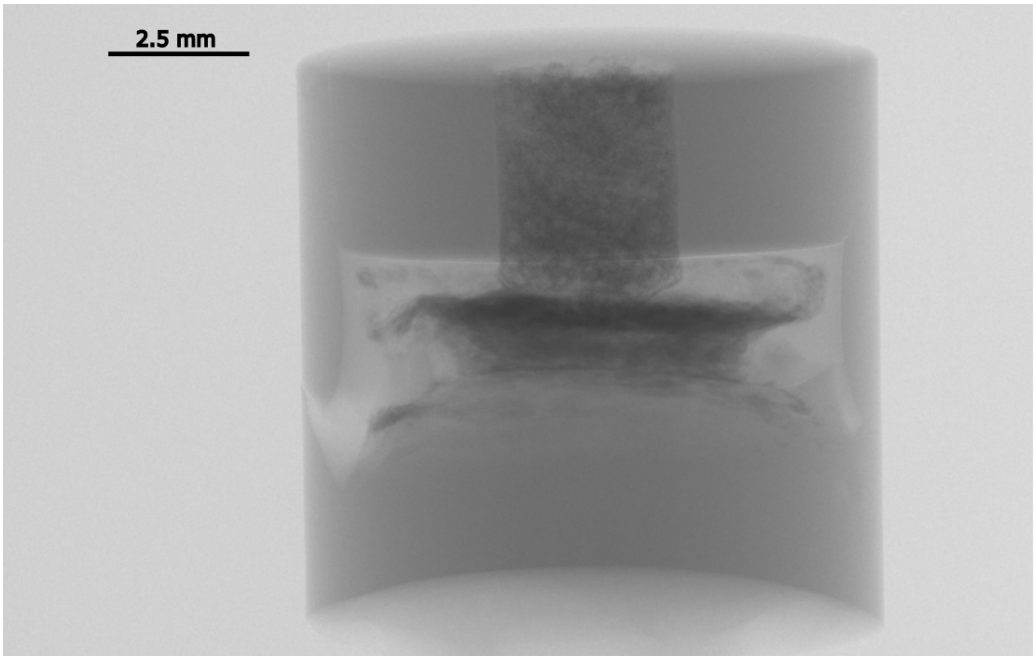


Figure 4.32: Image taken using the Bruker Skyscan 1273 3D X-ray microscope at Imperial College London. Relative to this image, the impact direction was vertically upwards. In this image is the aluminium-6061 capsule which has been machined to a 10 mm cylinder. The sample chamber can be seen through the centre of the capsule with the considerably more dense iron oxides (magnetite and hematite) appearing black throughout the image. Above the sample chamber is the drill thread that was used to pour in a temperature-resistant, non-magnetising cement so the sample would maintain its integrity throughout the machining processes.

The capsule was then machined to expose the sample using a Dremel rotary tool with a blade suitable for metalwork. The capsule was split 3 mm from the drilled surface (3 mm from the top of the capsule shown in Fig. 4.32), along the diameter of the capsule. A weakness in the centre of the capsule meant it separated itself once the tool was about halfway $\sim 3-5$ mm into the capsule. The sample was reddish in appearance which was expected from the hematite that was present, while the sipernat pillow had collapsed around the sample and was white in colour with an enamel-like appearance (Fig. 4.33). The sample was coarse but solid, no longer powdered, indicative of a depletion of porosity. The surface of the samples appeared as solid flakes where the capsule had been separated.

The exposed halves of the sample were placed into the SEM where they could be analysed.



Figure 4.33: The 10 mm capsule was divided into two to expose the sample suitable for SEM analysis. One of the capsule halves has a small nylon attachment glued on which was required for use in the Orion VSM. The reddish colour originates from the fine-grained hematite present.

The nature of the samples being raw and unpolished meant focusing the microscope onto the surface was difficult. In an effort to mitigate the focusing issues, I also took two small scrapings, one from each of the capsule halves, and mounted them using carbon tape onto an SEM specimen stub. These were then coated with a 15 nm gold layer to reduce charging. The sample was quite brittle as the surface was coming away in flakes and was unable to be polished. However, I was able to resolve sub-volumes of the sample on the micron-scale using the SEM (Fig. 4.34). This was sufficient to resolve pores between grains; the average grain size of the powdered sipernat was 7.5 μm prior to compaction, while the magnetite and hematite were <1 μm.

Using the SEM images to porosity calculation

The approach taken to analyse the porosity of the sample is by converting the SEM images into binary black and white, where black represents pore space and white represents solid material.

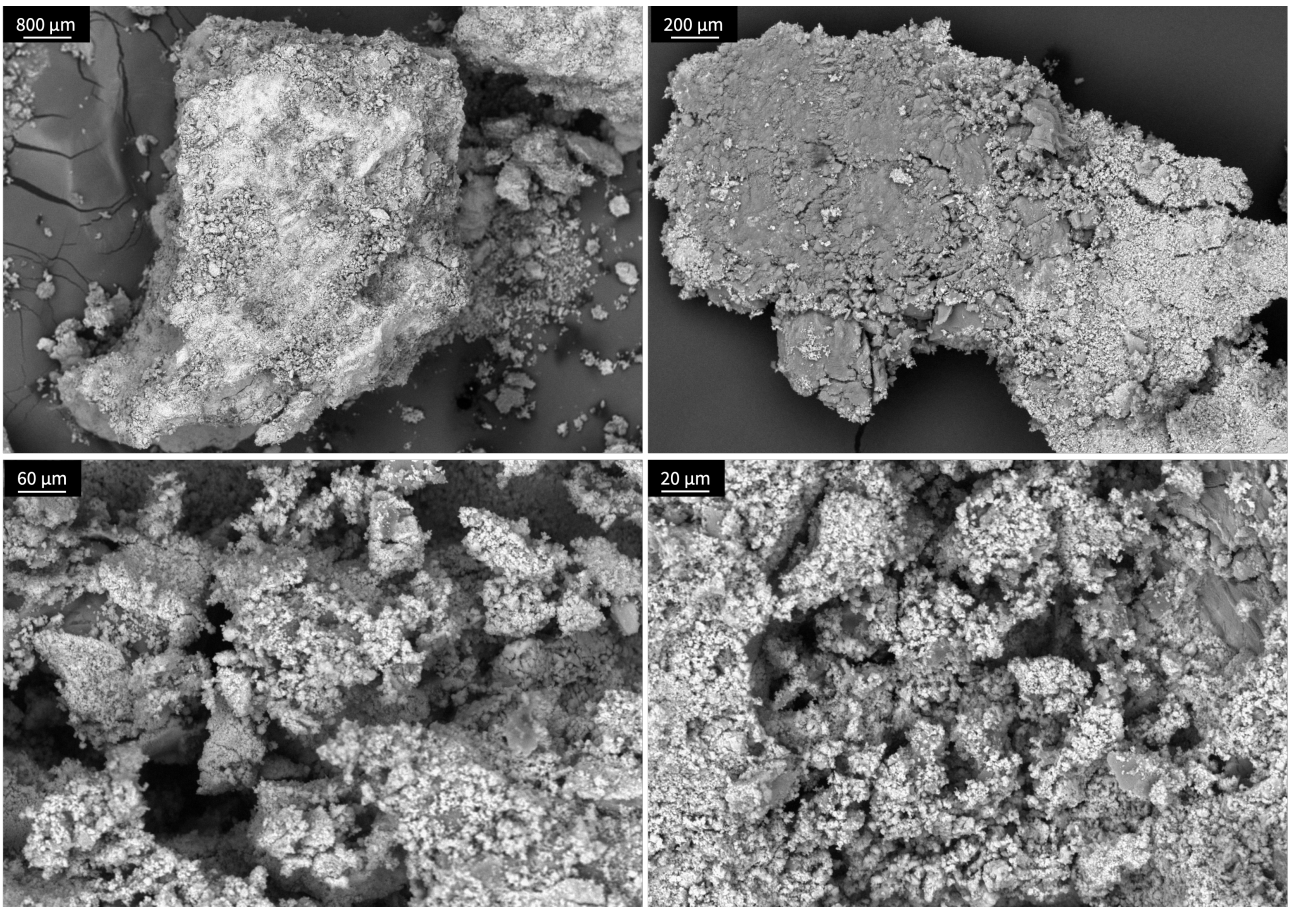


Figure 4.34: Four SEM images are presented from the synthetic chondrite produced during the impact experiment in the null magnetic field environment. These images were taken using the SEM from the top of two specimen stubs, created from two large flakes of the sample removed from the surface.

Determining the threshold at which a pixel was coloured black or white was challenging as sipernat was still present within some of the largest pores, but appeared to be dark, due to its depth within the sample. To analyse the pore space, I have investigated the images with the highest resolution, least distortion and greatest magnification that were able to taken.

As I have been unable to polish the samples and produce a thin section of the synthetic meteorite, the SEM images were not ideal for a porosity investigation. However, I have still attempted to analyse the pore space that is clearly visible in the images, though this is likely a significant source of error in the analysis and porosities derived from the SEM images can only be taken as an approximation.

Images returned from the SEM were 1920×2560 pixels, where pixel brightness is stored at integer values between 0 (black) and 255 (white). A suitable value to threshold the images was

chosen at one third of the maximum brightness, where this threshold was applied to the SEM images such that all pixels with a count of 85 and below were declared black (pore space), and pixels with a count above this were changed to white (Fig. 4.35). Using four SEM images of the synthetic meteorite section at slightly different spatial resolutions, between 3.07 μm^2 and 4.2 μm^2, the average porosity of the sample was found to be $\phi_{mf} \approx 25 \pm 3\%$. This porosity is comparable with the matrix porosity of CV3 chondrite Allende (25%), but slightly lower than the matrix porosity of CV3 chondrite Mokoia (30%) (Corrigan et al., 1997; Macke et al., 2011).

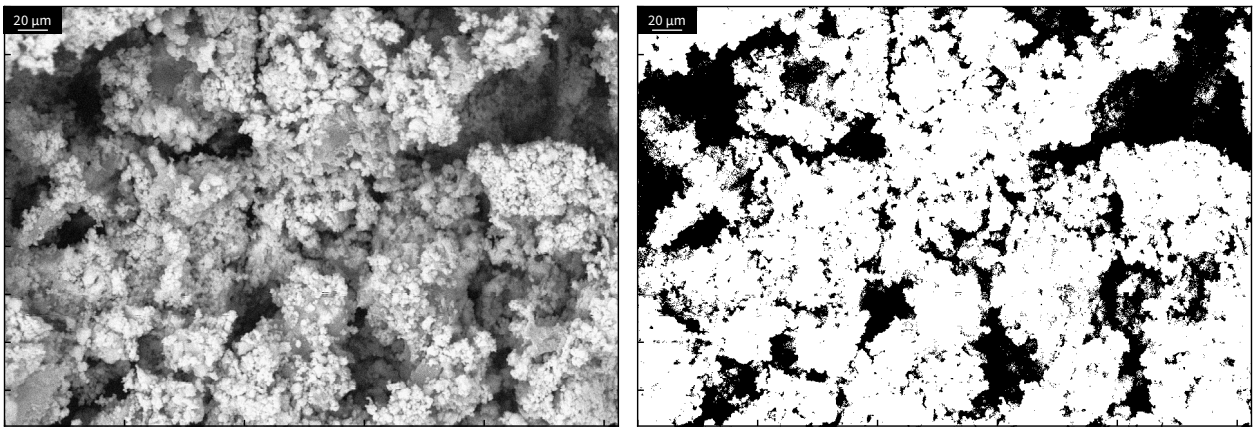


Figure 4.35: One of the four images used in the porosity calculation for the synthetic chondrite. Images were converted into binary black and white using a threshold value that was one third of the maximum pixel brightness to identify surface pore space, where black indicates pore space and white solid material. The matrix porosity calculated from this image ($\phi_{mf} = 28\%$) was the highest of the four SEM images.

4.7 Discussion

The magnetic analysis of the samples has demonstrated that the shock experiments have successfully imparted an NRM to the synthetic chondrite samples. The iSALE experimental modelling predicted peak temperatures around 390°C, consistent with the 375-410°C peak demagnetisation temperatures measured during the thermal demagnetisation of the samples. As the iSALE model has been found to be thermally consistent with the experimentally produced samples, it can be assumed that the bulk shock pressure (1.5 GPa) is also consistent between the model and the real samples.

4.7.1 Comparison of demagnetisation data to iSALE modelling

The unblocking spectra produced from thermal demagnetisation (Fig. 4.29) reveal peak temperatures recorded by magnetic carriers within the samples to be 375-410°C, which can be compared to the iSALE modelling results (Fig. 4.36). I have used iSALE to determine the temperature recorded by each of the $\sim$ 1200 tracers in the sample material (at 0.1 mm^2 resolution) and compared this to: (1) the peak temperature recovered from thermal demagnetisation, (2) the percentage of tracers heated between the minimum and peak temperature and (3) those heated above 535°C, the maximum temperature samples were able to be heated during thermal demagnetisation. The iSALE modelling predicted that $\sim$ 60% of tracers would be heated up to 375°C—the lowest peak temperature that was recovered from thermally demagnetising the synthetic chondrites (Fig. 4.36). The average temperature recorded by tracers, $T_{av} = 388 \pm 45$°C, was in good agreement with the average peak temperature recovered from the samples that were made in the 0, 100 and 150 μT shots (406°C, 386°C and 375°C, respectively), $T_{demag} = 389 \pm 13$°C. Around 40% of the simulation tracers experienced a peak temperature greater than 375°C, where $\sim$ 2% exceeded temperatures greater than were applied during experimental demagnetisation.

Using iSALE, the depletion in porosity of the sample during the impact can also be estimated. As well as tracking temperature and pressure, tracers inside the sample were set to record the distension, α, of the sample. As porosity (ϕ) in iSALE follows the $\epsilon - \alpha$ model ($\phi = 1 - 1/\alpha$), the minimum value of α during the simulation should reflect the porosity of the final sample. The sample was given an initial distension such that $\phi_{mi} = 70\%$ ($\alpha_0 = 3.33$). While the target porosity for the model was to be in agreement with the matrix porosities of recovered chondrites, the minimum distension recorded during the simulation was relatively high, $\alpha_{min} = 2.6$ ($\phi_{mf} \sim 60\%$). This is substantially larger than the porosity estimate of the manufactured sample (Fig. 4.35), inconsistent with real chondrites ($\phi_{mf} < 41\%$; Macke et al., 2011), and does not match the expected compaction from other numerical studies for a $\sim$ 1.5 GPa shock wave (Davison et al., 2016).

There are a number of possible causes for the discrepancy between the porosity calculated

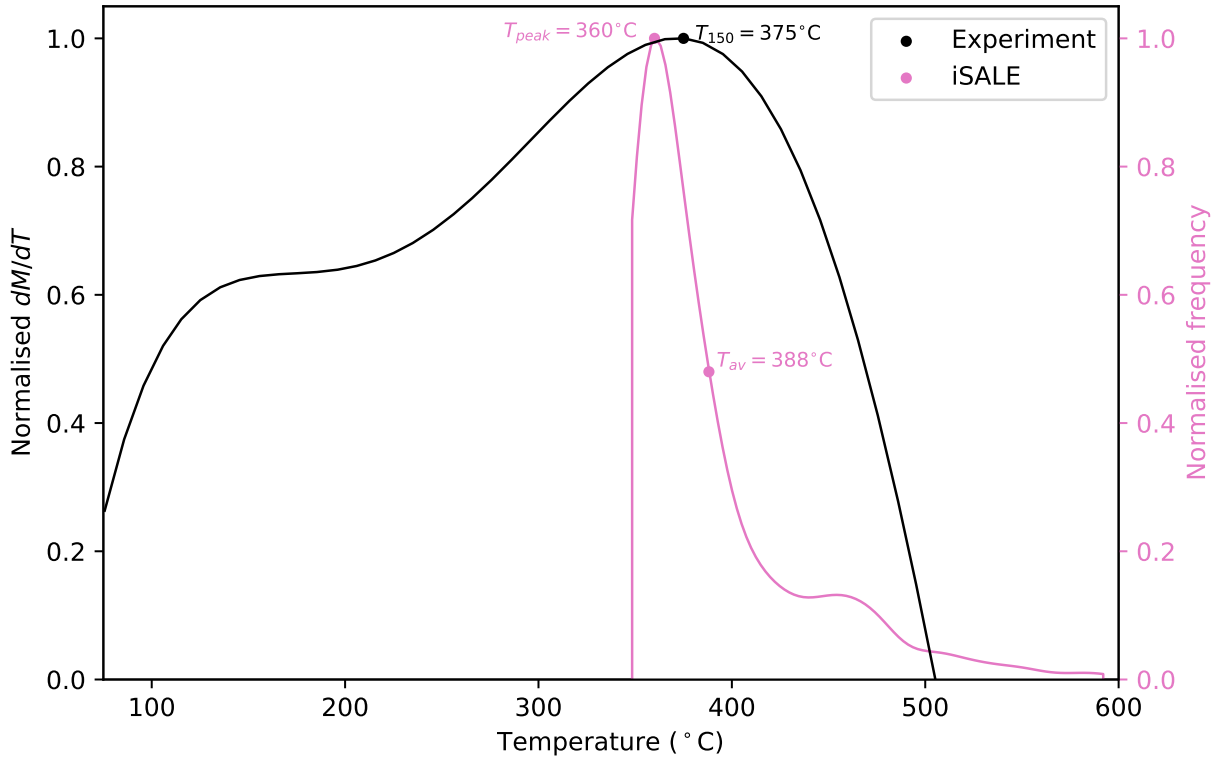


Figure 4.36: Demagnetisation data from the sample that was produced in the strongest field applied, 150 μT, compared to the iSALE estimate, plotted as a function of the frequency of tracers assigned to the bulk sample in the model. The minimum temperature reached by all tracers in the simulation was 349°C. Points drawn are the peak demagnetisation temperature for the 150 μT sample, $T_{150} = 375$°C, the average tracer temperature, $T_{av} = 388 \pm 45$°C and the value at which the majority of the tracers were heated to, $T_{peak} = 360$°C.

from the SEM images and the porosity derived from the iSALE distension measurement. The most significant factors are likely (1) the subjective choice of a pore-space threshold for the SEM images, (2) that the sample was modelled as a bulk material, when in reality it was a heterogeneous mixture of porous sipernat (90%vol) and non-porous magnetite and hematite (10%vol) and (3) only the macroscopic porosity is able to be determined in the SEM pictures. Future experiments using larger samples or with access to sophisticated polishing and microscopy techniques could likely accurately measure the pore space, addressing the error attributed to (1), while a thorough mesoscale model, similar to those by Davison et al. (2016) where grains within the sample mixture are explicitly resolved, may rectify the over-simplification made in (2). If the "grains" of sipernat themselves are porous, then there is an additional microscopic porosity which has not been accounted for in the SEM images.

However, the close agreement between the the temperatures recovered from the magnetic

results and those predicted by the numerical modelling, demonstrates that the material models used with iSALE capture the important bulk compaction behaviour for estimating the conditions experienced in laboratory impact experiments. Hence, the workflow presented here has demonstrated that iSALE simulations are able to act as a proxy for shock-recovery experiments where knowledge of the internal thermal evolution is important. In-situ thermal measurements during impact experiments are notoriously unreliable and difficult to obtain (e.g., Woodruff et al., 2022), often incurring high operating costs as well as a significant time investment in the experimental setup. Moreover, if future experiments using magnetic minerals are able to further demonstrate consistent results between iSALE modelling and laboratory experiments, this workflow could be adopted to make predictions about porosity depletion, damage and pressure heterogeneity that would otherwise not be possible using physical probes.

4.7.2 Relationship between the NRM and magnetising field

Up to $\sim 200 - 400$ μT, the relationship between the magnetising field and the recorded TRM is linear (Néel, 1949, 1955). I have measured whether this is true for the synthetic chondrites by plotting the NRM versus applied field intensity (Fig. 4.37).

The intensities loosely follow a linear trend ($R^2 = 0.74$), although the 100 μT and 150 μT do not cross the fit within error. It is difficult to draw conclusions from this graph with just four data points—future work at intermediate field strengths between those explored in this study would improve this. Furthermore, the NRMs also contain a contaminant component that was likely acquired during the machining process. Future studies should also improve the machining part of the process, namely to avoid re-heating the samples.

4.8 Shock classification of synthetic chondrites

An important result from this work is the inconsistency between the peak temperature of the samples and their shock classification if they were to be categorised. Based on traditional meteorite shock classification (Stöffler et al., 1991; Scott et al., 1992), the pressures reached in the

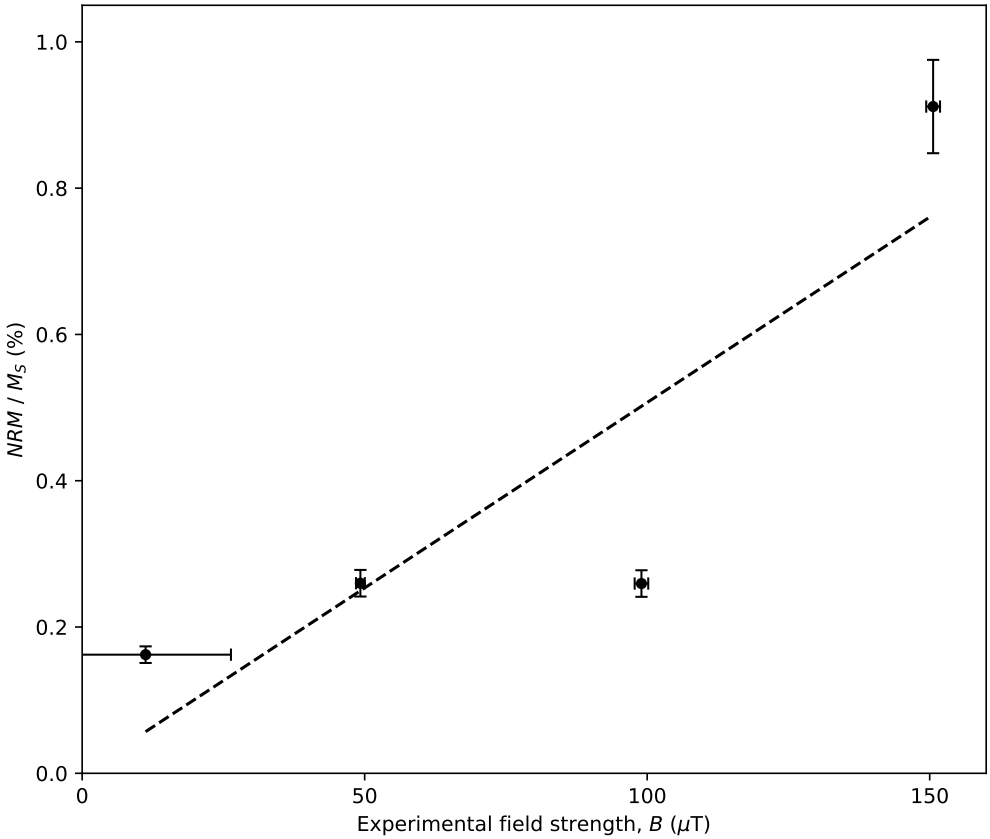


Figure 4.37: NRM at room temperature vs applied field intensity for each of the synthetic chondrites during the impact experiments. Errors derive from the (2σ) variability of the applied field across the chamber (Table 4.4, 4.5) and noise in the measurements of NRM and M_s.

synthetic chondrites classify them as **S1**, "unshocked", and suggest the meteorite experienced a maximum post-shock temperature increase between 10 - 20°C.

However, magnetic measurements of the synthetic chondrites have shown that peak temperatures up to 480°C were recorded by the magnetic carriers (Fig. 4.29). By the same classification system, this post-shock temperature increase would classify the samples between the upper limit of S4, "moderately shocked", and just below S5, "strongly shocked", indicative of bulk shock pressures in excess of 35 GPa (Stöffler et al., 1991). Microscopic textures of an S4- or S5-classified meteorite should display evidence of shock melting, which is not present in the micron-scale SEM images (Fig. 4.34).

The reason for the inconsistency between the shock classification and peak temperatures of these samples can be attributed to the compaction of porosity throughout the samples; the sample began with a very high initial bulk porosity ($\phi_{mi} \sim 70\%$) which was crushed out,

releasing heat locally within the sample. Target porosity is not accounted for in the traditional meteorite classification scheme.

Important differences between the thermal and mechanical response of porous and non-porous targets are well known, and have been specifically modelled for carbonaceous chondrites (Bland et al., 2014; Davison et al., 2016). Confirming the results from numerical modelling with the magnetic evidence obtained during this study highlights, again, a need for the reappraisal of the shock classification system for chondrites. This issue has already been realised for terrestrial sandstones (Kowitz et al., 2016). The traditional shock classification scheme for sandstone (Stöffler, 1984) was calibrated against nonporous quartz-feldspar, which failed to account for the shock melting observed in porous sandstones at low shock pressures, < 5 GPa (Kowitz et al., 2013). Additional experiments using synthetic (or real) chondrite material at different pressures could similarly be used to re-calibrate the chondrite shock classification system for different matrix porosities.

Alternatively, this work has shown the potential for the shock classification system to be calibrated numerically. When the pioneering work of Stöffler et al. (1991) was done, using tools such as iSALE to understand the in-situ shock response was not possible. However, in this study I have shown the advantages of modelling impact experiments and that the numerical results agree well with the experimental results, hence, iSALE could be used to perform such a shock calibration.

4.9 Implications for the chondrite parent body

Recent palaeomagnetic studies (O'Brien et al., 2020) suggest the magnetic fields recorded within chondritic meteorites originated from an external source, offering an alternative to the requirement for the parent body to have had an internally-generated dynamo. The most promising candidate for this external field are transient fields produced within the Solar nebula (Bland et al., 2014; Muxworthy et al., 2017). This is the scenario that has been tested in this study, where the heat released during low-velocity impacts could have rapdily recorded a magnetic field from within the nebula, removing the requirement for a long-lived static field on the parent

body which was instead acquired as either a viscous remanence or through cooling over millions of years (Weiss et al., 2010b).

This study confirms that low-velocity impacts on porous, synthetic chondrites, are capable of recording an impact-induced TRM. The remanence in the samples has been recorded during an impact where a shock wave heated the samples for a duration of <10 μs, then cooled in a background field for <10 minutes. These conditions are analogous to the proposed low-velocity impacts on the chondrite parent bodies as numerical modelling has shown impacts on similar targets, with ∼ 7 μs loading times and equilibration between 4-690 seconds, were able to lithify chondrites (Davison et al., 2016). Moreover, the depletion of porosity in the synthetic samples is consistent with a highly-porous chondritic precursor material undergoing densification during low-velocity impacts (Bland et al., 2014; Davison et al., 2016), supporting evidence that accretion was a relatively gentle process (Cuzzi et al., 2008).

4.10 Conclusions

Over the last 30 years, the shock classification of chondrites has been based on the traditional scheme (Stöffler et al., 1991; Scott et al., 1992), which predicts very low post-shock temperatures for primitive undifferentiated S1 chondrites. These low temperatures have led to impacts being dismissed as a potential magnetising mechanism in these meteorites, instead, palaeomagnetic studies have favoured long-lived internally-generated planetesimal dynamos (Elkins-Tanton et al., 2011; Weiss and Elkins-Tanton, 2013). However, recent work has suggested that the thermoremanence in chondrites was recorded during low-velocity impacts as magnetic carriers were heated, capturing a brief 'snapshot' of a transient nebula field (Bland et al., 2014; Muxworthy et al., 2017). In this study, I have demonstrated experimentally for the first time highly-porous synthetic chondrite material is capable of recording a TRM during a brief (< 10 μs), relatively gentle (< 2 GPa) impact, at temperatures similar to those measured in recovered chondrites (< 500°C).

During the impact experiments, a magnetic field with a strength between 0-150 μT was applied to the target—a synthetic silica-magnetite-hematite mixture, analogous to chondrite

precursor material. Samples were shocked and then remained in the field for a number of minutes before being recovered and stored inside a magnetically shielded box. All samples recorded a measurable TRM which increased in intensity from $\sim 3 - 14 \times 10^{-6}$ Am^2 with increasing field strength. Using an SEM, the porosity of one of the samples was analysed and found to be $\phi_{mf} \sim 25\%$, which is consistent with recovered CV3 chondrites such as Allende and Mokoia (Corrigan et al., 1997; Macke et al., 2011).

The high temperatures that were required to record the magnetic field arose from the crushing out of pore space in the samples. Although the depletion of porosity is known to raise temperatures in other rocks (e.g., Kowitz et al., 2016) and has been shown to do the same in meteorites by numerical models (Davison et al., 2016), this is yet to be realised when considering the shock classification of chondrites and other meteorites. The results in this study highlight the need to revisit the traditional shock classification of chondrites (Stöffler et al., 1991; Scott et al., 1992) to account for the effect of porosity on the peak temperatures experienced during an impact.

Impact experiments were designed using the shock physics code iSALE as a tool for predictive modelling. The iSALE models predicted an average peak temperature across all tracers of 388°C, in good agreement with the 389±13°C peak temperatures inferred from thermal demagnetisation of the synthetic chondrite material. The close agreement between the experimental and numerical results demonstrates that the material models used in the iSALE simulations are able to reliably predict the thermodynamic experience of laboratory-scale impact experiments. This workflow, where shock-recovery experiments designed to replicate specific thermal conditions are able to be planned with great accuracy, also presents a new opportunity for experiments to recover otherwise unavailable diagnostic measurements - such as material damage, internal shock pressure and temperature variation.

Finally, the successful recording of a TRM in a brief (<10 μs) impact means that there is no longer a requirement for the magnetic field recorded in chondrite matrices to have been a long-lived, static magnetic field. This conclusion is consistent with studies which suggest unstable fields in the Solar nebula (e.g., Muxworthy et al., 2017) could account for the palaeofield that has been recorded in chondrites.

Chapter 5

The Heterogeneous Response of a Martian Meteorite to Planar Shock

This chapter is a copy of my peer-reviewed paper, "The Heterogeneous Response of Martian Meteorite Allan Hills 84001 to Planar Shock" (North et al., 2023), and is written using American-English grammar. This article was accepted in October 2022 by Icarus, a journal devoted to the field of Solar System studies. The article is open-access and I have the rights to reproduce the work for the purpose of this thesis. The published study can be found here: `https://doi.org/10.1016/j.icarus.2022.115322`

5.1 Introduction

Intense shock waves generated by impacts on planetary surfaces are understood to be significant drivers of metamorphic and environmental evolution on a planet-wide scale. Impacts on Earth have led to mass extinctions and the beginning of ice ages (Schulte et al., 2010; Schmitz et al., 2019). While terrestrial impact sites are typically characterized following an investigation into the subsurface structure of a crater site, impacts on other planets can be characterised from either Earth-based observation or inspection of physical samples that have been collected in the form of meteorites. Meteorites in particular store a unique record of the surface and interior evolution of planetary bodies.

Martian meteorite Allan Hills 84001 (ALH 84001) was recovered from Antarctica in 1984 and became a highly prominent sample following the discovery of what was argued to be biogenic magnetite (McKay et al., 1996; Thomas-Keprta et al., 2000, 2001). While subsequent studies suggested an abiotic origin more likely for all minerals present in the meteorite (Brearley, 2003; Golden et al., 2004; Fortin and Langley, 2005; Steele et al., 2007), ALH 84001 remains of great interest as it hosts a unique record of the evolution of Mars, providing a window to further our understanding of the metamorphic, petrologic and paleomagnetic history of the planet (Kirschvink et al., 1997; Treiman, 1998; Hartmann and Neukum, 2001).

ALH 84001 is an orthopyroxenite meteorite containing coarse-grained inclusions of chromite, carbonates and plagioclase (feldspathic glass and maskelynite) and submicron crystals of iron oxides and sulfides, predominantly magnetite and pyrrhotite (Mittlefehldt, 1994). The parent rock is understood to be compositionally similar to the shergottite meteorites and derived from a basaltic magma that settled on or near to the Martian surface with an igneous age around 4.1 Ga (Lapen et al., 2010). Recovered sections of the meteorite exhibit a number of shock-induced textures, characteristic of multiple generations of impact events during its time buried on Mars (Treiman, 1998, 2021; Fritz et al., 2005a).

The meteorite is cut by narrow bands of granular orthopyroxene and chromite, with disaggregated chromite grains in close proximity, suggesting an early impact capable of intense and complex material shear (Treiman, 1995). The equigranular texture of these bands was likely established in an extensive thermal event caused by this impact. We refer to this deformation event as D1, keeping the convention established by Treiman (1998). These granular bands predate the deposition of carbonate material in the meteorite (Borg et al., 1999) and have an Rb-Sr age of approximately 4.0 Ga (Borg et al., 1999; Beard et al., 2013). A second, subsequent impact has been identified primarily by broken and fractured carbonate globules present in the rock (Mittlefehldt, 1994). Following the same convention, this is the D2 event. The fracturing of carbonates within the rock means D2 must post-date carbonate deposition within the meteorite. Further evidence includes the presence of silica, orthopyroxene and plagioclase glasses (Barber and Scott, 2006) and the formation of submicron magnetite by the decomposition of iron-rich carbonates (Treiman and Essene, 2011). Peak temperatures must have been capable

of melting plagioclase into glass, although a shock pressure for the event is unknown.

Historically, the strength of these impacts has been determined by comparison to experimental data from terrestrial analogs that produce similar shock-textures or temperatures (Lambert and Grieve, 1984; Fritz et al., 2005b). However, when compared to terrestrial samples, the relationship between pressure and temperature has been shown to be very different on the sub-millimeter scale due to differences in both the mineral properties and the porosities of meteorites (Davison et al., 2017).

Paleomagnetic investigations of ALH 84001 have posited a long-lived (3.9-4.1 Gyr) natural remanent magnetization (NRM) that is heterogeneously oriented on the millimeter-scale and predominantly hosted in pyrrhotite present in carbonates and chromite-sulfide assemblages (Kirschvink et al., 1997; Antretter and Fuller, 2002; Antretter et al., 2003; Weiss et al., 2000, 2002, 2004, 2008b; Steele et al., 2022). Below 40°C, there is remanent magnetization acquired either during ejection (Weiss et al., 2002) or terrestrially in Antarctica (Antretter et al., 2003). These observations support the hypothesis that the bulk meteorite has remained cold since it acquired its NRM, and that ALH 84001 experienced relatively low temperatures and pressures during its ejection (Weiss et al., 2000).

Heterogeneously oriented magnetizations, coupled with localized, intense and short-lived peak temperatures, point towards an unknown process able to produce strong thermal gradients on the grain-scale following an impact event. In this study we determine the thermodynamic response of a body like ALH 84001 to shock on the sub-millimeter scale. We present a suite of simulations of impacts on ALH 84001 using the iSALE-2D shock physics code (Collins et al., 2004; Wünnemann et al., 2006) to reconcile the independently reported shock and thermal histories of the meteorite, as well as offer insight into the feasibility of the heterogeneous impact remagnetization hypothesis (Weiss et al., 2008b; Steele et al., 2022).

5.2 Methods

To simulate the response of a meteorite sample such as ALH 84001 to impact, we designed a mesoscale numerical experiment that exposes the sample to a simplified shock loading process

approximating that produced by an impact. In reality, impact-induced shock loading of a sample is complex and will depend on many factors, such as the size and speed of the impactor, the distance of the sample from the impact site and the nature of the target between the impact site and the sample. These factors affect the peak amplitude of the shock pulse, the duration (or dwell time) of the shock as well as the loading pattern. For a homogeneous target, the loading pattern may be a simple, almost planar shock pulse with a short rise time, but for a heterogeneous target with porosity, fractures and lithological changes, the loading pattern may be complex and involve a long rise time and/or several shock reverberations, with multiple directions.

For practical reasons, here we consider only a simple loading pattern of a quasi-planar shock wave with a relatively short (microseconds) duration. From high-resolution images of a thin section of ALH 84001, we constructed a synthetic approximation of the meteorite using its four major constituents. Appropriate material models for each component were selected. We then simulated the passage of quasi-planar shock waves of a range of different shock pressures (3-67 GPa) through this synthetic meteorite sample using the iSALE2D shock physics code (Collins et al., 2004; Wünnemann et al., 2006). We recorded the mesoscale thermodynamic and mechanical response of the synthetic meteorite sample to the shock loading and then modeled subsequent thermal equilibration by conduction. In the following sections we describe each of the steps in our procedure and the codes used.

5.2.1 The iSALE-2D Shock Physics Code

An extension of the SALE hydrocode (Amsden et al., 1980), iSALE-2D is a multi-material, multi-rheology shock physics code (Collins et al., 2004; Wünnemann et al., 2006), benchmarked against other shock codes (Pierazzo et al., 2008) and validated against laboratory impact experiments (e.g. Pierazzo et al., 2008; Davison et al., 2011). Originally developed to study large-scale cratering, iSALE has recently been modified to examine the heterogeneous physical response of meteoritic materials to planar shock waves at the length scale of internal heterogeneities (Güldemeister et al., 2013; Davison et al., 2016; Derrick et al., 2019; Moreau et al., 2019). Such simulations are referred to as ‘mesoscale’ as they reveal phenomena present on an intermediate

scale between the micro or atomic scale and the macro or bulk scale (e.g. Nesterenko, 2001; Borg and Vogler, 2008). Past meteorite studies have defined the mesoscale as fully resolving a chondrule, $\sim 10\mu$m (e.g. Bland et al., 2014; Moreau et al., 2019). In this study, we maintain the same order of magnitude as previous models and define the mesoscale as the resolution required to observe physical changes in the coarse inclusions within our samples (10-100 μm).

5.2.2 ALH 84001 as a Four Material System

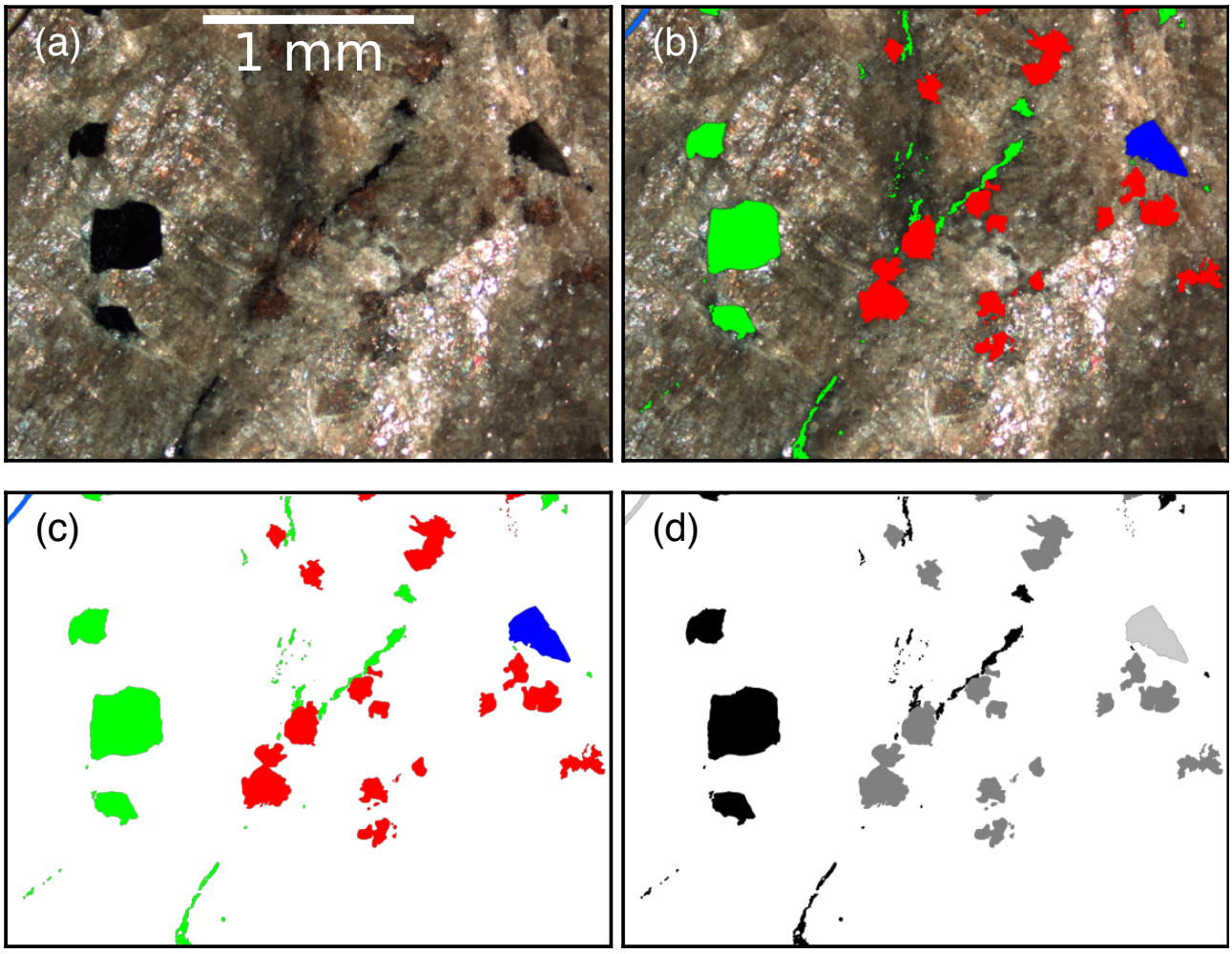


Figure 5.1: Sample selection for one of the meteorite cross-sections. The original 6.4 mm^2 image is presented with a scalebar (a). The following three images demonstrate the identification of inclusions (b), the reduction to an RGB colormap (c; red: calcite; green: chromite; blue: gabbro; white: dunite) and finally the conversion to a grayscale image ready for use with iSALE-2D (d).

Materials were selected on the basis of abundance and importance to our investigation. The criteria in our selection process aimed to replicate the natural heterogeneity of the system, while eliminating the rarest and smallest inclusions that would be difficult to adequately resolve

($<<$ 10 μm). An example of how the synthetic sample was constructed from the meteorite thin-section is shown in Figure 5.1. Consistent with our criteria, the mineralogy has been divided into four constituents: chromite (including iron oxides and sulfides), carbonate (coarse inclusions dominated by calcium carbonates), plagioclase (including maskelynite) and finally orthopyroxene, the bulk material.

5.2.3 Equations of State

Each of the constituent materials of ALH 84001 were described using the most appropriate material model available. In iSALE, the material model is defined by an Equation of State (EoS), which describes the response of a material to a change in volume, and a strength model, which describes the resistance of a material to changes in shape. The availability of accurate material models describing meteoritic components is limited. Therefore, we represented three of the four component materials with an equation of state using the closest analog material possible and strength model parameters representative of the material in question. For the fourth component material, chromite, we developed a new Tillotson EoS (Tillotson, 1962) for this study.

The EoS for chromite, $FeCr_2O_4$, represents the coarse chromite grains as well as the mixture of iron oxides and sulfides throughout the meteorite. As there is insufficient experimental shock data in the literature for chromite, the Tillotson parameters (a, b, α, β, B) were calculated by fitting to shock data for magnetite, Fe_3O_4, which is the predominant iron oxide found in the chromite inclusions (van Thiel et al., 1977; Marsh, 1980). The remaining Tillotson parameters and material constants (A, bulk modulus; E_0, E_{IV}, E_{C_V}, initial, incipient and complete vaporization energies, respectively; ρ_0, reference density; C_V, specific heat capacity) were chosen using available data for chromite (Klemme et al., 2000; Liu et al., 2016). Plagioclase was also described using a Tillotson EoS, with strength and material parameters fit to gabbroic anorthosite (O'Keefe and Ahrens, 1982). The Tillotson parameters used in this study for gabbroic anorthosite (gabbro hereafter) and chromite are summarized in Table 5.1.

Behavior of the carbonate and orthopyroxene were described using analytical equation of

Table 5.1: Tillotson parameters for the materials gabbroic anorthosite (O'Keefe and Ahrens, 1982) and chromite (developed for this study) which have been described using the Tillotson Equation of State.

Parameter	Gabbro	Chromite
a	0.50	0.50
b	1.45	0.47
α	5.00	5.00
β	5.00	5.00
A (Pa)	$7.10\text{x}10^{10}$	$1.80\text{x}10^{11}$
B (Pa)	$7.50\text{x}10^{10}$	$1.78\text{x}10^{11}$
E_0 (J/kg)	$4.87\text{x}10^{6}$	$1.20\text{x}10^{7}$
E_{IV} (J/kg)	$4.72\text{x}10^{6}$	$3.00\text{x}10^{6}$
E_{CV} (J/kg)	$1.82\text{x}10^{7}$	$1.60\text{x}10^{7}$

state (ANEOS)-derived tables for calcite (Pierazzo et al., 1998) and dunite (Benz et al., 1989), respectively. It is important to note that these are physical proxies and not chemical ones. Dunite, which is largely olivine ($> 90\%$), has been used in place of an orthopyroxene because its EoS provides a better match to shock wave data for pyroxenite than an alternative, simplified EoS (Moreau et al., 2019).

5.2.4 Strength Models

A pressure-, temperature- and strain-dependent strength model for geological materials (Ivanov et al., 1997; Collins et al., 2004) was used to describe the resistance of the carbonate, gabbro and dunite to shear deformation, while a constant-strength ductile model appropriate for metallic materials was used to describe the shear strength of chromite.

As ALH 84001 is understood to have suffered multiple impacts, the bulk rock material may have been damaged by impacts prior to the one(s) that produced the observed shock textures in the meteorite. In most of our simulations, we have assumed the dunite is intact, with its strength parameters fit to data for Horoman dunite (Shimada et al., 1983). However, to account for the possibility that the bulk material may have been weakened by previous impacts, our results also consider a second set of strength parameters that were determined by fitting the intact strength model envelope to strength data from a weaker Norwegian dunite, closer to peridotite (Murrell and Chakravarty, 1973; Ismail and Murrell, 1990). The fit to these models

is displayed in Fig. 5.2; the coefficients are summarized in Table 5.2.

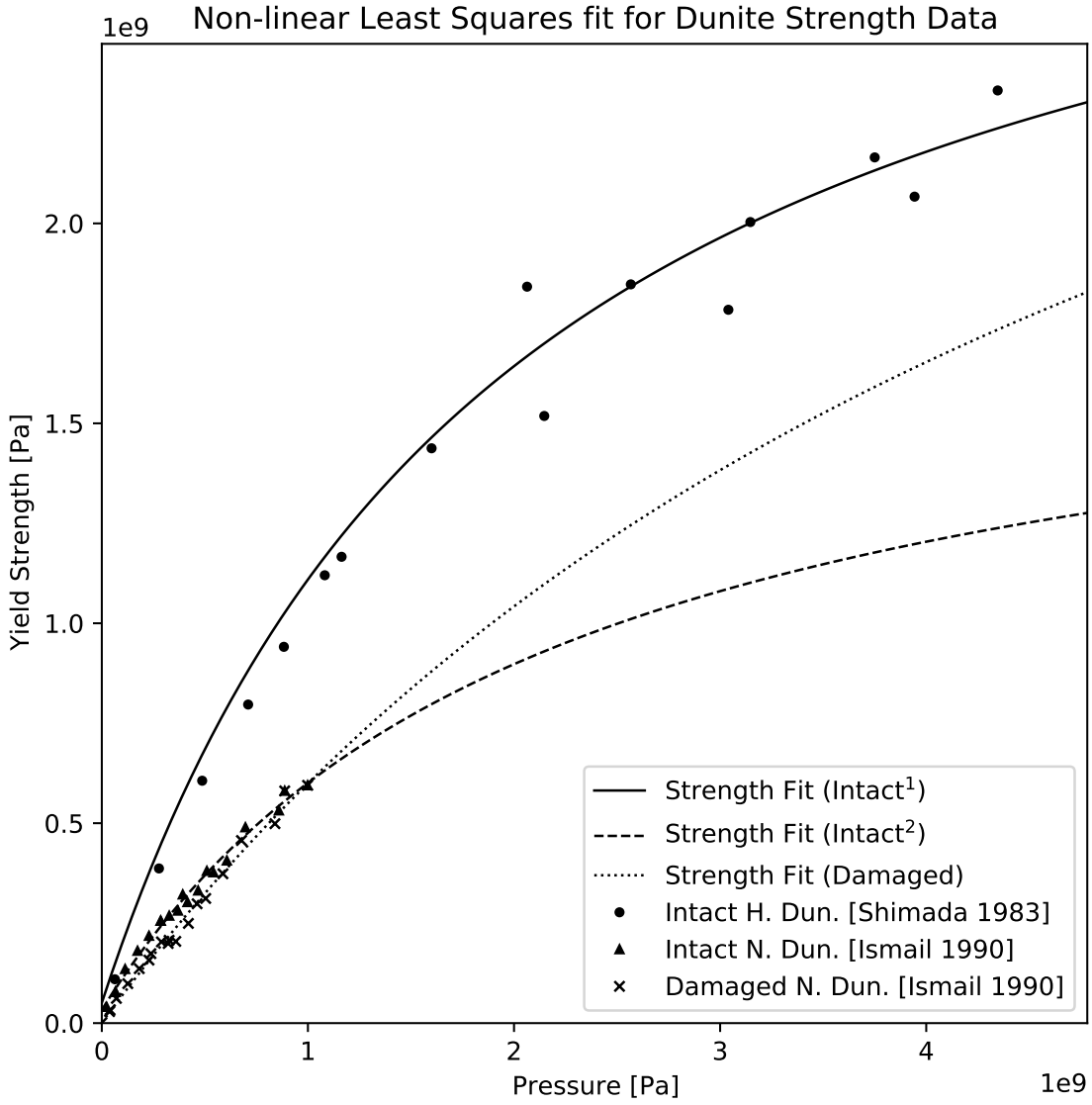


Figure 5.2: Strength models calculated from two different dunite datasets. Shown are strength models for intact Horoman dunite that we have used in the majority of our simulations (Intact^1) (Shimada et al., 1983), alongside a weaker strength model (Intact^2) produced from shock data on Norwegian dunite (Ismail and Murrell, 1990). In addition, we include the strength model for damaged dunite which is common to both the intact models. The coefficients for the intact models are listed in Table 5.2.

Table 5.2: Parameters for the strength models we have fit to intact Horoman dunite (Shimada et al., 1983) and intact Norwegian dunite (Ismail and Murrell, 1990). μ_i is the coefficient of friction for intact rock while Y_{i0} and Y_{im} are material strength parameters. We have based the parameters for Horoman dunite on those used by Potter et al. (2012).

Parameter	H. Dun.	N. Dun.
μ_i	1.58	0.83
Y_{i0} (MPa)	50.7	33.3
Y_{im} (GPa)	3.26	1.85

5.2.5 Simulation Design

We examined the response of two cross-sections of ALH 84001 (S1 and S2 hereafter) to a planar impact using iSALE-2D. We consider the two cross-sections of ALH 84001 to be approximately representative of the bulk meteorite. The simulation mesh was generated from high-resolution images of the meteorite cross-sections where the pixels of each image became the cells of the mesh. The size of the meteorite cross-sections, which measured 2.93 mm x 2.20 mm for S1 and 4.04 mm x 3.33 mm for S2, were maintained using a mesh resolution (cell area) of $20\mu m^2$. This resolution meant we recorded an average of 75 cells per particle radius (CPPR) as measured in calcite.

To generate a quasi-planar shock wave in the simulated mesh produced from the meteorite cross-sections, impact experiments were performed where we collided an impactor with an initially stationary target, comprised of a sample plate sandwiched between a cover plate adjacent to the impactor and buffer plate (Davison et al., 2016). All four plates were made from identical material as a simple mechanism to mitigate unwanted reflections between plate boundaries. Moving with a given velocity, the impactor plate collided with the cover plate, producing a shock that traveled through it and into the sample (Figure 5.3). The cover plate allowed the shock wave to reach a steady state before reaching the sample region. The shock then passed through the sample and into a buffer plate. Meanwhile, a release wave formed as the shock wave in the impactor plate reflected off the rear of the impactor. The release wave then passed back through the impactor, cover and sample plates. The simulation was allowed to run until the release wave had propagated all the way through the sample and it was released from its shocked state.

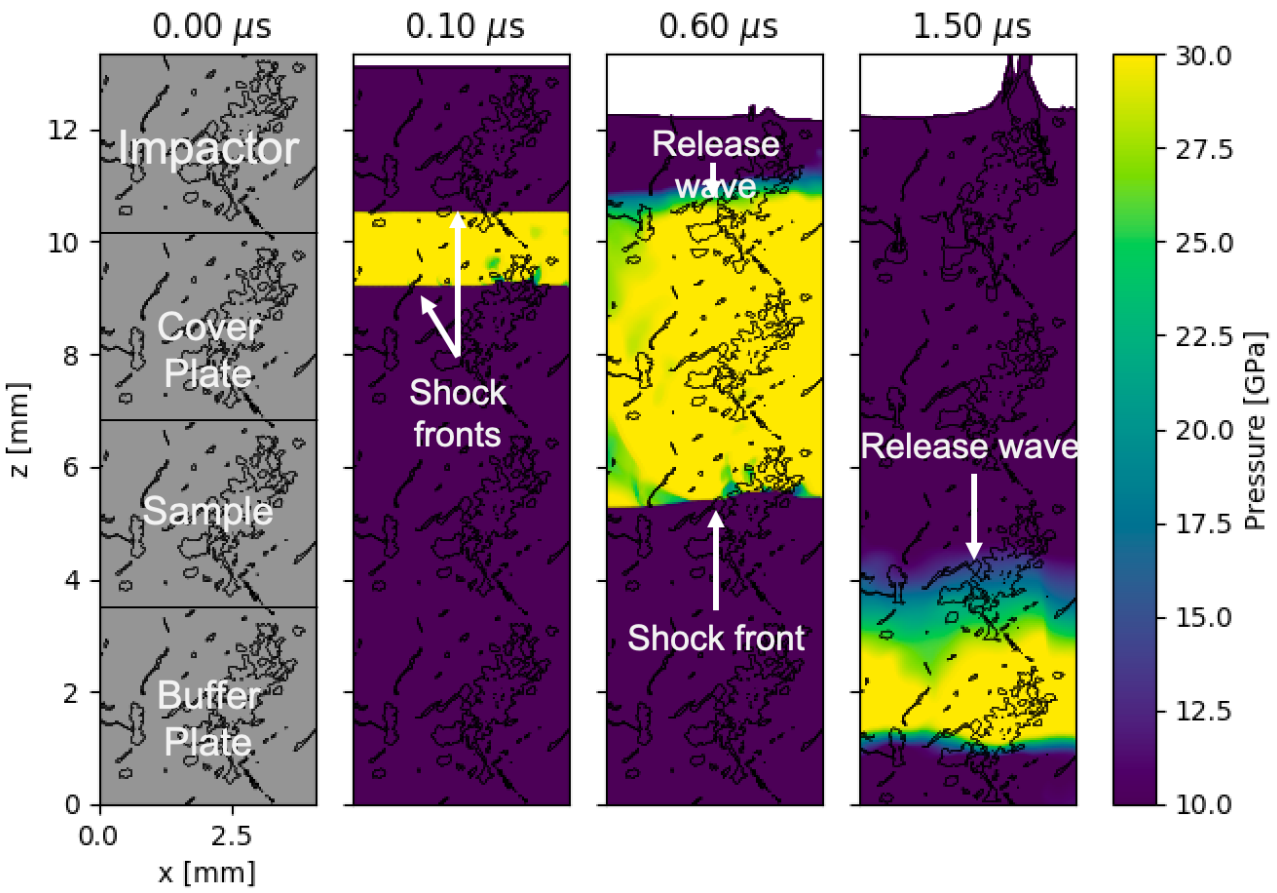


Figure 5.3: The impact "sandwich" model shown for the larger S2 cross-section. In this simulation, the impactor, cover, sample and buffer plates are all identical. The impactor is given an initial velocity in the $-z$ direction causing a collision to occur at the impactor-cover plate boundary. This collision generates two shock waves - one in the cover plate traveling in the $-z$ direction causing the initial shock loading, and a second in the impactor plate traveling in the $+z$ direction. Once the shock wave reaches the top of the impactor, it reflects off the top of the impactor plate and travels in the $-z$ direction towards the sample, releasing material from a shocked state as it passes through.

5.2.6 Lagrangian Tracers

Response of the sample to the planar shock was measured using Lagrangian tracers placed in each computational cell of the mesh. Tracers were moved through the Eulerian computational grid according to material volume fluxes using the algorithm described in Davison et al. (2016) to ensure that they record information specific to the material they were initially assigned to. These tracers allowed us to record the thermodynamic and mechanical experience of the materials during the simulation, as well as to perform statistical analyses on a per-material basis from the model.

5.2.7 Shock Wave Amplitude

The amplitude (bulk pressure) of the shock was controlled by the velocity of the impactor. As dunite was the dominant material component, we were able to estimate the impact speed necessary for a given shock pressure using the relationship between the particle velocity and shock velocity in dunite. For the simulations presented in this work, we have impact velocities that range from 300 ms^{-1} to 4700 ms^{-1} which correspond to bulk pressures generated in the sample between 3 GPa and 67 GPa. Within this range, we have included simulations at significant thresholds for ALH 84001 such as at 15 GPa, the pressure estimate for an ejection event from Mars that would preserve the 40°C 'cold' component of the remanence within the meteorite (DeCarli et al., 2007; Weiss et al., 2000), 33 GPa, the estimate bulk pressure experience of ALH 84001 from Fritz et al. (2005a) and 55 GPa, the maximum upper limit of the shock pressure reached during ejection as measured in Martian meteorite ALH77005 (Fritz et al., 2005a).

5.2.8 Temperature Nomenclature

In this study we refer to three distinct temperature measurements. The first is the maximum peak temperature. Peak temperature is the highest temperature experienced during passage of the shock wave, which can vary between materials and within grains of the same material. The maximum peak temperatures quoted in this study for a given material are the mean average of the hottest 1% of tracers in that material. The second important temperature is the average post-shock temperature. This is the average temperature recorded by tracers in a given material at the end of the iSALE-2D simulation, after the release wave has passed through the sample (approximately 1.1-1.2 μs after the beginning of the simulation in all cases). Finally, we define the "equilibrium temperature" of the meteorite as the temperature reached once the whole sample comes to thermal equilibrium. The peak and post-shock temperatures were calculated by iSALE-2D, while the equilibrium temperature was determined by a separate thermal equilibration calculation that accounted for cooling following an impact event.

5.2.9 Thermal Equilibrium

To calculate thermal equilibration of the sample we used a finite-difference approach to solve the 2D heat equation

$$\frac{\partial U}{\partial t} = D\left(\frac{\partial^2 U}{\partial x^2} + \frac{\partial^2 U}{\partial y^2}\right) \tag{5.1}$$

where D is the diffusion coefficient, x and y are the 2D Cartesian coordinates of the mesh cells, t is time and $U(x, y, t)$ is the temperature field, which is initialized with the average post-shock temperature as calculated from our iSALE-2D simulation. Each cell in the mesh was assigned a diffusivity coefficient. To reduce the computational expense when solving equation (5.1), we adjusted the spatial resolution of the mesh to be two times coarser than the mesh output from the iSALE simulation. The coarsening algorithm assigned an initial temperature and diffusivity to each cell in a manner that conserved the mass and total internal energy of the iSALE-2D cells that are being combined. In other words, the new, 'coarsened' cell, has a diffusivity and specific heat capacity comprised of a mass weighted-average of the four cells of the overlapping iSALE-2D mesh.

Equation 5.1 was solved using a simple forward-Euler integration in time. The maximum permissible timestep (Δt) without the equation becoming unstable is

$$\Delta t = \frac{1}{2D}\frac{(\Delta x \Delta y)^2}{(\Delta x)^2 + (\Delta y)^2} \tag{5.2}$$

The solution was allowed to run for a sufficient number of timesteps until the meteorite reached thermal equilibrium, defined as a change in thermal covariance across the sample of less than 0.1%. We treated the edges of the mesh using Neumann boundary conditions (zero temperature gradient normal to the boundary). Videos of the cooling process are included in the supplementary materials.

Thermochronology estimates of Martian paleotemperatures have shown ALH 84001 cannot have been at a constant long-term temperature greater than −60°C to −70°C since ∼4 Ga (Shuster and Weiss, 2005). More recent studies have refined this constraint to have an even

cooler upper limit of −63°C (Min and Reiners, 2007). For our thermal equilibrium estimates, we have assumed the 'warmest-case scenario', having chosen the initial temperature of ALH 84001 to be −60°C. In doing so, our estimates of equilibrium temperatures can be treated as conservative upper limits. As our iSALE-2D model was run using an initial temperature set to be the ANEOS reference temperature of 20°C, we adjust the temperature output of each simulation by subtracting 80°C at the start of the thermal equilibrium calculation.

5.3 Results

Across a number of different simulations, we varied impact velocities, meteorite composition, material strength and the orientation of the sample relative to the direction of the impact to investigate the length scale and heterogeneity of impact-induced thermal gradients within the meteorite. The results highlight the requirement for an appreciation of the mesoscale structure of meteorites which will, in turn, enable future studies to form more a complete understanding of their shock and thermal histories.

5.3.1 Reference Simulations

We first present two simulations, one for each of our cross-sections (S1 and S2), where the sample experienced an average 'bulk' shock pressure of 33 GPa (corresponding to a plate impact velocity of 2720 ms^{-1}) in both cases. This shock pressure falls in the center of our investigated range. We will refer to these as the reference simulations.

In the reference simulations, both samples displayed spatially heterogeneous peak pressures and heating in response to the passage of the planar shock wave (Fig. 5.4, Fig. 5.5). We observed small variation in the average shock pressure experienced in the minor material constituents, from a minimum of 32.5 GPa (gabbro, S1) to a maximum of 36 GPa (calcite, S2), but the overall bulk pressure (33 GPa) is controlled by the major constituent, dunite (Fig. 5.5). Peak pressure highs are generally associated with calcite and chromite regions which we have attributed to shock reverberations at material boundaries. However, the post-shock temperature varies

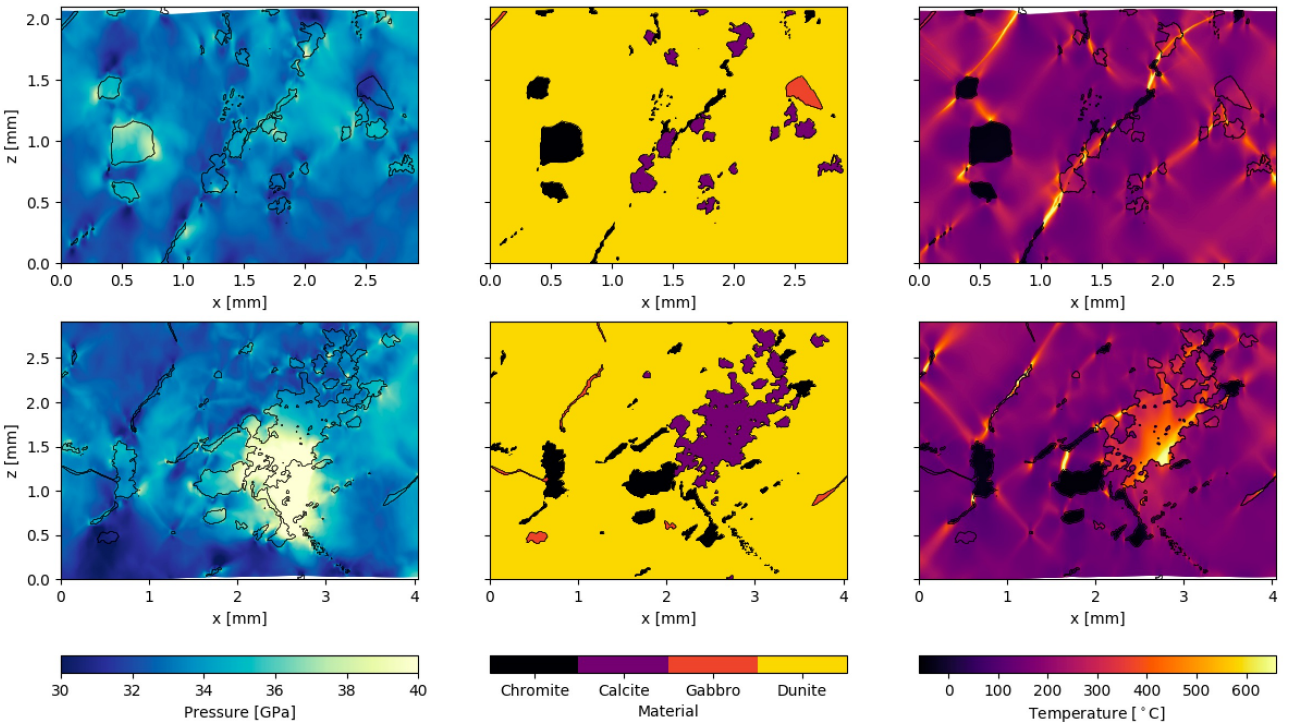


Figure 5.4: Peak pressure (left), material (center) and post-shock temperature (right) colormaps, plotted from data recorded by Lagrangian tracers present within each cell of the mesh of the models. The upper three panes display the response of cross-section S1, while the lower three panes are the larger S2. The sharp linear features in the temperature colormaps point to the locations where material shear occurs.

considerably between the constituents and we observe a wide distribution of temperatures within each material (Fig. 5.5). While the average post-shock temperature in both reference simulations was 170°C, the average post-shock temperature of each material varied from a minimum of −40°C in the chromite to 370°C in calcite.

Apart from chromite, we observe a broad distribution of temperatures around the median value. For example, while the response of the chromite is relatively consistent in both samples, the response of the calcite in S1 (Fig. 5.5) shows a broad range of post-shock temperatures. The median post-shock temperature is around 260°C, while some of the calcite reached ∼500°C and other regions remained below 0°C immediately following the impact. Calcite, which shows the greatest variability in temperature, exhibits no clear spatial pattern of heating. Some calcite regions are heated strongly, while others are hardly heated, particularly in S1 (Fig. 5.4). In dunite, on the other hand, there is clear pattern of heating, with narrow linear zones of strong heating separating regions of low to modest heating. Pressure fluctuations and reverberations caused by mesoscale heterogeneities and shear heating offer potential explanations

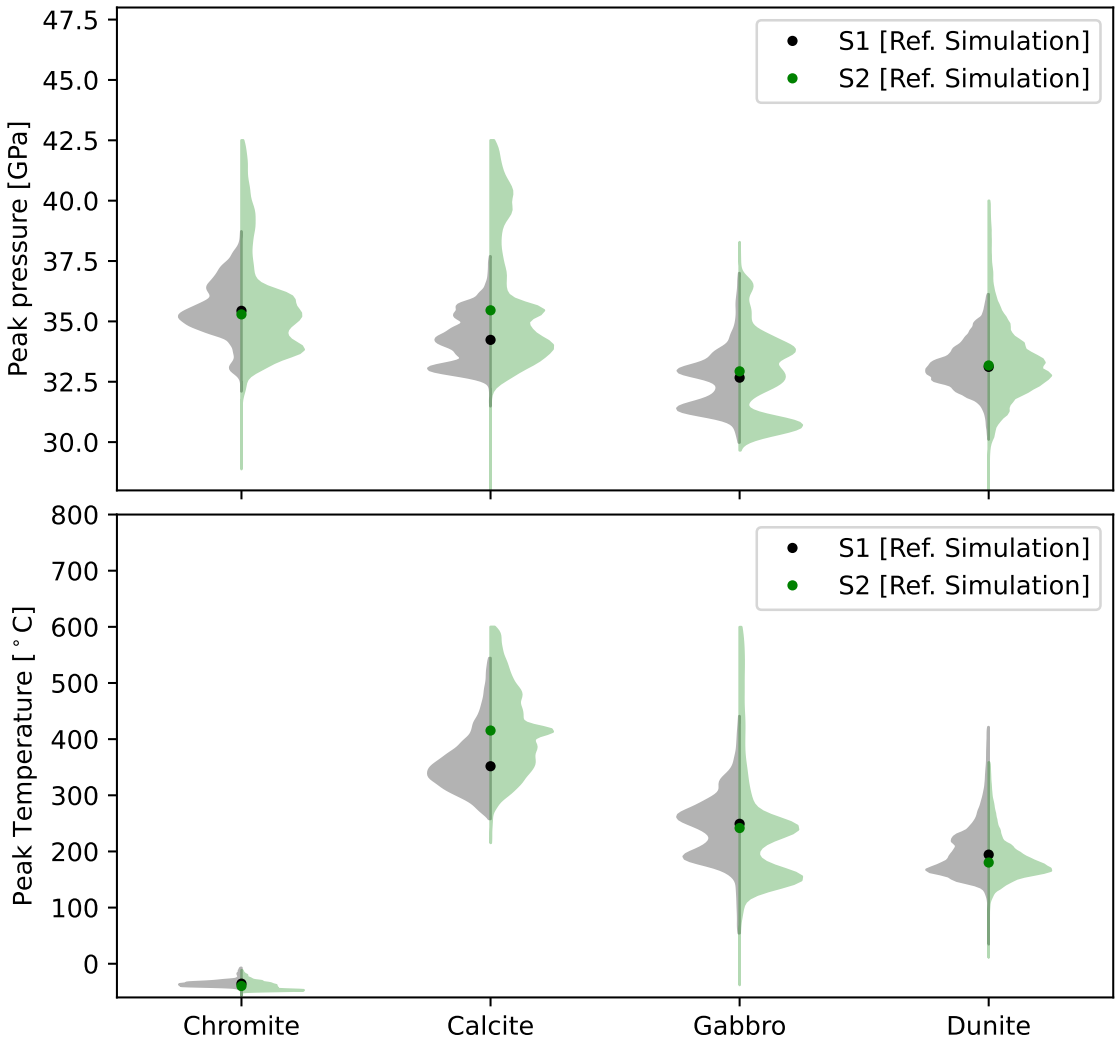


Figure 5.5: Peak pressure experienced (top) and post-shock temperature (bottom) distributions of tracers in each material in the reference (33 GPa) simulations for S1 and S2. The marker centered on each of the distributions is the median average of the data. The plots have been trimmed to display all tracers within three standard deviations of the mean.

for the observed spatial variation in heating.

5.3.2 Plastic Deformation and Shear Heating in ALH 84001

Impact-induced heating originates from the work done by both the isotropic compression (PdV work) and shear deformation (plastic work) of material. To visualize shear deformation, we

show a grid of the Lagrangian tracers over the sample images (Fig 5.6). Regions of the grid appear dislocated where shear has occurred and these dislocations clearly correlate with the most intensely heated areas of the sample. This suggests that shear heating represents an important contribution to impact-related heating of ALH 84001 within the orthopyroxene (dunite) component and possibly the carbonate (calcite) component.

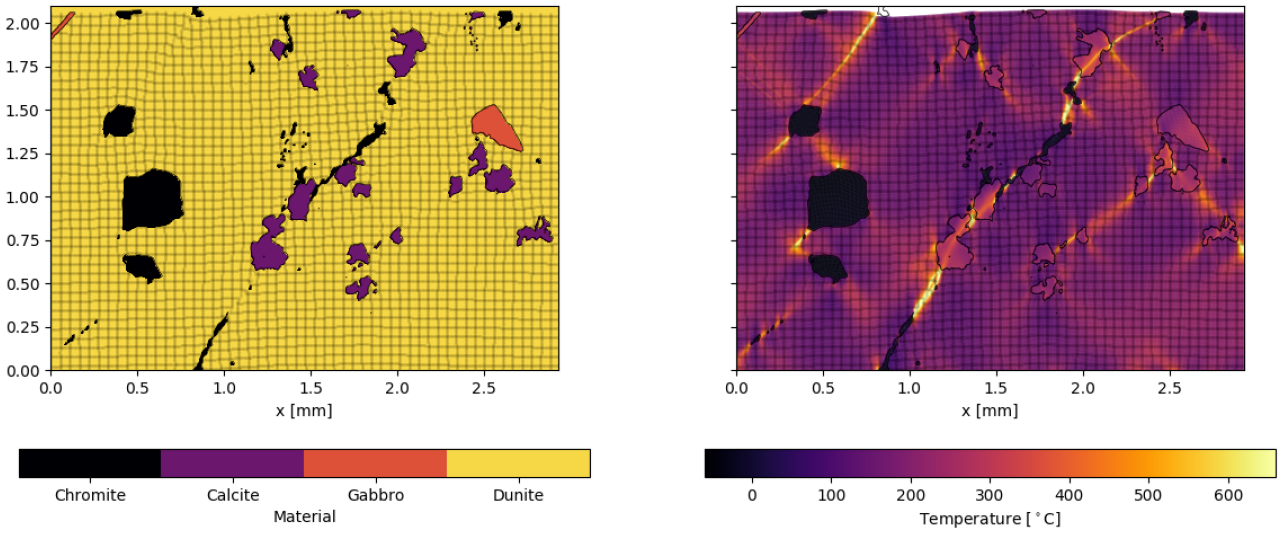


Figure 5.6: Colormaps produced from the S1 reference simulation using Lagrangian tracers to identify the material locations and post-shock temperature. Included is a grid of tracers; each cell in the grid represents approximately 360 tracers. Warping of the grid represents areas of shear deformation whereby sections of material have shifted apart.

5.3.3 Influence of Mesoscale Structure

The orientation of the meteorite sample with respect to the propagation direction of shock waves that engulfed it while on Mars is unknown. Moreover, the composition of the rock material immediately adjacent to the sample is unknown, and therefore the shape of the shock front as it enters the sample is also not known. To verify that our results are not dependent on sample orientation or architecture of our simulations (the mesoscale structure of the impactor and/or cover plate), we investigated the effects of rotating the angle of the incident shock, omitting materials from the sample as well as changing the mesoscale structure within the cover and buffer plates.

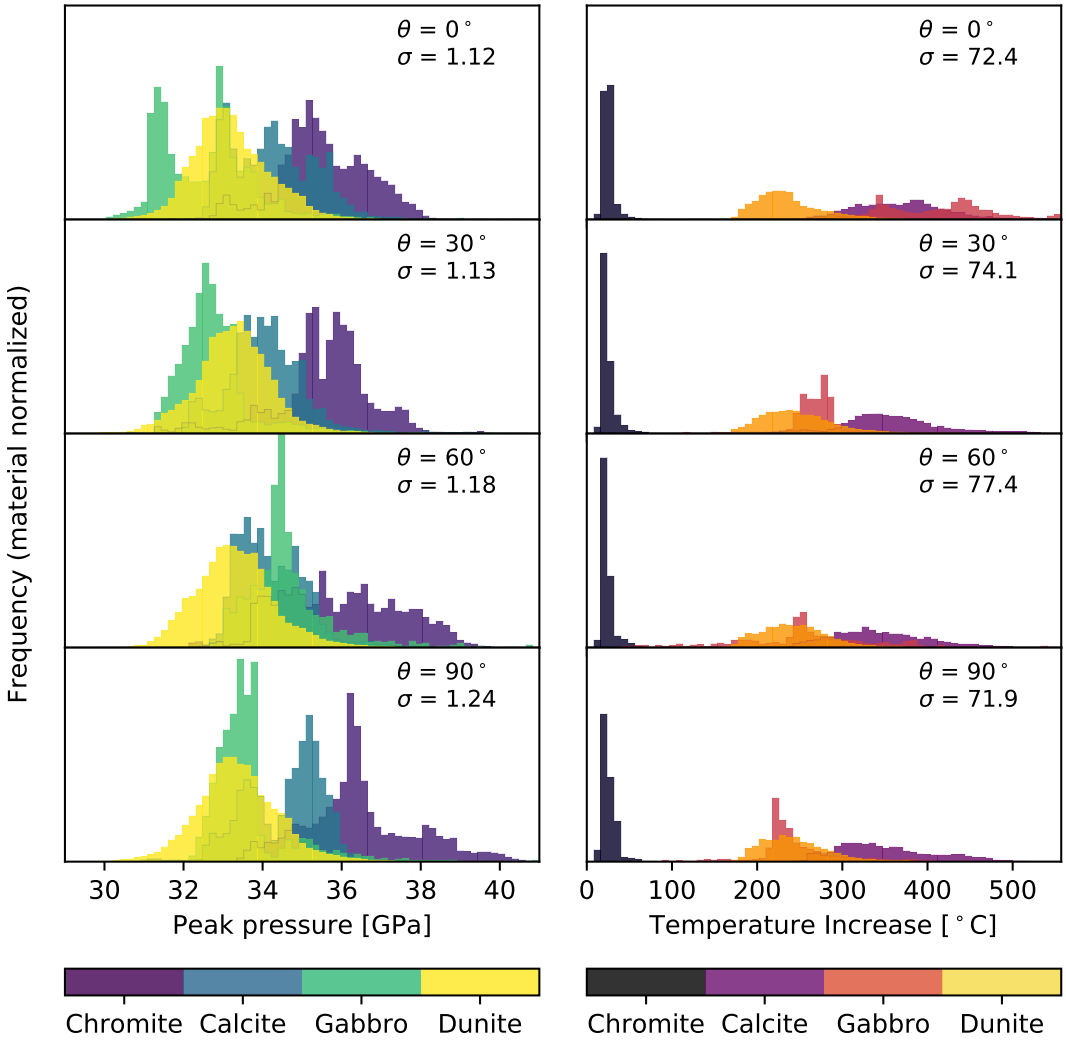


Figure 5.7: Response histograms divided by material for the reference simulation ($\theta = 0°$) and three additional sample orientations, $\theta = 30°$, $60°$, $90°$. Each histogram has been normalized to have equal area. The left hand side displays the peak pressure experienced in each material while the right hand side is the post-shock temperature increase, measured once the release wave has passed through the sample. The standard deviation for the bulk response, σ, is included in each pane. The low statistical variability between models implies there is little affect in the orientation of the sample to our results.

Sample orientation

S1 was rotated in three orientations in addition to the default orientation: 30°, 60° and 90°. The size of the cross-section and relative abundance of each material was kept consistent by tiling the cross-section in a 3×3 grid. We then took a slice with the same dimensions as the

original cross-section, rotated by the desired orientation.

When the sample was rotated relative to the original shock direction, we found low statistical variation between simulations (Fig. 5.7). Across the four orientations, the bulk pressure varied by $\Delta\sigma_p < 0.06$ GPa, while the difference in average post-shock temperature was found to be $\Delta\sigma_T < 2.8$°C. The chromite remained much colder than the other materials with a consistent temperature increase in all orientations. The response of the gabbro material showed the most variation with shock wave orientation, though this was by far the most minor constituent in our samples and was inherently the most susceptible to variation owing to its situation in one corner of the sample. This suggests that while shock direction can influence the fate of individual grains the bulk constituents of the meteorite would have a similar experience regardless of the shock direction.

Sample composition

To understand which components exerted the dominant control on the thermal heterogeneity observed, we adjusted the mineralogy of the S1 sample in two simulations. We performed this by omitting the chromite for the first simulation, followed by omitting calcite in the next. In each case, we substituted the removed material with the major constituent, dunite.

We found shear heating still occurred when each of these materials was removed from the system, although the location of some shear zones was clearly influenced by the minor components (Fig. 5.8). Shear deformation occurred predominantly in the dunite, though the shear zone locality differed in places when minor components were omitted compared to the reference simulation. For example, a shear zone in the lower right corner of the reference simulation between calcite grains (Fig. 5.8a) is absent when the calcite grains are removed (Fig. 5.8c). This suggests that the weaker calcite grains can act as nucleation points for shear fractures. The same is true for the chromite grains. While the location of shear deformation changed with the mesoscale structure of the sample, we can expect material shear to have occurred throughout ALH 84001 and that it is not unique to the samples studied here.

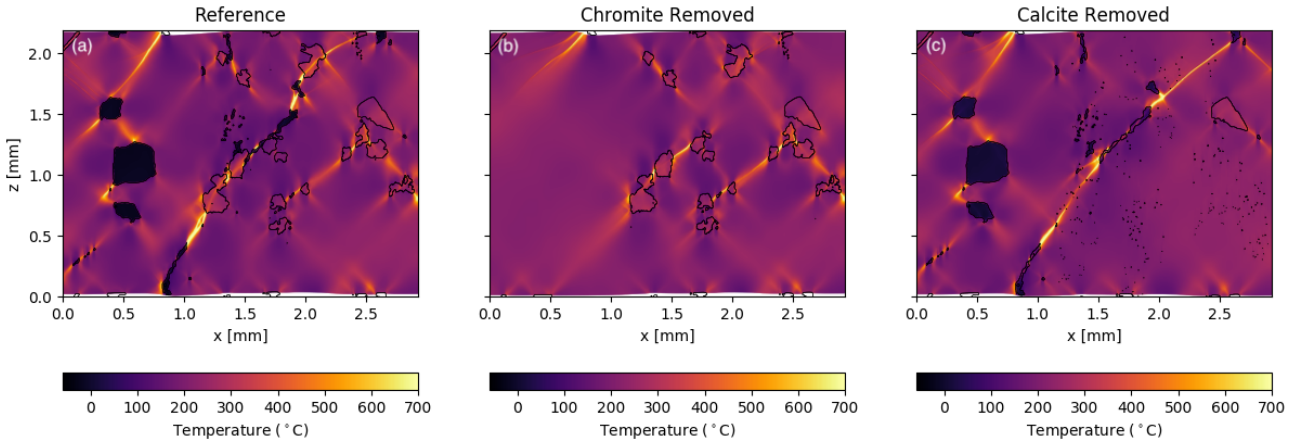


Figure 5.8: Post-shock temperature maps produced for three different sample compositions for S1. We have reproduced the reference simulation for the four-material system (a) in addition to the response of the sample when chromite has been removed from the system (b), while (c) shows the response when calcite has been removed.

Plate mesoscale structure

As the structure of material immediately adjacent to the meteorite when in-situ on Mars is unknown, we examined the response of the sample to a change in the mesoscale structure of the cover plate in which the shock front is generated and reaches a quasi-steady state. This was achieved by rotating the cover plate 180°. This transformation maintained the proportions of the constituent materials relative to one another while the mesoscale structure of the cover plate as seen by the incoming shock wave was different. When compared to the reference simulation, this reversed-cover simulation showed that the pressure and temperature distributions were prone to small variations, particularly for the minor components, but the mean and range of the pressure and post-shock temperature remained consistent (Fig. 5.9).

5.3.4 Limiting Shear Strength

ALH 84001 exhibits evidence of multiple impacts while on Mars. To examine whether impact-related damage from one impact may alter the response of the meteorite material to subsequent impacts we also investigated the effect of the bulk strength of the meteorite on its response to shock. Our reference simulations used a strength model based on a relatively strong, intact Horoman dunite. To examine the effect of an impact-damaged orthopyroxene component of ALH 84001, we compared the reference simulation result to those from a simulation that

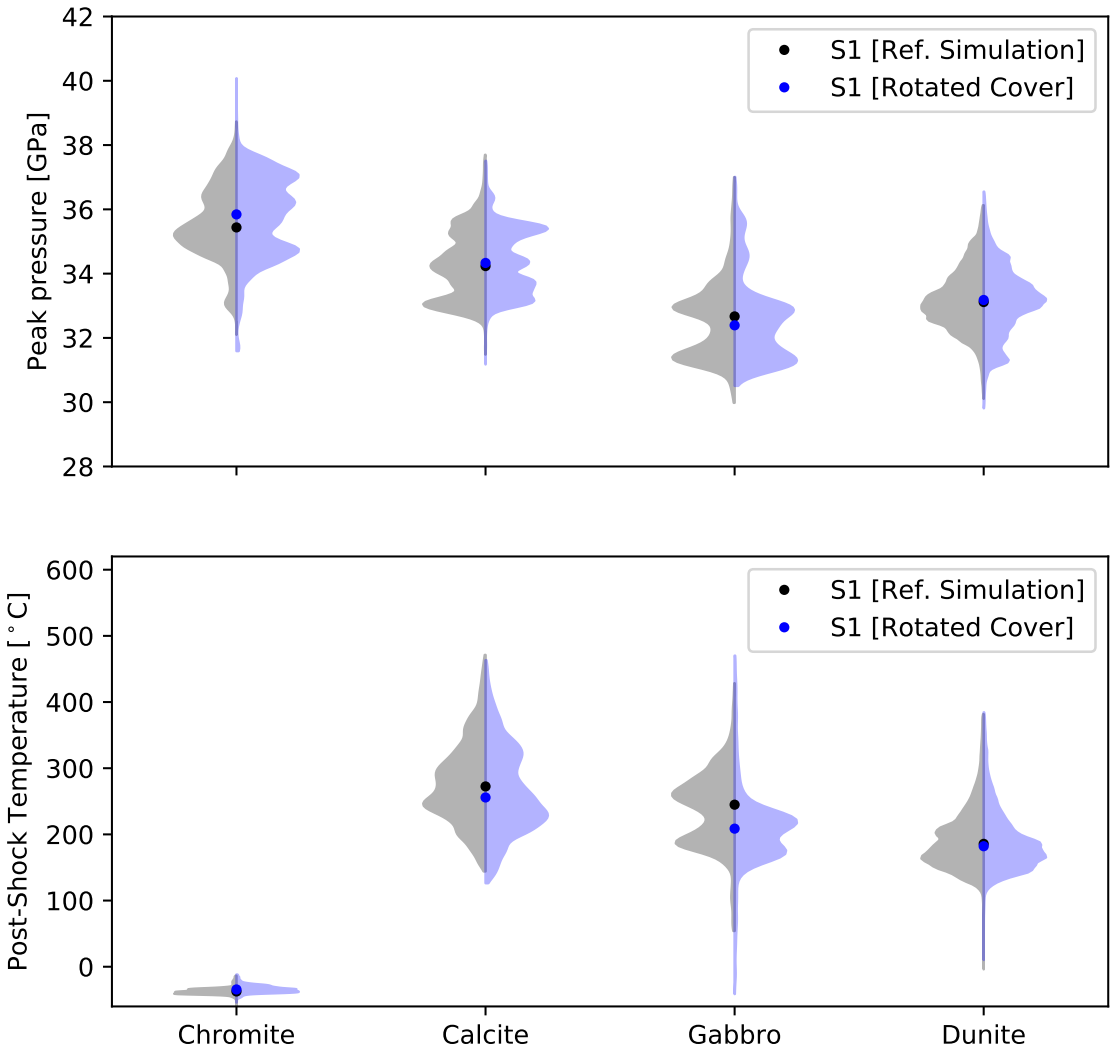


Figure 5.9: Comparison of the 'rotated cover' plate result to the reference simulation. The rotated cover refers to the model where the cover plate has been rotated 180 degrees to demonstrate the effect of the shock wave passing through a different mesoscale structure. The shockfront that enters the sample is then slightly different to the one in the reference simulation.

employed strength model parameters appropriate for a weaker Norwegian dunite (Fig. 5.2).

Figure 5.10 presents the comparison between two identical impact models where only the strength of the dunite has been changed. The initial conditions matched the reference simulation for S1. The impactor was set to have a velocity of 2720ms^{-1} which produced an average bulk pressure of 33 GPa in the reference simulation, however, this generated a slightly greater bulk

pressure of 34 GPa in the 'weak dunite' simulation. In contrast, while the average post-shock temperature in the reference simulation was 170°C, we have found it to be lower using the Norwegian dunite at 130°C. The difference in average post-shock temperature is due to the lower plastic work done in the Norwegian dunite when compared to the stronger Horoman dunite. The significantly higher post-shock temperature recorded in the stronger dunite further emphasizes the importance of shear heating to the overall impact heating of ALH 84001.

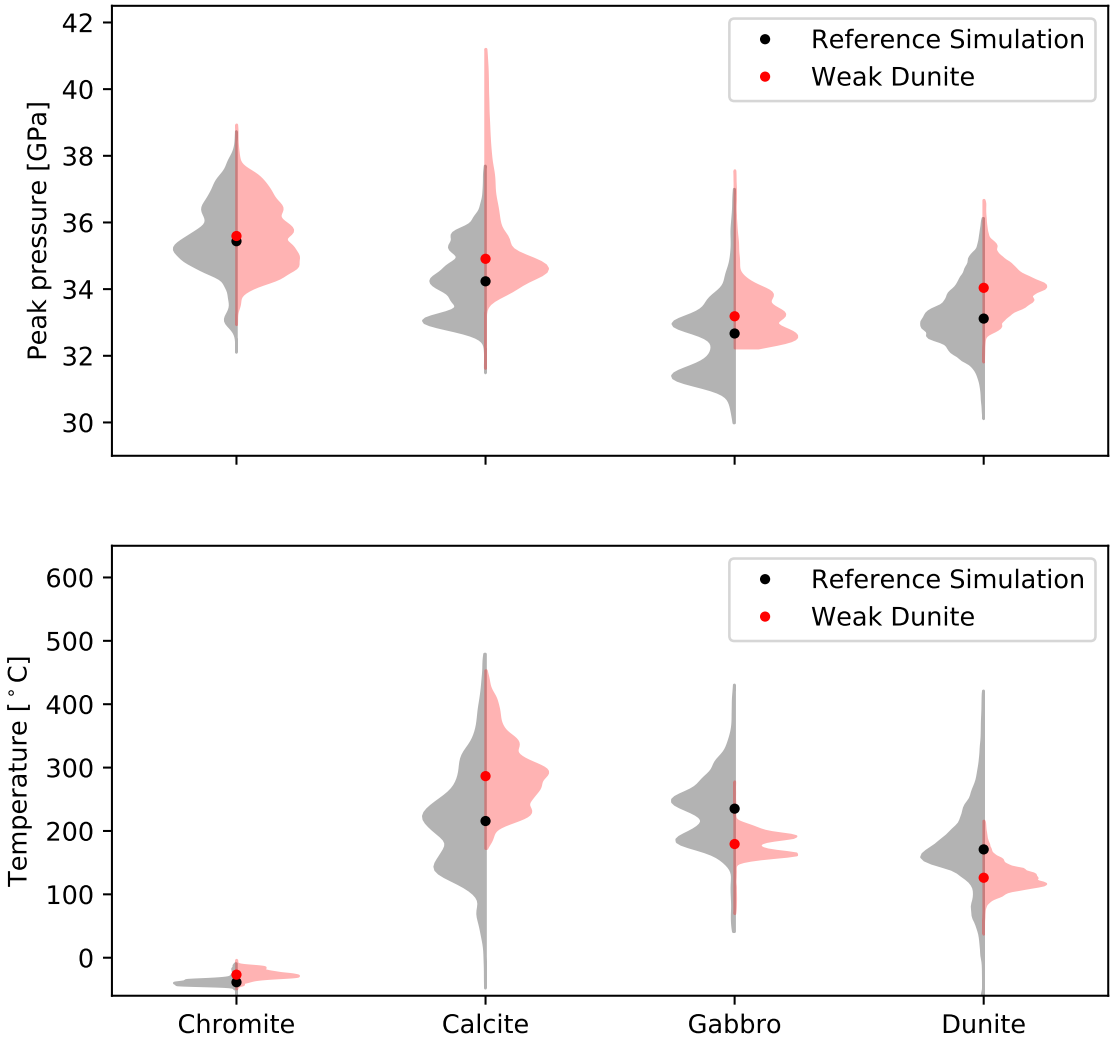


Figure 5.10: Pressure and temperature distributions for each material in the reference simulation (using Horoman dunite) alongside the same impact using a weaker, Norwegian dunite. Both simulations shared the same architecture using the S1 cross-section and the impactor was given an initial velocity of 2720ms^{-1}.

5.3.5 Temperature Dependence on Shock Wave Amplitude

By varying the plate velocity in our planar impact experiments, we simulated shock waves with twelve different bulk shock pressures between 3 GPa and 67 GPa. To quantify the effect of shock wave amplitude on heating in the sample, we were most interested in developing the relationship between the bulk shock pressure, peak temperature reached in each material and the equilibrium temperature reached by the meteorite. The post-shock temperatures in the sample at the end of the iSALE simulation were passed to the thermal equilibration code to determine the equilibrium temperature.

The relationship between the bulk pressure and equilibrium temperature of the sample is well-approximated by a linear fit above 22 GPa, while at lower pressures a non-linear polynomial (here we use a fifth-order polynomial) can adequately describe the trend (Fig. 5.11). However, the relationship between peak temperature and bulk pressure for individual constituent materials is more complex, non-linear and cannot be fully realized by looking at only the equilibrium temperature for the whole sample (Fig. 5.12).

In all the materials other than chromite, the maximum peak temperature experienced by a portion of the material is significantly greater than the equilibrium temperature measured in the sample (Table 5.3). While the chromite is heated by only tens of degrees for shock pressures below 50 GPa and subsequently warms up to reach the bulk temperature, the other materials are heated by hundreds of degrees and then rapidly cool to reach equilibrium (Figure 5.13).

5.4 Discussion

Our suite of planar impact simulations demonstrate that the constituent materials of ALH 84001 can experience significantly different temperature-time paths to each other during an impact event. Our results reveal substantial intra- and inter-component variation in the maximum temperature increase generated by the impact.

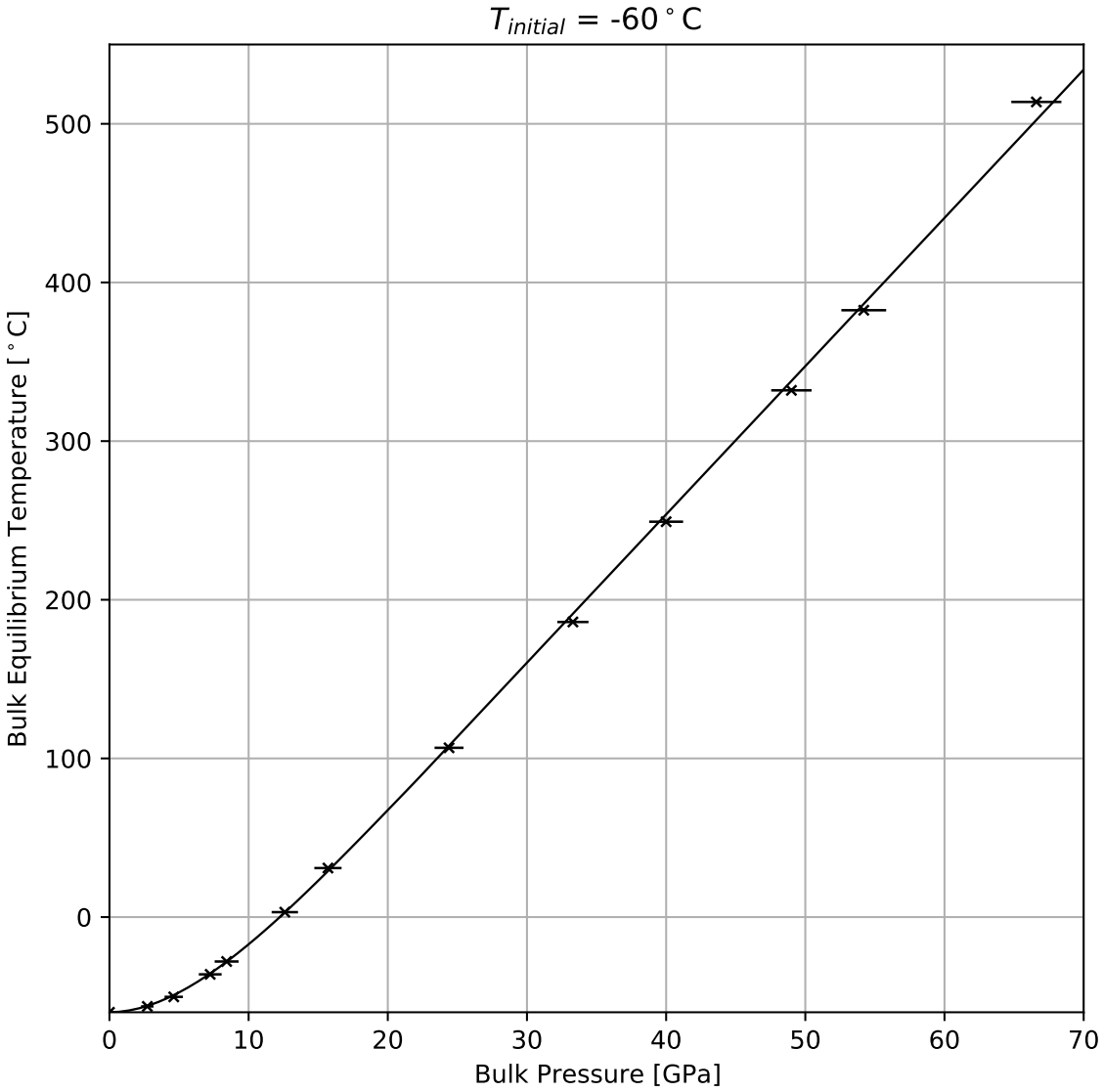


Figure 5.11: The relationship between bulk shock pressure and equilibrium temperature of S1, shocked in the range 3-67 GPa. Below 22 GPa, the data is well-described by a polynomial fit, calculated using
a non-linear least squares routine, fixed to intercept the axis at the initial simulation temperature, -60°C. Above 22 GPa, the relationship becomes linear.

5.4.1 A Mechanism for Heterogeneous Heating

While evidence of shear deformation in ALH 84001 is well documented (Treiman, 1998; Barber and Scott, 2006; Treiman, 2021), the associated temperature increase attributed to the plastic work done in shearing has not been quantified. The importance of bulk shear heating during relatively low-velocity impacts on asteroids and other planetary bodies has recently been

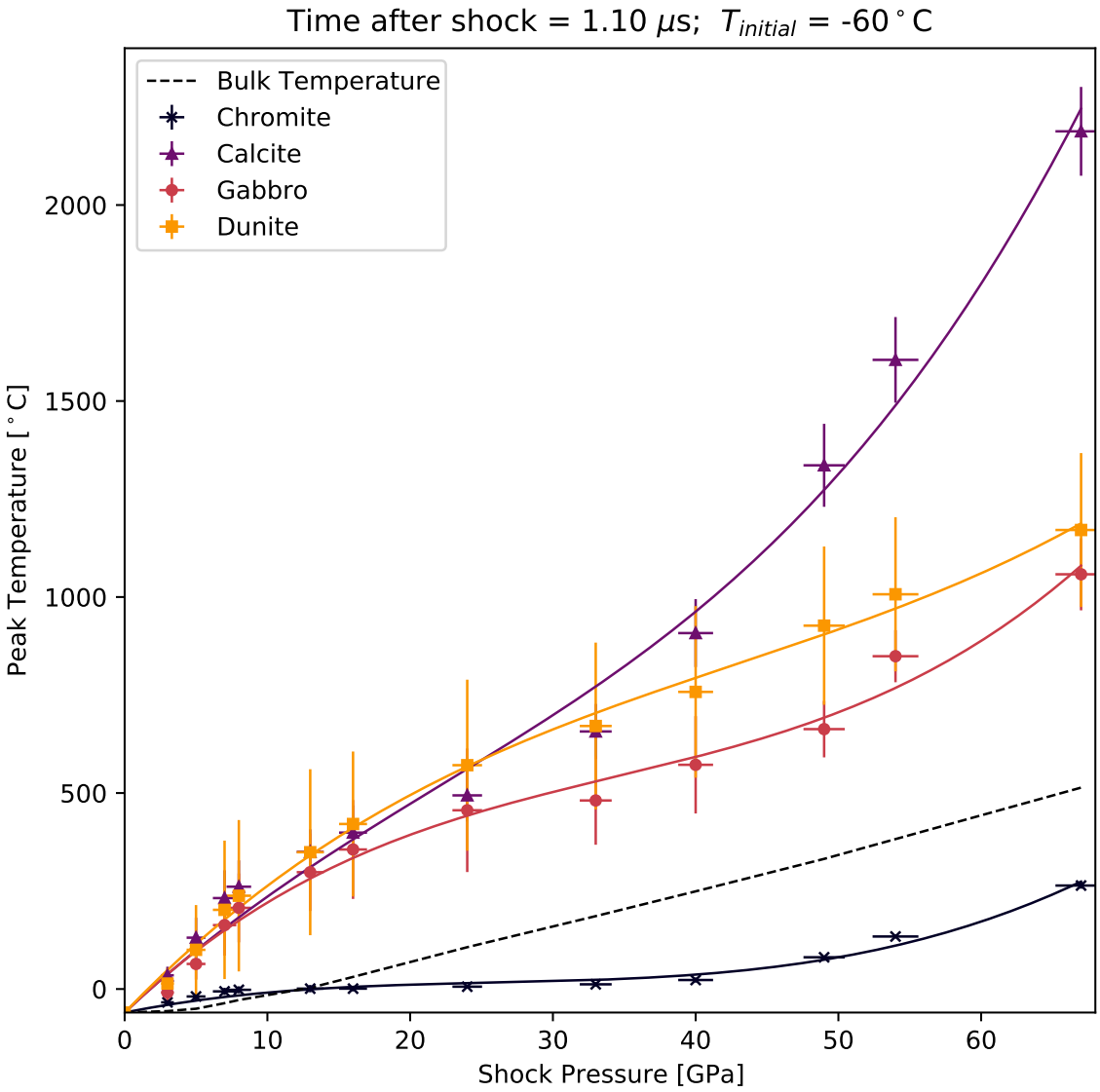


Figure 5.12: Maximum peak temperatures measured in each of the constituent materials of ALH 84001 during impacts across a range of amplitudes. All curves are third-order polynomials fit to the data using a non-linear least-squares routine. Errors shown are one standard deviation of the thermal distribution for the given material. Additionally, the bulk temperature is plotted as a dotted line (this is the same as the line fitted to the data in Figure 5.11).

highlighted (Kurosawa et al., 2018, 2021). In this study we have found that shear heating can cause large temperature variations on the sub-mm scale in response to a quasi-planar shock wave. We have shown across a range of impacts similar to those that ALH 84001 would have been subject to, the meteorite would have experienced significant shear deformation and the associated heating would have produced strong thermal gradients on a sub-mm scale.

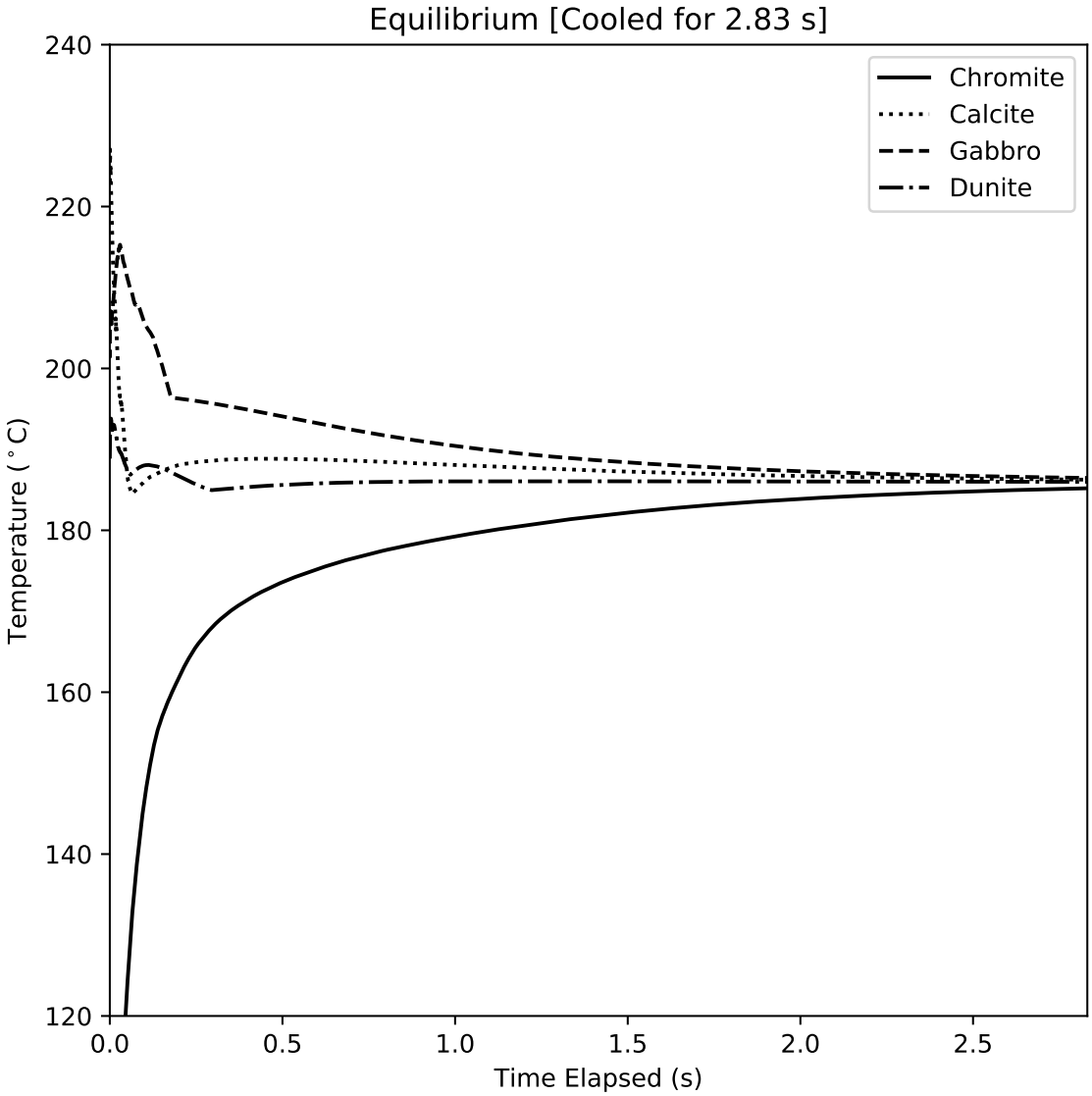


Figure 5.13: Temperature-time path for each of ALH 84001's constituent materials immediately following the end of the 33 GPa reference simulation. Each of the four materials were allowed to cool until thermal equilibrium was reached; approximately 2.8 seconds after the release. Calculated using equation 5.2, the step size was 19.7μs. The values that form the curves are the median temperature of each material.

5.4.2 Thermal History Recorded in Magnetic Carriers

The need for a mechanism that produces heterogeneous heating in the sample has been highlighted in previous paleomagnetic studies (Kirschvink et al., 1997; Antretter et al., 2003; Weiss et al., 2008a), but until now, the physical process responsible had been unknown. The heterogeneous pattern of magnetization observed in the meteorite can be explained by thermal

Table 5.3: For a given bulk pressure, we present the maximum peak temperatures (T^{pk}) for each material alongside the equilibrium temperature (T^{eq}) of the sample. The peak temperature recorded in the calcite, gabbro and dunite is far greater than the equilibrium temperature in all cases. After the 8 GPa impact, the peak temperature recorded in chromite remains well below the equilibrium temperature.

Pressure (GPa)	T^{pk}_{chr} (°C)	T^{pk}_{cal} (°C)	T^{pk}_{gab} (°C)	T^{pk}_{dun} (°C)	T^{eq} (°C)
3	-34	35	-9	14	-56
5	-19	131	64	100	-50
7	-6	232	163	202	-36
8	-2	261	207	238	-28
13	1	350	298	349	3
16	1	399	356	421	31
24	6	494	456	571	107
33	12	657	481	671	186
40	23	908	572	758	249
49	81	1336	663	927	332
54	134	1605	849	1007	383
67	264	2188	1058	1171	514

remagnetization of sub-volumes of the sample. The highly-localized, intense shearing we have observed in our simulations offers a mechanism that produces small regions of high temperature capable of remagnetizing these sub-volumes while not raising the rest of the sample to that temperature.

Magnetic reordering (the mechanism that allows the recording of an ancient magnetic field) occurs on timescales of nanoseconds, so even very brief transient heating events will overwrite existing NRMs within a sample. When examining the thermal evolution of the meteorite between the post-impact and thermal equilibrium temperatures, we found that in most parts of the sample, chromite warmed monotonically from its post-shock temperature to the equilibrium temperature. This shows that the temperature of the chromite, iron oxides and sulfides will rapidly (<3 s, plus shock wave dwell time) equilibrate via thermal diffusion. In this case, to overprint an existing NRM in the sample would require a shock event that heated the entire sample to an equilibrium temperature above the Curie temperature and all chromites would record the same magnetization direction.

On the other hand, an important consequence of the heterogeneous heating that we observe in our simulations of ALH 84001 is that in chromite grains next to shear zones, heat transfer from the shear zone into the chromite grain can lead to transient, local temperature excursions

where the chromite was rapidly heated and then dropped back to the equilibrium temperature (Fig. 5.14; see also videos in supplementary materials). In other words, small chromite grains in shear zones or portions of larger grains near shear zones can be heated briefly to temperatures exceeding the equilibrium temperature. This means a single impact can demagnetize or remagnetize sub-volumes of the meteorite: some magnetic assemblages near shear zones may be partially demagnetized or even remagnetized, should the maximum temperature exceed the Curie point, while other magnetic carriers that are isolated from shear zones will be unaffected (if the equilibrium temperature is below the Curie point). In our 'reference simulation' (bulk pressure 33 GPa), approximately 22% of the simulation domain is above 320°C once the meteorite is released from its shocked state. However, as shown in Figure 5.14, the chromites that are re- or demagnetized are actually heated by nearby shear zones during thermal equilibration. If the magnetic carriers are small and uniformly distributed throughout the sample, then approximately the same proportion of magnetic carriers are potentially re- or demagnetized. On the other hand, if the magnetic carriers are preferentially located close to the shear zones, this fraction could be much higher.

5.4.3 Effect of shock pulse width on heterogeneous heating

The design of our simulation means that the shock pulse width (the duration the sample is in a shocked state) is much shorter than the time taken for the sample to reach thermal equilibrium. While the shock duration was around $\sim$1 μs, thermal equilibrium was reached on a timescale of $\sim$1-3 seconds after the passage of the release wave through the sample. This provides the opportunity for small grains within the meteorite to experience brief shock- or shear-induced high-temperature excursions prior to thermal equilibration. On the other hand, if the impact produces a shock pulse with a similar duration to the equilibrium timescale, thermal equilibration would occur whilst the meteorite is still being shocked and sheared. In this case, we anticipate heterogeneous heating will still occur, but the variance of peak temperature among different components will be reduced.

Shock pulse duration can be approximated by the impactor size divided by the impact speed. So for a typical impact speed on Mars of 10 km/s, we anticipate that cm-scale impactors would

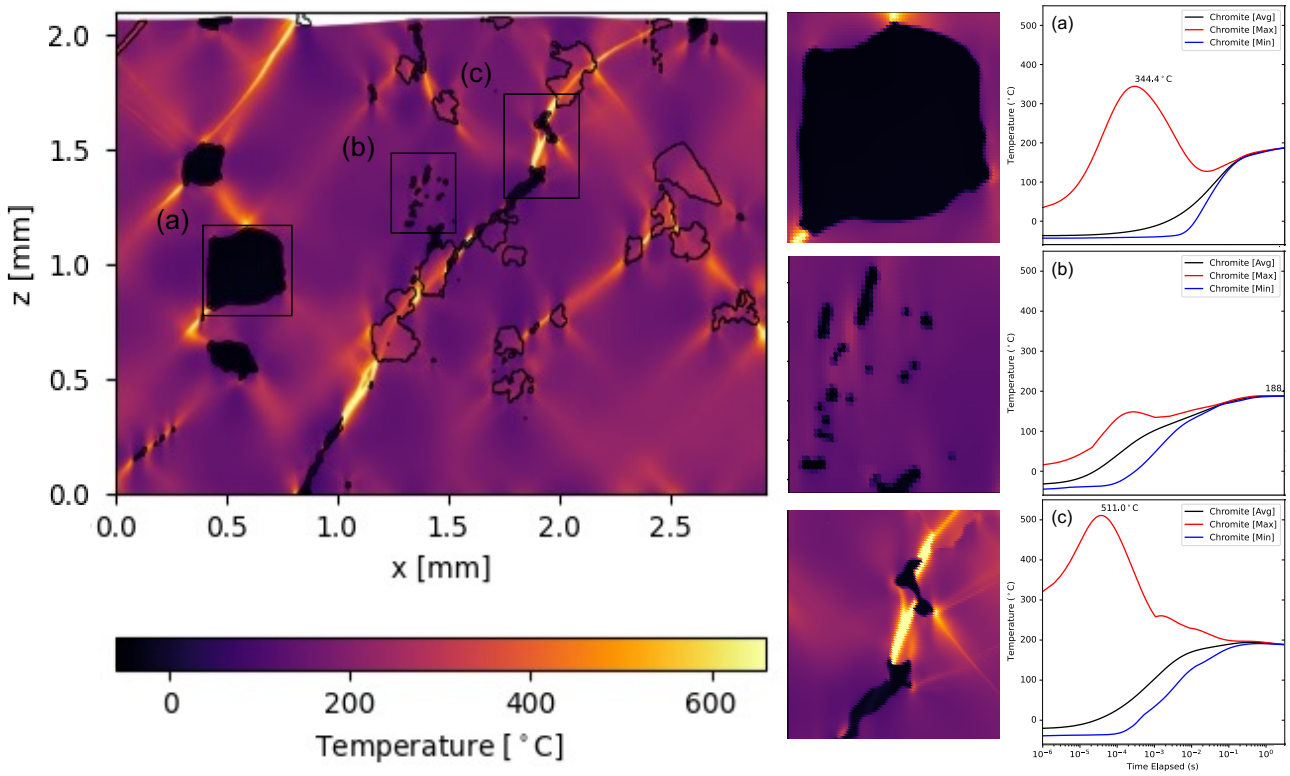


Figure 5.14: This figure demonstrates the thermal evolution of three areas of the reference simulation for cross-section S1. We have chosen three grains characteristic of the chromite inclusions we observe in the sample; (a) shows a large, coarse inclusion, (b) is an assemblage of grains several microns across and (c) is a vein of chromite located in a shear zone. We see that the chromite close to shear zones experience temperature maxima greater than the post-shock temperature and the thermal equilibrium temperature.

produce a shock wave similar to those we observe in our simulations. On the other hand, using the same impactor speed, impactors several hundred meters in size or larger would produce a shock duration comparable to the thermal equilibration timescale, which may diminish the thermal heterogeneity we observe for smaller impactors. Additional simulations to explore the influence of shock (and shear) duration on the variance of thermal heterogeneity would be valuable.

5.4.4 Constraints on Shock History from Paleomagnetism

The chromite-sulfide assemblages in ALH 84001 have been shown to record two distinct, statistically significant magnetization directions, which have been interpreted as evidence of at least two separate high-temperature deformation events in the presence of a martian surface magnetic field prior to 3.9 Ga (Weiss et al., 2002; Antretter et al., 2003). The first of these

magnetization directions, the primary magnetization, can be explained as a remanence from the Martian dynamo field at 4.1-4.0 Ga, recorded uniformly in chromite-sulfide assemblages throughout the meteorite (Weiss et al., 2008b). The recording of the primary magnetization would have required the temperature of the whole parent rock to exceed the Curie point of the pyrrhotite present in the chromite-sulfide assemblages, > 320°C (Dunlop and Özdemir, 1997), which dominates the stable component of the NRM (Weiss et al., 2008b; Steele et al., 2021). The second of these magnetization directions is then a partial remagnetization where sub-volumes of the meteorite were remagnetized at a later time, around 3.9 Ga, where the change in direction is possibly a record of the Martian dynamo polar reversal (Steele et al., 2022). To account for only partial remagnetization, this second impact must have allowed a fraction of the sulfides in the rock to exceed 320°C, while the equilibrium (bulk) temperature remained below the Curie temperature.

Also present in the meteorite is an incoherent pattern of weakly magnetized chromites and carbonates (Kirschvink et al., 1997; Antretter and Fuller, 2002; Weiss et al., 2002). This has been interpreted as evidence for a third, late impact event (D3) after the dynamo's cessation that demagnetized sub-volumes of the meteorite where some fraction of the magnetic carriers experienced very brief high-temperature excursions (Weiss et al., 2008b; Cassata et al., 2010) that were again insufficient to reset the NRM hosted elsewhere in the meteorite.

The paleomagnetic literature therefore impose the following constraints on the shock history of ALH 84001:

1. The first impact must have been sufficiently strong to raise the equilibrium temperature of the meteorite well in excess of 320°C.

2. The second, and possibly third, impact allowed a fraction of the chromites in the rock to exceed 300°C, but the equilibrium temperature remained below this temperature.

3. Since the first impact, the equilibrium temperature cannot have been raised above 300°C, else the NRM would have been completely reset.

5.4.5 New Constraints on the Shock History of ALH 84001

Early shock events

When combined with these paleomagnetic constraints, our simulation results can provide new constraints on the shock history of ALH 84001. The D1 event resulted in the granular bands seen throughout the meteorite, metamorphism above 875°C, and full remagnetization of the chromite-sulfide assemblages (Treiman, 1995, 2021). Our results suggest that for D1 to have raised the temperature of the meteorite well in excess of 320°C required a minimum shock pressure between 45-50 GPa. This is a conservative limit on the minimum bulk pressure as evidence attributed to D1 includes possible local bulk rock melting, requiring peak pressures in excess of 75 GPa (Treiman, 1998).

To achieve subsequent partial remagnetization of the sample, our results suggest that the D2 event was associated with a bulk shock pressure between 25-45 GPa. This range is compatible with small volumes of the sample experiencing the minimum shock pressure required to produce glass formed through shock-induced melt (40-45 GPa; Stöffler et al., 1991, Fig. 5) as well as the conversion of plagioclase to maskelynite which occurs in shocks in excess of 31 GPa (Kring et al., 1998; Treiman, 2021). Moreover, a shock wave of this amplitude would heat some fraction of the chromite-sulfide assemblages above $\sim$ 320°C allowing them to be remagnetized, while the remaining fraction would remain below 320°C and retain its earlier magnetization.

"Recent" shock events

Evidence for a significant impact since 3.9 Ga is more equivocal and is not easily explained by our model results. The D3 event may be responsible for demagnetization of sub-volumes of the meteorite and has been identified by an Ar-Ar kinetic crossover around 1.16 Ga (Cassata et al., 2010). According to this analysis, the apparently more complete degassing of orthopyroxene compared to plagioclase in multiple aliquots of ALH 84001 recording a 1.16 Ga plateau age is best explained by rapid ($\sim$1 s) heating up to and above 1400°C.

Adopting this temperature constraint, our simulation results are unable to explain the persistence of multiple generations of prior magnetization. The minimum pressure required to

produce peak temperatures in gabbro (our analog for plagioclase) around 1400°C is in excess of 60 GPa. At such pressures, the equilibrium temperature would be at least 440°C, well above the Curie temperature of chromite-sulfide assemblages, which would reset all the paleomagnetic data stored in these carriers. Furthermore, shock pressures in excess of 50 GPa are likely to produce molten flowed quartz and feldspar, making it highly unlikely the carbonates present in the meteorite would have survived intact (Kring et al., 1998). Finally, this 1.16 Ga plateau is fully present in only a single Ar-Ar aliquot while a 4.0-3.9 Ga plateau, likely associated with the D2 event, is prominent in a majority of analyzed ALH 84001 material (Turner et al., 1997; Cassata et al., 2010). Several such Ar-Ar aliquots show virtually undisturbed ∼3.9 Ga plateaus. A D3 event in excess of 60 GPa would be significantly stronger than estimates for the D2 event given above, contradicting the relative strengths of these events inferred from Ar-Ar data. Together, these observations suggest that simultaneous peak heating of orthopyroxene and plagioclase up to 1400°C during the D3 event is unlikely. In any case, a recent study of terrestrial impact material, analogous to Martian shergottite meteorites, has shown the classical interpretation of argon ages recovered from impact sites can be unreliable without proper context (Jaret et al., 2018).

An alternative interpretation of the 1.16 Ga Ar-Ar plateau data is that differential degassing of orthopyroxene and plagioclase may have been due to heterogeneous heating instead of a kinetic crossover. The 1400°C peak temperature estimate from the kinetic crossover analysis assumes that the plagioclase and orthopyroxene were both heated to this temperature. Our simulation results show that orthopyroxene can be heterogeneously heated to $100-200$°C above plagioclase separated at the sub-millimeter scale (Fig. 5.4). If this occurred during the D3 event, the peak temperature for plagioclase can be several hundred degrees below 1400°C while still degassing less than nearby orthopyroxene. With the most favorable modeled diffusion domain sizes, orthopyroxene heated to $\sim$ 1050°C can degas at a similar rate as plagioclase heated locally to $\sim$ 900°C (Cassata et al., 2010, Fig. 6A). Under this favorable scenario, we are able to realize a peak temperature of $\sim$ 1050°C in the bulk rock material within a 1σ uncertainty in a 45 GPa impact. At this shock pressure, the equilibrium temperature is 300°C and chromite-sulfide assemblages would not be completely remagnetized.

To further aid in explaining the locally extensive degassing event at 1.16 Ga, there may be a heating mechanism present not accounted for in our simulations. One possibility is the crushing out of pore space in the meteorite, responsible for the melting of gabbro. Compaction of a porous target would consume extra work during shock passage, resulting in higher localized temperatures surrounding the collapsed pore (Wünnemann et al., 2006; Güldemeister et al., 2013). When combined with shear heating, it could be possible this would raise the temperature of very localized regions in the meteorite significantly, producing localized excess orthopyroxene degassing at 1.16 Ga, as observed. However, as the porosity history of the meteorite is unknown, we cannot provide further evidence in this study.

5.4.6 Ejection from Mars

Cosmic ray ages of ALH 84001 have dated the ejection of the meteorite from Mars to around 14 Ma (Eugster et al., 1997). Previous studies have shown the minimum shock pressure required to eject material from Mars to be around 10 GPa (Artemieva and Ivanov, 2004), however the upper limit on the ejection pressure of ALH 84001 is unclear. Previous studies have suggested that some material in the meteorite reached peak temperatures around 430°C (Min and Reiners, 2007), while other studies have suggested that "cold" paleomagnetic data preserved in the meteorite required the equilibrium temperature to remain below 40°C (Weiss et al., 2000). It is unclear if this cold magnetization component was acquired during ejection from the Martian surface or if it is actually a viscous remanent magnetization (VRM) acquired on Earth (Antretter et al., 2003). Using Figure 5.12, we find an upper limit on the impact pressure to be 16 GPa to be consistent with both of these observations. In a 16 GPa impact, the maximum peak temperature experienced by any material in the meteorite is 430°C, while the equilibrium temperature remains just below 40°C.

Our results can reconcile these observations to determine a 10-16 GPa "launch window" that satisfies both constraints. This window corresponds to equilibrium temperatures of −17°C and 40°C, with peak temperatures in dunite of 260°C at 10 GPa, and 430°C at 16 GPa.

5.5 Conclusions

Through a suite of mesoscale shock wave simulations, we have quantified the thermodynamic and physical response of Martian meteorite ALH 84001 to strong planar shock waves, similar to those it would have experienced before and as it was ejected from Mars. Over a range of shock pressures between 3 GPa and 67 GPa, our results show that ALH 84001 would likely have experienced strong syn-impact thermal heterogeneity on the sub-millimeter mesoscale. The physical mechanisms responsible for these steep thermal gradients are localized shear, occurring predominantly in the orthopyroxene component, and shock fluctuations and reverberations caused by the spatial variation in material properties within the sample.

We have attempted to reconcile the thermal constraints placed on the meteorite in paleomagnetic studies and petrologic observation, by measuring the peak, post-shock and thermal equilibrium temperatures following an impact experienced by different components of the meteorite, including its magnetic carriers. Our results provide several new constraints on the impact history of ALH 84001:

1. Granular bands were formed in an early impact D1 with a minimum shock pressure between 45-50 GPa.

2. Impacts after the first major shock event were weaker and therefore must have exerted a bulk shock pressure less than 45 GPa to retain the magnetization associated with D1.

3. The second major impact D2 that fractured carbonates throughout ALH 84001 must have a shock pressure in the range 25 - 45 GPa.

4. Our simulation results are difficult to reconcile with an event around 1.16 Ga that produced Ar degassing consistent with peak temperatures in excess of 1400°C.

5. For event D3, our simulations suggest the differential heating of plagioclase and orthopyroxene in a 45 GPa shock event can tenuously explain both paleomagnetic and Ar-Ar thermochronometry data in the most extreme outliers.

6. If "cold" paleomagnetic data in the meteorite is not a VRM acquired on Earth, the maximum pressure upon ejection from Mars was 16 GPa.

The results presented here have wider implications for the meteorite record. We have demonstrated that peak temperatures recorded in some meteoritic materials are not representative of the thermal history of the bulk sample and might lead to misinterpretation of a meteorite's metamorphic history. This is especially pertinent for paleomagnetic investigations where ferromagnetic populations are remagnetized at different times and may hold record of different ancient paleofields. Our results emphasize the value of examining Martian meteorites on a per-material basis at the mesoscale, and highlight a need to incorporate the effects of heterogeneous heating, including heating by shear deformation, into the general shock classification of meteorites.

Chapter 6

Micromagnetic Modelling: Effects of Stress on Magnetic Recording Fidelity

6.1 Introduction

The recording of a shock remanent magnetisation (SRM) in unmagnetised samples has been shown possible in the presence of an external magnetic field, as low as 1 μT, where the resulting remanence was aligned along the direction of the external field (Gattacceca et al., 2007). Similarly, experiments into how shock waves affect pre-existing remanences have shown that shocks in zero field demagnetise grain assemblages (Cisowski and Fuller, 1978). However, the acquisition of SRM is thought to be a relatively inefficient process, affecting the lower part of the coercivity spectrum (Gattacceca et al., 2008), particularly at low shock pressures (< 10 GPa); in comparison, highly-stable TRM acquisition affects the entire coercivity spectrum (Kletetschka et al., 2004). This means that shock remanences are typically overlooked across meteorite studies, as even the most primitive and unaltered chondrites are known to have experienced high-temperature (~ 300°C) events (Bland et al., 2014).

However, in the case that a magnetisation exists prior to a shock event, the effect of pressure on the remanence is poorly understood. Impacts throughout the solar system were frequent and ubiquitous, long after planetesimal formation (Bottke and Norman, 2017) and were likely significant factors in the evolution of even the most primitive meteorites (Bland et al., 2011;

Hanna et al., 2015; Forman et al., 2016) right up until their ejection from their parent asteroid. Although, as many primitive meteorites are classified as 'unshocked', $< 4 - 5$ GPa (Stöffler et al., 1991; Scott et al., 1992), impacts are typically overlooked as a significant contributing factor towards the NRM. An understanding of how impacts process the NRM contained within SV particles may alter that perception.

Energy transferred into magnetic grains during shock events has long been known to irreversibly change the magnetisation state of natural samples (Brown, 1949). In the case that the remanence of a rock is altered due to a shock, it is categorised as a shock remanent magnetisation (SRM). Long-standing classical calculations for the pressure required to impart an SRM in single-domain (SD) grains require pressures in excess of 0.5-1 GPa (Hargraves and Perkins, 1969), but, as seen in the work already presented in this thesis, that would likely involve significant heating and a thermoremanent overprint. Hence, meteorite remanences acquired during impacts are generally assumed to be TRMs. However, there is evidence that at very low shock pressures ($<<$ 1 GPa) and in the absence of significant heating, rock magnetisations undergo irreversible change (Nagata, 1970, 1971; Tikoo et al., 2015), contradicting the classical model.

Classical domain theory (Kittel, 1949) predicts SD particles as the most stable and dominant carriers of the NRM in rocks and meteorites (Néel, 1949, 1955), while larger pseudo-single domain (PSD) or multi-domain (MD) magnetic particles have lower coercivities and are therefore unreliable. This has meant that while even though PSD and MD grains are more abundant than SD grains in naturally occurring samples, their shorter relaxation times and lower coercivities have led them to be considered unstable on geological (billion-year) timescales (Néel, 1949, 1955; Lederman et al., 1994) and palaeomagnetically less important.

However, the reliance on interpreting the NRM as being hosted solely by SD particles is now under question. Experimental (Almeida et al., 2016; Shah et al., 2018; Nichols et al., 2019) and numerical work (Nagy et al., 2017, 2019) in recent years has demonstrated that magnetic carriers with non-uniform magnetisations, namely those with a 'single-vortex' (SV) domain structure (Fig. 6.1), dominate the stable component of the NRM in rocks and meteorites. These new findings suggest the threshold at which the remanence in rocks may be altered by pressure needs to be re-analysed for SV states; there is a newfound requirement to develop and

understandthe effect of pressure on SV particles.

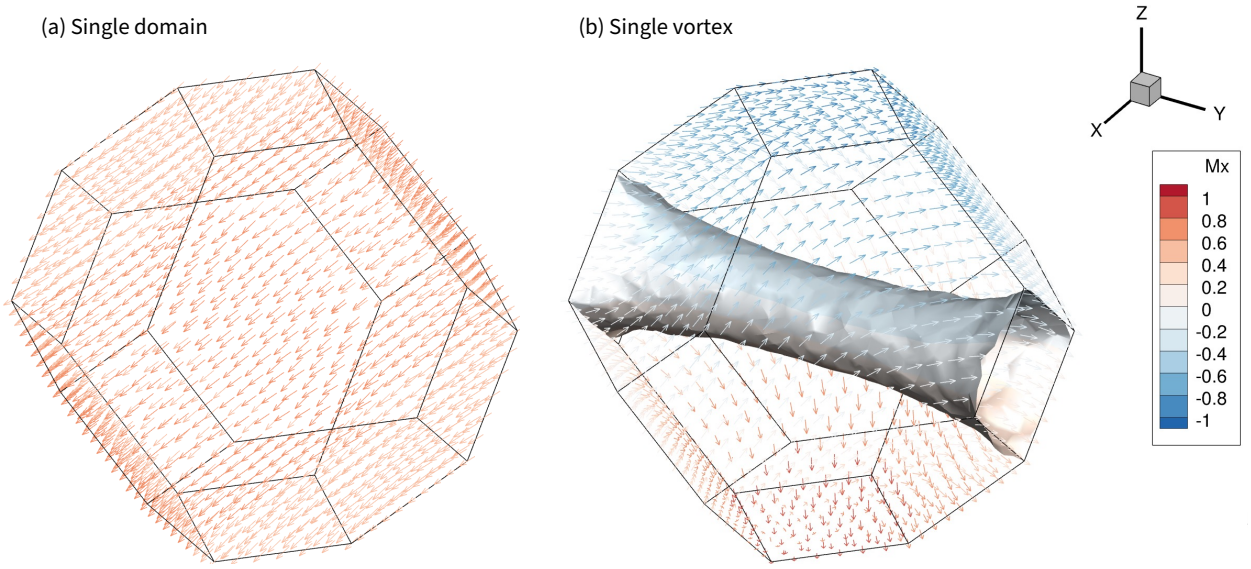


Figure 6.1: Three-dimensional micromagnetic model of (a) single domain and (b) single vortex grains of magnetite. The SD structure is produced within an 80 nm grain, aligned with the x-axis, while the SV structure shown is a 100 nm grain aligned with the easy axis. Magnetisation vectors are normalised and shown by small arrows, coloured according to their direction relative to the positive x-direction, and the core in (b) is produced by an isosurface that represents a space where the relative helicity is ± 0.98. These models were produced using the MERRILL micromagnetic modelling code (Conbhuí et al., 2018).

In this chapter, I present the results of a suite of simulations where a an instantaneous, uniaxial stress is applied to single-domain and single-vortex magnetites, across a range of grain sizes and orientations. While past experiments have investigated the response of SD and MD particles to a static stress (e.g., Gilder et al., 2006), the response of SV particles has never before been explored. I attempt to quantify the experience of the SD and SV remanence stored within a grain when subject to an applied stress, in turn developing an understanding of the relationship between the pressure and magnetic remanence. Ultimately, the aim of this is to identify the impact-induced stress that is required to irreversibly alter the remanence of an assemblage of SV grains, in the absence of high-temperatures.

6.2 Micromagnetic modelling code: MERRILL

I have used the micromagnetic modelling code, Micromagnetic Earth Related Robust Interpreted Language Laboratory (MERRILL; Conbhuí et al., 2018), to simulate a uniaxial stress

applied instantaneously on individual grains of magnetite. MERRILL is a three-dimensional open-source palaeomagnetic code that is optimised for calculation the local energy minima (LEM) state of individual magnetic grains. Grain shape, size, elongation and initial magnetic state are able to be specified, along with external factors including the temperature and external field strength.

The magnetic structure and grain geometry is built from a large number of tetrahedral components, where the magnetisation is then defined by a vector, $\boldsymbol{m}$, that acts along the node of each component. MERRILL then determines the total energy, E_{tot}, for the model by summing the magnetic free energy over all the individual tetrahedra. The code then minimises the magnetostatic energy, solving for interactions between all components, and records the LEM state.

To minimise some initial magnetic state ($\boldsymbol{m}$) at each node of each tetrahedra, the total energy is calculated using a finite-element method (FEM). The minimisation routine determines the total energy for a particle with volume V by:

$$E_{tot} = \int_{\Omega} [A|\nabla \boldsymbol{m}| + K_1[m_x^2 m_y^2 + m_x^2 m_z^2 + m_y^2 m_z^2] - M_s[\boldsymbol{H_z} \cdot \boldsymbol{m}] - \frac{M_s}{2}[\boldsymbol{H_d} \cdot \boldsymbol{m}]]dV \qquad (6.1)$$

where $\boldsymbol{H_z}$ and $\boldsymbol{H_d}$ are the external and demagnetising fields, respectively, m_x, m_y, m_z are the planar components of the magnetisation $\boldsymbol{m}$, and the three material parameters are functions of temperature: the exchange constant, A, the magnetocrystalline anisotropy constant, K_1, and the saturation magnetisation, M_s (Conbhuí et al., 2018). For magnetite at room temperature (20°C), these values are: $A = 1.3 \times 10^{-10}$ Jm^{-1} (Heider and Williams, 1988), $K_1 = 1.3 \times 10^4$ Jm^{-3} (Fletcher and O'Reilly, 1974) and $M_s = 4.8 \times 10^5$ Am^{-1} (Pauthenet and Bochirol, 1951).

The solution for E_{tot} comprises four terms. The first of these, $\int_{\Omega} A|\nabla \boldsymbol{m}|dV$, is a calculation of the exchange energy over the total volume of the grain. The second, $\int_{\Omega} K_1[m_x^2 m_y^2 + m_x^2 m_z^2 + m_y^2 m_z^2]dV$, calculates the anisotropic energy of the grain. The third term, $\int_{\Omega} M_s[\boldsymbol{H_z} \cdot \boldsymbol{m}]dV$, describes the interaction between the internal magnetisation and external magnetic field while the final term, $\int_{\Omega} \frac{M_s}{2}[\boldsymbol{H_d} \cdot \boldsymbol{m}]dV$, is a calculation of the demagnetising energy.

6.3 Methods

Meshes where grain size < 100 nm can typically be modelled in MERRILL very quickly with little computing power, however, the larger 200 nm meshes that form the suite of models presented in this work have required significant computing power. I have conducted the modelling in this chapter using the high performance computing facility at the University of Edinburgh within Professor Wyn Williams' group. Throughout all simulations, magnetite has been used as the grain material. MERRILL has a good material model for magnetite and as it occurs in abundance in recovered meteorites, it is highly relevant to the scope of this thesis. All simulations take place at 20°C room temperature and in the absence of any external magnetic field.

6.3.1 Grain size and shape

The aim of these simulations was to explore how an applied stress of varying strength affects the magnetic state of magnetite particles carrying a remanent magnetisation. I considered a number of grains with different sizes and elongations that were initialised with either a uniaxial SD or non-uniform SV domain state. The grain morphology (shape) was a truncated cuboctahedron (Fig. 6.1), which were elongated along the x-direction (prolate). I considered elongations of 1% (this can be considered essentially equidimensional, but perfectly symmetrical grains have been omitted to avoid spurious computational errors), 50% or 100%. The symmetrical grains that were given initial SD states had equivalent spherical volume diameter (ESVD) sizes of 50, 80 and 100 nm, while symmetrical SV grains had ESVD sizes of 80, 100, 150 and 200 nm.

The dependence on the domain state of the grain is intrinsically linked to its physical size and axial ratio (AR; the ratio between long and short axes). The critical grain size under which the behaviour is purely SD, d_{min}, and above which the grain size is MD, d_{max}, is a function of grain elongation: as grains become increasingly elongated and AR decreases, d_0 increases (Muxworthy and Williams, 2006).

Table 6.1: Summary of the magnetic states explored in our suite of simulations. A total of 5 grain sizes (50, 80, 100, 150 and 200 nm) and three percentage elongations per grain size (1%, 50% and 100%) were explored. The checkmarks (✓) indicate the models that have been investigated in this study. The single domain states are aligned either to the easy magnetocrystalline (easy) or with the elongation axis (long), while the vortex (V) states have additional axis alignments: hard magnetocrystalline (hard), short shape (short; A and B, where B is a higher energy state), curved (connecting the easy crystal faces) and an intermediate direction (int.) between the easy and short axes.

	50 nm			80 nm			100 nm			150 nm			200 nm		
Elongation	1%	50%	100%	1%	50%	100%	1%	50%	100%	1%	50%	100%	1%	50%	100%
SD Easy	✓			✓											
SD Long		✓	✓			✓			✓						
V Easy							✓			✓	✓		✓	✓	
V Hard				✓											
V Short A								✓	✓		✓			✓	
V Short B											✓				
V Long					✓			✓	✓			✓			
V Curve												✓		✓	✓
V Int.														✓	✓

6.3.2 Initial magnetic states

Uniaxial SD magnetisations were initially aligned along either the easy magnetocrystalline (easy) or the elongation (long) axis, while SV states were aligned by the core direction across a broader range of axes. The vortex was aligned along one of the easy or hard axis (for magnetite, the easy axis is the [1 1 1] direction and hard axis is [1 0 0]; Kittel (1949)), the short or long shape axis, an intermediate direction midway between the easy crystalline and short shape axes, or in a curved shape that connected the easy crystal faces (Table 6.1).

6.3.3 Applying stress in MERRILL

The MERRILL code has the capability to apply a uniform, isovolumetric stress throughout the mesh. However, MERRILL does not have the capability to evolve a stress state temporally. Instead, stress is switched instantaneously on/off and the LEM state is calculated each time there is a switch in stress. This means that LEM states are calculated when the sample is in the stress field and in a post-stress remanence state. To recover the point at which an applied stress alters the remanence state the stress has been applied in progressively higher intervals.

MERRILL incorporates stress into the magnetic energy by calculating an expression for

the uniaxial stress anisotropy. This depends on the anisotropy constant, λ_s, which, under the assumption that any spontaneous changes to the crystal dimensions when magnetised (magnetostriction) are isotropic, is:

$$\lambda_s = \frac{2}{5}\lambda_{100} + \frac{3}{5}\lambda_{111} \tag{6.2}$$

where λ_{100} and λ_{111} are the values of saturation magnetostriction in the [1 0 0] and [1 1 1] directions, respectively (Kittel, 1949; Ye et al., 1994), and are derived experimentally (Moskowitz, 1993). Using the isotropic assumption, this yields an approximation for the stress anisotropy energy:

$$E_\sigma = \lambda\sigma V = \frac{3}{2}\lambda_s\sigma V \sin^2\theta \tag{6.3}$$

where λ is the isotropic magnetostriction and θ is the angle between the magnetisation, $\boldsymbol{M}$, and the axis along which the stress is applied (Kittel, 1949).

Stress direction

To imitate the response of isotropic natural systems, each of the models in Table 6.1 was subject to stress in 20 directions. These directions were evenly-distributed across an octant of a sphere, separated according to a Fibonacci distribution (Fig. 6.2). This means that each model listed in Table 6.1 consists of an assemblage of 20 uniquely oriented grains, whose initial magnetisation directions which are evenly distributed over 90°, relative to a stress field (Fig. 6.3).

The 20 grains within each model were initialised with the same magnetisation state, i.e., the magnetisation vector direction and domain state of each of the grains are identical. Instead of rotating the grains to imitate a system like that in Figure 6.3, the stress axes were varied according to the Fibonacci distribution. This is easier, less computationally expensive and the modelled grains share the same frame of reference.

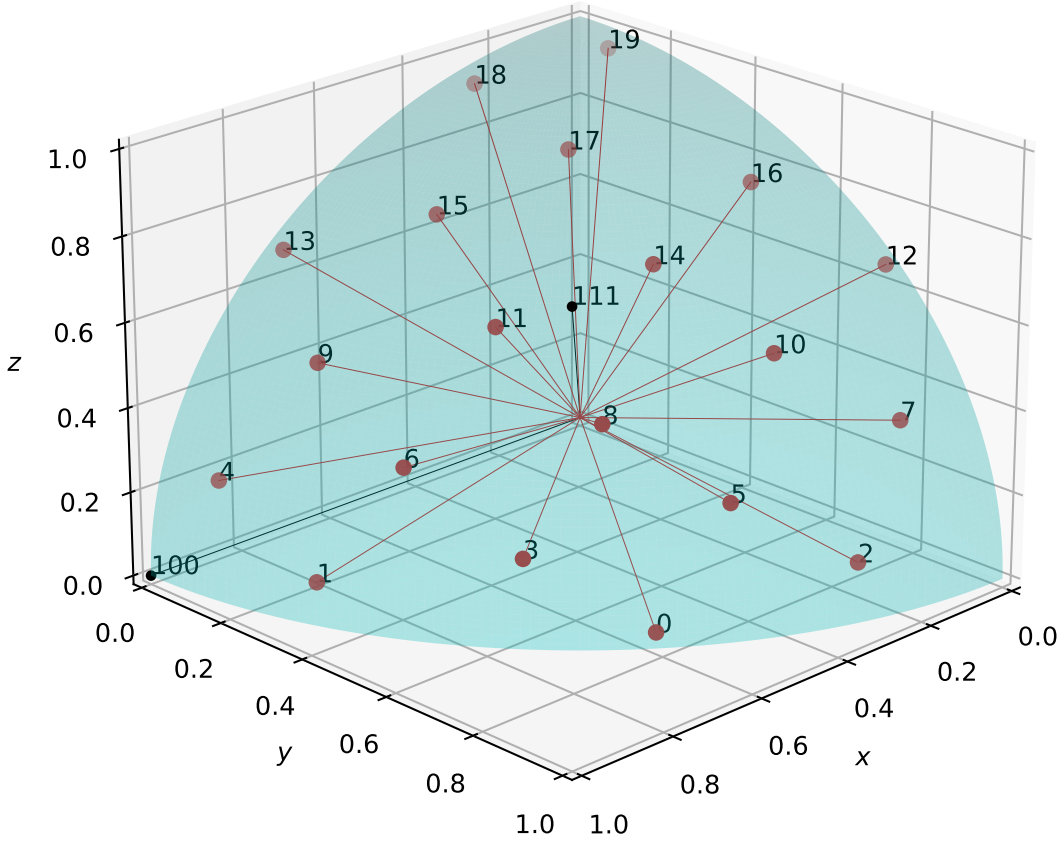


Figure 6.2: Stress orientations that have been applied to the grain. Stress was applied along 20 orientations, here numbered 0-19, evenly distributed across a spherical octant using the Fibonacci sequence to separate stress axes. Due to symmetry, this is equivalent to applying 160 (20×8) directions across an entire sphere. Each direction is represented by a red point and line towards the origin. Also plotted are the [1 1 1] and [1 0 0] directions with a solid black line and point.

Cyclic stress application

Alignment of the magnetisation with the stress field during a stressed phase is anticipated (Gattacceca et al., 2008), but this is not indicative of an irreversible change in the magnetic moment of the grain (Brown, 1949). To observe changes in the remanence state, stress was cycled between 'on/off' states, and was progressively increased in strength each time the 'on'

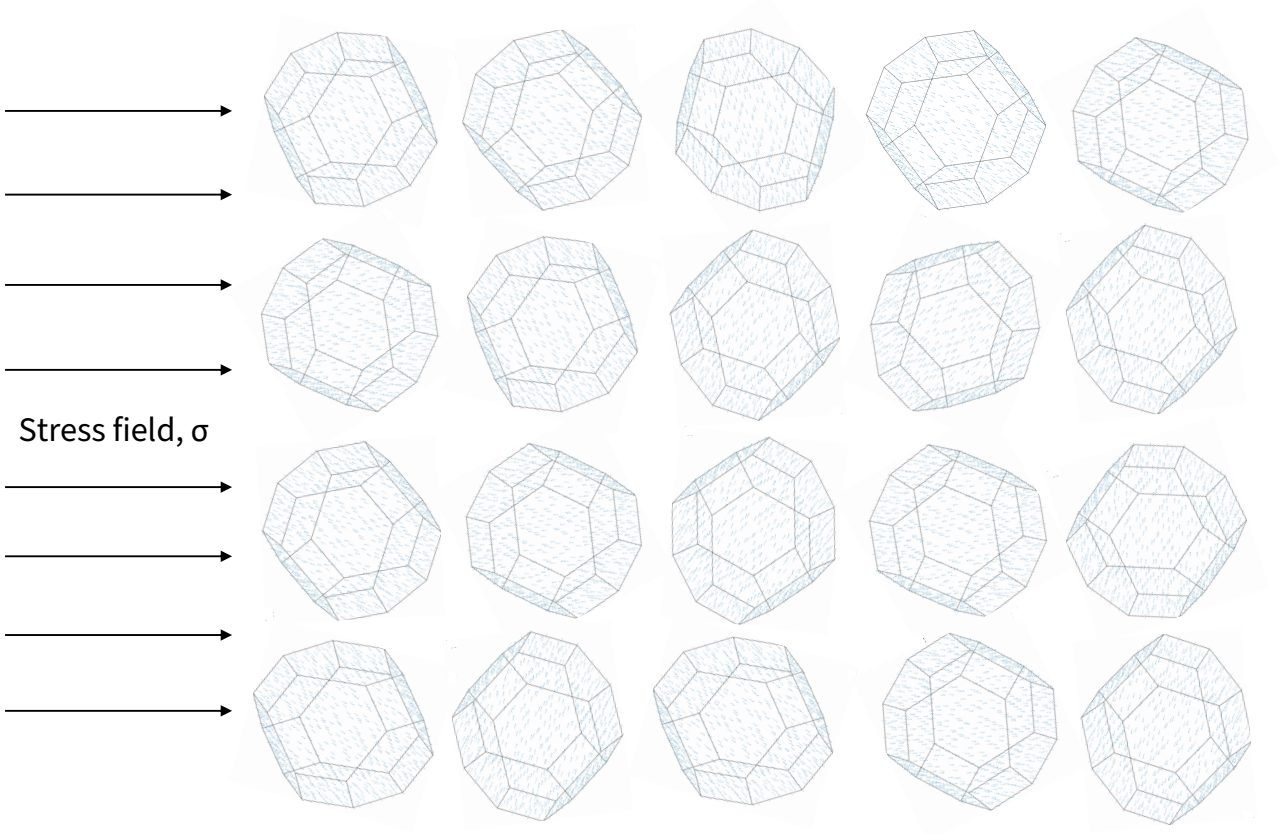


Figure 6.3: The experimental process is representative of 20 different, evenly-distributed orientations of identical grains that experience a single stress field, $\boldsymbol{\sigma}$.

state was applied. In practice, this allowed the grain to be measured in an unstressed state, before being stressed again at a greater value than previous. The unstressed state is effectively a remanence state, meaning the stress-induced threshold at which the remanence state undergoes irreversible change is able to be determined.

Stress was applied between 10 MPa and 3 GPa over three intervals:

1. From 0 to 100 MPa in 10 MPa intervals
2. Between 100 MPa and 1 GPa in 20 MPa intervals
3. Between 1 GPa and 3 GPa in 0.1 GPa intervals

which made for a total of 152 LEM solutions per simulation: 76 stressed and 76 remanence states. Varying the interval widths has allowed the modelling to be computationally inexpensive while ensuring enough precision to capture changes between magnetic states.

6.3.4 Crystalline (Miller) indices and equal area projection

Using equal area projections, any changes in the in-stress magnetisation and remanence of the magnetites can be quickly observed as a rotation of the magnetisation vector. As stress is applied cyclically, the remanence and in-stress magnetisation can be plotted at each interval. Where an irreversible change to the magnetic moment of the grain occurs, the remanence should move from one direction to another. Equal area projections transfer three-dimensional magnetic vectors into a two-dimensional, inclination, I, and declination, D, coordinate system (Tauxe et al., 2010). The Cartesian directions x, y, z are related to I and D as follows:

$$x = \cos D \cos I \tag{6.4}$$

$$y = \cos D \sin I \tag{6.5}$$

$$z = \sin I \tag{6.6}$$

For the crystalline indices relevant to the results presented in this work, it is pertinent to be aware where on the equal area projection certain crystalline axes lie, such as the easy [1 1 1] or long [1 0 0] axes (Fig. 6.4). When the Cartesian z-direction is negative (e.g., $[1\,1\,\overline{1}]$), markers will appear hollowed-out instead of as filled-block shapes.

6.4 Results

Using nine different initial magnetic states, five grain sizes, three shape elongations and 20 orientations within the stress field, a total of 520 simulations have been investigated which produce a comprehensive suite of results that are able to be used to examine the effect of a uniaxial stress on SD and SV magnetites.

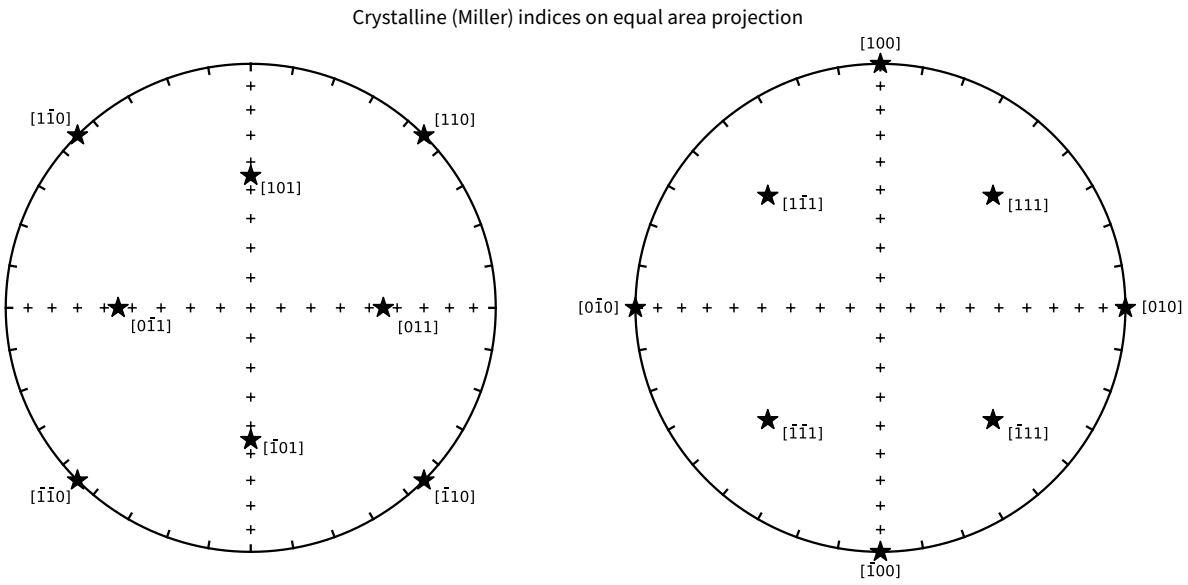


Figure 6.4: Schematic drawing demonstrating the location of positive-z crystalline directions on an equal area plot. The crystalline indices that are used in the results have been plotted on two separate diagrams for ease of reference. All the equal area projections share this same coordinate system where the x-direction [1 0 0] is vertical.

6.4.1 Effect of uniaxial stress on equidimensional SD magnetite

The suite of simulations (Table 6.1) included two equidimensional SD magnetite models with ESVDs of 50 nm and 80 nm, where grains were initialised with a magnetisation aligned with the easy $[1\,\bar{1}\,\bar{1}]$ direction. To examine the response of equidimensional SD grains to stress, in particular for an irreversible transition between domain states (SD to SV transition), the magnetisation is measured in a frame of reference that is in the direction of the remanence vector, $\boldsymbol{M_r}$. For an assemblage of magnetised grains, normalising this by the saturation magnetisation (M_s) means the domain state can be estimated quickly; for a single particle, SD magnetite typically has a ratio of remanence saturation to saturation magnetisation close to unity, $M_r/M_s > 0.8$, while SV states have M_{rs}/M_s ratios less than this (Muxworthy and Williams, 2006).

In the 50 nm grain, SD remanence was expected at all stresses; for equidimensional magnetite (where AR= 1), 50 nm is smaller than the minimum grain size for SV domain behaviour ($d_{min} = 64$ nm; Muxworthy and Williams, 2006). While the domain state remained unchanged, in some grains both the in-stress magnetisation, M_σ, and remanence, M_r, were rotated into an easy direction closer to the stress axis (Fig. 6.5). In the example shown in Fig. 6.5a, the

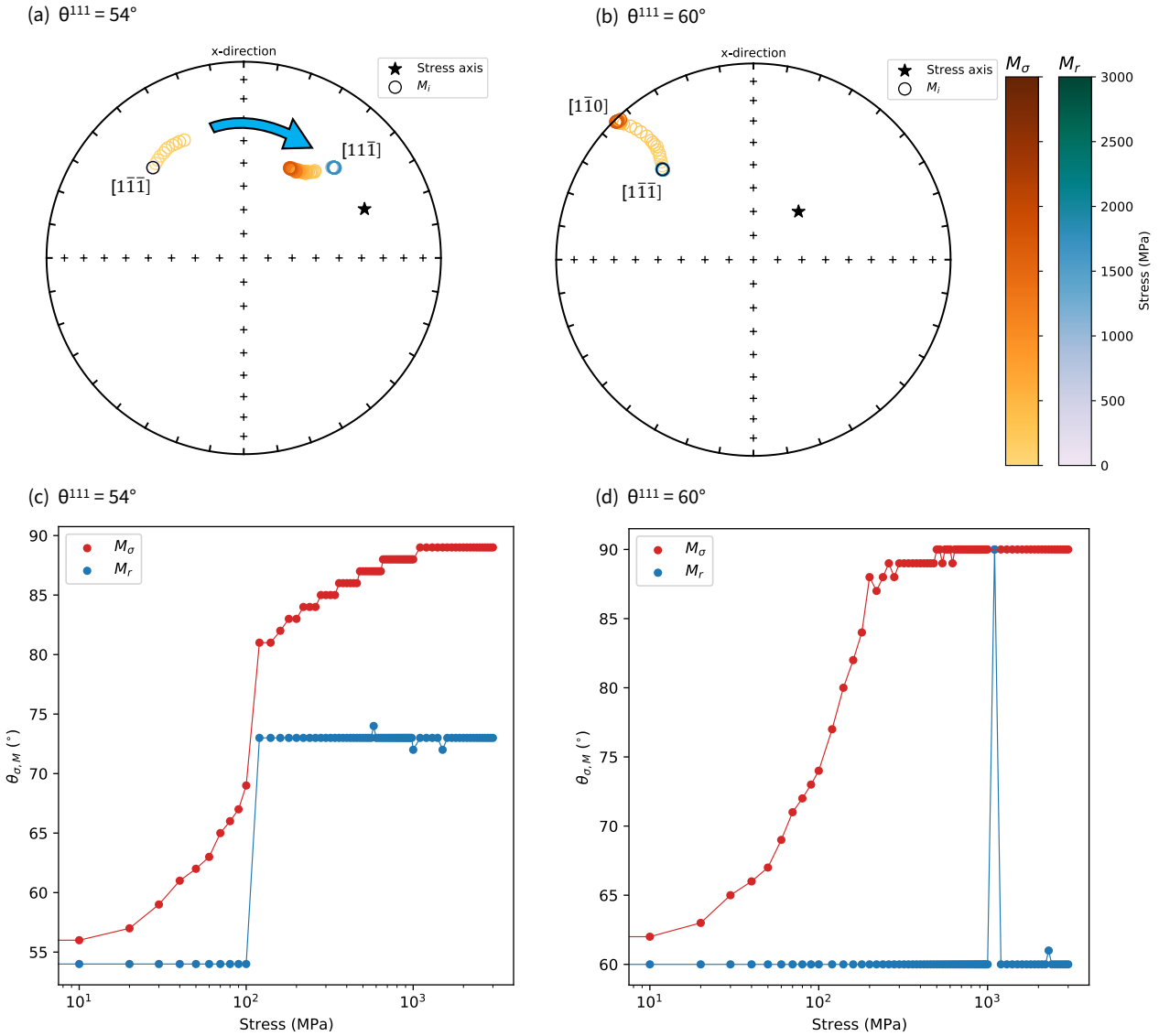


Figure 6.5: Equal area projections for 50 nm equidimensional SD magnetite grain where the grain was initialised with an SD remanence in the easy $[1\,\bar{1}\,\bar{1}]$ direction and stress was applied at an angle (a) $\theta^{1\bar{1}\bar{1}} = 54°$ and (b) $\theta^{1\bar{1}\bar{1}} = 60°$ from the initial magnetisation direction. Plots (c) and (d) show the angle between the stress axis and magnetisation vector ($\theta_{\sigma,M}$) at each stress interval for $\theta^{1\bar{1}\bar{1}} = 54°$ and $\theta^{1\bar{1}\bar{1}} = 60°$, respectively.

magnetisation was initially aligned with the easy $[1\,\bar{1}\,\bar{1}]$ direction. The remanence was then rotated into the easy $[1\,1\,\bar{1}]$ direction after the grain was subject to a 'rotation stress', σ_R, of 80 MPa, where it was then stable for the remainder of the 3 GPa cycle (Fig. 6.5c). In grains where the angle between the initial magnetisation and stress axis ($\theta^{1\bar{1}\bar{1}}$) was $\geq 60°$, the remanence remained unchanged from its initial orientation (Fig. 6.5b, d). However, for $\theta^{1\bar{1}\bar{1}} < 60°$, the remanence was deflected away from the initial magnetisation direction and rotated into a new easy direction, close to the stress axis.

For the larger 80 nm grain starting in a SD state, the results were similar to the 50 nm grain where magnetisations were rotated from the initial easy direction to another easy direction. However, one of the 80 nm grain orientations, where $\theta^{1\bar{1}\bar{1}} = 37°$, experienced a temporary change in remanence state from SD to SV (Fig. 6.6). The remanence was initialised in the easy $[1\,\bar{1}\,\bar{1}]$ direction, then transitioned domain state from SD to SV under a 'transition stress', σ_T, of 60 MPa. In addition to the domain state transition, the vortex that formed (Fig. 6.6c,d) was rotated into the hard $[1\,0\,0]$ direction (Fig. 6.6b). A second SD state then resulted from a much higher pressure, $\sigma_T = 900$ MPa (Fig. 6.6f), which was rotated perpendicular to the stress axis, into the easy $[1\,1\,\bar{1}]$ direction. Similar to the 50 nm case, this remanence was then stable up to the end of the stress cycle.

6.4.2 SV-SD threshold for equidimensional SV magnetite

This section looks at the case where equidimensional 80 nm magnetite, initialised with an SV remanence along the hard $[0\,1\,0]$ direction, experienced a change in remanence and in-stress domain states from SV to SD in every stress orientation that was modelled (Fig. 6.7). Magnetite grain sizes in this range, where $d_{min} < 80$ nm $< d_{max}$, may host either SD or SV domain states (Muxworthy and Williams, 2006). Hence, this assemblage allowed me to study the SV-SD domain state transition and the threshold stress, σ_T, at which transitions occur. σ_T has a strong dependence on θ, the angle between the initial magnetisation vector ($\boldsymbol{M_i}$) and the stress axis, and the starting state.

As the domain behaviour transitioned from SV to SD, the new SD remanence was aligned with the easy axis (Fig. 6.7d), similar to the SV-SD transition that was observed in the 80 nm particle (Fig. 6.6). The remanence was stressed into a number of easy axes, however, the specific easy axis the magnetisation was rotated into shared no obvious relationship with the angle between the initial magnetisation and stress axis, θ^{010}. The angle between the stress vector and the final remanence direction also appeared to share no correlation with θ^{010}.

On the other hand, the transition stress, σ_T, was dependent on θ^{010}. The 20 stress axes corresponded to values of θ^{010} between $19 - 88°$. Of these, the lowest σ_T occurred as θ^{010}

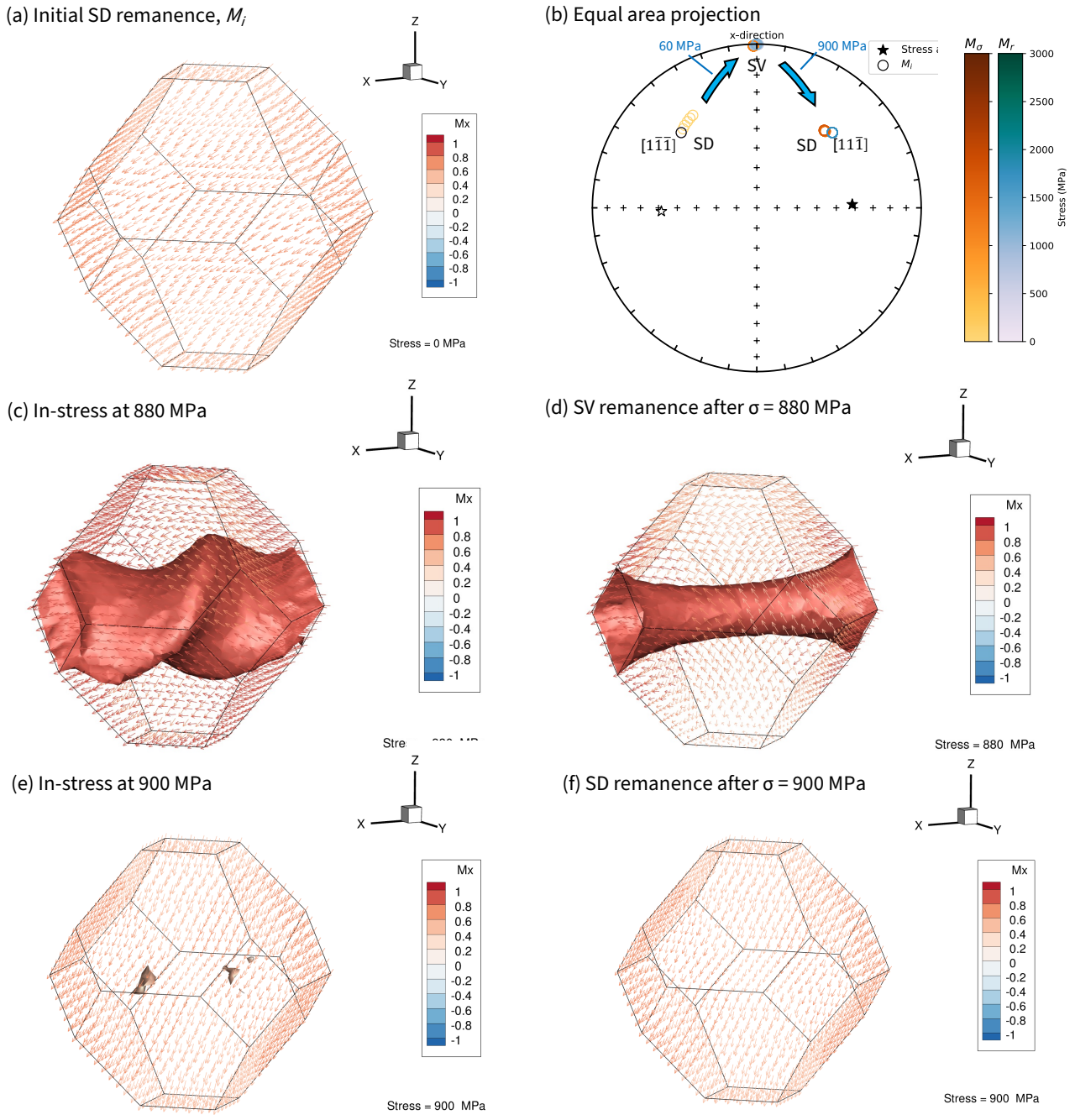


Figure 6.6: Equidimensional 80 nm magnetite grain where the angle between the stress field and easy axis, $\theta^{1\bar{1}\bar{1}}$, was 37°. (a) shows the initial SD remanence in the easy $[1\,\bar{1}\,\bar{1}]$ direction. (b) shows an equal area projection for remanence and in-stress magnetisations. Plots (c) and (e) show the in-stress magnetisation at 880 MPa and 900 MPa, respectively, while (d) and (f) show the remanence after these stresses were removed. The remanence state initially transitioned from SD to SV at 60 MPa, rotating into the $[1\,0\,0]$ direction, returning to an SD state aligned with the $[1\,1\,\bar{1}]$ direction after a 900 MPa stress had been applied.

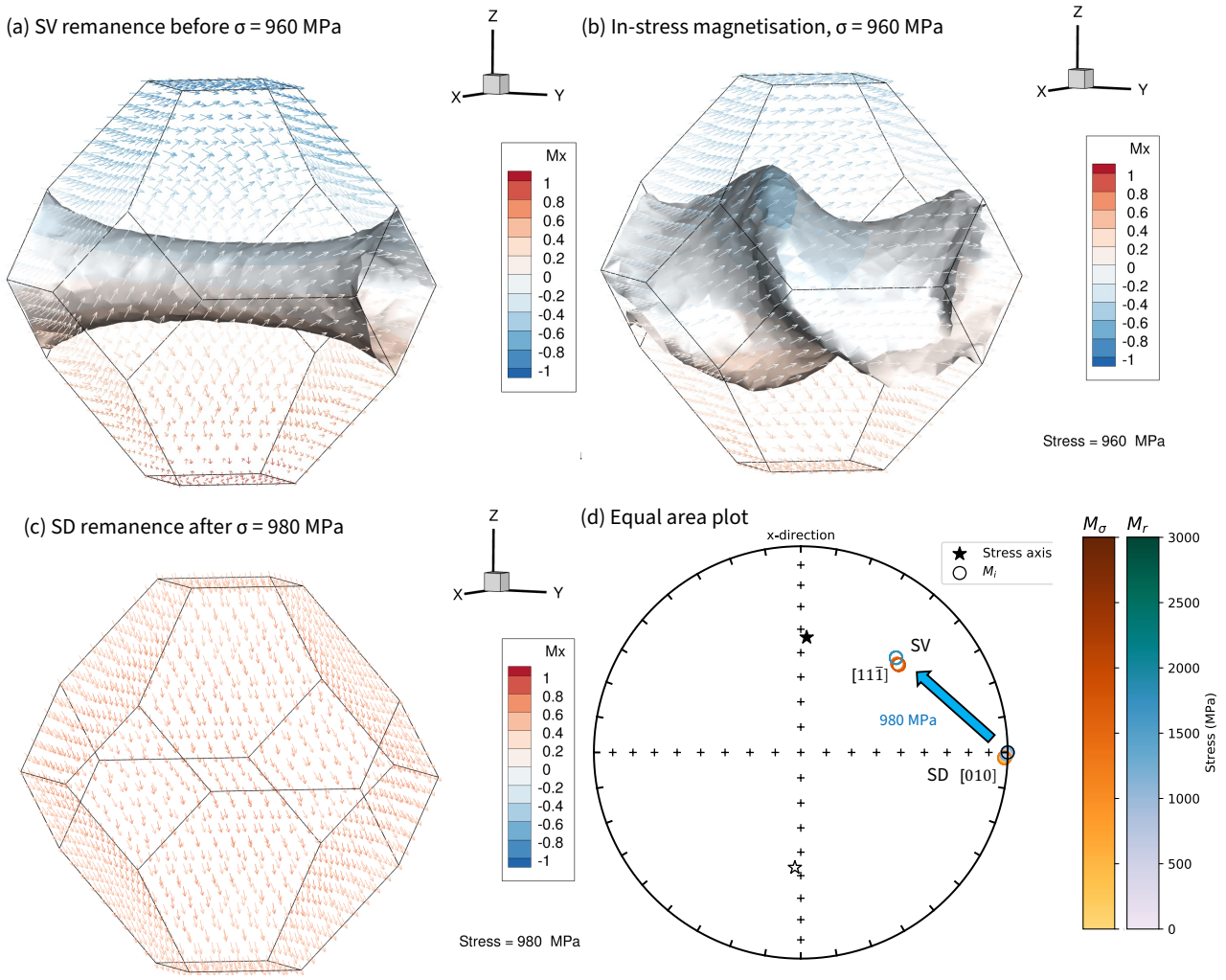


Figure 6.7: (a) The 80 nm equidimensional grain, initialised in an SV domain state aligned with the hard axis. For the grain shown, stress was applied close to perpendicular to the initial magnetisation vector, where $\theta^{010} = 88°$. (b) Following a stress applied at $\sigma_T = 960$ MPa, the grain underwent a transition from SV to (c), SD behaviour. This was the highest stress required to alter any of grains in the assemblage.

approached 45° (Fig. 6.8). As the angle θ^{010} approached zero or antiparallel, σ_T increased to much higher values; the maximum transition threshold was found at $\theta^{010} = 88°$, where $\sigma_T = 980$ MPa, though this value is a noticeable outlier as when viewed in context of the other data—the fit suggests this should be ~ 750 MPa (Fig. 6.8).

Observing the response of the magnetisation to stress on the assemblage-scale, the domain state changes from SV to SD after a stress of ∼500 MPa was applied, indicated by an initial remanence to saturation magnetisation ratio of $M_r/M_s \sim 0.7$, changing to M_r/M_s ∼1.0 (Fig. 6.9a). The remanence direction also changed in this range, rotating perpendicular to the hard [0 1 0] direction, aligning with the easy axis (Fig. 6.9b).

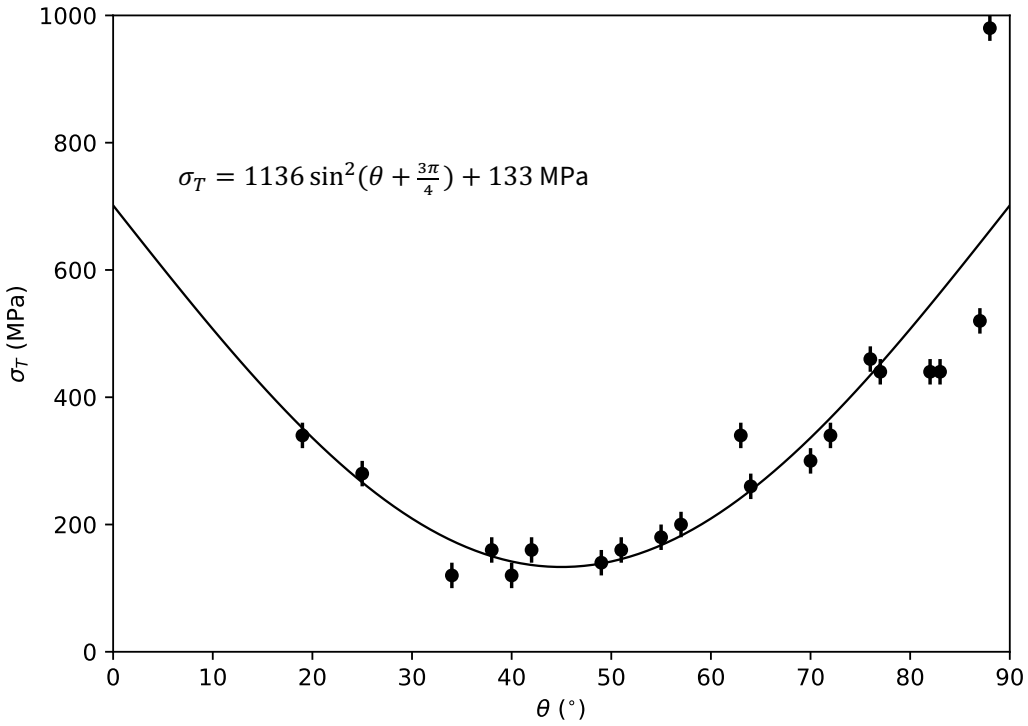


Figure 6.8: Stress threshold (σ_T) at which the SV to SD transition occurs, versus the angle between the stress field and the hard axis for the 80 nm, equidimensional grain described in Figure 6.7. The data is well described by a cosine function. Errors in the stress threshold are given as ±20 MPa due to this being the stress-cycle interval range.

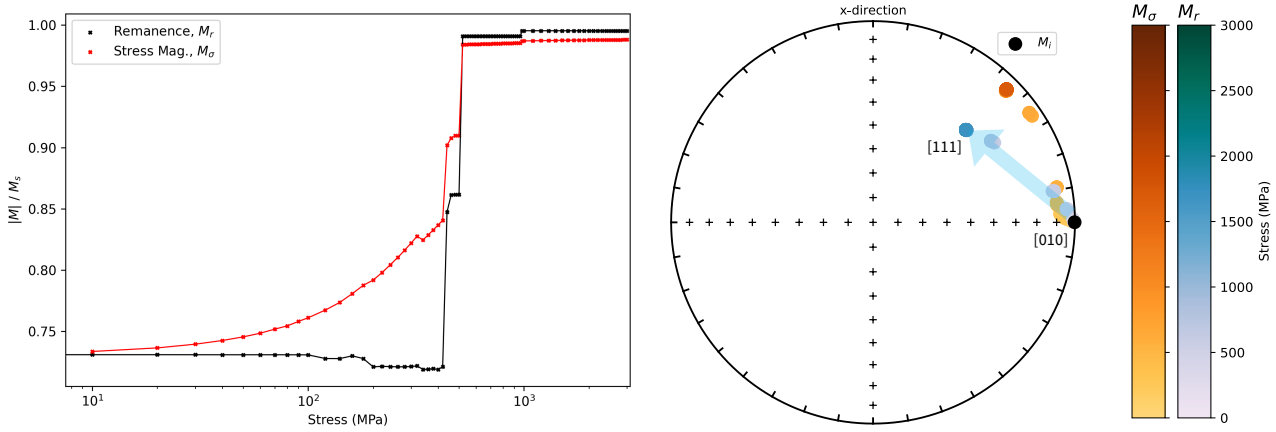


Figure 6.9: Average response of 20 grain 80 nm assemblage where grains were initialised with an SV remanence aligned with the hard axis. On average, grains underwent a domain state transition from SV to SD between 450-500 MPa, where the original magnetisation direction rotates into the easy [1 1 1] direction, perpendicular to the initial magnetisation's hard [0 1 0] direction.

6.4.3 Effect of uniaxial stress on equidimensional SV magnetite ≥ 100 nm

Three equidimensional magnetites with ESVDs of 100, 150 and 200 nm were modelled which were initialised with an SV domain state aligned with the easy direction: the 100 nm and 150

nm grains were initialised with a magnetisation aligned along the $[1\,\bar{1}\,1]$ direction, while the 200 nm grain was aligned with the $[1\,1\,1]$ direction. Rather than a change in domain state occurring, as was the case with the smaller 80 nm grain, the remanences of the 100 and 150 nm grains were irreversibly changed and aligned with an easy direction that was close ($\theta_{\sigma,M} < 20°$) to the axis along which the stress was applied (Fig. 6.10).

Using the $\theta^{1\bar{1}1} = 86°$ as an example, the smaller 100 nm grain was rotated from the $[1\,\bar{1}\,1]$ direction into the $[1\,1\,1]$ direction at 180 MPa (Fig. 6.10c), while the larger 150 nm grain was less easily coerced into the same direction, aligning with the $[1\,1\,1]$ direction at 240 MPa (Fig. 6.10d). On the other hand, the 200 nm grain was much less influenced by the stress cycle. The remanence of the 200 nm grain was only coerced away from the $[1\,1\,1]$ in one case, where $\theta^{1\bar{1}1} = 41°$. In this simulation, the alignment of the remanence shifted within 13° of the $[1\,\bar{1}\,\bar{1}]$ easy axis, however similar values for $\theta^{1\bar{1}1}$ did not reproduce this result.

6.4.4 Effect of uniaxial stress on elongated SD magnetites

The elongated grains were stretched in the $[1\,0\,0]$ direction. Four models with ESVDs of 50, 80 and 100 nm were initialised with an SD magnetisation that was aligned with the long $[1\,0\,0]$ direction, elongated by $50 - 100\%$ (AR$= 0.67 - 0.5$). There was no change in the M_r/M_s ratio across the assemblages and the direction between initial and final remanence states varied by $\leq 1°$ (Fig. 6.11). The only exception to this rule was observed in one 100 nm grain, where $\theta^{100} = 17°$ and the elongation was 50%, in which the remanence direction 'flipped' 180° after being stressed at 1.3 GPa.

The resistance of the in-stress magnetisation, M_σ, to alignment with the stress field, appeared to be dependent on θ^{100}. M_σ was seemingly unaffected by the applied stress where θ^{100} was close to 90° (Fig. 6.11a), whereas for grains where $\theta^{100} < 45°$ (Fig. 6.11b), M_σ moved towards the $[0\,\bar{1}\,\bar{1}]$ direction.

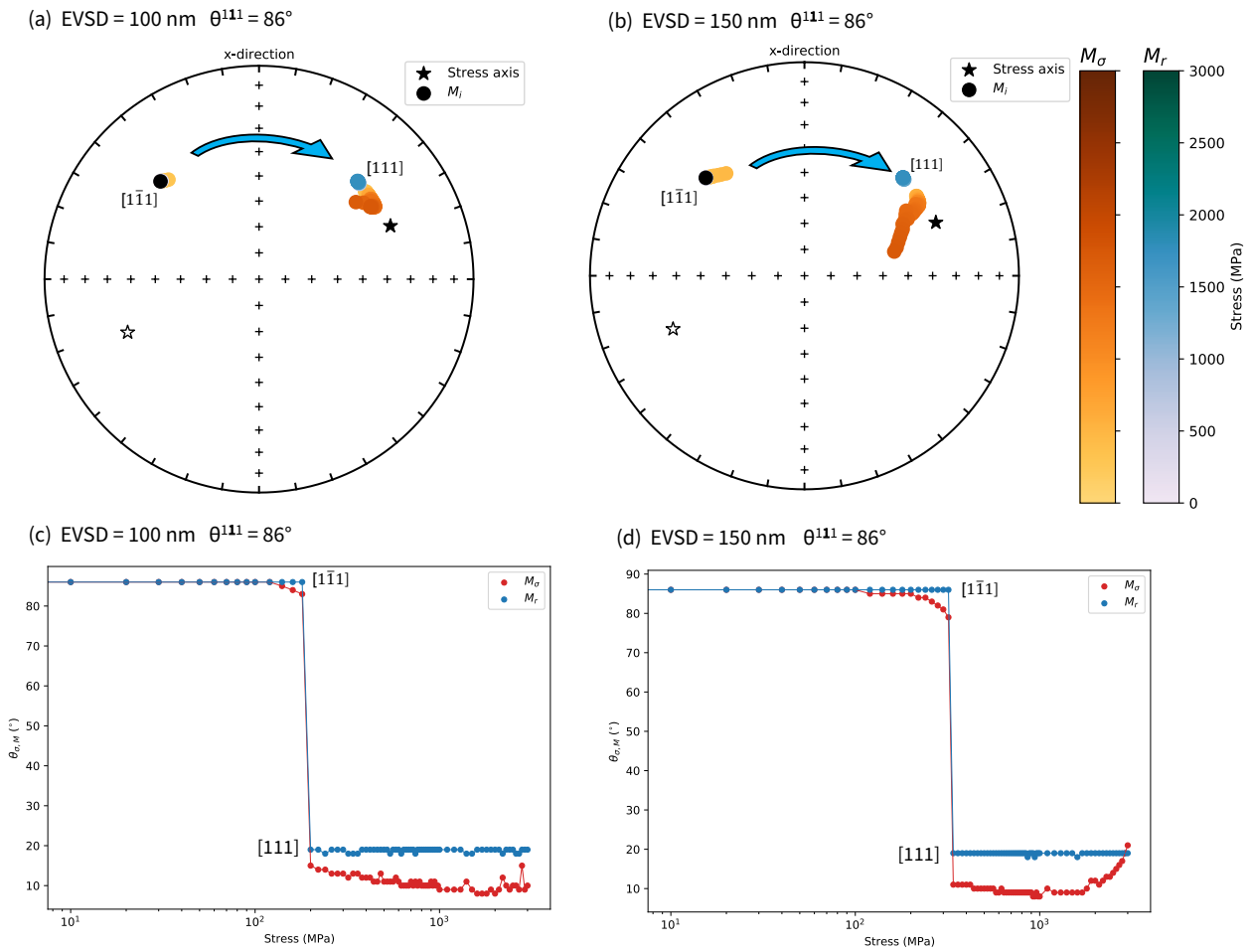


Figure 6.10: Equal area projections for equidimensional (a) 100 nm and (b) 150 nm magnetite grains which were initialised with an SV remanence aligned with the easy $[1\,\bar{1}\,1]$ direction. For both grains, this directional data was taken where the angle between the stress axis and easy direction were close to perpendicular, $\theta^{1\bar{1}1} = 86°$. The stress at which the rotation into the new easy axes occurred can be seen in (c) for the 100 nm grain, $\sigma_R = 180$ MPa, and (d) for the 150 nm grain, $\sigma_R = 240$ MPa.

6.4.5 Effect of uniaxial stress on elongated SV magnetites

A number of elongated grains initialised with SV remanences were modelled and subject to stress cycling. In this section I will compare the results of these simulations systematically: first by observing the effect of changing grain size, secondly by changing the alignment of the vortex from the short to the long axis and thirdly by comparing the effect of 50% and 100% elongation.

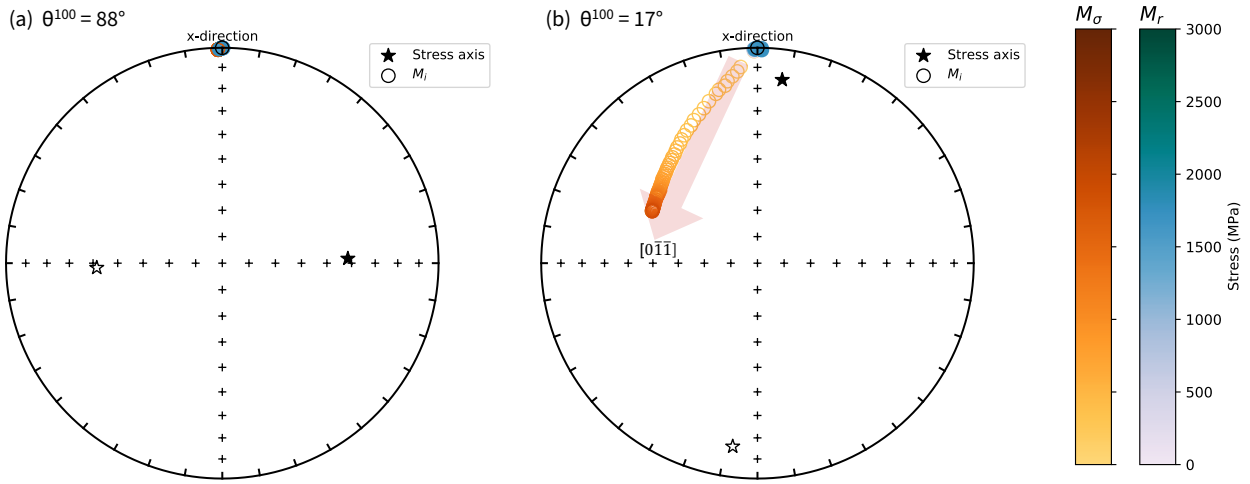


Figure 6.11: Equal area projections for 50 nm, 50% elongated SD magnetite where the initial magnetisation was aligned with the long [1 0 0] axis. Examples where (a) $\theta^{100} = 88°$ and (b) $\theta^{100} = 17°$ are shown.

Effect of grain size

Three grains were initialised with a vortex aligned along the short $[0\,\bar{1}\,\bar{1}]$ axis, each elongated by 50% and with ESVDs of 100, 150 and 200 nm. Across all stress axes, the 100 nm grain was generally unaffected throughout the stress cycle; there was some minor 'jitter' where the remanence vector moved slightly throughout the stress cycle, though the maximum change in remanence direction for any grain in the assemblage was 4°. However, the 150 nm grain was more easily coerced by the stress cycle. The 150 nm grain experienced a rotation between the initial and final remanence in a number of grains, where for angles $\theta^{short} < 33°$, the remanence direction was changed by up to $\sim 30°$ towards an intermediate direction between crystalline faces. Where $\theta^{short} = 45°$, the remanence rotated into the $[0\,0\,\bar{1}]$ axis, but for $\theta^{short} > 45°$, no rotation of the remanence vector was observed.

The 150 nm "V Short B" model (Table 6.1), a higher-energy domain state of a similar grain, was affected much more by the applied stress. In this model, the initial magnetisation was aligned with the $[0\,\bar{1}\,0]$ direction. Of the 20 grains simulated, 17 of the final remanences were aligned $< 4°$ with the $[0\,\bar{1}\,\bar{1}]$ direction. There was no observed correlation between the initial stress angle and the stress at which the remanence was rotated (σ_R). For the 17 grains which were rotated into the $[0\,\bar{1}\,\bar{1}]$ direction, it was found that the stress required to rotate the remanence was in the range 20 MPa $\leq \sigma_R \leq$ 80 MPa. The three remanences that were not

aligned were those at $\theta^{short} = 84°$ and $\theta^{short} = 81°$, where the final remanence aligned with the easy $[\bar{1}\,\bar{1}\,\bar{1}]$ axis at $\sigma_R = 90$ MPa and $\sigma_R = 50$ MPa, respectively, and at $\theta^{short} = 51°$, where the remanence first rotated into the $[0\,\bar{1}\,\bar{1}]$ direction at $\sigma_R = 40$ MPa, before rotating into the $[0\,0\,\bar{1}]$ direction after $\sigma_R = 160$ MPa was applied.

The larger 200 nm grain was the most easily coerced of the three grain sizes during the stress cycle. A total of 80% of the stress axes that were tested caused a permanent rotation of the remanence vector to within $\leq 5°$ of the easy $[1\,1\,1]$ or $[\bar{1}\,\bar{1}\,\bar{1}]$ directions, while three of the 20 grains rotated the remanence into the $[0\,1\,1]$ direction. The 13 grains which were coerced into the $[1\,1\,1]$ direction were done so at stresses such that 20 MPa $\leq \sigma_R \leq$ 80 MPa, similar to the 150 nm grain, while the two grains that 'flipped' to align with the $[\bar{1}\,\bar{1}\,\bar{1}]$ direction did so at much higher stresses, 220 MPa$\leq \sigma_R \leq$260 MPa. The remaining two grains rotated into nondescript intermediate directions.

Effect of vortex orientation: short vs long axis alignment

The result for the 50% elongated 100 nm grain, initialised with a remanence aligned with the short $[0\,\bar{1}\,\bar{1}]$ axis from the previous section, can be compared to a similar 50% elongated 100 nm grain that was initialised with a vortex aligned with the long $[1\,0\,0]$ axis. Where $\theta^{100} > 40°$, this grain was unaffected by the stress cycle. However, in four stress axis orientations, where $\theta^{100} \leq 35°$, the remanence vector was rotated perpendicular to the long axis, into the short $[0\,1\,1]$ direction (Fig. 6.12). This rotation was observed to occur at low-pressures: where $\theta^{100} = 17°$ and $\theta^{100} = 21°$, $\sigma_R = 220$ MPa, whereas for $\theta^{100} = 34°$, $\sigma_R = 440$ MPa and $\theta^{100} = 35°$, $\sigma_R = 420$ MPa.

Effect of grain elongation

Using another model of a 100 nm grain, with an SV remanence in the short $[0\,1\,0]$ direction, but elongated by 100%, the effect of elongation can be compared directly to the results from the previous section. Similar to the previous 50% elongated grain, the remanence stored inside this longer grain was also unaffected by the stress cycling. The 4° 'jitter' that was present between

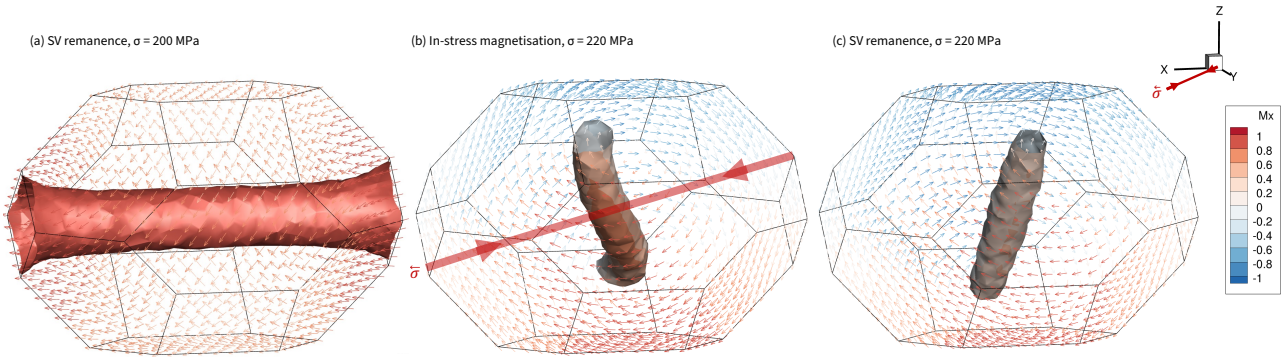


Figure 6.12: Meshes showing the vortex rotation from (a) the long [1 0 0] to (c) short [0 1 1] direction for 100 nm 50% elongated magnetite. In this model, the stress was applied such that $\theta^{100} = 21°$; the stress direction, $\vec{\sigma}$, is included for reference. The remanence was rotated from its alignment with the [1 0 0] direction to the [0 1 1] direction after being subject to a stress of 220 MPa (b).

start and end remanence states for the 50% elongated grain was almost eliminated here, where the maximum rotation of the remanence vector was $\leq 1°$ over the assemblage.

Investigating the effects of elongation further, I compare the two models of 200 nm magnetite that were initialised with an SV remanence along an intermediate crystalline axis. The intermediate core direction was most closely aligned with the easy [1 $\bar{1}$ 1] direction, though the 50% elongated grain was offset by 5°, and the 100% elongated grain offset by 23° from this axis.

For the 50% elongated grain, only two grains in the assemblage remained unaffected by the stress cycle, while the rest underwent remanence vector rotation from the initial intermediate SV remanence to their final axis, where 120 MPa $\leq \sigma_R \leq$ 260 MPa. Correlation was unclear between the angle of the stress direction relative to the initial 'intermediate' magnetisation (θ^{int}) and final remanence orientation. In most cases, the remanence vector rotated within $< 20°$ of the stress axis. However, where θ^{int} was between $\sim 45 - 70°$, the remanence instead favoured alignment with the easy [1 1 1] direction.

On the other hand, the 100% elongated 200 nm model underwent rotation at lower stresses, where 40 MPa $\leq \sigma_R \leq$ 140 MPa, although many of the grains in this model saw a two-phase stress rotation. Here, the remanence vector was first rotated into one crystalline direction before being pushed into a new direction at higher stress. The most common sequence was a rotation from the initial remanence into the [1 0 0] direction, followed by a subsequent rotation into the [1 1 1] direction (Fig. 6.13). The stress at which the second rotation occurred—this happened in 17 out of the 20-grain assemblage—was unpredictable and appeared uncorrelated with the

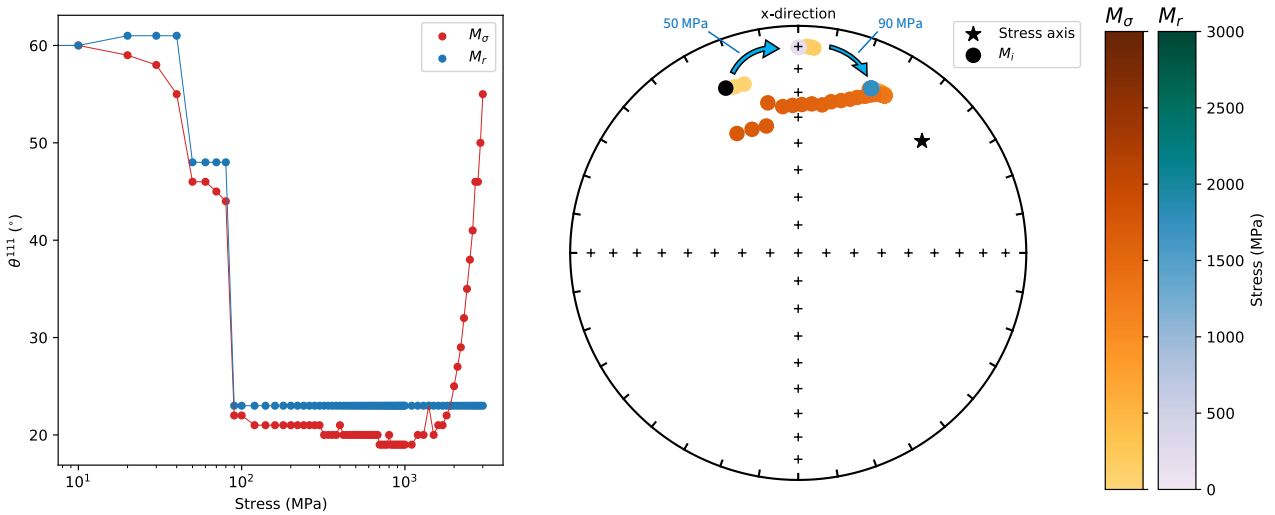


Figure 6.13: Vortex rotation for the 200 nm, 100% elongated particle as it undergoes the stress cycle. (a) the angle between the $[1\,\bar{1}\,1]$ axis and magnetisation vector ($\theta^{1\bar{1}1}$) and (b) an equal area projection showing relative directions during the stress cycle. The initial alignment was with an intermediate direction, close to the $[1\,\bar{1}\,1]$ easy axis ($\theta^{1\bar{1}1} = 23°$). The grain is rotated close to the $[1\,0\,0]$ long (x) axis at $\sigma_R = 100$ MPa, before undergoing a second rotation at $\sigma_R = 160$ MPa towards the $[1\,1\,1]$ easy axis.

stress axis. The range in which the second rotation occurred was 90 MPa $\leq \sigma_R \leq$ 360 MPa.

6.5 Discussion

The numerical modelling results presented in this study have shown that when subject to low stress, < 1 GPa (Fig. 6.14), the remanence stored within a number of crystalline shapes, domain structures and sizes of magnetite grains will undergo irreversible change. In cases where $d_{min} < d < d_{max}$, this can include a change of magnetic domain state, from SV to SD and vice versa (Fig. 6.7), but for most of the models where a change in remanence occurred, this was a rotation of the remanent magnetisation vector. For an assemblage of grains that are heterogeneously or randomly magnetised with respect to the direction of an applied stress field, this can be interpreted as acquiring a new remanent magnetisation, or a demagnetisation that randomises the preexisting remanence.

The results have shown that the response of the grains studied to an applied stress is dependent on a number of factors: (1) the angle at which the stress field is applied with respect to the initial magnetisation vector and magnetocrystalline axes directions, (2) the elongation of

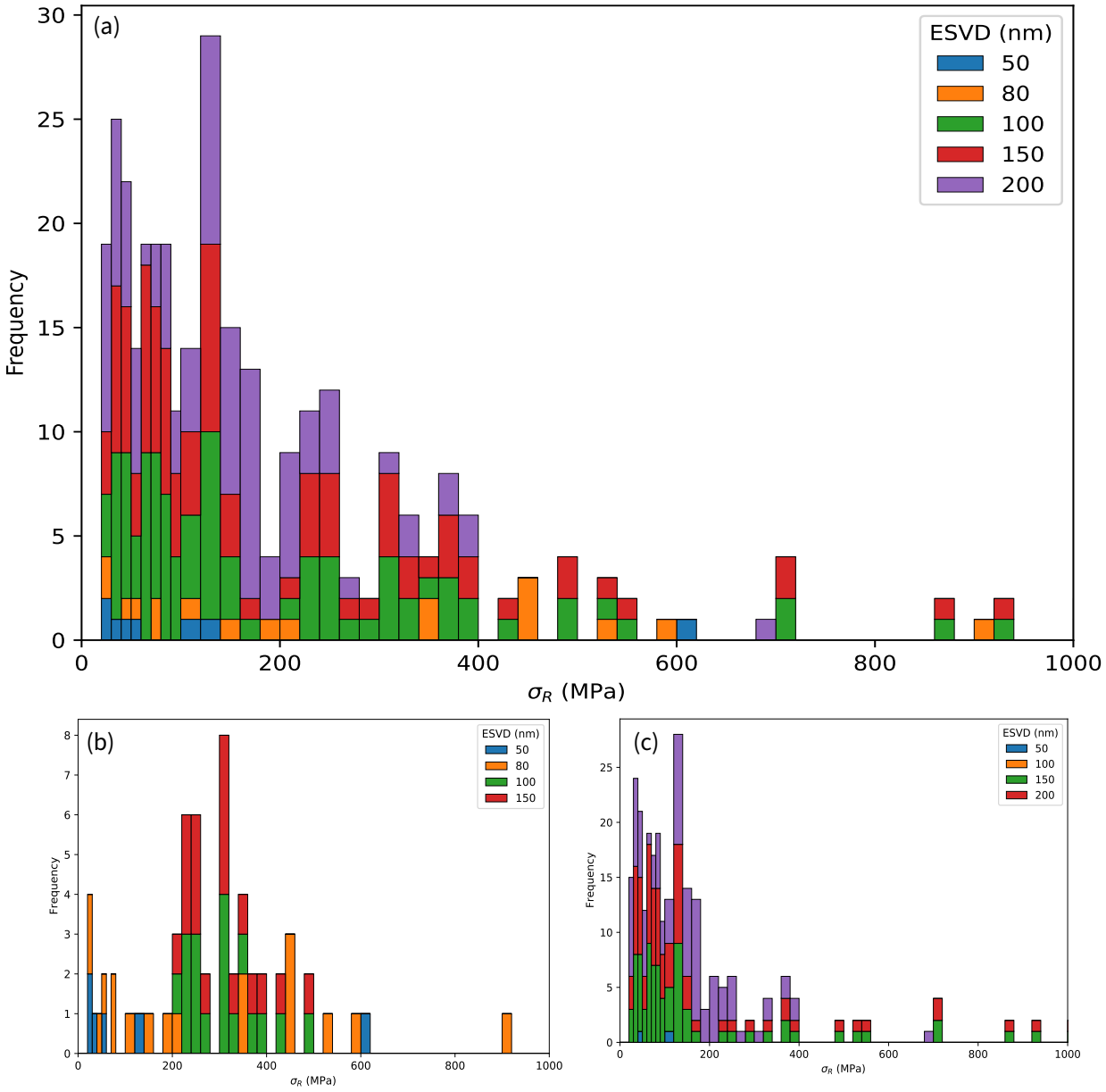


Figure 6.14: Histograms demonstrating the stress, σ_R, at which the remanence vector was rotated into a new axis. Rotations are determined as a change from the initial direction to another crystalline axis and the histogram bars are then coloured by grain size of the model. In models where more than one rotation occurred, only the first has been shown. (a) includes 258/520 models where a rotation was observed—two models, where $\sigma_R > 1000$ MPa, are not shown—while there was no rotation observed in the other 260 models. (b) separates out just equidimensional (AR= 1) models and (c) the elongated (AR$\neq$ 1) models.

the grain, (3) the initial domain state, (4) the amount of stress applied and (5) the size of the grain. This has significant implications for future interpretations of the remanences carried by meteorites, which are known to have experienced impact-induced stresses similar to those that have been applied in this study, between 10 and 3000 MPa. In this section, I will discuss the

results of the numerical modelling and attempt to identify patterns in the magnetic behaviours.

6.5.1 Stress-induced change to the remanence of SD magnetites

Equidimensional SD magnetites

Magnetite grains with ESVD sizes of 50, 80 and 100 nm were given an initial SD remanent magnetisation before being subject to stress cycling. In the equidimensional grains studied (AR= 1), this initial magnetisation was aligned with the easy [1 1 1] axis.

Where equidimensional SD magnetites were aligned with the easy axis, applying stress rotated the remanence away from the stress axis and into a new easy direction, perpendicular to the stress axis. This effect occurred in grains where the angle between the stress axis and initial magnetisation was $< 60°$ at rotation stresses, σ_R, which were < 100 MPa (Fig. 6.5). For grains where the angle was $\geq 60°$ the final remanence remained unchanged from its initial orientation. These observations would suggest that in the case of a meteorite where the remanence direction is found to be approximately uniaxial, the stress direction can be recovered as it would have been perpendicular to the remanence vector.

All of the 50 nm magnetites retained their SD remanence state as this was simply rotated into the new easy direction. This was also the case for the majority of the 80 nm grains, however, one of the 80 nm magnetites was seen to change domain state from SD into SV, aligned with the original SD remanence $[1\,\bar{1}\,\bar{1}]$ direction (Fig. 6.6a). The SD-SV transition occurred at very low pressure, $\sigma_T = 60$ MPa, as the SV configuration was lower energy than the SD one. The core of the vortex was aligned with the hard [1 0 0] direction, until the grain transitioned back to an SD state at higher pressure, $\sigma_T = 900$ MPa (Fig. 6.6c), which was rotated into the easy $[1\,\bar{1}\,1]$ direction, perpendicular to the stress axis (Fig. 6.6b). This grain size falls very close to the 'unstable zone' (Nagy et al., 2017)—a region in which the thermal blocking temperature in magnetite grains $\sim 80 - 100$ nm ESVD decreases with increasing grain size—and was the only grain throughout the investigation in which an SD state was observed to transition into an SV one. This suggests that the SD-SV transition is unusual and may be unique to this case where the stress direction, initial magnetisation and amount of stress applied produced a

'near-perfect' opportunity for the transition to occur.

Elongated SD magnetites

Elongated magnetites (AR= $0.67-0.5$) were initialised with an SD remanence that was aligned with the long [1 0 0] axis. These grains were resistant to both remanence rotation and domain state changes. In cases where the stress axis was $< 45°$ from the long axis, the in-stress magnetisation moved to align perpendicular with the stress axis, although the remanence direction remained unchanged (Fig. 6.11). For cases where the stress was applied $> 45°$ from the initial SD remanence, neither the remanent nor stressed magnetisations were affected, up to 3 GPa. This would suggest that SD remanences aligned with the long axis have remained unaltered by stress. The remanence within a grain that has been stressed and then heated, for example, may be coerced into alignment with the stress direction, so long as the angle between the initial remanence and stress direction is $< 45°$.

6.5.2 Stress-induced change to the remanence of SV magnetites

SV-SD transition for equidimensional 80 nm magnetite

The SV-SD transition was observed in all of the 80 nm grains investigated, where $d_{min} < 80$ nm $< d_{max}$ (Fig. 6.7). Where 80 nm equidimensional magnetites were initialised with an SV remanence aligned with the hard direction, the remanence was seen to transition from SV to SD in all cases. The final SD remanence was always aligned with the easy axis. Contradictory to the uniaxial SD grains, this easy direction was found to be close ($< 20°$) to the stress axis. The stress required to transition an SV remanence into an SD structure was found across a range, 160 MPa $\leq \sigma_T \leq$ 980 MPa, where σ_T was found to depend on the angle between the initial remanence and the stress axis (Fig. 6.8). Grains were seen to most easily transition between domain states where $\theta = 45°$, increasing as this angle approached the parallel or perpendicular directions.

Understanding the SV-SD transition due to an external stress may be the most important magnetic transition when reviewing palaeomagnetic interpretations for magnetite-bearing

meteorites. The evidence suggests that meteorites with a preexisting SV remanence will be overwritten at stresses commonly experienced in planetesimal-scale collisions (>> 1 GPa). Moreover, the new remanence(s) will align closely to the applied stress direction, along the easy axis. For an assemblage of SD and SV magnetites which are similar in size, a narrow range of pressures could be responsible for the domain-mixture. For example, a 250 MPa shock wave (which did not significantly heat the target) would be seen to transition all SV particles with a magnetisation vector between $\sim 30 - 60°$ from the applied stress into SD remanences, aligned along an easy axis close to the stress direction (Fig. 6.8). For angles that are outside of this range, grains would remain unaffected, retaining their initial magnetisation.

These results support the findings of Gilder et al. (2002) which found a $\sim 200\%$ increase in the M_{rs}/M_s ratio with an an applied stress of ~ 2.5 GPa to an SD-PSD mixture of 'chiton teeth' (Kirschvink and Lowenstam, 1979). Using magnetite samples with an average grain size of 100 nm, Gilder et al. (2002) found with increasing pressure the SD-PSD assemblage became 'truer' SD behaviour, which suggests that some of the PSD grains had transitioned into SD domain states. The increase in M_{rs}/M_s with increasing stress has also been observed in other experiments (Nagata and Kinoshita, 1964, 1965) and could now be explained by the SV-SD transition observed in this study.

Equidimensional SV magnetites

Where equidimensional magnetites were initialised with SV magnetisations in the easy direction, with ESVD sizes $d > d_{max}$, the remanence was coerced into alignment with new easy axes close to the stress direction (Fig. 6.10). This is the opposite effect observed in the equidimensional SD grains, which instead were rotated into easy axes perpendicular to the stress axes. The rotation of the SV remanence into new easy directions was seen to happen at very low pressures, < 0.2 GPa, although the threshold required to rotate the remanence direction increased with increasing grain size. For the same stress direction, at an ESVD of 100 nm, $\sigma_R = 180$ MPa, whereas for the 150 nm grain, $\sigma_R = 240$ MPa. The 200 nm grain was far more resistant to the stress cycle, where the remanence only changed in one of the 20 stress directions applied. This suggests that SV remanences in equidimensional magnetites are only

likely to rotate due to an applied stress as d_0 approaches d_{max}.

Elongated SV magnetites

The majority of the models tested in this study were elongated (AR< 1) magnetites with ESVD sizes between 100-200 nm, initialised with a non-uniform SV magnetisation. As it has been shown that these types of grains are the most likely to carry the stable, long-lived component of the NRM hosted within meteorites (Nagy et al., 2017, 2019), it is imperative that the response of these grains and assemblages to stress are better understood.

Where the initial magnetisation and axial ratio were kept consistent (AR= 0.67), the effect of increasing grain size decreased the resistance of the grains to stress, meaning the larger grains were more easily coerced into a remanence rotation than smaller ones. Comparing grains with an initial magnetisation aligned with the short axis, those with an ESVD of 100 nm were largely unaffected, other than a small $< 5°$ 'jitter'. Larger grains, however, saw their magnetic moment rotated at very low pressures; $\sigma_R < 0.1$ GPa for both 150 nm and 200 nm grains (Fig. 6.14). The final remanence direction varied, most often aligning with either the $\pm[0\,1\,1]$ direction (Fig. 6.12) or the easy $\pm[1\,1\,1]$ axes, with no apparent dependence on the angle between the stress vector and initial magnetisation.

In the case that the initial magnetisation was already aligned with the long $[1\,0\,0]$ axis, the applied stress had little effect when the angle between the stress and initial remanence was $> 40°$. However, in the cases where this angle was sufficiently small, $\leq 35°$, the remanence was rotated into the favoured $[0\,1\,1]$ direction for low stresses, where $\sigma_R < 0.45$ GPa. These observations indicate a preference for SV magnetites to favour the short axis over other remanence orientations. Moreover, the low stresses these effects occurred at implies that meteorites containing such grains would experience a reorientation in most impact events.

Finally, the effect of increasing the elongation of the grain from AR=0.67 to AR=0.5 appeared to increase the stability of a 100 nm grain which was initialised with a remanence along the short axis, but decrease the coercivity of a 200 nm grain which was initialised with a remanence aligned along an intermediate axis between crystalline faces. The latter case presented a

new phenomenon that was not observed in previous models; where the elongation was greater (AR= 0.5), remanences initialised along an 'intermediate' direction were found to first rotate into the long [1 0 0] direction at very low stresses, $\sigma_R < 0.15$ GPa, before later rotating into the easy [1 1 1] direction at higher stresses, $\sigma_R < 0.4$ GPa (Fig. 6.13). For similar remanence states, but where AR= 0.67, the remanence favoured intermediate directions, $< 20°$ from the stress axis. This string of results are difficult to reconcile with one another; for already-stable smaller grains, elongation seems to improve their stability. For large grains with a poorly defined initial magnetisation, the decrease in axial ratio to AR= 0.5 instead means the grain tries to rotate the remanence into the easy axis, though insufficiently elongated grains rotate into a new, poorly-defined final remanence state, close to the stress axis.

6.5.3 Comparison to analytical SD theory and experimental data

Equidimensional SD magnetite was found to rotate into easy axes close to the stress field in grains where the angle between the initial magnetisation and the stress axis was $< 60°$ (Fig. 6.5). This implies that, for a large assemblage of randomly distributed grains of equidimensional SD magnetite, around two-thirds of grains would experience a permanent magnetic moment (remanence vector) rotation when subject to stress < 0.1 GPa. On the other hand, the remanence contained within elongated SD grains remained unchanged over the entirety of the 3 GPa stress cycle.

For the magnetic moment of an SD grain to undergo permanent rotation, the stress supplied must overcome the microscopic coercive force, H_K, of that particular grain (see §2.4.3). Derived from classical single domain theory, for a grain under a stress σ, the microscopic coercive force is replaced by H'_K (Dunlop et al., 1969), which is:

$$H'_K(\theta) = \left(M_s(N_b - N_a) - \frac{3\lambda_s\sigma}{\mu_0 M_s} \right) \sin^2\theta = \left(H_K - \frac{3\lambda_s\sigma}{\mu_0 M_s} \right) \sin^2\theta \tag{6.7}$$

where N_a and N_b are demagnetising factors which apply when M_s is pointing parallel or perpendicular to the easy axis, respectively. The first term, $M_s(N_b - N_a)$, arises from shape anisotropy, while the second term is a reduction of coercivity due to the applied stress. For magnetite,

$3\lambda_s\sigma/\mu_0 M_s \approx 0.25$ mT/MPa (Dunlop et al., 1969; Dunlop and Özdemir, 1997), although due to the many possible combinations of grain shape, size and relative remanence orientations, in practice this reduction is much lower.

Gilder et al. (2006) experimentally investigated the effects of static stresses between 160 MPa and 2.22 GPa on organic SD magnetite ('chiton teeth'; Kirschvink and Lowenstam, 1979). Their experiments found that 85% of the magnetisation in their samples was lost when subject to stresses ~ 1.8 GPa. The decrease in the magnetisation of SD samples was found to be well described by two regimes: for pressures below 1.5 GPa, the percentage decrease in magnetisation followed a linear law, $\Delta M_\% \approx 1 - 0.45P$, where $\Delta M_\%$ is the percentage of the the initial magnetisation remaining and P is the pressure in GPa, while above 1.5 GPa the relationship changed to a general approximation where $\Delta M_\% \sim 1/P$.

These stress demagnetisation regimes are inconsistent with the findings in this study for purely SD magnetite; in the two-thirds of the assemblage, where the remanence vector was rotated, the vector aligned perpendicular to both the initial magnetisation and the stress axis and this had occurred by $\sigma_R < 0.1$ GPa. From the regimes above, $P = 0.1$ GPa would suggest that $\Delta M_\% \approx 95\%$. This inconsistency may be due to the chiton teeth sample; chiton teeth have an average grain size of 100 nm and contain a significant fraction ($\sim 30\%$) of PSD grains (Kirschvink and Lowenstam, 1979). As shown in the results, PSD grains are generally more susceptible to stress-induced remanence rotation than SD grains, but at the time of these experiments, the widespread understanding of PSD grains was that they did not significantly contribute to the remanence—which is now known to be incorrect (Nagy et al., 2017). It is therefore difficult to reconcile the results of Gilder et al. (2006) for an SD-PSD magnetite mixture with the idealised SD and SV magnetite grains that have been examined in this study.

6.5.4 Palaeomagnetic implications for meteorites

The widespread use of hysteresis parameters magnetic mineralogy characterisation has long-identified PSD and MD particles as the most abundant magnetic particle domain state present in natural rock and meteorite samples (Day, 1977). Meteorites with M_{rs}/M_s ratios consistent

with PSD and MD particles have been shown to host strong, oblate magnetic fabrics acquired billions of years ago, close to the age of the Solar System (Muxworthy et al., 2017). Since the magnetic recording fidelity of MD particles is known to be poor (Dunlop and Xu, 1994) and the interpretation that only SD particles carry the dominant stable component(s) of the NRM is known to be wrong (Nagy et al., 2017), the NRM is likely dominated by PSD particles which is why it is pertinent to understand how the remanence may have been affected by impacts since it was recorded.

The results in this study suggest that the remanence stored within PSD and SD particles is permanently altered at very low stress (Fig. 6.14). Meteorites are known to have been exposed to shock pressures in the 1-10 GPa range (Stöffler et al., 1991; Scott et al., 1992), hence, their magnetisations are highly likely to have been altered during impacts—even in the absence of any thermal activation or external magnetic field. In the context of primitive chondrites, for example, this could mean a remanence that is of Solar nebula origin is altered long after the cessation of the nebula field as remanences are rotated out of their initial orientations.

When considering an assemblage of grains similar to those examined in this study, the rotation of many remanences into arbitrary easy axes would effectively cause a demagnetisation of that assemblage; as remanent magnetisations of SV grains were coerced into alignment with the stress direction, while SD grains tended towards the perpendicular (Fig. 6.15). Many grains examined in this study were shown to be resistant to an applied stress, whether that be due to the angle between their initial remanence and the applied stress field, the crystalline-axis alignment of the remanence, the grain size or shape elongation. This implied that in a natural assemblage where there exists a distribution of many grain sizes, shapes and domain states, many of them will be affected and demagnetised when subject to stress but some fraction will retain their original remanences.

The most stable grains were elongated $d_0 \leq 100$ nm SD grains as the remanence was seen to be unaffected by the stress cycle (Fig. 6.15b). Elongated magnetite found in an SD state can assumed to have been unaltered by a stress up to 3 GPa since it acquired this magnetisation. SV magnetisations tend to rotate towards the stress direction (Fig. 6.15a, c), which, as seen throughout the modelling, generally favours rotation into a short or easy direction that is close

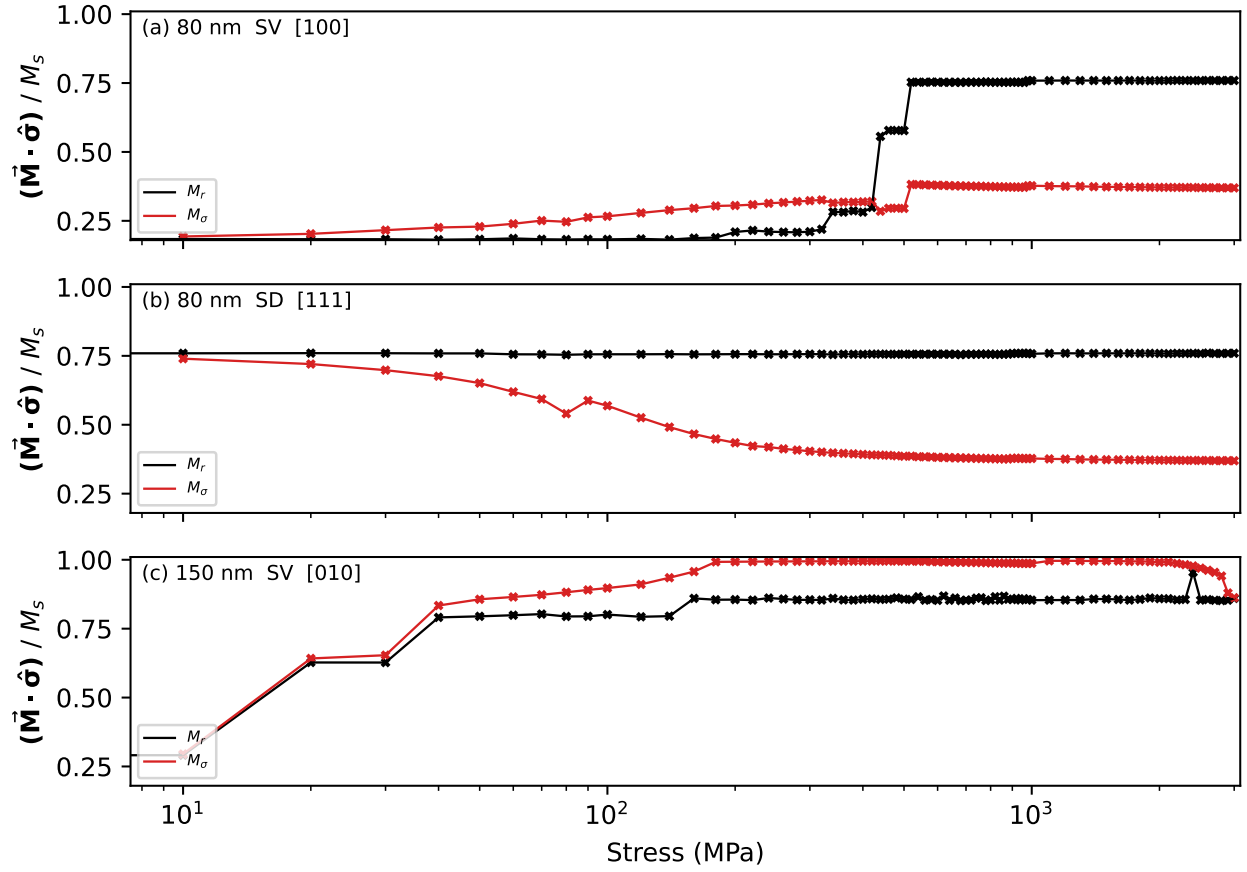


Figure 6.15: Averaged across the 20-grain assemblage, the magnetisation in the stress direction, $\hat{\sigma}$, is shown for (a) an assemblage of 80 nm ESVD grains, initialised with an SV magnetisation in the long $[1\,0\,0]$ direction, (b) an assemblage of 80 nm ESVD grains, initialised with an SD magnetisation in the easy $[1\,\bar{1}\,\bar{1}]$ direction and (c) an assemblage of 150 nm ESVD grains, initialised with an SV magnetisation in the short $[0\,\bar{1}\,0]$ direction.

to the stress axis (Fig. 6.10).

6.6 Conclusions

Using the micromagnetic modelling code MERRILL (Conbhuí et al., 2018), this work has uncovered new insights into the effects of an applied stress on SD and SV magnetites, observing stress-induced transitions between domain states in grains of cuboctahedral magnetite for the first time. As SV grains are now understood to be the dominant stable component of the NRM in rocks and meteorites (Nagy et al., 2019), the understanding of the response of these grains to stress is pertinent—particularly for remanence carriers within primitive meteorites, which are known to have been subject to many shock events (Stöffler et al., 1991; Scott et al., 1992)

subsequent to acquiring their original magnetisation (Bland et al., 2014).

Models were designed such that a static, time-independent stress was applied to grains of magnetite which carried a pre-existing remanent magnetisation. Stress was applied to each grain across 20 evenly-distributed orientations within a stress field while grain shape and volume remained constant. LEM states were calculated as stress was cyclically increased between 10 MPa and 3 GPa, where both remanence and stressed states were measured at each interval. A total of 26 different models were investigated, across which the grain size, elongation and initial magnetisation state were all varied.

While a theoretical framework for the effects of stress on magnetic grains does not yet exist, I attempt to comprehensively summarise the observations made in this investigation. This is a first step in developing an understanding of the relationship of stress on the grain scale for magnetite:

1. SD remanences in equidimensional grains were rotated into easy axes perpendicular to the direction of an applied stress, where the angle between the magnetisation vector and applied stress was $< 60°$. Rotation occurred at very low stress, < 0.1 GPa.

2. SD remanences in elongated grains were resistant to rotation at stresses up to 3 GPa. Where the angle between the magnetisation vector and applied stress was $< 45°$, the SD in-stress magnetisation was coerced into a direction that was perpendicular with the applied stress.

3. SV remanences in equidimensional grains were susceptible to a domain state transition, from SV to SD, where $d_{min} < d_0 < d_{max}$. Transition between domain state was found to occur at stresses between $0.1 - 1$ GPa, where the SD state favoured alignment with the easy [1 1 1] axis. The transition stress was found to depend strongly on the angle between the initial magnetisation and the stress axis, θ, and was well-approximated by a cosine relationship, with a minimum at $\theta = 45°$. This evidence supports experimental findings which observe an increase in the M_{rs}/M_s ratio with an increase in applied stress (Nagata and Kinoshita, 1964, 1965; Gilder et al., 2002, e.g.,).

4. SV remanences in equidimensional grains, where $d_0 > d_{max}$, are rotated into the easy axis at low stresses, < 0.3 GPa. The stress required to rotate the remanence increased with increasing grain size.

5. SV remanences in elongated grains are dependent on grain size, initial magnetisation direction and axial ratio. In general:

   (a) Remanences in larger grains are more easily rotated than in smaller ones.

   (b) Remanences prefer alignment with the short axis to the long axis. Rotation occurred where $\theta \leq 35°$, at pressures < 0.5 GPa.

   (c) Elongation improved stability of grains which were initialised with a remanence already aligned with the short axis.

   (d) Elongated grains with poorly-defined initial remanences preferred rotation into the easy axis, at pressures < 0.4 GPa.

These results demonstrate that very low stresses are capable of irreversibly altering SV and SD remanences. Similarly, evidence was found that SD remanences transition to SV states at pressures as low as 60 MPa. This suggests that, in the absence of high-temperatures or chemical alterations, the remanences carried by SV particles which are present in meteorites may have been misinterpreted as characteristic remanent magnetisations from early events in their formation histories, or dismissed as unreliable carriers of remanence—which is now known to not be true (Almeida et al., 2016; Nagy et al., 2017, 2019). Instead, these are likely shock remanences whose fabric have been controlled by the direction of the stress vector.

The 26 models tested in this study are by no means an exhaustive list of possible magnetite domain states. Instead, they form a comprehensive suite of results for one particular grain shape of magnetite that has enabled broad identification of cases where the magnetisation is subject to change. Where remanences generally favour rotation into new crystalline axes under the influence of very low shock-induced stresses, the interpretation of directional data from meteorite palaeomagnetism may now need to be revisited.

Chapter 7

Conclusions

This thesis has set out to understand the relationship between the remanent magnetisation hosted within meteorites and the role that impacts play in its recording, alteration and removal. Over the course of three distinct work chapters, I have successfully demonstrated for the first time that chondrites likely recorded their remanence as they were lithified by low-velocity collisions, developed a workflow where the shock-response of Martian meteorites are able to be studied in great detail and improved the understanding of how single-vortex remanence in magnetite is affected when subject to stress.

Meteorite palaeomagnetism allows for the recovery of some of the earliest and most well-preserved data from within the Solar System. The remanent magnetisations stored within meteorites is stable on geologic, billion-year timescales that exceed the known age of the Universe (Nagy et al., 2017), hence, their intensities, relative directions and methods of acquisition are able to reveal otherwise unobtainable information about the nature of the early Solar System and the formation of planets. Impacts are known to have played a key part in the formation and evolution of meteorites, so they must also have affected the remanent magnetisation stored within them. Understanding how the magnetism stored inside meteorites for billions of years has been shaped by and survived these collisions can inform how the planets formed, how impacts have affected the geochemistry of rocky bodies in the Solar System and even about the conditions necessary for life.

7.1 Summary of Results

7.1.1 TRM recorded in shock experiments on synthetic chondrites

The study in Chapter 4 showed that during an impact on highly-porous, synthetic chondrite precursor material, a TRM was recorded due to the heating resulting from the crushing out of pore space. Using the iSALE shock physics code (Collins et al., 2004; Wünnemann et al., 2006), the series of experiments presented here were exhaustively planned and provided close agreement with the magnetic results that were recovered from the samples.

This investigation found an impact-induced TRM recorded an average peak temperature of 389 ± 13°C from three synthetic chondrite samples, magnetised in fields of up to 150 μT. This result was in good agreement with the temperature that was predicted from the iSALE model, where the average tracer peak temperature was 388 ± 45°C. The shock pressures were low, relative to other impacts on meteorites (< 2 GPa), and brief (< 10 μs), while samples were removed from the magnetic environment within minutes of being shocked. This meant that the TRM was recorded rapidly. These findings suggest that there is no longer a palaeomagnetic requirement for the chondrite parent bodies to have had an internally-generated, long-lived, stable magnetic field. Instead, the remanence may be a rapidly recorded 'snapshot' of the nebula field at the time of the impact.

In addition, the high temperatures recovered from the magnetic measurements, coupled with the relatively low shock pressure, highlights a need for the reappraisal of the chondrite shock-classification system. Pioneering work by Stöffler et al. (1991) and Scott et al. (1992) is in widespread use for classifying meteorite shock histories based on optical shock features and textures. However, this classification is based on experiments on non-porous targets and does not account for the extra heat released when porous targets are shocked—it is this mechanism which has enabled the 'unshocked' (S1; $< 4 - 5$ GPa) synthetic chondrite samples to have recorded a TRM. The temperatures reached in the experiments would classify them as S4, 'moderately shocked', or S5,'strongly shocked' (> 30 GPa). The close agreement between the temperatures measured from the magnetic data and the temperatures predicted by the iSALE model, suggests that shock reclassification of chondrites could even be carried out numerically,

though this likely requires further experimental investigation.

7.1.2 Heterogeneous heating in Martian meteorite ALH 84001

Across a range of shock pressures between 3-67 GPa, the work in Chapter 5 numerically explored the thermal and mechanical response of Martian meteorite ALH 84001 to a planar shock wave. Once again, this work was carried out using the iSALE shock physics code (Collins et al., 2004; Wünnemann et al., 2006) and was a mesoscale study, where the resolution of the mesh was ~ 8 μm^2. This meant individual grains several microns in diameter within the meteorite could be resolved. This study includes the development of a new workflow for meteorite shock response, where, using the publicly available pySALESetup module developed by James Derrick (`https://github.com/jgd10/PySALESetup`), high-resolution images of cross-sections of the meteorite were imported into iSALE and shocked.

ALH 84001 displays features indicative of a multiple-impact history (Treiman, 1998, 2021). This includes evidence of homogenisation and granular bands formed in an initial impact event, 'D1', which heated the meteorite > 875°C (Treiman, 1995), fracturing of carbonate globules and silica glasses in a second, but less intense, ~ 320°C impact, 'D2' (Mittlefehldt, 1994), a more recent event, 'D3', identified by a 1400°C Ar-Ar plateau around ~ 1 Ga (Cassata et al., 2010) and finally 'D4', a relatively cold (< 40°C) Mars-to-Earth ejection, that managed to preserve low-temperature palaeomagnetic information (Weiss et al., 2000). However, the temperatures and pressures of the impact events have remained unknown or poorly constrained.

Until now, these studies have been seen to contradict one another, as palaeomagnetic measurements find an NRM which contains multiple components (Antretter et al., 2003), but inconsistent with the suggested temperatures and pressures associated with the impact events D1-D4. Palaeomagnetic studies posit a long-lived (4.1-3.9 Ga) component of the NRM that is stable below the Curie temperature of pyrrhotite ~ 320°C (Antretter and Fuller, 2002). This largely ruled out evidence for the D3 event, as well as the estimated temperatures reached by even the minimum impact strength required for ejecta to escape the Martian surface (10 GPa; Artemieva and Ivanov, 2004).

However, in the work presented in Chapter 5, I have managed to reconcile events D1, D2, D3 and D4 by carefully observing both the bulk and per-material response to planar shock. Impacts in the range 25-45 GPa have been shown to leave small sub-volumes of magnetic carriers within the sample below 320°C, the Curie temperature of the magnetic carrier in the meteorite, chromite, while other materials within the sample reach temperatures in excess of 1000°C. The mechanism responsible for this strong thermal heterogeneity in the meteorite is material shear. The bulk matrix material was seen to experience shear heating, using inclusions as nucleation points. This also meant that submicron chromites near these shear zones were heated up briefly after the shock wave had passed, sufficiently hot enough (> 320°C) to have recorded a new TRM from a still-active Martian dynamo, or undergone demagnetisation in the case there was zero magnetic field.

7.1.3 On the relationship between stress and remanence in SV magnetite

Using the micromagnetic modelling code MERRILL, I have investigated the response of individual grains and assemblages of magnetite to a static stress in the absence of a magnetic field. Grains of magnetite were initialised with a single-domain (SD) or single-vortex (SV) magnetisation before being subjected to a stress, progressively cycled from 10 MPa up to 3 GPa. The stress was 'switched' on/off so that the unstressed remanence state could be measured between progressive stresses. A range of grain sizes, with equivalent spherical volume diameter (ESVD) sizes between 50 - 200 nm were explored, along with three different elongation shapes.

The remanence state was irreversibly changed in exactly half of the models that were explored. This irreversible 'change' was either a transition from one grain state to another, for example from SV to SD, or rotation of the remanence into a new plane. The transition from an SV to SD domain state was found to occur at stresses between $0.1 - 1$ GPa and depended strongly on the angle between the stress axis and remanent magnetisation vector—this relationship was found to be well described with a cosine function. For the equidimensional grain where this effect occurred, the resulting SD remanence favoured alignment with the easy axis.

On the other hand, the rotation of SV remanences into a new direction was found to occur at very low stresses, < 0.5 GPa in most cases. The threshold stress at which rotation occurred was controlled by the grain shape and size, as well as the relative angle between the remanent magnetisation vector and the stress axis.

The numerical modelling carried out here has demonstrated that the remanence carried by SD and SV grains (which are now known to dominate the stable part of the NRM; Nagy et al., 2017, 2019) in meteorites has likely been altered by the stress caused by impacts since the NRM was acquired. Many palaeomagnetic studies have determined the age of NRMs in meteorites to be close to the age of the Solar System, acquired > 4 Ga, and many meteorites are known to have suffered impacts which generate pressures $>> 1$ GPa. While impacts are an important factor in the evolution and destruction of meteorite parent bodies and planetesimals, they are not often considered when interpreting the NRM stored within meteorites. Having found for a number of typical states of magnetite that at very low stress, < 50 MPa in some cases, the remanence rotates relative to the applied stress, it is pertinent that the theoretical understanding between stress and remanent magnetisation is developed.

7.2 Future Work

7.2.1 Manufacturing more synthetic chondrites

While the impact experiments have successfully recorded a TRM, here I share a few lessons that were learned that would improve upon the experimental method developed for the study.

The numerical modelling appears to have been a successful proxy to the laboratory experiments. The temperatures predicted in the iSALE simulations were largely consistent with the palaeomagnetic peak temperature measured within the sample (Fig. 4.36). However, further work could be done to improve the equation of state that was developed for the sample. A simple Mie-Grüneisen EoS was used for fused quartz (silica/sipernat) and porosity was applied to the material using the $\epsilon - \alpha$ porosity model, however the sample was actually a silica (90%)-magnetite (2%)-hematite(8%) mixture which could be better represented and would

marginally improve the quantitative results from the pre-experiment modelling. Moreover, the distension (porosity) that was estimated by the iSALE modelling was inconsistent with the porosity recovered from the SEM images. This is a difficult result to reconcile as the synthetic meteorite samples were unsuitable for proper thin-section examination. In future experiments, the samples could be made larger in order to produce proper thin sections.

The machining process should be refined to avoid the undesired low-temperature peak in the demagnetisation spectra (Fig. 4.29). The heating involved during the lathe process was higher than anticipated and could have been avoided using either a coolant or using a lathe in a magnetically controlled environment, though the latter is likely unpractical. Time spent inside the target chamber, within the applied field, following the impact could also be increased. While this is not an issue for the reordering time and initial magnetic recording, the capsules were still warm to the touch when recovered ∼10 minutes after the impact. It would have been more representative of the natural system to have allowed them to fully cool before recovering them from the target chamber.

7.2.2 Meteorite shock response: investigating cross-sections with iSALE

The workflow developed in this investigation, where geometrically-complex meshes formed from meteorite cross-sections are able to be subject to planar shock, opens up new opportunities for revisiting meteorites which are known to have been intensely shocked, in particular those which have complicated thermal histories. Using iSALE, I have managed to reconcile data from petrologic, palaeomagnetic and microscopic studies to form a coherent shock history for the ALH 84001 meteorite, comparing the thermal and mechanical response of the meteorite in the simulations to the reported history in the literature.

This method is limited, however, as it makes the assumption that the meteorite was shocked in its current physical state. It is not able to recover whether there was pore space that was crushed out, for example, nor is it able to determine whether features such as fractures or impact melts were present during previous impacts that occurred prior to its ejection from the parent

body. Improvements could be made to identify the compaction history of the sample, using techniques such as electron backscatter diffraction to map the submicron granular structure and reconstruct initial porosity (Bland et al., 2011). Other limitations include the limited shock data available for meteoritic materials and the constant improvements that are being made to the material models and equations of state. The outcome of these simulations—and all the modelling done in this thesis—is reliant on the accuracy of these material models, so for meteorite studies, it would be excellent if future shock investigations are able to improve the amount of data available for extraterrestrial materials.

7.2.3 Further research on the importance of the single-vortex domain state in meteorites

The evidence provided by the suite of micromagnetic simulations in Chapter 6 offer a foundation that begins the development of a theoretical framework around how non-uniformly magnetised particles respond to an applied stress. However, these models could be supplemented by both an investigation into intermediary grain sizes to those investigated here, as well as using a larger number of stress axes and grain shapes. Moreover, limitations of the model, such as the lack of temperature variation and exclusion of magnetostriction, could be mitigated with future developments to the code. The modelling may also be extended to investigate other materials, such as iron-nickel or iron sulphides, with the ultimate goal of developing a theoretical framework that describes the relationship between an applied stress and (1) the remanent magnetisation domain state behaviour and (2) changes to the magnetisation orientation. This would build on the work here which has discovered some of the characteristic behaviours of single-vortex grains when subject to stresses.

Furthermore, the results presented in this chapter could be experimentally verified using transmission electron microscopy (TEM) off-axis electron holography, which would allow the predicted states to produce nanometric magnetic images (Almeida et al., 2016; Shah et al., 2018). Such images would be able to inform if the uniaxial stress algorithm is operating correctly and whether the structures predicted by MERRILL are in agreement with physical

observations.

Data Availability

All input files for Chapters 4 and 6 are available at the following DOI: 10.5281/zenodo.7663998. This includes all the iSALE models for the aluminium capsule as well as the MERRILL files used in Chapter 6 for each of the 520 grains that were modelled. Input files for the iSALE simulations in Chapter 5, along with a video of the thermal equilibration process, are publicly available and can be found at the following DOI: 10.5281/zenodo.6637894.

Acknowledgements

This project was funded by the STFC under grant number ST/S505420/1 and project code 2151024.

Bibliography

Almeida, T. P., Muxworthy, A. R., Kovács, A., Williams, W., Brown, P. D., and Dunin-Borkowski, R. E. (2016). Direct visualization of the thermomagnetic behavior of pseudo-single-domain magnetite particles. *Science Advances*, 2(4).

Amelin, Y., Krot, A., Hutcheon, I., Ulyanov, A., Shukolyukov, A., Lugmair, G. W., Amelin, Y., Krot, A., Hutcheon, I., Ulyanov, A., Shukolyukov, A., and Lugmair, G. W. (2002). Lead isotopic ages of chondrules and calcium-aluminum-rich inclusions. *Science*, 297(5587):1678–1683.

Amsden, A. A., Ruppel, H. M., and Hirt, C. W. (1980). SALE: A Simplified ALE computer program for fluid flow at all speeds. Technical Report June, Los Alamos Scientific Laboratory.

Anderson, C. E. (1987). An overview of the theory of hydrocodes. *International Journal of Impact Engineering*, 5(1-4):33–59.

Antretter, M. and Fuller, M. (2002). Paleomagnetism and rock magnetism of martian meteorite ALH 84001. *Physics and Chemistry of the Earth*, 27(25-31):1299–1303.

Antretter, M., Fuller, M., Scott, E., Jackson, M., Moskowitz, B., and Solheid, P. (2003). Paleomagnetic record of Martian meteorite ALH84001. *Journal of Geophysical Research E: Planets*, 108(6):5049.

Artemieva, N. and Ivanov, B. (2004). Launch of martian meteorites in oblique impacts. *Icarus*, 171(1):84–101.

Bai, X. N. (2014). Hall-effect-controlled gas dynamics in protoplanetary disks. I. wind solutions at the inner disk. *Astrophysical Journal*, 791(2):1–24.

Bai, X. N. and Stone, J. M. (2013). Local study of accretion disks with a strong vertical magnetic field: Magnetorotational instability and disk outflow. *Astrophysical Journal*, 767(1):30.

Balbus, S. A. and Hawley, J. F. (1992). A Powerful Local Shear Instability in Weakly Magnetized Disks. IV. Nonaxisymmetric Perturbations. *The Astrophysical Journal*, 400:610.

Banerjee, S. K. and Hargraves, R. B. (1972). Natural remanent magnetizations of carbonaceous chondrites and the magnetic field in the early solar system. *Earth and Planetary Science Letters*, 17(1):110–119.

Barber, D. J. and Scott, E. R. (2006). Shock and thermal history of Martian meteorite Allan Hills 84001 from transmission electron microscopy. *Meteoritics and Planetary Science*, 41(4):643–662.

Barrie, C. D., Boyle, A. P., Cook, N. J., and Prior, D. J. (2010). Pyrite deformation textures in the massive sulfide ore deposits of the Norwegian Caledonides. *Tectonophysics*, 483(3-4):269–286.

Beard, B. L., Ludois, J. M., Lapen, T. J., and Johnson, C. M. (2013). Pre-4.0 billion year weathering on Mars constrained by Rb-Sr geochronology on meteorite ALH84001. *Earth and Planetary Science Letters*, 361:173–182.

Beitz, E., Tsuchiyama, A., Güttler, C., Blum, J., Nakamura, A. M., Tsuchiyama, A., Blum, J., Beitz, E., Güttler, C., Blum, J., and Nakamura, A. M. (2013). Experiments on the consolidation of chondrites and the formation of dense rims around chondrules. *Icarus*, 225(1):558–569.

Benson, D. J. (1994). An analysis by direct numerical simulation of the effects of particle morphology on the shock compaction of copper powder. *Modelling and Simulation in Materials Science and Engineering*, 2(3 A):535–550.

Benson, D. J., Nesterenko, V. F., Jonsdottir, F., and Meyers, M. A. (1997). Quasistatic and dynamic regimes of granular material deformation under impulse loading. *Journal of the Mechanics and Physics of Solids*, 45(11-12):1955–1999.

Benz, W., Cameron, A. G., and Melosh, H. J. (1989). The origin of the Moon and the single-impact hypothesis III. *Icarus*, 81(1):113–131.

Bischoff, A. and Geiger, T. (1995). Meteorites from the Sahara: find locations, shock classification, degree of weathering and pairing. *Meteoritics*, 30(1):113–122.

Bland, P. A., Collins, G. S., Davison, T. M., Abreu, N. M., Ciesla, F. J., Muxworthy, A. R., and Moore, J. (2014). Pressure-temperature evolution of primordial solar system solids during impact-induced compaction. *Nature Communications*, 5:5451.

Bland, P. A., Howard, L. E., Prior, D. J., Wheeler, J., Hough, R. M., and Dyl, K. A. (2011). Earliest rock fabric formed in the Solar System preserved in a chondrule rim. *Nature Geoscience*, 4(4):244–247.

Blandford, R. D. and Payne, D. G. (1982). Hydromagnetic flows from accretion discs and the production of radio jets. *Monthly Notices of the Royal Astronomical Society*, 199(4):883–903.

Bollard, J., Kawasaki, N., Sakamoto, N., Olsen, M., Itoh, S., Larsen, K., Wielandt, D., Schiller, M., Connelly, J. N., Yurimoto, H., and Bizzarro, M. (2019). Combined U-corrected Pb-Pb dating and 26Al-26Mg systematics of individual chondrules – Evidence for a reduced initial abundance of 26Al amongst inner Solar System chondrules. *Geochimica et Cosmochimica Acta*, 260:62–83.

Bonal, L., Bourot-Denise, M., Quirico, E., Montagnac, G., and Lewin, E. (2007). Organic matter and metamorphic history of CO chondrites. *Geochimica et Cosmochimica Acta*, 71(6):1605–1623.

Borg, J. P., Chapman, D. J., Tsembelis, K., Proud, W. G., and Cogar, J. R. (2005). Dynamic compaction of porous silica powder. *Journal of Applied Physics*, 98(7):073509.

Borg, J. P. and Vogler, T. J. (2008). Mesoscale calculations of the dynamic behavior of a granular ceramic. *International Journal of Solids and Structures*, 45(6):1676–1696.

Borg, L. E., Connelly, J. N., Nyquist, L. E., Shih, C. Y., Wiesmann, H., and Reese, Y. (1999). The age of the carbonates in martian meteorite ALH84001. *Science*, 286(5437):90–94.

Borlina, C. S., Weiss, B. P., Bryson, J. F., Bai, X. N., Lima, E. A., Chatterjee, N., and Mansbach, E. N. (2021). Paleomagnetic evidence for a disk substructure in the early solar system. *Science Advances*, 7(42):6928–6943.

Bottke, W. F. and Norman, M. D. (2017). The Late Heavy Bombardment. *Annual Review of Earth and Planetary Sciences*, 45:619–647.

Bouvier, A. and Wadhwa, M. (2010). The age of the Solar System redefined by the oldest Pb-b age of a meteoritic inclusion. *Nature Geoscience*, 3(9):637–641.

Bozorth, R. M. (1951). *Ferromagnetism*. Van Nostrand, New York, 2nd, (bell edition.

Brearley, A. J. (2003). Magnetite in ALH 84001: An origin by shock-induced thermal decomposition of iron carbonate. *Meteoritics and Planetary Science*, 38(6):849–870.

Brearley, A. J. and Krot, A. N. (2013). Metasomatism in the early solar system: The record from chondritic meteorites. In *Metasomatism and the Chemical Transformation of Rock*, pages 659–789. Springer International Publishing.

Brecher, A. and Albright, L. (1977). The Thermoremanence Hypothesis and the Origin of Magnetization in Iron Meteorites. *Journal of geomagnetism and geoelectricity*, 29(4):379–400.

Brecher, A. and Arrhenius, G. (1974). The paleomagnetic record in carbonaceous chondrites: Natural remanence and magnetic properties. *Journal of Geophysical Research*, 79(14):2081–2106.

Britt, D. T., Yeomans, D., Housen, K., and Consolmagno, G. (2002). Asteroid Density, Porosity, and Structure. In *Asteroids III*, pages 485–500.

Brown, W. F. (1949). Irreversible magnetic effects of stress. *Physical Review*, 75(1):147–154.

Brunhes, B. (1906). Recherches sur la direction d'aimantation des roches volcaniques. *Journal de Physique Théorique et Appliquée*, 5(1):705–724.

Bryson, J. F., Weiss, B. P., Getzin, B., Abrahams, J. N., Nimmo, F., and Scholl, A. (2019). Paleomagnetic Evidence for a Partially Differentiated Ordinary Chondrite Parent Asteroid. *Journal of Geophysical Research: Planets*, 124(7):1880–1898.

Bryson, J. F., Weiss, B. P., Harrison, R. J., Herrero-Albillos, J., and Kronast, F. (2017). Paleomagnetic evidence for dynamo activity driven by inward crystallisation of a metallic asteroid. *Earth and Planetary Science Letters*, 472:152–163.

Bryson, J. F. J., Weiss, B. P., Biersteker, J. B., King, A. J., and Russell, S. S. (2020a). Constraints on the Distances and Timescales of Solid Migration in the Early Solar System from Meteorite Magnetism. *The Astrophysical Journal*, 896(2):103.

Bryson, J. F. J., Weiss, B. P., Lima, E. A., Gattacceca, J., and Cassata, W. S. (2020b). Evidence for Asteroid Scattering and Distal Solar System Solids From Meteorite Paleomagnetism. *The Astrophysical Journal*, 892(2):126.

Butler, R. F. (1992). Paleomagnetism: magnetic domains to geologic terranes. *Paleomagnetism: magnetic domains to geologic terranes*.

Cain, P. M., McSween, H. Y., and Woodward, N. B. (1986). Structural deformation of the Leoville chondrite. *Earth and Planetary Science Letters*, 77(2):165–175.

Carporzen, L., Weiss, B. P., Gattacceca, J., Elkins-Tanton, L. T., Ebel, D., Shuster, D. L., Ebel, D., and Gattacceca, J. (2011). Magnetic evidence for a partially differentiated carbonaceous chondrite parent body. *Proceedings of the National Academy of Sciences*, 108(16):6386–6389.

Carvallo, C., Roberts, A. P., Leonhardt, R., Laj, C., Kissel, C., Perrin, M., and Camps, P. (2006). Increasing the efficiency of paleointensity analyses by selection of samples using first-order reversal curve diagrams. *Journal of Geophysical Research: Solid Earth*.

Cassata, W. S., Shuster, D. L., Renne, P. R., and Weiss, B. P. (2010). Evidence for shock heating and constraints on Martian surface temperatures revealed by 40Ar/39Ar thermochronometry of Martian meteorites. *Geochimica et Cosmochimica Acta*, 74(23):6900–6920.

Cisowski, S. M. and Fuller, M. (1978). The effect of shock on the magnetism of terrestrial rocks. *Journal of Geophysical Research: Solid Earth*, 83(B7):3441–3458.

Clark, D. A. (1984). Hysteresis properties of sized dispersed monoclinic pyrrhotite grains. *Geophysical Research Letters*, 11(3):173–176.

Clayton, R. N. and Mayeda, T. K. (1999). Oxygen isotope studies of carbonaceous chondrites. *Geochimica et Cosmochimica Acta*, 63(13-14):2089–2104.

Collins, G. and Melosh, H. (2002). SALES 2: A multi-material extension to the SALE hydrocode with improved equation of state and constitutive model. *Cycle*, (October 2002).

Collins, G. S., Melosh, H. J., and Ivanov, B. A. (2004). Modeling damage and deformation in impact simulations. *Meteoritics and Planetary Science*, 39(2):217–231.

Collins, G. S., Melosh, H. J., and Wünnemann, K. (2011). Improvements to the ϵ-α Porous compaction model for simulating impacts into high-porosity solar system objects. *International Journal of Impact Engineering*, 38(6):434–439.

Collinson, D. W. (1983). Controlled fields and field-free space. In *Methods in Rock Magnetism and Palaeomagnetism*, chapter 5, page 503. Springer Netherlands, Newcastle upon Tyne.

Compton, A. H. (1921). The magnetic electron. *Journal of the Franklin Institute*, 192(2):145–155.

Conbhuí, P., Williams, W., Fabian, K., Ridley, P., Nagy, L., and Muxworthy, A. R. (2018). Merrill: Micromagnetic earth related robust interpreted language laboratory. *Geochemistry, Geophysics, Geosystems*, 19(4):1080–1106.

Connelly, J. N., Bizzarro, M., Krot, A. N., Nordlund, , Wielandt, D., and Ivanova, M. A. (2012). The absolute chronology and thermal processing of solids in the solar protoplanetary disk. *Science*, 338(6107):651–655.

Connelly, J. N., Bollard, J., and Bizzarro, M. (2017). Pb–Pb chronometry and the early Solar System. *Geochimica et Cosmochimica Acta*, 201:345–363.

Consolmagno, G. J., Britt, D. T., and Macke, R. J. (2008). The significance of meteorite density and porosity. *Chemie der Erde*, 68(1):1–29.

Corrigan, C. M., Zolensky, M. E., Dahl, J., Long, M., Weir, J., Sapp, C., and Burkett, P. J. (1997). The porosity and permeability of chondritic meteorites and interplanetary dust particles. *Meteoritics and Planetary Science*, 32(4):509–515.

Cournede, C., Gattacceca, J., Gounelle, M., Rochette, P., Weiss, B. P., and Zanda, B. (2015). An early solar system magnetic field recorded in CM chondrites. *Earth and Planetary Science Letters*, 410:62–74.

Craig, J. R. and Vokes, F. M. (1993). The metamorphism of pyrite and pyritic ores: an overview. *Mineralogical Magazine*, 57(386):3–18.

Crutcher, R. M. (2012). Magnetic Fields in Molecular Clouds. *Annual Review of Astronomy and Astrophysics*, 50(1):29–63.

Cuzzi, J. N., Hogan, R. C., and Shariff, K. (2008). Toward Planetesimals: Dense Chondrule Clumps in the Protoplanetary Nebula. *The Astrophysical Journal*, 687(2):1432–1447.

Cuzzi, J. N. and Weidenschilling, S. J. (2006). Particle-Gas Dynamics and Primary Accretion. In *Meteorites and the Early Solar System II*, pages 353–382. Klahr and Bodenheimer.

Daalderop, G. H., Kelly, P. J., and Schuurmans, M. F. (1990). First-principles calculation of the magnetocrystalline anisotropy energy of iron, cobalt, and nickel. *Physical Review B*, 41(17):11919–11937.

Darby, M. I. (1967). Tables of the Brillouin function and of the related function for the spontaneous magnetization. *British Journal of Applied Physics*, 18(10):1415–1417.

Davison, T. M., Collins, G. S., and Bland, P. A. (2016). Mesoscale Modeling of Impact Compaction of Primitive Solar System Solids. *The Astrophysical Journal*, 821(1):68.

Davison, T. M., Collins, G. S., and Ciesla, F. J. (2010). Numerical modelling of heating in porous planetesimal collisions. *Icarus*, 208(1):468–481.

Davison, T. M., Collins, G. S., Elbeshausen, D., Wünnemann, K., and Kearsley, A. (2011). Numerical modeling of oblique hypervelocity impacts on strong ductile targets. *Meteoritics and Planetary Science*, 46(10):1510–1524.

Davison, T. M., Derrick, J. G., Collins, G. S., Bland, P. A., Rutherford, M. E., Chapman, D. J., and Eakins, D. E. (2017). Impact-induced compaction of primitive solar system solids: The need for mesoscale modelling and experiments. In *Procedia Engineering*, volume 204, pages 405–412.

Day, R. (1977). TRM and Its Variation with Grain Size. In *Origin of Thermoremanent Magnetization*, pages 1–33. Springer, Dordrecht.

Day, R., Fuller, M., and Schmidt, V. A. (1977). Hysteresis properties of titanomagnetites: Grain-size and compositional dependence. *Physics of the Earth and Planetary Interiors*, 13(4):260–267.

DeCarli, P. S., Goresy, A. E., Xie, Z., and Sharp, T. G. (2007). Ejection mechanisms for Martian meteorites. In *AIP Conference Proceedings*, volume 955, pages 1371–1374.

Derrick, J. G., Rutherford, M. E., Chapman, D. J., Davison, T. M., Duarte, J. P. P., Farbaniec, L., Bland, P. A., Eakins, D. E., and Collins, G. S. (2019). Investigating shock processes in bimodal powder compaction through modelling and experiment at the mesoscale. *International Journal of Solids and Structures*, 163:211–219.

Dodds, K. H., Bryson, J. F., Neufeld, J. A., and Harrison, R. J. (2021). The Thermal Evolution of Planetesimals During Accretion and Differentiation: Consequences for Dynamo Generation by Thermally-Driven Convection. *Journal of Geophysical Research: Planets*, 126(3).

Doyle, P. M., Jogo, K., Nagashima, K., Krot, A. N., Wakita, S., Ciesla, F. J., and Hutcheon, I. D. (2015). Early aqueous activity on the ordinary and carbonaceous chondrite parent bodies recorded by fayalite. *Nature Communications*, 6.

Drucker, D. C. and Prager, W. (1952). Soil mechanics and plastic analysis or limit design. *Quarterly of Applied Mathematics*, 10(2):157–165.

Dunlop, D. and Özdemir, (1997). *Rock Magnetism: Fundamentals and Frontiers*. Cambridge University Press, Cambridge, first edition.

Dunlop, D. J. (2002a). Theory and application of the Day plot (M rs / M s versus H cr / H c) 2. Application to data for rocks, sediments, and soils . *Journal of Geophysical Research*, 107(B3).

Dunlop, D. J. (2002b). Theory and application of the Day plot (M rs / M s versus H cr / H c) 1. Theoretical curves and tests using titanomagnetite data. *Journal of Geophysical Research*, 107(B3).

Dunlop, D. J., Ozima, M., and Kinoshita, H. (1969). Piezomagnetization of Single-Domain Grains: A Graphical Approach. *Journal of geomagnetism and geoelectricity*, 21(2):513–518.

Dunlop, D. J. and Xu, S. (1994). Theory of partial thermoremanent magnetization in multidomain grains. 1. Repeated identical barriers to wall motion (single microcoercivity). *Journal of Geophysical Research*, 99(B5):9005–9023.

Eakins, D. E. and Thadhani, N. N. (2009). Shock compression of reactive powder mixtures. *International Materials Reviews*, 54(4):181–213.

Elbeshausen, D. and Wünnemann, K. (2011). iSALE-3D: A three-dimensional, multi-material, multi-rheology hydrocode and its applications to large scale geodynamic processes. *Proceedings of 11th Hypervelocity Impact Symposium*, pages 287–301.

Elkins-Tanton, L. T., Weiss, B. P., and Zuber, M. T. (2011). Chondrites as samples of differentiated planetesimals. *Earth and Planetary Science Letters*, 305(1-2):1–10.

Emmerton, S., Muxworthy, A. R., Hezel, D. C., and Bland, P. A. (2011). Magnetic characteristics of CV chondrules with paleointensity implications. *Journal of Geophysical Research E: Planets*, 116(12):E12007.

Eugster, O., Weigel, A., and Polnau, E. (1997). Ejection times of Martian meteorites. *Geochimica et Cosmochimica Acta*, 61(13):2749–2757.

Ewing, J. A. (1886). On hysteresis in the relation of strain to stress. *Science*, 8(190):502–504.

Faraday, M. (1846). On new magnetic actions and on the magnetic condition of all matter. *On new magnetic actions and on the magnetic condition of all matter*, c. 1:1–28.

Fletcher, E. J. and O'Reilly, W. (1974). Contribution of Fe2+ ions to the magnetocrystalline anisotropy constant K1 of Fe3-xTixO4 (0¡x¡0.1). *Journal of Physics C: Solid State Physics*, 7(1):171–178.

Forman, L. V., Bland, P. A., Timms, N. E., Collins, G. S., Davison, T. M., Ciesla, F. J., Benedix, G. K., Daly, L., Trimby, P. W., Yang, L., and Ringer, S. P. (2016). Hidden secrets of deformation: Impact-induced compaction within a CV chondrite. *Earth and Planetary Science Letters*, 452:133–145.

Forman, L. V., Bland, P. A., Timms, N. E., Daly, L., Benedix, G. K., Trimby, P. W., Collins, G. S., and Davison, T. M. (2017). Defining the mechanism for compaction of the CV chondrite parent body. *Geology*, 45(6):559–562.

Fortin, D. and Langley, S. (2005). Formation and occurrence of biogenic iron-rich minerals. *Earth-Science Reviews*, 72(1-2):1–19.

Fritz, J., Artemieva, N., and Greshake, A. (2005a). Ejection of Martian meteorites. *Meteoritics and Planetary Science*, 40(9-10):1393–1411.

Fritz, J., Greshake, A., and Stoffler, D. (2005b). Micro-Raman spectroscopy of plagioclase and maskelynite in Martian meteorites: Evidence of progressive shock metamorphism. *Antarctic Meteorite Research*, 18:96–116.

Fu, R. R., Weiss, B. P., Lima, E. A., Harrison, R. J., Bai, X. N., Desch, S. J., Ebel, D. S., Suavet, C., Wang, H., Glenn, D., Le Sage, D., Kasama, T., Walsworth, R. L., and Kuan, A. T. (2014). Solar nebula magnetic fields recorded in the Semarkona meteorite. *Science*, 346(6213):1089–1092.

Fujimura, A., Kato, M., and Kumazawa, M. (1983). Preferred orientation of phyllosilicate [001] in matrix of Murchison meteorite and possible mechanisms of generating the oriented texture in chondrites. *Earth and Planetary Science Letters*, 66(C):25–32.

Gammie, C. F. (2002). Nonlinear Outcome of Gravitational Instability in Cooling, Gaseous Disks. *The Astrophysical Journal*, 553(1):174–183.

Ganino, C. and Libourel, G. (2017). Reduced and unstratified crust in CV chondrite parent body. *Nature Communications*, 8(1):261.

Gattacceca, J., Berthe, L., Boustie, M., Vadeboin, F., Rochette, P., and De Resseguier, T. (2008). On the efficiency of shock magnetization processes. *Physics of the Earth and Planetary Interiors*, 166:1–10.

Gattacceca, J., Lamali, A., Rochette, P., Boustie, M., and Berthe, L. (2007). The effects of explosive-driven shocks on the natural remanent magnetization and the magnetic properties of rocks. *Physics of the Earth and Planetary Interiors*, 162:85–98.

Gattacceca, J., Rochette, P., Denise, M., Consolmagno, G., and Folco, L. (2005). An impact origin for the foliation of chondrites. *Earth and Planetary Science Letters*, 234(3-4):351–368.

Gattacceca, J., Weiss, B. P., and Gounelle, M. (2016). New constraints on the magnetic history of the CV parent body and the solar nebula from the Kaba meteorite. *Earth and Planetary Science Letters*, 455:166–175.

Gilder, S. A., Goff, M. L., and Chervin, J. C. (2006). Static stress demagnetization of single and multidomain magnetite with implications for meteorite impacts. In *High Pressure Research*, volume 26, pages 539–547.

Gilder, S. A., LeGoff, M., Peyronneau, J., and Chervin, J. C. (2002). Novel high pressure magnetic measurements with application to magnetite. *Geophysical Research Letters*, 29(10):30–1.

Glen, W. (1982). *The Road to Jaramillo: Critical Years of the Revolution in Earth Science*. Stanford University Press, 1st edition.

Golden, D. C., Ming, D. W., Morris, R. V., Brearley, A. J., Lauer, H. V., Treiman, A. H., Zolensky, M. E., Schwandt, C. S., Lofgren, G. E., and McKay, G. A. (2004). Evidence for exclusively inorganic formation of magnetite in Martian meteorite ALH84001. *American Mineralogist*, 89(5-6):681–695.

Goldin, T. J., Wünnemann, K., Melosh, H. J., and Collins, G. S. (2006). Hydrocode modeling of the Sierra Madera impact structure. *Meteoritics and Planetary Science*, 41(12):1947–1958.

Güldemeister, N., Wünnemann, K., Durr, N., and Hiermaier, S. (2013). Propagation of impact-induced shock waves in porous sandstone using mesoscale modeling. *Meteoritics and Planetary Science*, 48(1):115–133.

Haisch, Jr., K. E., Jayawardhana, R., and Alves, J. (2005). Constraints on Inner Disk Evolution Timescales: A Disk Census of the η Chamaeleontis Young Cluster. *The Astrophysical Journal*, 627(1):L57–L60.

Hanna, R. D., Ketcham, R. A., Zolensky, M., and Behr, W. M. (2015). Impact-induced brittle deformation, porosity loss, and aqueous alteration in the Murchison CM chondrite. *Geochimica et Cosmochimica Acta*, 171:256–282.

Hargraves, R. B. and Perkins, W. E. (1969). Investigations of the effect of shock on natural remanent magnetism. *Journal of Geophysical Research*, 74(10):2576–2589.

Hartmann, W. K. and Neukum, G. (2001). Cratering chronology and the evolution of Mars. *Space Science Reviews*, 96(1-4):165–194.

Heider, F. and Williams, W. (1988). Note on temperature dependence of exchange constant in magnetite. *Geophysical Research Letters*, 15(2):184–187.

Heuzé, O. (2012). General form of the Mie-Grüneisen equation of state. *Comptes Rendus - Mecanique*, 340(10):679–687.

Hevey, P. J. and Sanders, I. S. (2006). A model for planetesimal meltdown by 26Al and its implications for meteorite parent bodies. *Meteoritics and Planetary Science*, 41(1):95–106.

Honda, O., Kaya, S., and Masuyama, Y. (1926). On the magnetic properties of single crystals of iron.

Ismail, I. A. and Murrell, S. A. (1990). The effect of confining pressure on stress-drop in compressive rock fracture. *Tectonophysics*, 175(1-3):237–248.

Ivanov, B. A. and Artemieva, N. A. (2002). Numerical modeling of the formation of large impact craters. *Special Paper of the Geological Society of America*, 356:619–630.

Ivanov, B. A., Deniem, D., and Neukum, G. (1997). Implementation of dynamic strength models into 2D hydrocodes: Applications for atmospheric breakup and impact cratering. *International Journal of Impact Engineering*, 20(1-5):411–430.

Ivanov, B. A. and Deutsch, A. (1999). Sudbury impact event: Cratering mechanics and thermal history. *Special Paper of the Geological Society of America*, 339:389–397.

Ivanov, B. A., Melosh, H. J., and Pierazzo, E. (2010). Basin-forming impacts: Reconnaissance modeling. *Special Paper of the Geological Society of America*, 465:29–49.

Jacobsen, B., Yin, Q. z., Moynier, F., Amelin, Y., Krot, A. N., Nagashima, K., Hutcheon, I. D., and Palme, H. (2008). 26Al-26Mg and 207Pb-206Pb systematics of Allende CAIs: Canonical solar initial 26Al/27Al ratio reinstated. *Earth and Planetary Science Letters*, 272(1-2):353–364.

Jaret, S. J., Hemming, S. R., Rasbury, E. T., Thompson, L. M., Glotch, T. D., Ramezani, J., and Spray, J. G. (2018). Context matters – Ar–Ar results from in and around the Manicouagan Impact Structure, Canada: Implications for martian meteorite chronology. *Earth and Planetary Science Letters*, 501:78–89.

Johnson, B. C., Minton, D. A., Melosh, H. J., and Zuber, M. T. (2015). Impact jetting as the origin of chondrules. *Nature*, 517(7534):339–341.

Johnson, G. R. and Cook, W. H. (1983). A Constitutive Model and Data for Metals Subjected to Large Strains, High Strain Rates, and High Temperatures. In *The 7th International Symposium on Ballistics*, volume 7, pages 541–547.

Kannan, A., Esakkiraja, K., and Nataraj, M. (2013). Modeling and Analysis for Cutting Temperature in Turning of Aluminium 6063 Using Response Surface Methodology. *IOSR Journal of Mechanical and Civil Engineering*, 9(4):59–64.

Kereszturi, A., Blumberger, Z., Józsa, S., May, Z., Müller, A., Szabó, M., and Tóth, M. (2014). Alteration processes in the CV chondrite parent body based on analysis of NWA 2086 meteorite. *Meteoritics and Planetary Science*, 49(8):1350–1364.

Kieffer, S. W., Phakey, P. P., and Christie, J. M. (1976). Shock processes in porous quartzite: Transmission electron microscope observations and theory. *Contributions to Mineralogy and Petrology*, 59(1):41–93.

Kirschvink, J. L. and Lowenstam, H. A. (1979). Mineralization and magnetization of chiton teeth: paleomagnetic, sedimentologic, and biologic implications of organic magnetite. *Earth and Planetary Science Letters*, 44(2):193–204.

Kirschvink, J. L., Maine, A. T., and Vali, H. (1997). Paleomagnetic evidence of a low-temperature origin of carbonate in the martian meteorite ALH84001. *Science*, 275(5306):1629–1633.

Kittel, C. (1949). Physical Theory of Ferromagnetic Domains. *Reviews of Modern Physics*, 21(4):541–583.

Kittel, C. (1976). *Introduction to Solid State Physics*. John Wiley, New York, 5 edition.

Klahr, H. H. and Bodenheimer, P. (2003). Turbulence in Accretion Disks: Vorticity Generation and Angular Momentum Transport via the Global Baroclinic Instability. *The Astrophysical Journal*, 582(2):869–892.

Kleine, T. and Wadhwa, M. (2017). Chronology of planetesimal differentiation. In Elkins-Tanton, L. T. and Weiss, B. P., editors, *Planetesimals: Early Differentiation and Consequences for Planets*, pages 224–245. Cambridge University Press, Cambridge.

Klemme, S., O'Neill, H. S. C., Schnelle, W., and Gmelin, E. (2000). The heat capacity of MgCr2O4, FeCr2O4, and Cr2O3 at low temperatures and derived thermodynamic properties. *American Mineralogist*, 85:1686–1693.

Kletetschka, G., Acuna, M. H., Kohout, T., Wasilewski, P. J., and Connerney, J. E. (2004). An

empirical scaling law for acquisition of thermoremanent magnetization. *Earth and Planetary Science Letters*, 226(3-4):521–528.

Kletetschka, G., Kohout, T., and Wasilewski, P. J. (2003). Magnetic remanence in the Murchison meteorite. *Meteoritics and Planetary Science*, 38(3):399–405.

Knudsen, O. (1976). The Faraday effect and physical theory, 1845-1873. *Archive for History of Exact Sciences*, 15(3):235–281.

Kojima, T., Yada, S., and Tomeoka, K. (1995). Ca-Al-Rich Inclusions in Three Antarctic CO3 Chondrites, Yamato-81020, Yamato-82050 and Yamato-790992: Record of Low-Temperature Alteration. In *Proc. NIPR Symp. Antarct. Meteorites 8*, pages 79–96.

Kowitz, A., Güldemeister, N., Reimold, W. U., Schmitt, R. T., and Wünnemann, K. (2013). Diaplectic quartz glass and SiO2 melt experimentally generated at only 5 GPa shock pressure in porous sandstone: Laboratory observations and meso-scale numerical modeling. *Earth and Planetary Science Letters*, 384:17–26.

Kowitz, A., Güldemeister, N., Schmitt, R. T., Reimold, W. U., Wünnemann, K., and Holzwarth, A. (2016). Revision and recalibration of existing shock classifications for quartzose rocks using low-shock pressure (2.5–20 GPa) recovery experiments and mesoscale numerical modeling. *Meteoritics and Planetary Science*, 51(10):1741–1761.

Krähenbühl, U., Noll, K., Döbeli, M., Grambole, D., Herrmann, F., and Tobler, L. (1998). Exposure of Allan Hills 84001 and other achondrites on the Antarctic ice. *Meteoritics and Planetary Science*, 33(4):665–670.

Kring, D. A., Swindle, T. D., Gleason, J. D., and Grier, J. A. (1998). Formation and relative ages of maskelynite and carbonate in ALH84001. *Geochimica et Cosmochimica Acta*, 62(12):2155–2166.

Krot, A. N., Scott, E. R., and Zolensky, M. E. (1995). Mineralogical and chemical modification of components in CV3 chondrites: nebular or asteroidal processing? *Meteoritics*, 30(6):748–775.

Kunihiro, T., Rubin, A. E., McKeegan, K. D., and Wasson, J. T. (2004). Initial 26Al/27Al in carbonaceous-chondrite chondrules: Too little 26Al to melt asteroids. *Geochimica et Cosmochimica Acta*, 68(13):2947–2957.

Kurosawa, K., Genda, H., Azuma, S., and Okazaki, K. (2021). The Role of Post-Shock Heating by Plastic Deformation During Impact Devolatilization of Calcite (CaCO3).

Kurosawa, K., Okamoto, T., and Genda, H. (2018). Hydrocode modeling of the spallation process during hypervelocity impacts: Implications for the ejection of Martian meteorites. *Icarus*, 301:219–234.

Lambert, P. and Grieve, R. A. (1984). Shock experiments on maskelynite-bearing anorthosite. *Earth and Planetary Science Letters*, 68(1):159–171.

Landé, A. (1921). Über den anomalen Zeemaneffekt (Teil I). *Zeitschrift für Physik*, 5(4):231–241.

Lapen, T. J., Righter, M., Brandon, A. D., Debaille, V., Beard, B. L., Shafer, J. T., and Peslier, A. H. (2010). A younger age for ALH84001 and Its geochemical link to shergottite sources in mars. *Science*, 328(5976):347–351.

Latter, H. N. (2016). On the convective overstability in protoplanetary discs. *Monthly Notices of the Royal Astronomical Society*, 455(3):2608–2618.

Lederman, M., Schultz, S., and Ozaki, M. (1994). Measurement of the dynamics of the magnetization reversal in individual single-domain ferromagnetic particles. *Physical Review Letters*, 73(14):1986–1989.

Lee, T., Papanastassiou, D. A., and Wasserburg, G. J. (1977). Aluminum-26 in the early solar system - Fossil or fuel. *The Astrophysical Journal*, 211:L107.

Levy, E. H. (1978). Magnetic field in the primitive solar nebula [4].

Levy, R. A. (1968). *Principles of Solid State Physics*. Academic Press.

Li, M. and Xiao, L. (2016). Lifetimes and Accretion Rates of Protoplanetary Disks. *The Astrophysical Journal*, 820(1):36.

Lindgren, P., Hanna, R. D., Dobson, K. J., Tomkinson, T., and Lee, M. R. (2015). The paradox between low shock-stage and evidence for compaction in CM carbonaceous chondrites explained by multiple low-intensity impacts. *Geochimica et Cosmochimica Acta*, 148:159–178.

Liu, Y., Xing, J., Li, Y., Tan, J., Sun, L., and Yan, J. (2016). Mechanical properties and anisotropy of thermal conductivity of Fe3-xCrXO4 (x = 0-3). *Journal of Materials Research*, 31(23):3805–3813.

Lovelace, R. V. E. and Romanova, M. M. (2014). Rossby wave instability in astrophysical discs. *Fluid Dynamics Research*, 46(4):041401.

Macke, R. J., Consolmagno, G. J., and Britt, D. T. (2011). Density, porosity, and magnetic susceptibility of carbonaceous chondrites. *Meteoritics and Planetary Science*, 46(12):1842–1862.

Marsh, S. P. (1980). *LASL Shock Hugoniot Data*. University of California Press.

Matsumoto, Y., Oshino, S., Hasegawa, Y., and Wakita, S. (2017). Chondrule Accretion with a Growing Protoplanet. *The Astrophysical Journal*, 837(2):103.

McKay, D. S., Gibson, E. K., Thomas-Keprta, K. L., Vali, H., Romanek, C. S., Clemett, S. J., Chillier, X. D., Maechling, C. R., and Zare, R. N. (1996). Search for past life on Mars: Possible relic biogenic activity in martian meteorite ALH84001. *Science*, 273(5277):924–930.

McSween, H. Y. (1979). Are carbonaceous chondrites primitive or processed? A review. *Reviews of Geophysics*, 17(5):1059–1078.

Melosh, H. J. (1989). Impact Cratering: A Geologic Process. *The Journal of Geology*, 97(6):773–773.

Melosh, H. J. (2007). A hydrocode equation of state for SiO2. *Meteoritics and Planetary Science*, 42(12):2079–2098.

Melosh, H. J., Ryan, E. V., and Asphaug, E. (1992). Dynamic fragmentation in impacts: hydrocode simulation of laboratory impacts. *Journal of Geophysical Research*, 97(E9).

Merrill, R. T. (1975). Magnetic effects associated with chemical changes in igneous rocks. *Geophysical Surveys*, 2(3):277–311.

Min, K. and Reiners, P. W. (2007). High-temperature Mars-to-Earth transfer of meteorite ALH84001. *Earth and Planetary Science Letters*, 260(1-2):72–85.

Mittlefehldt, D. W. (1994). ALH84001, a cumulate orthopyroxenite member of the martian meteorite clan. *Meteoritics*, 29(2):214–221.

Moreau, J. G., Kohout, T., Wünnemann, K., Halodova, P., and Haloda, J. (2019). Shock physics mesoscale modeling of shock stage 5 and 6 in ordinary and enstatite chondrites. *Icarus*, 332:50–65.

Moskowitz, B. M. (1993). High-temperature magnetostriction of magnetite and titanomagnetites. *Journal of Geophysical Research*, 98(B1):359–371.

Murrell, S. A. and Chakravarty, S. (1973). Some New Rheological Experiments on Igneous Rocks at Temperatures up to 1120°C. *Geophysical Journal of the Royal Astronomical Society*, 34(2):211–250.

Muxworthy, A. R., Bland, P. A., Davison, T. M., Moore, J., Collins, G. S., and Ciesla, F. J. (2017). Evidence for an impact-induced magnetic fabric in Allende, and exogenous alternatives to the core dynamo theory for Allende magnetization. *Meteoritics and Planetary Science*, 52(10):2132–2146.

Muxworthy, A. R. and Dunlop, D. J. (2002). First-order reversal curve (FORC) diagrams for pseudo-single-domain magnetites at igh temperature. *Earth and Planetary Science Letters*, 203(1):369–382.

Muxworthy, A. R. and Roberts, A. P. (2007). First-Order Reversal Curve (FORC) Diagrams. In *Encyclopedia of Geomagnetism and Paleomagnetism*, pages 266–272. Springer.

Muxworthy, A. R. and Williams, W. (2006). Critical single-domain/multidomain grain sizes in noninteracting and interacting elongated magnetite particles: Implications for magnetosomes. *Journal of Geophysical Research: Solid Earth*, 111(12).

Nagata, T. (1970). Effects of a uniaxial compression on remanent magnetizations of igneous rocks. *Pure and Applied Geophysics PAGEOPH*, 78(1):100–109.

Nagata, T. (1971). Introductory notes on shock remanent magnetization and shock demagnetization of igneous rocks. *Pure and Applied Geophysics PAGEOPH*, 89(1):159–177.

Nagata, T. (1979). Meteorite magnetism and the early solar system magnetic field. In *Physics of the Earth and Planetary Interiors*, volume 20, pages 324–341.

Nagata, T., Fisher, R. M., and Schwerer, F. C. (1972). Lunar rock magnetism. *The Moon*, 4(1-2):160–186.

Nagata, T. and Funaki, M. (1982). Magnetic properties of tetrataenite-rich stony meteorites. *Memoirs, National Institute of Polar Research, Toyko, Special Issue,*, 25:222–250.

Nagata, T. and Kinoshita, H. (1964). Effect of release of compression on magnetization of rocks and assemblies of magnetic minerals.

Nagata, T. and Kinoshita, H. (1965). Studies on piezo-magnetization (I) Magnetization of titaniferous magnetite under uniaxial compression. *Journal of geomagnetism and geoelectricity*, 17(2):121–135.

Nagy, L., Williams, W., Muxworthy, A. R., Fabian, K., Almeida, T. P., Conbhuí, P., and Shcherbakov, V. P. (2017). Stability of equidimensional pseudo–single-domain magnetite over billion-year timescales. *Proceedings of the National Academy of Sciences of the United States of America*, 114(39):10356–10360.

Nagy, L., Williams, W., Tauxe, L., Muxworthy, A. R., and Ferreira, I. (2019). Thermomagnetic recording fidelity of nanometer-sized iron and implications for planetary magnetism. *Proceedings of the National Academy of Sciences of the United States of America*, 116(6):1984–1991.

Néel, L. (1949). Théorie du traînage magnétique des ferromagnétiques en grains fins avec application aux terres cuites. *Annales de Geophysique*, 5:99–136.

Néel, L. (1952). Antiferromagnetism and ferrimagnetism. *Proceedings of the Physical Society. Section A*, 65(11):869–885.

Néel, L. (1955). Some theoretical aspects of rock-magnetism. *Advances in Physics*, 4(14):191–243.

Néel, M. L. (1948). Propriétés magnétiques des ferrites ; ferrimagnétisme et antiferromagnétisme. *Annales de Physique*, 12(3):137–198.

Nesterenko, V. F. (2001). *Dynamics of Heterogeneous Materials*. Berlin: Springer.

Nichols, C. I., Bryson, J. F., Cottrell, R. D., Fu, R. R., Harrison, R. J., Herrero-Albillos, J., Kronast, F., Tarduno, J. A., and Weiss, B. P. (2021). A Time-Resolved Paleomagnetic Record of Main Group Pallasites: Evidence for a Large-Cored, Thin-Mantled Parent Body. *Journal of Geophysical Research: Planets*, 126(7).

Nichols, C. I., Bryson, J. F., Herrero-Albillos, J., Kronast, F., Nimmo, F., and Harrison, R. J. (2016). Pallasite paleomagnetism: Quiescence of a core dynamo. *Earth and Planetary Science Letters*, 441:103–112.

Nichols, C. I., Einsle, J. F., Im, M. Y., Kasama, T., Saghi, Z., Midgley, P. A., and Harrison, R. J. (2019). Field Response of Magnetic Vortices in Dusty Olivine From the Semarkona Chondrite. *Geochemistry, Geophysics, Geosystems*, 20(3):1441–1453.

Nichols, C. I., Krakow, R., Herrero-Albillos, J., Kronast, F., Northwood-Smith, G., and Harrison, R. J. (2018). Microstructural and paleomagnetic insight into the cooling history of the IAB parent body. *Geochimica et Cosmochimica Acta*, 229:1–19.

North, T. L., Collins, G. S., Davison, T. M., Muxworthy, A. R., Steele, S. C., and Fu, R. R. (2023). The heterogeneous response of martian meteorite Allan Hills 84001 to planar shock. *Icarus*, 390:115322.

Nunes et al., R. (1990). *ASM handbook Volume 2 - Properties and selection: Nonferrous alloys and special-purpose materials*, volume 2. The Materials Information Company, 10 edition.

Nyquist, L. E., Bogard, D. D., Shih, C. Y., Greshake, A., Stöffler, D., and Eugster, O. (2001). Ages and geologic histories of Martian meteorites. In *Space Science Reviews*, volume 96, pages 105–164.

Ohnaka, M. (1995). A shear failure strength law of rock in the brittle-plastic transition regime. *Geophysical Research Letters*, 22(1):25–28.

O'Keefe, J. D. and Ahrens, T. J. (1982). Impact mechanics of the cretaceous-tertiary extinction bolide. *Nature*, 298(5870):123–127.

Özdemir, (2000). Coercive force of single crystals of magnetite at low temperatures. *Geophysical Journal International*, 141(2):351–356.

Özdemir, and Dunlop, D. J. (2014). Hysteresis and coercivity of hematite. *Journal of Geophysical Research: Solid Earth*, 119(4):2582–2594.

O'Brien, T., Tarduno, J. A., Anand, A., Smirnov, A. V., Blackman, E. G., Carroll-Nellenback, J., and Krot, A. N. (2020). Arrival and magnetization of carbonaceous chondrites in the asteroid belt before 4562 million years ago. *Communications Earth and Environment*, 1(54).

Paulevé, J., Dautreppe, D., Laugier, J., and Néel, L. (1962). Establishment of an ordered FeNi structure by neutron irradiation. *Comptes Rendus de L'Académie des Sciences*, 254:965.

Pauli, W. (1927). Zur Quantenmechanik des magnetischen Elektrons. *Zeitschrift für Physik*, 43(9-10):601–623.

Pauthenet, R. and Bochirol, L. (1951). Aimantation spontanée des ferrites. *Journal de Physique et le Radium*, 12(3):249–251.

Pierazzo, E., Artemieva, N., Asphaug, E., Baldwin, E. C., Cazamias, J., Coker, R., Collins, G. S., Crawford, D. A., Davison, T., Elbeshausen, D., Holsapple, K. A., Housen, K. R., Korycansky, D. G., and Wünnemann, K. (2008). Validation of numerical codes for impact

and explosion cratering: Impacts on strengthless and metal targets. *Meteoritics and Planetary Science*, 43(12):1917–1938.

Pierazzo, E. and Collins, G. (2004). A Brief Introduction to Hydrocode Modeling of Impact Cratering. In *Impact Studies*, pages 323–340. Springer, Berlin, Heidelberg.

Pierazzo, E., Kring, D. A., and Jay Melosh, H. (1998). Hydrocode simulation of the Chicxulub impact event and the production of climatically active gases. *Journal of Geophysical Research E: Planets*, 103(E12):28607–28625.

Pike, C. R., Roberts, A. P., and Verosub, K. L. (1999). Characterizing interactions in fine magnetic particle systems using first order reversal curves. *Journal of Applied Physics*.

Pike, C. R., Roberts, A. P., and Verosub, K. L. (2001). First-order reversal curve diagrams and thermal relaxation effects in magnetic particles. *Geophysical Journal International*.

Potter, R. W., Collins, G. S., Kiefer, W. S., McGovern, P. J., and Kring, D. A. (2012). Constraining the size of the South Pole-Aitken basin impact. *Icarus*, 220(2):730–743.

Potter, R. W., Kring, D. A., Collins, G. S., Kiefer, W. S., and McGovern, P. J. (2013). Numerical modeling of the formation and structure of the Orientale impact basin. *Journal of Geophysical Research: Planets*, 118(5):963–979.

Ramsden, A. and Cameron, E. (1966). Kamacite and taenite superstructures and a metastable tetragonal phase in iron meteorites. *The America Mineralogist*, 51(9-10):37–55.

Richert, A. J., Getman, K. V., Feigelson, E. D., Kuhn, M. A., Broos, P. S., Povich, M. S., Bate, M. R., and Garmire, G. P. (2018). Circumstellar disc lifetimes in numerous galactic young stellar clusters. *Monthly Notices of the Royal Astronomical Society*, 477(4):5191–5206.

Rietmeijer, F. J. and Mackinnon, I. D. (1985). Poorly graphitized carbon as a new cosmothermometer for primitive extraterrestrial materials. *Nature*, 315(6022):733–736.

Roberts, A. P., Heslop, D., Zhao, X., Oda, H., Egli, R., Harrison, R. J., Hu, P., Muxworthy, A. R., and Sato, T. (2022). Unlocking information about fine magnetic particle assemblages from first-order reversal curve diagrams: Recent advances.

Roberts, A. P., Heslop, D., Zhao, X., and Pike, C. R. (2014). Understanding fine magnetic particle systems through use of first-order reversal curve diagrams.

Roberts, A. P., Pike, C. R., and Verosub, K. L. (2004). First-order reversal curve diagrams: A new tool for characterizing the magnetic properties of natural samples. *Journal of Geophysical Research: Solid Earth*, 105(B12):28461–28475.

Roberts, A. P., Tauxe, L., Heslop, D., Zhao, X., and Jiang, Z. (2018). A Critical Appraisal of the "Day" Diagram. *Journal of Geophysical Research: Solid Earth*, 123(4):2618–2644.

Russell, S. S., Zolensky, M., Righter, K., Folco, L., Jones, R., Connolly, H. C., Grady, M. M., and Grossman, J. N. (2005). The Meteoritical Bulletin, No. 89, 2005 September. *Meteoritics & Planetary Science*, 40(S9):A201–A263.

Rutherford, M. E., Chapman, D. J., Derrick, J. G., Patten, J. R., Bland, P. A., Rack, A., Collins, G. S., and Eakins, D. E. (2017). Probing the early stages of shock-induced chondritic meteorite formation at the mesoscale. *Scientific Reports*, 7:45206.

Sahijpal, S., Soni, P., and Gupta, G. (2007). Numerical simulations of the differentiation of accreting planetesimals with 26Al and 60Fe as the heat sources. *Meteoritics and Planetary Science*, 42(9):1529–1548.

Sawaoka, A. B. (1993). *Shock Waves in Materials Science*. Springer, Tokyo, 1 edition.

Schmitz, B., Farley, K. A., Goderis, S., Heck, P. R., Bergström, S. M., Boschi, S., Claeys, P., Debaille, V., Dronov, A., van Ginneken, M., Harper, D. A., Iqbal, F., Friberg, J., Liao, S., Martin, E., Meier, M. M., Peucker-Ehrenbrink, B., Soens, B., Wieler, R., and Terfelt, F. (2019). An extraterrestrial trigger for the mid-Ordovician ice age: Dust from the breakup of the L-chondrite parent body. *Science Advances*, 5(9):4184–4202.

Schulte, P., Alegret, L., Arenillas, I., Arz, J. A., Barton, P. J., Bown, P. R., Bralower, T. J., Christeson, G. L., Claeys, P., Cockell, C. S., Collins, G. S., Deutsch, A., Goldin, T. J., Goto, K., Grajales-Nishimura, J. M., Grieve, R. A., Gulick, S. P., Johnson, K. R., Kiessling, W., Koeberl, C., Kring, D. A., MacLeod, K. G., Matsui, T., Melosh, J., Montanari, A., Morgan,

J. V., Neal, C. R., Nichols, D. J., Norris, R. D., Pierazzo, E., Ravizza, G., Rebolledo-Vieyra, M., Reimold, W. U., Robin, E., Salge, T., Speijer, R. P., Sweet, A. R., Urrutia-Fucugauchi, J., Vajda, V., Whalen, M. T., and Willumsen, P. S. (2010). The chicxulub asteroid impact and mass extinction at the cretaceous-paleogene boundary.

Scott, E. R., Keil, K., and Stöffler, D. (1992). Shock metamorphism of carbonaceous chondrites. *Geochimica et Cosmochimica Acta*, 56(12):4281–4293.

Shah, J., Bates, H. C., Muxworthy, A. R., Hezel, D. C., Russell, S. S., and Genge, M. J. (2017). Long-lived magnetism on chondrite parent bodies. *Earth and Planetary Science Letters*, 475:106–118.

Shah, J., Williams, W., Almeida, T. P., Nagy, L., Muxworthy, A. R., Kovács, A., Valdez-Grijalva, M. A., Fabian, K., Russell, S. S., Genge, M. J., and Dunin-Borkowski, R. E. (2018). The oldest magnetic record in our solar system identified using nanometric imaging and numerical modeling. *Nature Communications*, 9(1):9–14.

Shimada, M., Cho, A., and Yukutake, H. (1983). Fracture strength of dry silicate rocks at high confining pressures and activity of acoustic emission. *Tectonophysics*, 96(1-2):159–172.

Shuster, D. L. and Weiss, B. P. (2005). Planetary science: Martian surface paleotemperatures from thermochronology of meteorites. *Science*, 309(5734):594–597.

Snoek, J. L. (1947). *New Developments in Ferromagnetic Materials: With Introductory Chapters on the Statics and the Dynamics of Ferromagnetism.* Monographs on the progress of research in Holland during the war, 19. Elsevier Publishing Company.

Song, I. and Thadhani, N. N. (1992). Shock-induced chemical reactions and synthesis of nickel aluminides. *Metallurgical Transactions A*, 23(1):41–48.

Stacey, F. D. (1976). Paleomagnetism of Meteorites. *Annual Review of Earth and Planetary Sciences*, 4(1):147–157.

Stacey, F. D., Lovering, J. F., and Parry, L. G. (1961). Thermomagnetic properties, natural

magnetic moments, and magnetic anisotropies of some chondritic meteorites. *Journal of Geophysical Research*, 66(5):1523–1534.

Steele, A., Fries, M. D., Amundsen, H. E., Mysen, B. O., Fogel, M. L., Schweizer, M., and Boctor, N. Z. (2007). Comprehensive imaging and Raman spectroscopy of carbonate globules from Martian meteorite ALH 84001 and a terrestrial analogue from Svalbard. *Meteoritics and Planetary Science*, 42(9):1549–1566.

Steele, A., McCubbin, F. M., and Fries, M. D. (2016). The provenance, formation, and implications of reduced carbon phases in Martian meteorites. *Meteoritics and Planetary Science*, 51(11):2203–2225.

Steele, S., Volk, M., Fu, R. R., North, T. L., Brenner, A. R., Collins, G. S., Davison, T. M., and Muxworthy, A. R. (2022). Paleomagnetic Evidence for a Long-Lived Reversing Martian Dynamo at 3.9 Ga. In *53rd Lunar and Planetary Science Conference*.

Steele, S. C., Fu, R. R., Volk, M. W. R., North, T. L., Brenner, A. R., Collins, G. S., Davison, T. M., and Muxworthy, A. R. (2021). Paleomagnetic evidence for a long-lived reversing martian dynamo at ˜3.9 Ga. *Preprint*.

Stöffler, D. (1984). Glasses formed by hypervelocity impact. *Journal of Non-Crystalline Solids*, 67(1-3):465–502.

Stöffler, D., Keil, K., and Edward R.D, S. (1991). Shock metamorphism of ordinary chondrites. *Geochimica et Cosmochimica Acta*, 55(12):3845–3867.

Stoll, M. H. and Kley, W. (2014). Vertical shear instability in accretion disc models with radiation transport. *Astronomy and Astrophysics*, 572(A77):A77.

Sugiura, N. (1977). Magnetic Properties and Remanent Magnetization of Stony Meteorites. *Journal of geomagnetism and geoelectricity*, 29(6):519–539.

Tarduno, J. A., Cottrell, R. D., Nimmo, F., Hopkins, J., Voronov, J., Erickson, A., Blackman, E., Scott, E. R., and McKinley, R. (2012). Evidence for a dynamo in the main group pallasite parent body. *Science*, 338(6109):939–942.

Tarduno, J. A., O'brien, T. M., Blackman, E. G., and Smirnov, A. V. (2017). Magnetization of CV Meteorites in the Absence of a Parent Body Core Dynamo. In *Lunar and Planetary Science XLVIII*, page 2850.

Tauxe, L., Butler, R. F., van der Voo, R., and Banerjee, S. K. (2010). *Essentials of Paleomagnetism*. University of California Press, 1st edition.

Taylor, G. J. (1992). Core formation in asteroids. *Journal of Geophysical Research*, 97(E9):14717.

Thomas-Keprta, K. L., Bazylinski, D. A., Kirschvink, J. L., Clemett, S. J., McKay, D. S., Wentworth, S. J., Vali, H., Gibson, E. K., and Romanek, C. S. (2000). Elongated prismatic magnetite crystals in ALH84001 carbonate globules: Potential Martian magnetofossils. *Geochimica et Cosmochimica Acta*, 64(23):4049–4081.

Thomas-Keprta, K. L., Clemett, S. J., Bazylinski, D. A., Kirschvink, J. L., McKay, D. S., Wentworth, S. J., Vali, H., Gibson, E. K., McKay, M. F., and Romanek, C. S. (2001). Truncated hexa-octahedral magnetite crystals in ALH84001: Presumptive biosignatures. *Proceedings of the National Academy of Sciences of the United States of America*, 98(5):2164–2169.

Thompson, S. L. and Lauson, H. S. (1972). Improvements in the CHART D radiation-hydrodynamic code III: revised analytic equations of state. *Sandia National Laboratory Report*, SC-RR-71 0:113p.

Tikoo, S. M., Gattacceca, J., Swanson-Hysell, N. L., Weiss, B. P., Suavet, C., and Cournède, C. (2015). Preservation and detectability of shock-induced magnetization. *Journal of Geophysical Research E: Planets*, 120(9):1461–1475.

Tillotson, J. H. (1962). Metallic equations of state for hypervelocity impacts. *Report No. GA-3216, General Atomic, San Diego, CA*, page 43.

Treiman, A. H. (1995). A petrographic history of martian meteorite ALH84001: Two shocks and an ancient age. *Meteoritics*, 30(3):294–302.

Treiman, A. H. (1998). The history of Allan Hills 84001 revised: multiple shock events. *Meteoritics and Planetary Science*, 33(4):753–764.

Treiman, A. H. (2021). Uninhabitable and Potentially Habitable Environments on Mars: Evidence from Meteorite ALH 84001. *Astrobiology*, 21(8):940–953.

Treiman, A. H. and Essene, E. J. (2011). Chemical composition of magnetite in Martian meteorite ALH 84001: Revised appraisal from thermochemistry of phases in Fe-Mg-C-O. *Geochimica et Cosmochimica Acta*, 75(18):5324–5335.

Trigo-Rodriguez, J. M., Rubin, A. E., and Wasson, J. T. (2006). Non-nebular origin of dark mantles around chondrules and inclusions in CM chondrites. *Geochimica et Cosmochimica Acta*, 70(5):1271–1290.

Turner, G., Knott, S. F., Ash, R. D., and Gilmour, J. D. (1997). Ar-Ar chronology of the Martian meteorite ALH84001: Evidence for the timing of the early bombardment of Mars. *Geochimica et Cosmochimica Acta*, 61(18):3835–3850.

Turner, N. J., Fromang, S., Gammie, C., Klahr, H., Lesur, G., Wardle, M., and Bai, X.-N. (2014). Transport and Accretion in Planet-Forming Disks. In *Protostars and Planets VI*, page 411. University of Arizona Press.

Urpin, V. and Brandenburg, A. (1998). Magnetic and vertical shear instabilities in accretion discs. *Monthly Notices of the Royal Astronomical Society*, 294(3):399–406.

Van Schmus, W. R. and Wood, J. A. (1967). A chemical-petrologic classification for the chondritic meteorites. *Geochimica et Cosmochimica Acta*, 31(5):747–765.

van Thiel, M., Shaner, J., and Salinas, E. (1977). *Compendium of shock wave data*. Defense Technical Information Center, United States.

Wadhwa, M., Amelin, Y., Davis, a. M., Lugmair, G. W., Meyer, B., Gounelle, M., and Desch, S. (2007). From dust to planetesimals: implications for the solar protoplanetary disk from short-lived radionuclides in meteorites. In *Protostars and Planets V*, page 835. University of Arizona Press, 1st edition.

Wakita, S., Matsumoto, Y., Oshino, S., and Hasegawa, Y. (2017). Planetesimal Collisions As a Chondrule Forming Event. *The Astrophysical Journal*, 834(2):125.

Walsh, K. J., Morbidelli, A., Raymond, S. N., O'Brien, D. P., and Mandell, A. M. (2012). Populating the asteroid belt from two parent source regions due to the migration of giant planets-"The Grand Tack". *Meteoritics and Planetary Science*, 47(12):1941–1947.

Wang, H., Weiss, B. P., Bai, X. N., Downey, B. G., Wang, J., Wang, J., Suavet, C., Fu, R. R., and Zucolotto, M. E. (2017). Lifetime of the solar nebula constrained by meteorite paleomagnetism. *Science*, 355(6325):623–627.

Wang, H., Weiss, B. P., Downey, B. G., Wang, J., Chen-Wiegart, Y. K., Wang, J., Suavet, C. R., Fu, R. R., Lima, E. A., and Zucolotto, M. E. (2015). Onset of a Planetesimal Dynamo and the Lifetime of the Solar Nebular Magnetic Field. *46th Lunar and Planetary Science Conference*, 46(1832):2516.

Wardle, M. (2007). Magnetic fields in protoplanetary disks. In *Astrophysics and Space Science*.

Wasilewski, P. (1988). Magnetic characterization of the new magnetic mineral tetrataenite and its contrast with isochemical taenite. *Physics of the Earth and Planetary Interiors*, 52(1-2):150–158.

Watt, L. E., Bland, P. A., Prior, D. J., and Russell, S. S. (2006). Fabric analysis of Allende matrix using EBSD. *Meteoritics and Planetary Science*, 41(7):989–1001.

Weidenschilling and Cuzzi (2006). *Accretion Dynamics and Timescales: Relation to Chondrites*. University of Arizona Press, 1st edition.

Weidenschilling, S. J. (2000). Formation of planetesimals and accretion of the terrestrial planets. In *Space Science Reviews*, volume 92, pages 295–310. Springer.

Weinbruch, S., Armstrong, J., and Palme, H. (1994). Constraints on the thermal history of the Allende parent body as derived from olivine-spinel thermometry and Fe/Mg interdiffusion in olivine. *Geochimica et Cosmochimica Acta*, 58(2):1019–1030.

Weiss, B. P., Bai, X. N., and Fu, R. R. (2021). History of the solar nebula from meteorite paleomagnetism. *Science Advances*, 7(1).

Weiss, B. P., Berdahl, J. S., Elkins-Tanton, L., Stanley, S., Lima, E. A., and Carporzen, L. (2008a). Magnetism on the angrite parent body and the early differentiation of planetesimals. *Science*, 322(5902):713–716.

Weiss, B. P., Carporzen, L., Elkins-Tanton, L. T., Zuber, M. T., Shuster, D. L., Ebel, D. S., and Gattacceca, J. (2010a). Magnetic tests for partially differentiated chondrite parent bodies. Technical report, Lunar and Planetary Institute.

Weiss, B. P. and Elkins-Tanton, L. T. (2013). Differentiated Planetesimals and the Parent Bodies of Chondrites. *Annual Review of Earth and Planetary Sciences*, 41(1):529–560.

Weiss, B. P., Fong, L. E., Vali, H., Lima, E. A., and Baudenbacher, F. J. (2008b). Paleointensity of the ancient Martian magnetic field. *Geophysical Research Letters*, 35(23):23207.

Weiss, B. P., Gattacceca, J., Stanley, S., Rochette, P., and Christensen, U. R. (2010b). Paleomagnetic records of meteorites and early planetesimal differentiation. *Space Science Reviews*, 152(1-4):341–390.

Weiss, B. P., Kim, S. S., Kirschvink, J. L., Kopp, R. E., Sankaran, M., Kobayashi, A., and Komeili, A. (2004). Magnetic tests magnetosome chains in Martian meteorite ALH84001. *Proceedings of the National Academy of Sciences of the United States of America*, 101(22):8281–8284.

Weiss, B. P., Kirschvink, J. L., Baudenbacher, F. J., Vali, H., Peters, N. T., Macdonald, F. A., and Wikswo, J. P. (2000). A low temperature transfer of ALH84001 from Mars to Earth. *Science*, 290(5492):791–795.

Weiss, B. P., Vali, H., Baudenbacher, F. J., Kirschvink, J. L., Stewart, S. T., and Shuster, D. L. (2002). Records of an ancient Martian magnetic field in ALH84001. *Earth and Planetary Science Letters*, 201(3-4):449–463.

Weiss, P. (1907). L'hypothèse du champ moléculaire et la propriété ferromagnétique. *Journal de Physique Théorique et Appliquée*, 6(1):661–690.

Williamson, R. L. and Berry, R. A. (1986). Microlevel Numerical Modeling of the Shock Wave Induced Consolidation of Metal Powders. In *Shock Waves in Condensed Matter*, pages 341–346. Springer, Boston, MA.

Wlotzka, F. (1993). A weathering scale for the ordinary chondrites.

Wood, J. A. (1958). *Silicate Meteorite Structures and the Origin of Meteorites*. PhD thesis, MIT.

Woodruff, C., Dean, S. W., Cagle, C., Luke Croessmann, C., and Pantoya, M. L. (2022). Comparing pyrometry and thermography in ballistic impact experiments. *Measurement: Journal of the International Measurement Confederation*, 189:110488.

Wünnemann, K., Collins, G. S., and Melosh, H. J. (2006). A strain-based porosity model for use in hydrocode simulations of impacts and implications for transient crater growth in porous targets. *Icarus*, 180(2):514–527.

Wünnemann, K. and Ivanov, B. A. (2003). Numerical modelling of the impact crater depth-diameter dependence in an acoustically fluidized target. *Planetary and Space Science*, 51(13):831–845.

Wünnemann, K., Morgan, J. V., and Jödicke, H. (2005). Is ries crater typical for its size? An analysis based upon old and new geophysical data and numerical modeling. *Special Paper of the Geological Society of America*, 384:67–83.

Wurm, G., Paraskov, G., and Krauss, O. (2004). On the Importance of Gas Flow through Porous Bodies for the Formation of Planetesimals. *The Astrophysical Journal*, 606(2):983–987.

Ye, J., Newell, A. J., and Merrill, R. T. (1994). A re-evaluation of magnetocrystalline anisotropy and magnetostriction constants. *Geophysical Research Letters*, 21(1):25–28.